NORTHWESTERN UNIVERSITY

THE NATURE OF TRANSVERSE BEAM INSTABILITIES AT INJECTION IN THE FERMILAB MAIN RING

A DISSERTATION

SUBMITTED TO THE GRADUATE SCHOOL

IN PARTIAL FULFILLMENT OF THE REQUIREMENTS

for the degree

DOCTOR OF PHILOSOPHY

Field of Physics

By

Ping-Jung Chou

EVANSTON, ILLINOIS

December 1995

ABSTRACT

The Nature of Transverse Beam Instabilities at Injection in the Fermilab Main Ring

Ping-Jung Chou

Transverse beam instabilities have been observed in the Fermilab Main Ring since 1972. It was well controlled by two active feedback systems until the last fix target run in 1991. The current upgrade of accelerator facilities, where the replacement of the Main Ring by the Main Injector will allow acceleration of higher proton intensities, makes the importance of this issue surface again. Experimental studies were conducted to understand the nature and the cause of these transverse beam instabilities. The interplay between accelerator parameters and the growth rate of transverse beam oscillations is investigated. Some previously puzzling behavior of the Main Ring is now understood because of the knowledge gained from these studies. Experimental techniques were implemented to measure some important parameters of the Main Ring, such as the vertical impedance, bunch form factor, and the wake function. Empirical theory is devised to understand the coupled bunch instability with many distributed gaps, and a satisfactory agreement is obtained between the analysis and the measured data. The cause of the transverse beam instabilities is identified to be the resistive wall impedance. Anomalous behavior in the frequency dependence of the impedance below the MHz range suggests that impedance sources other than the resistive wall also exist in the Main Ring. The performance of two active feedback systems is found to be inadequate to meet the goal of the Main Injector accelerator upgrade. Suggestions for hardware improvements and the choice of accelerator parameters are given.

to my Parents

for their persistent support in my education.

ACKNOWLEDGMENTS

When I was a physics major in college, I wanted to be a theoretician. My mind was not changed until I met my thesis advisor, Dr. Gerald P. Jackson of Fermilab, who was a visiting professor teaching a class at Northwestern University in 1990. I was intrigued by the broad scope of experimental accelerator physics and its interrelation to other disciplines of science. Eventually he persuaded me to choose an experimental subject as my thesis topic. During my time at Fermilab, he taught me to appreciate the joy of hands-on work and how physics should be done. Through private discussions, his style of doing physics had a definite impact on my own. That experience is the best lesson I have learned from him, and I am very grateful.

I want to thank my academic advisor at Northwestern University, Professor Robert Oakes, for his constant encouragement and concern about the progress of my learning at Fermilab. I also want to thank Dr. Patrick Colestock and Dr. Alan Hahn at Fermilab for many instructive discussions. A number of people in the RF/ Instrumentation Department of the Accelerator Division at Fermilab taught me the hands-on knowledge of rf electronics. I thank them for their kind help. Especially I want to thank Brian Fellenz for his devoted assistance in the construction of diagnostic devices which were essential to the success of my thesis project.

During this lengthy period of accelerator study, I received a great deal of help from many people in the Operation Department of the Accelerator Division. I thank them for their help and tolerance of my excessive demand for beam study time. I also want to thank former and fellow graduate students at Fermilab, Xianping, Linda, Yi-Cheng, Ssu-Min and Eric for their friendship and enjoyable stimulating discussions.

Finally I want to express my gratitude to my college advisor, Professor Cheng-Shiung Hsue at National Tsing Hua University in Taiwan, for introducing me to accelerator physics when I was a senior in college.

TABLE OF CONTENTS

CHAPTER 6. DISCUSSIONS AND SUGGESTIONS

LIST OF FIGURES

LIST OF TABLES

CHAPTER 1

INTRODUCTION

A. The relevant issues at Fermilab

1. A brief description about Fermilab facilities

Fermi National Accelerator Laboratory was started in 1968[1] and led by Robert Rathbun Wilson, who was the head of the cyclotron group in the Manhattan project.[2] A 400 GeV proton accelerator was commissioned[1] in 1972 and named the Main Ring.

Historically the Main Ring was used to provide high energy protons for fixed target experiments. Main Ring is a circular accelerator with a mean radius of 1 km. It employs the alternating-gradient strong focusing design[3] for the accelerator lattice. It has 18 rf cavities for particle acceleration.[3] When it is completely filled, the Main Ring can store 1113 equally spaced bunches. It takes approximately 13 booster batches to fill the Main Ring, where a booster batch is composed of 84 bunches.

In order to double the beam energy, Fermilab built a 1 TeV accelerator in the same tunnel as the Main Ring, called the Tevatron. At that time the Main Ring was converted into an injector for the Tevatron. Nowadays the Main Ring is mainly used to produce antiprotons for collider physics experiments performed in the Tevatron. Proton beams are injected into the Main Ring at 8 GeV from the Booster synchrotron and accelerated to 120 GeV. When the proton beams reach 120 GeV, they are directed towards a target to produce antiprotons. An aerial layout of Fermilab is depicted in Fig. 1.1.

2. A review of transverse beam instabilities in the Main Ring

There are two types of beam instabilities present in the Main Ring: incoherent single particle effects and coherent collective effects. The single particle effects result from the interaction between a charged particle and the imperfections of the magnetic fields in the magnets. The collective effects result from the electromagnetic interaction between a charged particle and other particles (and itself) through a coupling mechanism provided by the vacuum chamber. The collective instability depends on the beam intensity. The larger the beam intensity, the more severe the instability. The effects created by the collective beam instabilities are: limitation of maximum stored beam intensity, deterioration of beam quality, and the possibility of beam loss.

During the commissioning of the Main Ring in early 1972, people already noticed the existence of transverse collective instabilities at injection in the Main Ring.[4] It was found to have a threshold intensity of approximately 10^{12} protons. It was also found that the vertical direction had a lower threshold, presumably because of the smaller size of vacuum chamber in the vertical direction. An active damper system with a frequency bandwidth from 5 kHz to 2.5 MHz was built to damp the transverse collective instabilities. It was installed in both horizontal and vertical planes. The 2.5 MHz damper system was named the slow damper. Later on a bunch-by-bunch damper system was installed in the vertical plane and named the super damper. The super damper has a frequency bandwidth from 5 kHz to 27 MHz.

During the last fixed target run from 1989 to 1991, Main Ring suffered from vertical beam instabilities which limited the maximum beam intensity in the Main Ring to 2×10^{13} protons. The results of machine studies suggest that the resistive wall impedance is responsible for the observed multibunch instability.[5] It was also found that the growth rate of the vertical instability was sensitive to the bunch length and machine

chromaticity. Those findings indicate the possibility of vertical head-tail instability in the Main Ring.

3. Motivation of this thesis work

Currently there is an accelerator upgrade called Fermilab III underway to improve the performance of the Tevatron. A new 150 GeV accelerator, the Main Injector, is under construction which will replace the existing Main Ring in 1999. The design parameters of the Main Injector are shown in Table 1.1.[6, 7] Since the beam intensity will be higher and the bunch length will be much shorter in the Main Injector, issues about transverse beam instabilities need to be studied.

In the meantime, the Main Ring will still serve as the injector of the Tevatron for the next fixed target run beginning in mid 1996. The goal for the next fixed target run is shown in Table 1.2,[6, 7] a factor of two increase in the Main Ring intensity from the previous run. This prompts the concern about the vertical beam instabilities observed during the last fixed target run. There has been observations of a horizontal beam instability in the Tevatron at 800 GeV flattop during fixed target runs when the beam intensity was over 2×10^{13}. However, it was not observed during the last fixed target run since the beam intensity was relatively low.

At present the total proton intensity in the Tevatron is 1.4×10^{12}. The goal of the Fermilab III upgrade is to store 1×10^{13} protons in the Tevatron as shown in Table 1.3.[6, 7] The upgrade project also calls for an increase of total antiprotons by a factor of five in the Tevatron. The bunch spacing after the Tevatron upgrade will be one ninth of the previous value. Those changes will make Tevatron more susceptible to beam instabilities.

From a short-term point of view, it is very important to understand and solve the transverse beam instabilities which plagued the performance of Main Ring during the last fixed target run. From a long-term point of view, this thesis work can provide a training ground or head start for dealing with possible transverse beam instabilities in the Main Injector and Tevatron after the Fermilab III upgrade.

4. Units and dimensions

The goal of this thesis work is to answer some operational issues faced by a circular accelerator. Therefore, the MKS units will be used throughout the entire contents. The convention $\exp(ikz\text{-}i\omega t)$ is used throughout the text to describe the time evolution of a sinusoidal wave.

Table 1.1. Current parameters for the Main Ring and the design goal for the Main Injector.

Parameter	Main Ring	Main Injector
total protons ($\times 10^{13}$)	2.0	3
protons/bunch ($\times 10^{10}$)	1.98	6
bunch length (nsec)	11	5

Table 1.2. Main Ring parameters for the last and the next fixed target runs.

	1991 best record	1996 goal
total protons ($\times 10^{13}$)	2	4
protons/bunch ($\times 10^{10}$)	2	4

Table 1.3. Tevatron parameters for the current collider run and the future upgrade.

	1995 Run Ib	1999 Run II	Ratio of parameters (1999 / 1995)
total protons ($\times 10^{13}$)	0.14	0.97	6.5
total antiprotons ($\times 10^{12}$)	0.39	2.0	5.1
protons/bunch ($\times 10^{11}$)	2.3	2.7	1.2
antiprotons/bunch ($\times 10^{10}$)	6.5	5.5	0.9
number of bunches	6	36	6
bunch spacing (nsec)	3500	396	0.11

B. Single particle motion in a circular accelerator

1. Longitudinal motion

When one wants to accelerate charged particles in a circular accelerator, the naive idea is to use dc acceleration. Since the electrostatic field is conservative, the line integral of the electric field along the accelerator is zero for one revolution. Faraday's Law shows that there will be no net energy gain. Therefore, one needs to use a time-alternating electrical field to accelerate charged particles for nonzero energy gain after one revolution. High power rf cavities are used for particle acceleration in modern accelerators.

For a charged particle in a circular accelerator traveling with speed υ, the revolution period is $T = L/\upsilon$, where L is the circumference of accelerator. The revolution period is different for particles with different energy. The fractional change of revolution period relative to the particle of design energy is given by the following derivations:

$$\frac{dT}{T} = \frac{dL}{L} - \frac{d\upsilon}{\upsilon} \tag{1.1}$$

$$dp = m_0\, d\left(\frac{\upsilon}{\sqrt{1-\upsilon^2/c^2}}\right) \tag{1.2}$$

$$\upsilon\frac{dp}{d\upsilon} = \frac{m_0\upsilon}{(1-\upsilon^2/c^2)^{3/2}} = \gamma^2 p \tag{1.3}$$

$$\therefore \frac{dT}{T} = \frac{dL}{L} - \frac{1}{\gamma^2}\frac{dp}{p} \tag{1.4}$$

Introducing the following definitions:

$$\frac{dL}{L} \equiv \frac{1}{\gamma_t^2}\frac{dp}{p} \tag{1.5}$$

$$\eta \equiv \frac{1}{\gamma_t^2} - \frac{1}{\gamma^2} \tag{1.6}$$

$$\therefore \frac{dT}{T} = \eta\frac{dp}{p} \tag{1.7}$$

where p is the kinetic momentum, γ_t is a parameter dependent on the accelerator lattice design, γ is the Lorentz relativistic factor and dp, dT are the deviations of momentum and revolution period with respect to the synchronous particle which satisfies the design parameters.

Accelerator physicists call η as the phase slip factor. Apparently one will get $\eta = 0$ for particle energy at $\gamma = \gamma_t$. This is called the transition energy of accelerator, which depends on the lattice design of each individual accelerator. When the particle energy is above transition ($\eta > 0$), those particles which have higher energy than the design value will take a longer time to travel around the accelerator according to Eq.(1.7). When the particle energy is below transition ($\eta < 0$), those particles which have higher energy than the design value will take less time to travel around the accelerator. With proper arrangement of the accelerating phase between the particles and the rf accelerating voltage, one can get longitudinal focusing. Figure 1.2 depicts the longitudinal positions for off-energy particles in the presence of rf accelerating voltage in two successive turns.

For the case of below transition ($\eta < 0$) in Fig. 1.2, the particle with $dp > 0$ will arrive earlier than the synchronous particle in the next turn and the particle with $dp < 0$ will

arrive later according to Eq.(1.7). Therefore, the dp> 0 particle will receive less accelerating voltage than the synchronous particle and the dp< 0 particle will receive more accelerating voltage than the synchronous particle in the next turn. This process will keep the off-energy particles in the vicinity of synchronous particle, in other words the energy spread of particles will be confined within certain limit. This is the mechanism of longitudinal focusing. Since those particles trapped in the local potential well created by the rf accelerating voltage will always stay in the vicinity of synchronous particle, the result of longitudinal focusing is the beam bunching. If one looks at the longitudinal phase space corresponding to Fig. 1.2, one will get the picture depicted in Fig. 1.3.

The longitudinal focusing effect keeps particles inside a stable bucket area whose shape and size are determined by the rf accelerating voltage and other accelerator parameters. Inside this bucket area, the particles undergo periodic circulation in longitudinal phase space. Outside this bucket area, particles with too large a momentum error cannot gain or lose enough energy to reverse sign, and are therefore not focussed. The longitudinal motion of particles inside a beam bunch is called the synchrotron oscillation. If one defines the longitudinal phase of a test particle in the n-th turn according to Fig. 1.4, one can write down the phase of the test particle in the next turn as following:

$$\phi_{n+1} = \phi_n + \omega_{rf} \cdot dT_{n+1} \tag{1.8}$$

The relation between the particle energy and momentum is given by the following relations:

$$E = \gamma m_0 c^2 = pc^2 / \upsilon \tag{1.9}$$

$$E^2 = p^2 c^2 + m_0^2 c^4 \tag{1.10}$$

The differential equations following after Eqs.(1.9) and (1.10) are:

$$E \cdot dE = c^2 p \cdot dp \tag{1.11}$$

$$\frac{dp}{p} = \frac{1}{\beta^2}\frac{dE}{E} \tag{1.12}$$

By using Eqs.(1.7) and (1.12) one has the expression for the longitudinal phase of the test particle in the next turn:

$$\phi_{n+1} = \phi_n + \frac{\eta \omega_{rf} T_s}{\beta^2 E_s} \Delta E_n \tag{1.13}$$

, and the energy deviation is:

$$\Delta E_{n+1} = \Delta E_n + eV(\sin\phi_n - \sin\phi_s) \tag{1.14}$$

where e= the charge of a particle, ϕ_n= the phase of the particle relative to the rf voltage in the n-th turn, ω_{rf}= the angular rf frequency, V= the amplitude of rf voltage, ϕ_s= the phase of synchronous particle relative to the rf voltage, $\beta = \upsilon/c$, ΔE= the energy deviation relative to the synchronous particle, T_s= the revolution period of the synchronous particle, and E_s= the design energy.

If one combines Eqs.(1.13) and (1.14) and assumes that the variations are small enough to use the time average over one revolution period, one will get a second order differential equation[3] which describes the synchrotron oscillation:

$$\frac{d^2\phi}{dn^2} - \frac{\eta e V \omega_{rf} T_s}{\beta^2 E_s}(\sin\phi - \sin\phi_s) = 0 \tag{1.15}$$

The above approximation scheme is called the smooth approximation.

Equation (1.15) is inherently nonlinear because of the nonlinear nature of the sinusoidal accelerating voltage. When the phase deviation relative to the synchronous particle is small, one can linearize Eq.(1.15) as:

$$\frac{d^2\bar{\phi}}{dn^2} - \frac{\eta e V \omega_{rf} T_s}{\beta^2 E_s}\cos\phi_s \cdot \bar{\phi} \approx 0 \tag{1.16}$$
$$\bar{\phi} = \phi - \phi_s$$

where $\bar{\phi}$ is the relative phase deviation with respect to the synchronous particle. If one changes the variable from the turn index to time, the equation of motion will become:

$$\frac{d^2\bar{\phi}}{dt^2} - \frac{\eta e V \omega_{rf}}{\beta^2 E_s T_s}\cos\phi_s \cdot \bar{\phi} \approx 0 \tag{1.17}$$

For small phase deviation the synchrotron oscillation has exactly the same form as the motion of a harmonic oscillator. From Eq.(1.17) one has the frequency of synchrotron oscillation f_s as:

$$f_s = \frac{1}{2\pi}\sqrt{\frac{-\eta eV\omega_{rf}\cos\phi_s}{\beta^2 E_s T_s}} \tag{1.18}$$

The equivalent form of potential energy for this synchrotron harmonic oscillator can be derived from Eq.(1.16), the result is:

$$\text{P.E.} = -\frac{\eta eV\omega_{rf}T_s\cos\phi_s}{2\beta^2 E_s}\cdot\bar{\phi}^2 \tag{1.19}$$

From Eqs.(1.7) and (1.12) one can write down the equivalent form of velocity for this oscillator, which is:

$$\frac{d\bar{\phi}}{dn} = \frac{\eta\omega_{rf}T_s}{\beta^2 E_s}\Delta E \tag{1.20}$$

The Hamiltonian of this oscillator is given by:

$$\begin{aligned}&\text{P.E.} + \frac{1}{2}\left(\frac{d\bar{\phi}}{dn}\right)^2 \\ &= (\Delta E)^2 + \left(\frac{\beta^2 E_s eV\cos\phi_s}{-\eta\omega_{rf}T_s}\right)\cdot\bar{\phi}^2 = \text{constant}\end{aligned} \tag{1.21}$$

Equation (1.21) gives the particle trajectory in the ΔE-ϕ phase space for a given initial condition. The trajectory is an ellipse in the ΔE-ϕ phase space, just what one will expect from a harmonic oscillator. For larger oscillation amplitudes, the general result for the Hamiltonian is given by:[3]

$$\Delta E^2 + \frac{2\beta^2 E_s eV}{\eta \omega_{rf} T_s}\left(\cos(\bar{\phi} + \phi_s) + (\bar{\phi} + \phi_s)\sin\phi_s\right) = \text{constant.} \qquad (1.22)$$

An example of the longitudinal phase space is depicted in Figs. 1.5.

The number of synchrotron oscillation cycles completed per turn is defined as the synchrotron tune. The synchrotron tune equals the synchrotron frequency divided by the revolution frequency. The ratio of the rf frequency to the revolution frequency is defined as the harmonic number, *h*, an integer which gives the maximum number of bunches in an accelerator.

The stable area in the phase space occupied by the particle beams is called the longitudinal emittance. In the non-accelerating case, the longitudinal emittance, S, for particles undergoing small oscillation is given by the area of the following ellipse:

$$\frac{(\Delta E)^2}{\left(\frac{\beta^2 E_s eV\cos\phi_s}{-\eta\omega_{rf}T_s}\right)\hat{\phi}^2} + \frac{\bar{\phi}^2}{\hat{\phi}^2} = 1 \qquad (1.23)$$

where $\hat{\phi}$ is the maximum phase excursion from the synchronous particle for a given initial condition. The area of this ellipse in the ΔE-$\bar{\phi}$ coordinate space is given by:

$$S = \pi\hat{\phi}^2\sqrt{\frac{\beta^2 E_s eV\cos\phi_s}{-\eta\omega_{rf}T_s}} \qquad (1.24)$$

The longitudinal emittance is an invariant quantity for a non-accelerating beam. From Eq.(1.24) one readily realizes that the bunch length is proportional to $V^{-1/4}$ when

the linear approximation is valid. Generally one has to calculate the bunch length numerically.

2. Transverse motion

The coordinate system used to describe particle motion in an accelerator is depicted in Fig. 1.6, where $\overline{R}$ is the mean radius of accelerator, s is the tangential coordinate along the design orbit, y is the vertical displacement and x is the horizontal displacement with respect to the design orbit.

In a circular accelerator, dipole magnets are used to provide a uniform magnetic field to guide the charged particles and quadrupole magnets are used to focus those particles which deviate from the design orbit. An example of conventional, iron-cored, direct-current magnets is depicted in Fig. 1.7.

Assume there is no magnetic solenoid in the accelerator. A particle traveling in a circular accelerator in the horizontal plane with speed υ will experience the transverse force described by the following equations:

$$\begin{aligned} m\ddot{x}(t) &= (e\bar{\upsilon}\times\bar{B})_x + \frac{m\upsilon^2}{\overline{R}+x} \\ &= -e\upsilon B_y + \frac{m\upsilon^2}{\overline{R}+x} \end{aligned} \tag{1.25}$$

$$\begin{aligned} m\ddot{y}(t) &= (e\bar{\upsilon}\times\bar{B})_y \\ &= e\upsilon B_x \end{aligned} \tag{1.26}$$

where $\upsilon=\upsilon_0 + d\upsilon$, υ_0 is the velocity corresponding to the design energy. For the lowest order approximation, the magnetic fields near the design orbit can be approximated as:

$$B_x(s,x,y) = B_x(s,0,0) + x\frac{\partial B_x(s,0,0)}{\partial x} + y\frac{\partial B_x(s,0,0)}{\partial y} \tag{1.27}$$

$$B_y(s,x,y) = B_y(s,0,0) + y\frac{\partial B_y(s,0,0)}{\partial y} + x\frac{\partial B_y(s,0,0)}{\partial x} \tag{1.28}$$

The design field of a dipole magnet is given by $B_y(s, 0, 0)$ only. The design field of a quadrupole magnet is given by $x\cdot(\partial B_y/\partial x)$ for the x direction and $y\cdot(\partial B_x/\partial y)$ for the y direction. Therefore, one can rewrite Eqs.(1.25) and (1.26) as:

$$m\ddot{x}(t) + \left[e\upsilon\frac{\partial B_y}{\partial x} + \frac{m\upsilon^2}{\bar{R}^2}\right]x(t) = -e\upsilon B_y + \frac{m\upsilon^2}{\bar{R}} \tag{1.29}$$

$$m\ddot{y}(t) - e\upsilon\frac{\partial B_x}{\partial y}y(t) = 0 \tag{1.30}$$

The design field of a dipole magnet is related to the design energy by the following relation:

$$\frac{p_0}{\bar{R}} = eB_y(s,0,0) \tag{1.31}$$

where p_0 is the design momentum. Substituting Eq.(1.31) to Eqs.(1.29), (1.30) and replacing $\frac{d}{dt}$ by $\upsilon\frac{d}{ds}$, one will get the following results:

$$x''(s) + \left[\frac{1}{\bar{R}B_y}\frac{\partial B_y}{\partial x}(1-\frac{dp}{p_0}) + \frac{1}{\bar{R}^2}\right]x(s) = \left(\frac{dp}{p_0}\right)\frac{1}{\bar{R}} \tag{1.32}$$

$$y''(s)+\left[\frac{-1}{\bar{R}B_y}\frac{\partial B_x}{\partial y}(1-\frac{dp}{p_0})\right]y(s)=0 \qquad (1.33)$$

Equations (1.32) and (1.33) describe the transverse motion of a charged particle in a circular accelerator.

When the particle is in the straight sections where only quadrupole magnets reside, one has the curl condition as $\nabla\times\bar{B}=0$. This gives the following relation:

$$\frac{\partial B_y}{\partial x}=\frac{\partial B_x}{\partial y} \qquad (1.34)$$

From Eqs.(1.32)– (1.34) one can conclude that it is not possible to have focusing in both transverse directions simultaneously. To keep charged particles near the design orbit, one needs to provide an alternating array of quadrupole magnets, e.g. Fig. 1.8.

The effect produced by an alternating array of quadrupole magnets is a potential well which causes particles to oscillate around the design orbit. This oscillatory motion is called the betatron oscillation. The number of betatron oscillation cycles completed in one revolution period is called the betatron tune, Q_β.

For particles at the design energy, the transverse motion described by Eqs.(1.32) and (1.33) can be expressed as:

$$x''(s)+K(s)x(s)=0 \qquad (1.35)$$

where K(s)= K(s+L) for a circular accelerator, L= $2\pi\bar{R}$= circumference of accelerator.

Equation (1.35) is known as the Hill's equation. Its solution can be written in a closed form which closely resembles the solution of a simple harmonic oscillator:[8]

$$x(s) = \sqrt{\varepsilon\beta_x(s)}\cos\phi(s) \text{ or } \sqrt{\varepsilon\beta_x(s)}\sin\phi(s)$$
$$\phi(s) = \int_{s_0}^{s} \frac{ds'}{\beta_x(s')} \tag{1.36}$$

where $\beta_x(s)$ is called the betatron function, $\phi(s)$ is the betatron phase and ε is a constant of motion called the Courant-Synder invariant.[8] The betatron function is determined by the arrangement of all magnets in the accelerator.

For given initial conditions, the solution of betatron oscillation can be written as:[8]

$$\begin{bmatrix} x(s) \\ x'(s) \end{bmatrix} = \begin{bmatrix} C(s,s_0) & S(s,s_0) \\ C'(s,s_0) & S'(s,s_0) \end{bmatrix} \cdot \begin{bmatrix} x(s_0) \\ x'(s_0) \end{bmatrix} \tag{1.37}$$

where $C(s, s_0)$ is a cosine-like function and $S(s, s_0)$ is a sine-like function. The transfer matrix in Eq.(1.37) is given by:[8]

$$M(s,s_0) = \begin{bmatrix} C(s,s_0) & S(s,s_0) \\ C'(s,s_0) & S'(s,s_0) \end{bmatrix} =$$
$$\begin{bmatrix} \sqrt{\frac{\beta_x}{\beta_{x0}}}(\cos\phi + \alpha_0 \sin\phi) & \sqrt{\beta_x\beta_{x0}}\sin\phi \\ \frac{\alpha_0-\alpha}{\sqrt{\beta_x\beta_{x0}}}\cos\phi - \frac{1+\alpha\alpha_0}{\sqrt{\beta_x\beta_{x0}}}\sin\phi & \sqrt{\frac{\beta_{x0}}{\beta_x}}(\cos\phi - \alpha\sin\phi) \end{bmatrix} \tag{1.38}$$

where $\alpha(s) = -\beta_x'(s)/2$. The transverse betatron motion has the following property:

$$\begin{bmatrix} x(s_2) \\ x'(s_2) \end{bmatrix} = M(s,s_1)M(s_1,s_0)\begin{bmatrix} x(s_0) \\ x'(s_0) \end{bmatrix} \tag{1.39}$$

For the off-energy particles, the equation of motion is given by:

$$x''(s) + K(s)x(s) = \left(\frac{dp}{p_0}\right)\frac{1}{\overline{R}} \tag{1.40}$$

One needs to find the inhomogeneous solution $x_p(s)$ which satisfies the closure condition after on revolution in a circular accelerator. The inhomogeneous solution is given by:[8]

$$\begin{aligned} x_p(s) &= \frac{dp}{p_0}D(s) \\ D(s) &= \int_0^s \frac{1}{\overline{R}}[S(s)C(s') - C(s)S(s')]ds' \end{aligned} \tag{1.41}$$

where D(s) is called the dispersion function and D(s)=D(s+L). The transverse displacement x(s) equals to $x_\beta(s)$ + $(dp/p_0)D(s)$, where $x_\beta(s)$= the betatron oscillation given by Eq.(1.36), and $(dp/p_0)D(s)$= the dispersion displacement caused by bending magnets.

The energy spread among particles will cause the off-energy particles to experience different focusing strength when they pass through quadrupole magnets according to Eqs.(1.32) and (1.33). This effect results in a slightly different betatron tune for particles with different energies. To characterize this energy-dependent effect, a quantity called chromaticity, ξ, is defined as the following:

$$\xi = \frac{dQ_\beta}{dp/p} \tag{1.42}$$

where dQ_β is the deviation of tune with respect to the design value.

So one can approximate Eq.(1.35) as a pseudo-harmonic oscillation:

$$x''(s)+\left(\frac{Q_\beta}{\bar{R}}\right)^2 x(s)=0 \tag{1.43}$$

The above result can also be written in terms of the time derivative as:

$$\begin{aligned}&\ddot{x}(t)+\omega_\beta^2 x(t)=0\\&\omega_\beta=Q_\beta\omega_0=\frac{2\pi Q_\beta}{T}\end{aligned} \tag{1.44}$$

where ω_β equals to the product of betatron tune Q_β and the angular revolution frequency ω_0, ω_β is called the angular betatron frequency.

In reality there are always imperfections of the magnetic fields in the magnets. When the transverse tune is not chosen properly, those imperfections of magnetic fields can drive the beam resonantly to unbounded betatron oscillation amplitudes. When the horizontal and the vertical tune, Q_x and Q_y, satisfy the following relation:[3]

$$MQ_x+NQ_y=P \tag{1.45}$$

where M, N, and P are integers all of the same sign; the transverse motion may be unstable. The sum of the absolute values of M and N is the order of the resonance. An example of the tune plot showing resonances is depicted in Fig. 1.9. The most common field errors are: *i)* dipole and quadrupole errors which cause the integer and the half-integer resonance respectively *ii)* sextupole errors which cause the third-integer resonance *iii)* octupole and decapole errors which cause the fourth order and the fifth order resonance respectively. A summary table of Main Ring parameters at the injection stage is depicted in Table 1.4.

Table 1.4. Main Ring parameters at the injection energy (8 GeV).

Parameter	Value
transition energy (γ_t)	18.75
mean radius ($\overline{R}$)	1 km
revolution frequency (f_0)	47.4 kHz
nominal tune ($Q_{x,y}$)	19.44
phase slip factor (η)	-0.0083
harmonic number (h)	1113
chromatic frequency ($f_\xi = \xi f_0/\eta$)[a]	5.7 MHz
synchrotron frequency (f_s)[b]	546 Hz

[a]For one unit of chromaticity.
[b]For rf voltage set at 0.8 MV.

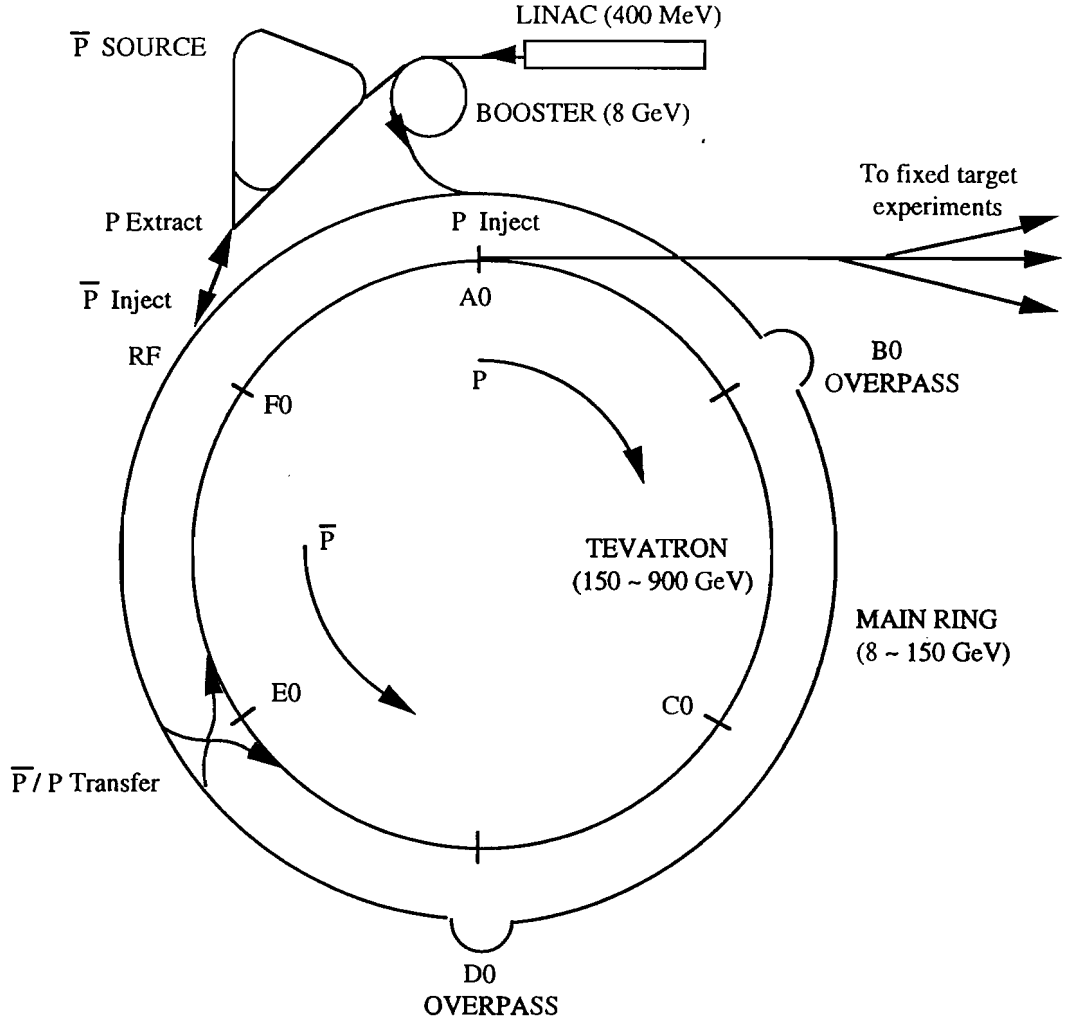

Fig. 1.1. The current layout of accelerator facilities at Fermi National Accelerator Laboratory, Chicago, Illinois, U.S.A. Currently there are two detectors for collider experiments at the B0 and D0 locations respectively. A new circular accelerator called the Main Injector is under construction. It will replace the Main Ring in Collider Run II in 1999.[6]

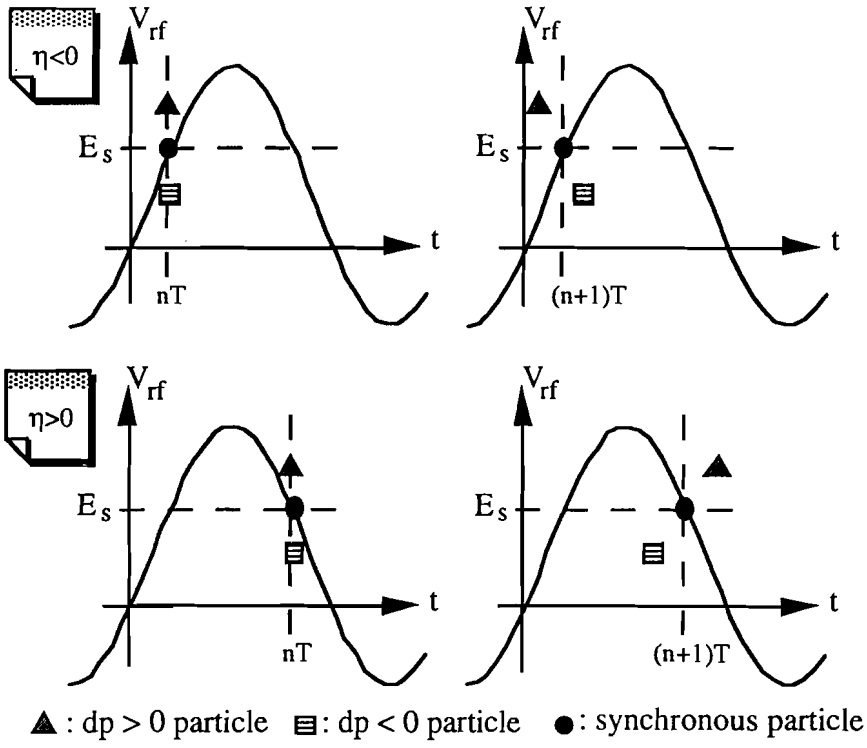

Fig. 1.2. The longitudinal positions for off-energy particles in the presence of rf accelerating voltage in two successive turns.

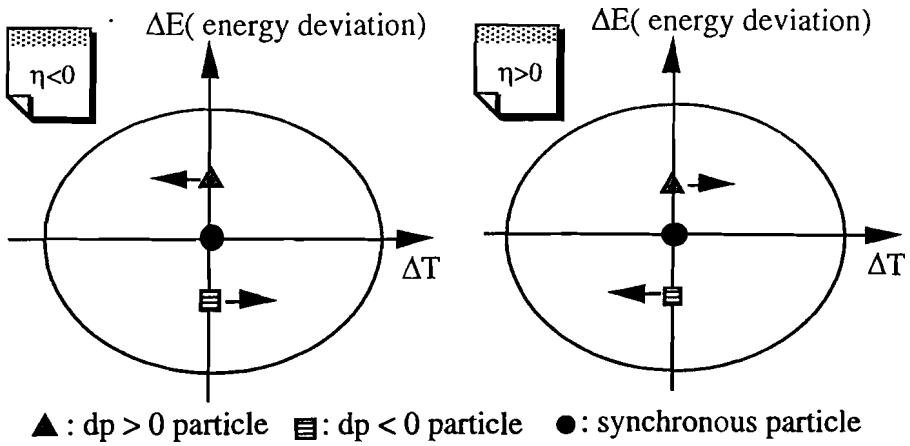

Fig. 1.3. The motion of off-energy particles relative to the synchronous particle in longitudinal phase space. The horizontal coordinate is the temporal position relative to the synchronous particle.

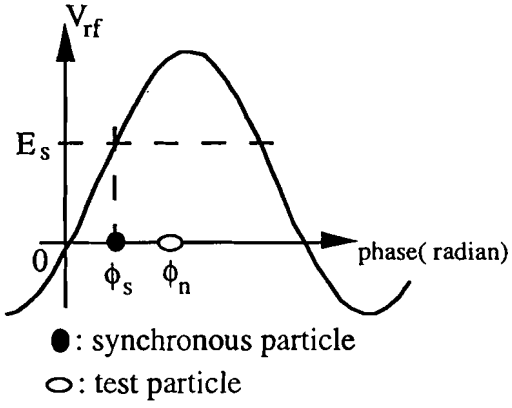

Fig. 1.4. The definition of longitudinal phase for a test particle.

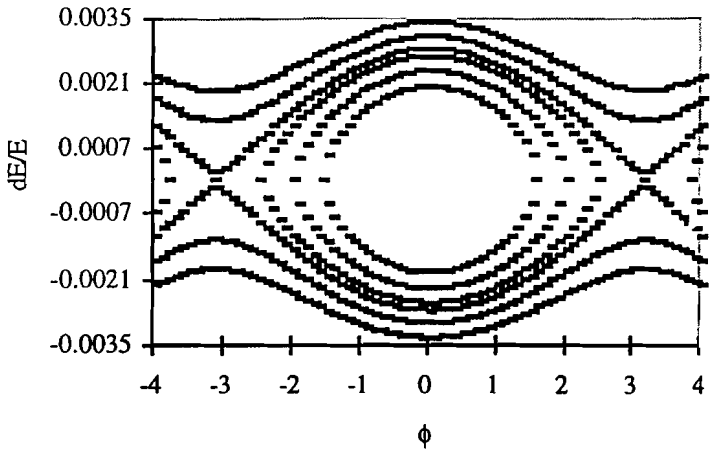

Fig. 1.5. Particle trajectories in the longitudinal phase space for different initial conditions. This contour plot repeats with a period of 2π.

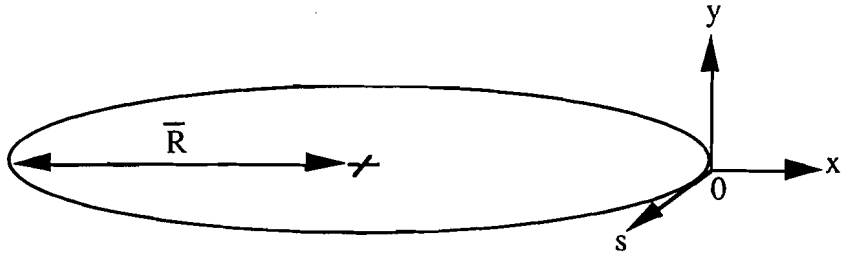

Fig. 1.6. The coordinate system used in the analysis.

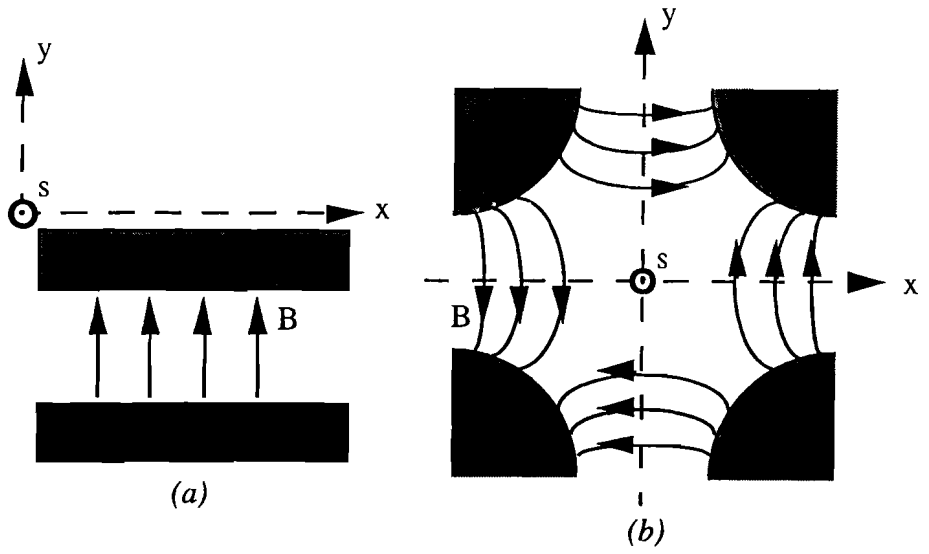

Fig. 1.7. A cross-sectional view of magnetic field lines for various kinds of magnets *(a)* the pole face of a dipole bending magnet *(b)* the pole face of a quadrupole magnet.

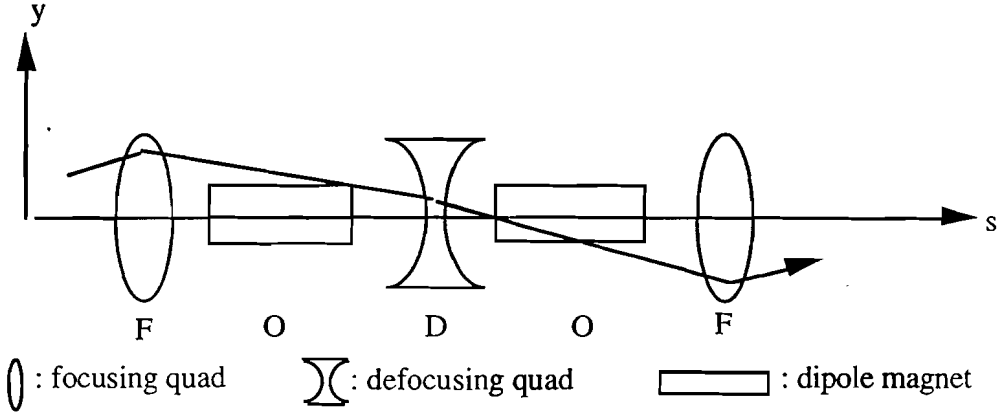

Fig. 1.8. An example of the FODO lattice design. The particle is oscillating around the design orbit because of the alternating focusing scheme.

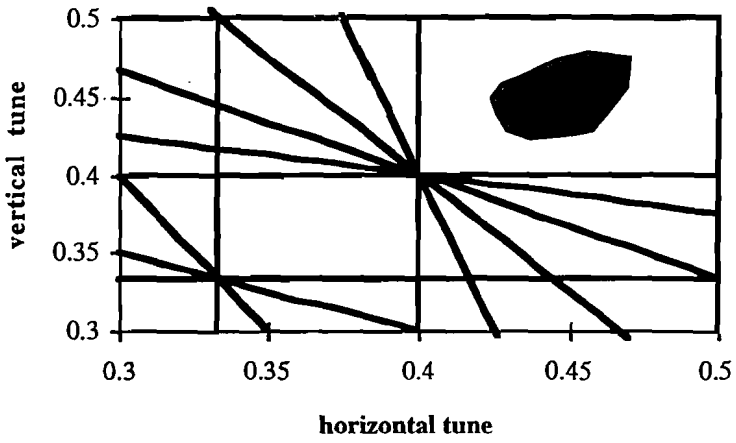

Fig. 1.9. The transverse tune plane with resonances from the 2nd to the 5th order. Solid lines are those tune settings which will lead to the high order resonance. The shaded region is the normal working area for the Main Ring operation.

CHAPTER 2

BEAM DIAGNOSIS AND INSTRUMENTATION

Since the electromagnetic field emitted by a moving charged particle contains information about its trajectory, various beam monitors were built to intercept the electromagnetic fields inside the vacuum chamber. Thus, it is essential to understand the nature of induced beam signal and its interaction with the diagnostic hardware. Also it is important to learn about the response of hardware to the beam trajectory for a correct interpretation of observed beam signal.

A. The nature of observed beam signals

1. Beam signal for a single bunch

One can normalize the longitudinal phase deviation by the angular rf frequency, and express the longitudinal deviation in units of [sec]. If only small deviations in the longitudinal direction are considered, one can rewrite the equation of motion for synchrotron oscillation in terms of time deviation:

$$\ddot{\tau}(t) + \omega_s^2 \tau(t) = 0 \tag{2.1}$$

where $\tau(t)$ is the deviation of the particle position relative to the synchronous particle, $\omega_s = 2\pi f_s$, and f_s is the synchrotron frequency given by Eq.(1.18).

If one projects the synchrotron oscillation on the time deviation axis, one will see a periodic modulation of revolution period. The period of modulation is the time needed for a particle to complete one cycle of synchrotron oscillation. The modulation of revolution period is comparable to the modulation of revolution frequency, which can be represented by the following mathematical expression:

$$y(t) = \cos[(\omega_0 + \alpha\cos\bar{\omega}t)t] \tag{2.2}$$

This is known in electric engineering as the frequency modulation[9]. The nominal revolution frequency acts as the carrier. The spectrum of frequency modulation conveys information about the longitudinal beam motion. This information will appear as symmetrical sidebands around the carrier; the sidebands are separated from the carrier by the modulating frequency (synchrotron frequency). A conceptual illustration of frequency modulation is depicted in Fig. 2.1.

Suppose only small deviations in the transverse direction are considered. Then, one can get a pseudo-harmonic description for the betatron oscillation from Eq.(1.45). If one projects the betatron oscillation on the transverse position axis of transverse phase space, one will see a periodic modulation of transverse displacement due to the focusing effect provided by quadrupole magnets. Since particle beams circulate in accelerators periodically, this is in fact a modulation in the amplitude of transverse beam motion, which can be described by the following mathematical expression:

$$y(t) = (1 + \alpha\cos\bar{\omega}t)\cos\omega_0 t \tag{2.3}$$

This is known in electric engineering as the amplitude modulation.[9] Again, the carrier is the revolution frequency. Amplitude modulation has similar properties as frequency modulation; the information about transverse beam motion is contained in the symmetrical sidebands around the carrier and separated by the modulation frequency (betatron frequency). An illustration for amplitude modulation is depicted in Fig. 2.2.

1.1 Transverse beam spectrum Transverse motion can be decomposed as:

$$x(t) = x_c + x_\beta(t) + x_d(t) \tag{2.4}$$

where x_c is the closed orbit offset, $x_\beta(t)$ is the betatron oscillation, and $x_d(t)$ is the dispersion displacement given by Eq.(1.41). One can express the particle motion with the harmonic representation $x(t)= \exp(ik s - i\omega t)$. The longitudinal reference $s= 0$ is chosen to be at the location of a beam position monitor.

The induced monitor signal of a single particle is described by the product of the beam current and transverse displacement:

$$\begin{aligned} d(t) &= x(t) I_b(t) \\ &= [x_c + D(0)\frac{dp}{p} + A_\beta e^{-i\omega_\beta t}] \cdot e \sum_{n=-\infty}^{\infty} \delta(t - nT) \end{aligned} \tag{2.5}$$

For a particle also undergoing synchrotron oscillations, the transverse signal is described by:

$$\begin{aligned} d(t) &= x(t) I_b(t) \\ &= [x_c + D(0)\frac{\dot{\tau}(t)}{\eta} + A_\beta e^{-i\psi_\beta(t)}] \cdot e \sum_{n=-\infty}^{\infty} \delta(t - \tau(t) - nT) \end{aligned} \tag{2.6}$$

$$\tau(t) = \tau_a \cos(\omega_s t + \phi_0)$$
$$\psi_\beta(t) = \omega_\beta t + \omega_\xi \tau(t) + \psi_0 \tag{2.7}$$

where e= proton charge, ξ= chromaticity, $\omega_\xi = \xi\omega_0/\eta$ is the angular chromatic frequency, τ_a= amplitude of the synchrotron oscillation in units of [sec], ϕ_0= initial synchrotron phase, A_β= betatron oscillation amplitude, D(0)= dispersion function at the location of the beam monitor, and ψ_0= initial betatron phase.

Since one typically observes a beam signal at a fixed location by means of the beam monitor, the finest time resolution is a turn-by-turn picture. Only the fractional part of betatron tune will affect the observation, because of $\exp(-in\omega_0 T) = 1$ where n= any integer. Thus, one can use the following expression for ω_β in Eq.(2.7):

$$\omega_\beta = q_\beta \omega_0$$
$$q_\beta = Q_\beta - [Q_\beta] \tag{2.8}$$

where $[Q_\beta]$ is the integer part of Q_β, and $[Q_\beta]$ is smaller than Q_β. The frequency spectrum of this current is given by the Fourier transform of Eq.(2.6):

$$\tilde{d}(\omega) = \frac{1}{2\pi}\int_{-\infty}^{\infty} d(t) e^{i\omega t}\, dt$$
$$= \frac{eA_\beta}{2\pi} e^{-i\psi_0} \sum_{n=-\infty}^{\infty} \int_{-\infty}^{\infty} \exp[-i(q_\beta\omega_0 - \omega)t - i\omega_\xi \tau(t)]\,\delta(t - \tau(t) - nT)\, dt \tag{2.9}$$

where one only considers the signal induced by the betatron oscillation.

If one ignores the second order effects, the frequency spectrum can be approximated as:

$$\tilde{d}(\omega) = \frac{eA_\beta}{2\pi} e^{-i\psi_0} \sum_{n=-\infty}^{\infty} \exp[-i(q_\beta\omega_0 - \omega)(nT + \tau(nT)) - i\omega_\xi \tau(nT)] \qquad (2.10)$$

A very important relationship is the Bessel function sum rule:[10]

$$e^{iz\cos\alpha} = \sum_{k=-\infty}^{\infty} i^k \cdot J_k(z) e^{ik\alpha} \qquad (2.11)$$

where $J_k(z)$ is the Bessel function of the k-th order. One can apply Eq.(2.11) to Eq.(2.10) and obtain the following result:

$$\tilde{d}(\omega) = \frac{eA_\beta}{2\pi} \sum_{n,k=-\infty}^{\infty} i^k e^{-i(k\phi_0+\psi_0)} J_k[(q_\beta\omega_0 + \omega_\xi - \omega)\tau_a] e^{-i(q_\beta\omega_0 + k\omega_s - \omega)nT} \qquad (2.12)$$

By using the Poisson's sum rule:[11]

$$\sum_{n=-\infty}^{\infty} e^{i\omega nT} = \frac{2\pi}{T} \sum_{m=-\infty}^{\infty} \delta(\omega - \frac{2\pi m}{T}) \qquad (2.13)$$

one can get the frequency spectrum:

$$\tilde{d}(\omega) = \sum_{n,k=-\infty}^{\infty} \tilde{d}_{nk}\, \delta(n\omega_0 + q_\beta\omega_0 + k\omega_s - \omega) \qquad (2.14)$$

$$\tilde{d}_{nk} = i^k e^{-i(k\phi_0+\psi_0)} ef_0 A_\beta J_k[(q_\beta\omega_0 + \omega_\xi - \omega)\tau_a] \qquad (2.15)$$

The particle distribution in a beam bunch is described by a 4-dimensional charge density $\rho_4(A_\beta, \tau_a, \phi_0, \psi_0)$, which is defined by:

$$\text{charge in phase space volume } (A_\beta\, dA_\beta\, \tau_a\, d\tau_a\, d\phi_0\, d\psi_0)$$
$$\equiv \rho_4(A_\beta, \tau_a, \phi_0, \psi_0) A_\beta\, dA_\beta\, \tau_a\, d\tau_a\, d\phi_0\, d\psi_0 \tag{2.16}$$

The signal of a beam bunch is given by integrating the product of single particle spectrum and charge density ρ_4 over the 4-dimensional phase space.

Gaussian bunches are observed for both electron and proton beams, for different reasons: (1) electrons– due to the random excitation caused by the synchrotron quantum emission. (2) protons– emittance dilution due to small random errors. The average charge density for a Gaussian beam is given by:[12]

$$\bar{\rho}_4(A_\beta, \tau_a, \phi_0, \psi_0) = \frac{eP}{4\pi^2 \sigma_\tau^2 \sigma_\beta^2} \exp\left(-\frac{\tau_a^2}{\sigma_\tau^2} - \frac{A_\beta^2}{\sigma_\beta^2}\right) \tag{2.17}$$

where P is the total number of particles in a beam bunch.

When particles move dependently, the beam will develop phase-space structure by interacting with the vacuum chamber. This interaction will feed back on the beam itself and modify the phase-space structure. A qualitative expression for the charge density can be given by decomposing the phase-space structure with Fourier expansion:

$$\rho_4(A_\beta, \tau_a, \phi_0, \psi_0) = \sum_{k=-\infty}^{\infty} e^{i(k\phi_0 + \psi_0)} \rho_k(\tau_a, A_\beta) \tag{2.18}$$

The detailed phase-space structure can only be found by solving the equation of motion in a self-consistent way.

An incoherent beam signal is caused by the fluctuation of discrete particles from the average distribution, known as Schottky noise.[9] For a Gaussian beam, the transverse Schottky signal is:

$$\left\langle \tilde{d}(f) \right\rangle = \sum_{n,k=-\infty}^{\infty} \left\langle \tilde{d}_{nk} \right\rangle \delta(nf_0 + q_\beta f_0 + kf_s - f) \tag{2.19}$$

$$\left\langle \tilde{d}_{nk} \right\rangle = ef_0\sigma_\beta\sqrt{P}\left[\exp[-(q_\beta\omega_0 + \omega_\xi - \omega)^2\sigma_\tau^2] I_k[(q_\beta\omega_0 + \omega_\xi - \omega)^2\sigma_\tau^2]\right]^{1/2} \tag{2.20}$$

$$\omega = 2\pi(nf_0 + q_\beta f_0 + kf_s) \tag{2.21}$$

, where $I_k(x)$ is the modified Bessel function of the 1st kind.

For the coherent beam signal, the amplitude of transverse beam spectrum is:

$$\begin{aligned} \left\langle \tilde{d}_{nk} \right\rangle &\propto ef_0 \iint \rho_k(A_\beta, \tau_a) J_k[(q_\beta\omega_0 + \omega_\xi - \omega)\tau_a] A_\beta^2 \, dA_\beta \tau_a d\tau_a \\ &\propto ef_0 \, \Delta P \, \lambda_k[(q_\beta\omega_0 + \omega_\xi - \omega)\sigma_\tau] \end{aligned} \tag{2.22}$$

where λ_k is the envelope of the spectral amplitude, and Δ is the amplitude of the coherent oscillation. Since the Schottky signal is caused by the random fluctuation of discrete particles, the signal level is proportional to the square root of total number of particles. In contrast, the coherent signal is caused by the coherent particle motion; the signal level is proportional to the total number of particles.

The contribution of closed orbit offsets to the transverse beam spectrum is shown in the following results:[12]

$$\left\langle \tilde{d}(f) \right\rangle = \sum_{n,k=-\infty}^{\infty} \left\langle \tilde{d}_{nk} \right\rangle \delta(nf_0 + kf_s - f) \tag{2.23}$$

i) incoherent signal: $\left\langle \tilde{d}_{nk} \right\rangle = ef_0 x_c \sqrt{P/2} \left[\exp[-\omega^2\sigma_\tau^2] I_k(\omega^2\sigma_\tau^2) \right]^{1/2}$ (2.24)

ii) coherent signal: $\left\langle \tilde{d}_{nk} \right\rangle \propto ef_0 x_c P \lambda_k(\omega\sigma_\tau)$ (2.25)

$$\omega = 2\pi(nf_0 + kf_s) \tag{2.26}$$

The above results can be summarized in Figs. 2.3, 2.4 and 2.5.

Fig. 2.3 depicts the power spectrum of the transverse signal when the chromaticity is 0 and there is no closed orbit error. The betatron oscillation shows up in the form of betatron sidebands separated from the revolution harmonic lines nf_0 by the fractional betatron frequency $q_\beta f_0$. The power of corresponding spectral lines is approximately proportional to the square of Bessel functions $\{J_k[(n\omega_0+k\omega_s)\sigma_\tau]\}^2$. The synchrotron sidebands of each betatron line are separated from each other by the synchrotron frequency f_s. The asymmetry of the spectral amplitude is the result of the bunch shape. The amplitude of each betatron line is proportional to the betatron oscillation amplitude as implied by Eqs.(2.22). For the case of a single particle, the Bessel function dependence will disappear; and synchrotron sidebands will have the same symmetry as shown in Figs. 2.1 and 2.2. Note that there is no response at frequencies corresponding to the harmonics of the revolution frequency in the spectrum, since there is no closed orbit error.

As indicated in Eq.(2.19), betatron sidebands also exist in the negative frequency domain when $n+q_\beta < 0$. In a measuring instrument, betatron sidebands of negative

frequencies will be folded into the positive frequency domain as spectral lines at frequencies of $|n+q_\beta|f_0$. Thus, the observed beam spectrum will have two betatron sidebands between adjacent revolution harmonic lines.

When the chromaticity is not zero, the envelope of beam spectrum will be shifted along the frequency axis by the chromatic frequency, $f_\xi = \xi f_0/\eta$. Fig. 2.4 depicts the beam spectrum with the same conditions as in Fig. 2.3, except that the chromaticity is not zero. The magnitude of spectral lines will be changed according to the Bessel function dependence, $\{J_k[(n\omega_0+k\omega_s-\omega_\xi)\sigma_\tau]\}^2$.

When there is a closed orbit offset, there will be a response at harmonics of revolution frequency as depicted in Fig. 2.5. In addition to the betatron sidebands caused by the betatron oscillation, the revolution harmonic lines will also show up in the beam spectrum because of the closed orbit offset.

In reality each individual particle in a beam bunch has slightly different betatron frequency from the synchronous particle because of the imperfection of magnetic fields in the magnets. Therefore, the betatron sidebands will not be like delta-function spikes. Instead the spectral lines will smear out like narrow bands. For each betatron sideband, the dependence of the spectral magnitude on the frequency gives the betatron tune spread of particles in a beam bunch.

1.2 Longitudinal beam spectrum The longitudinal beam current for a single particle in a beam bunch is given by:

$$I_b(t) = e \sum_{n=-\infty}^{\infty} \delta(t - \tau(t) - nT) \tag{2.27}$$

The frequency spectrum of a longitudinal signal for a single particle is:

$$\tilde{I}_b(\omega) = \frac{1}{2\pi}\int_{-\infty}^{\infty} e^{i\omega t} I_b(t)\,dt = \sum_{n,k=-\infty}^{\infty} \tilde{I}_{nk}\,\delta(n\omega_0 + k\omega_s - \omega) \tag{2.28}$$

$$\tilde{I}_{nk} = i^k e^{-ik\phi_0} e f_0 J_k(\omega\tau_a) \tag{2.29}$$

The particle distribution is described by a 2-dimensional charge density $\rho_2(\tau_a,\phi_0)$. For a Gaussian beam, the longitudinal Schottky signal can be calculated by using the distribution:[12]

$$\bar{\rho}_2(\tau_a,\phi_0) = \frac{eP}{2\pi\sigma_\tau^2}\exp(-\frac{\tau_a^2}{\sigma_\tau^2}) \tag{2.30}$$

For the coherent beam signal, the qualitative expression for the charge density is:

$$\rho_2(\tau_a,\phi_0) = \sum_{k=-\infty}^{\infty} e^{ik\phi_0}\rho_k(\tau_a) \tag{2.31}$$

The longitudinal beam spectrum for a Gaussian beam is given by the following results:[12]

$$\left\langle \tilde{I}_b(f) \right\rangle = \sum_{n,k=-\infty}^{\infty} \left\langle \tilde{I}_{nk} \right\rangle \delta(nf_0 + kf_s - f) \tag{2.32}$$

i) incoherent signal: $\left\langle \tilde{I}_{nk} \right\rangle = ef_0\sqrt{P/2}\left[\exp[-\omega^2\sigma_\tau^2] I_k(\omega^2\sigma_\tau^2)\right]^{1/2}$ (2.33)

ii) coherent signal: $\left\langle \tilde{I}_{nk} \right\rangle \propto eP f_0 \lambda_k(\omega\sigma_\tau)$ (2.34)

$$\omega = 2\pi(nf_0 + kf_s) \tag{2.35}$$

The above results are summarized in Fig. 2.6. The envelope of the longitudinal spectrum has the same Bessel function dependence as the transverse case, except that there is no frequency shift due to nonzero chromaticity. The amplitude of each spectral line is a function of the bunch length as indicated by Eqs. (2.33) and (2.34). The amplitude of the revolution harmonic lines decreases as the frequency increases. In contrast, the amplitude of synchrotron sidebands increases as the frequency increases. In a measuring instrument, revolution harmonic lines of negative frequencies will be folded into the positive frequency domain as spectral lines at frequencies of $|n|f_0$. Therefore, the spectral lines of negative frequencies will overlap with those corresponding to positive frequencies. The spectral lines of ac components will have amplitudes twice the values given by Eqs.(2.33) and (2.34). This is a characteristics of longitudinal beam spectrum which is different from the transverse one.

The synchrotron sidebands of an actual beam spectrum also smear out and look like narrow bands. For the longitudinal case, the synchrotron tune spread is caused by the nonlinearity of the rf voltage. There is also frequency spread in the revolution harmonic lines because of the momentum spread among particles in a beam bunch, especially near transition.

2. Spectrum aliasing

Due to the limitations of diagnostic hardware, some unphysical signals may show up in the measured beam spectrum. Consider a single beam bunch undergoes betatron oscillation in a storage ring. The transverse beam position monitor (BPM) can only sample the beam motion at a turn by turn interval, $y(nT) = A_\beta e^{-in\omega_\beta T}$. A conceptual

sketch of the induced signal on the BPM is depicted in Fig. 2.7. The betatron oscillation sampled by the BPM results in a sequence of discrete pulses separated by the revolution period (sampling period).

Suppose y(t) is an analog signal whose frequency spectrum contains information within the bandwidth w_a. The frequency spectrum of its discrete sample $y(nT_s)$ is related to the spectrum of analog signal by the following relation:[10]

$$S(f) = \frac{1}{T_s} \sum_{k=-\infty}^{\infty} S_a(f - \frac{k}{T_s}) \tag{2.36}$$

where T_s= sampling period, $S_a(f)$= frequency spectrum of the analog signal, and $S(f)$= frequency spectrum of the discretely sampled signal. The results of a discrete-time Fourier transform of the induced signal on the BPM is illustrated in Fig. 2.8.

When the sampling frequency $1/T_s$ is smaller than one half of the highest frequency of signals contained in the analog waveform, i.e. $1/T_s < w_a/2$, the spectral bands containing information of waveform will overlap with its adjacent alias as depicted in Fig. 2.9. This is called the aliasing effect. A demonstration of aliasing effect in the time domain is depicted in Fig. 2.10. Because of the aliasing effect, one will not be able to distinguish those two traces in Fig. 2.10.

When the aliasing effect occurs, there will be some unphysical responses in the low frequency range of the spectrum. To avoid the spectrum being contaminated, the sampling frequency should be larger than twice the highest frequency of signal one intends to measure, i.e. $1/T_s > w_a/2$. This is known as the Nyquist theorem.[10]

In reality each measuring instrument has only finite amount of memory to store the sampled data points; a window function has to be imposed on the infinite pulse train. The actual data used by the measuring instrument is only a portion of the infinite pulse train.

The windowing procedure is depicted in Fig. 2.11. The windowing procedure is equivalent to convoluting the infinite pulse train with a finite window function. The resulting spectrum is the product of pulse train spectrum and the window spectrum. For a rectangular window, g(t)= 1, its frequency spectrum is $\tilde{g}(f) = \sin f / f$ as depicted in Fig. 2.12. The width of the spectral band is inversely proportional to the length, τ, of window function in the time domain. The ripples in the frequency spectrum are caused by the truncation of windowing procedure. Therefore, the windowing procedure has the effect of broadening the measured spectral lines. This will affect the result of beam measurements in the frequency domain.

B. Design and implementation of beam monitors

Since the frequency spectrum of beam signals contains rich information about various beam properties, it is necessary to understand the frequency response of beam monitors in order to correctly extract the beam parameters from the measured output signal correctly.

The response of beam monitors to the particle beam is characterized by the detector sensitivity, which is defined by the following expressions for the longitudinal and the transverse monitors respectively:[12]

$$S_{\parallel}(f) = \frac{V_p(f)}{\tilde{I}_b(f)}$$
$$S_{\perp}(f) = \frac{V_p(f)}{\tilde{d}(f)} \qquad (2.37)$$

where $V_p(f)$= the output voltage of beam monitor, $\tilde{I}_b(f)$= beam current, and $\tilde{d}(f)$= transverse displacement current. The longitudinal detector sensitivity $S_{\parallel}(f)$ and the transverse detector sensitivity $S_{\perp}(f)$ are defined in such a way that they do not depend on the beam properties nor its transverse displacement. The longitudinal detector sensitivity $S_{\parallel}(f)$ has the dimension of ohm, and the transverse one $S_{\perp}(f)$ has the MKS dimension of ohm per meter.

When an excitation voltage is applied to a beam kicker, the response of particle beam to the excitation is characterized by the kicker constant. The kicker constant is defined by the following expressions for the longitudinal and the transverse kickers respectively:[13]

$$K_{\parallel}(f) = \frac{\Delta E / e}{V_k(f)}$$
$$K_{\perp}(f) = \frac{\Delta p_{\perp} \beta c}{e V_k(f)} \qquad (2.38)$$

where $V_k(f)$= the applied excitation voltage, ΔE= the energy change of the beam, $\Delta p_{\perp}$= the transverse momentum change of the beam, $K_{\parallel}(f)$= the longitudinal kicker constant, and $K_{\perp}(f)$= the transverse kicker constant.

1. Longitudinal beam monitors

There are three longitudinal beam parameters pertinent to the studies of transverse beam instabilities: beam intensity, bunch length and beam current spectrum.

1.1 Beam intensity measurement The beam intensity, N, can be derived from the measured dc beam current I_0 according to the following relation:

$$N = \frac{I_0}{e f_0} \qquad (2.39)$$

Since the dc component of beam current does not provide any form of time variation, we can not apply Faraday's law to measure it. It is measured by using the nonlinear characteristics of B-H curve for magnetic materials. The intensity monitor used in the Main Ring is a dc current transformer (DCCT) which is sensitive to the variation of 1 μA in the beam current.[14] The DCCT is capable of providing a dynamic range of 100 dB or greater. For beam intensity N= 1×10^{12} protons, the dc current equals to 7.6 mA for the Main Ring.

1.2 Bunch length measurement The real-time bunch length monitoring in the Main Ring is achieved by utilizing the longitudinal beam spectrum. From Eqs.(2.33) to (2.35), one can determine the rms bunch length from the relative ratio of spectral amplitudes between two revolution harmonic lines. The signals are measured by a stripline detector and the full bunch length is chosen to be the 95% interval of temporal distribution of beam, i.e. four times the rms bunch length. The dynamic range of bunch length monitor is 30 dB.[15]

1.3 Wideband current spectrum A resistive wall current monitor[16] with 3 dB frequency bandwidth of 2 GHz is used to monitor the longitudinal bunch profile in the Main Ring, as depicted in Fig. 2.13. When charged particles travel in an accelerator, they induce image charges on the wall surface of beam pipe. Those image charges will travel along the beam pipe as the source particles traverse the accelerator. This flow of image charges produces an induced current on the wall of the beam pipe. A gap in the beam pipe is designed to disrupt the flow of induced wall current. Then a resistor is provided for the wall current to cross the gap. When the wall current encounters the gap, it will flow onto the resistor and induce a signal in the output cable. A high permeability ferrite core is used to increase the shunt inductance of the enclosure box. The enclosure box shields the monitor from outside noise.

The equivalent circuit model of the resistive wall current monitor is given in Fig. 2.14. The capacitance of the circuit is mainly contributed by the ceramic pipe, the inductance is contributed by the ferrite and the resistance is from the resistor across the gap. The 3 dB frequencies for the lower corner and the higher one are shown in Fig. 2.14. Microwave absorbers were placed both upstream and downstream of the beam pipe to attenuate the beam induced signals in other accelerator locations whose frequencies are

above the cutoff of waveguide modes in the beam pipe. When the beam is off-center, the induced wall current will not be distributed uniformly around the beam pipe. To reduced the dependence of output signal on the beam displacement, four resistors are placed equally around the gap. The sum of signals from those four resistors gives the final output. The variation of output signal due to the beam displacement is only 1.5%, and the lower corner of 3 dB bandwidth is 3 kHz for the Main Ring resistive wall current monitor.[17]

2. Transverse beam monitors

Three transverse beam position monitors were built specifically to study transverse beam instabilities. Since there were indications of resistive wall instability, a beam position monitor (BPM) of capacitive type was designed to observe the low frequency spectrum. A BPM of resonant type was built to detect the transverse Schottky signal and tune spread, and a long stripline BPM was built to monitor the temporal profile of transverse beam signal for a single bunch.

2.1 Low frequency capacitive BPM A detector at E49 location of Main Ring tunnel was built to couple strongly with the electric field induced by the beam. A schematic sketch of the BPM configuration is depicted in Fig. 2.15, and the mechanical layout is in Fig. 2.16. The detector electrodes were made from a concentric tube cut diagonally. The radius of the inner pipe is 2.5 inches, the length is 40 cm. The heliax cable is connected directly into a high input impedance op amp. The electrical parameters of the heliax cable are: C= 75 pF/m, L= 0.187 μH/m. The equivalent circuit model corresponding to each output port is depicted in Fig. 2.17.

The measured capacitance between the electrode plate and the feedthrough is denoted by C_p, the capacitance of the heliax cable is C_c, the series resistor is R_s, and the op amp input impedance of is R_t. The total impedance looking into point *a* from the current source is given by Z:

$$Z = \frac{R_s + \dfrac{R_t}{1 + i\omega R_t C_c}}{1 + i\omega\left[\dfrac{R_t C_p}{1 + i\omega R_t C_c} + R_s C_p\right]} \tag{2.40}$$

The voltage across point *a* and the ground is $I_w Z$. The final output voltage across the termination resistor R_t (point *c*) is:

$$V_{out} = \frac{I_w Z}{1 + \dfrac{R_s}{R_t} + i\omega R_s C_c} \tag{2.41}$$

For a diagonally-cut cylinder BPM, the induced wall current which flows onto the upstream end of the top electrode plate is:[18]

$$I_{t1} = \frac{-I_b(\omega)}{2}\left(1 + \frac{\delta y}{b}\right) \tag{2.42}$$

where I_b= beam current, *b*= the radius of electrode pipe, and δy= transverse displacement. The induced wall current flowing onto the downstream end of the top electrode plate is:

$$I_{t2} = -I_{t1}\, e^{-i\omega \ell / c} \tag{2.43}$$

where ℓ= the length of electrode plate. Therefore, the total induced wall current flowing onto the top electrode plate in the low frequency range is:

$$I_w = \frac{-I_b}{2}\left(1+\frac{\delta y}{b}\right)\frac{i\omega\ell}{c} \tag{2.44}$$

In a similar fashion, the total wall current flowing onto the bottom plate is:

$$I_w = \frac{-I_b}{2}\left(1-\frac{\delta y}{b}\right)\frac{i\omega\ell}{c} \tag{2.45}$$

The detector sensitivity is derived by taking the difference of two output voltages and divided by $I_w\delta y$:

$$S_\perp(f) = \frac{i2\pi f\ell\left(R_s+\dfrac{R_t}{1+i2\pi f R_t C_c}\right)}{bc\left(1+i2\pi f\left(\dfrac{R_t C_p}{1+i2\pi f R_t C_c}+R_s C_p\right)\right)\left(1+\dfrac{R_s}{R_t}+i2\pi f R_s C_c\right)} \tag{2.46}$$

The calculated detector sensitivity $S_\perp(f)$ is depicted in Fig. 2.18. The whole system is represented by the following scheme:

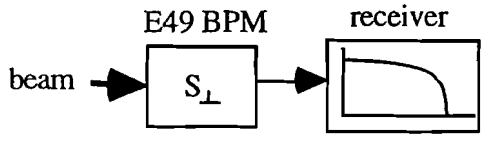

The conceptual block diagram of receiver design is depicted in Fig. 2.19, and the measured frequency response of the receiver is depicted in Fig. 2.20.

2.2 Main Ring Schottky detector Because Schottky noise is caused by the random fluctuation of discrete particles, the signal level is pretty low. A high sensitivity BPM can be achieved by making the system as a resonant circuit. The mechanical layout of Schottky detector is depicted in Fig. 2.21, and the equivalent circuit model is depicted in Fig. 2.22. The detailed design procedures can be found in an internal report.[19]

The sensitivity of the Schottky detector is given by:[19]

$$S_{\perp}(f) = \frac{|V_{out}|}{\delta y\, I_b(f)} = \frac{\ell}{bc}\sqrt{\frac{R_0 2\pi f_c Q_0}{C_t}\frac{Q_{load}}{Q_0}\left(1-\frac{Q_{load}}{Q_0}\right)} \tag{2.47}$$

where R_0= 50 Ω, f_c= the resonant frequency of the Schottky detector, Q_0= the unloaded quality factor of the resonant circuit model depicted in Fig. 2.22, Q_{load}= the loaded quality factor of the resonant circuit model, and C_t= the total capacitance across the two feedthroughs. A list of detector parameters is depicted in Table 2.1.

The detector sensitivity was calibrated by performing both bench and beam measurements, and the results are shown in Figs. 2.23 and 2.24 respectively. A conceptual block diagram of the signal processing scheme is depicted in Fig. 2.25. The measured signal is mixed down to the baseband by using the Main Ring turn-by-turn clock signal. The detector sensitivity was compromised to accommodate the large frequency drift during the acceleration process.[19]

Table 2.1. The parameters of the Main Ring Schottky detector.

parameter	value
resonant frequency f_c (MHz)	7.6
length of electrode pipe ℓ (cm)	40
radius of electrode pipe b (cm)	5.35
unloaded quality factor Q_0	400
inductance of primary inductor L (μH)	6.804
total capacitance C_t (pF)	48

2.3 Quarter wavelength stripline BPM A long stripline BPM was built and installed at the F14 location to monitor the transverse single bunch motion. The mechanical layout of the stripline BPM is depicted in Fig. 2.26. The electrode plate and the beam pipe form a transmission line. The characteristic impedance of this transmission line can be estimated by using the formula for the microstrip line. For the configuration of microstrip line as depicted in Fig. 2.27, the characteristic impedance is given by the following formula:[20]

$$Z_c(x) = \frac{377}{4\pi} \ln[1 + \frac{x}{2}(x + \sqrt{x^2 + \pi^2})], \; x = \frac{8\delta}{w} \qquad (2.48)$$

where w= the width of electrode plate, and δ= the gap between the electrode plate and the beam pipe.

When the incident voltage propagates from one device to another which has different characteristic impedance, a portion of the incident voltage will be reflected. This reflected voltage will alter the resulting voltage one measures. The reflection coefficient, Γ, for the incident voltage is defined by the following expression:[21]

$$\Gamma = \frac{V_R}{V_I} = \frac{Z_L - Z_0}{Z_L + Z_0} \tag{2.49}$$

where V_R and V_I is the reflected and the incident voltage respectively, Z_0 and Z_L is the characteristic impedance of the diagnostic device and the external load respectively.

In order to transfer the most of the signal power to the measuring instrument, one needs to match the load impedance to the diagnostic device. This is known as the maximum power transfer theorem in electric engineering.[9]

From the physical dimension shown in Fig. 2.26, we use w= 5.5 cm, the estimated gap height for achieving a 50 Ω transmission line is δ= 1.24 cm. The calculated result is depicted in Fig. 2.28. The actual gap height was determined by bench measurements, and the result was 0.5 inch, which is very close to the calculated value given by Fig. 2.28.

When a bunch passes through the stripline BPM, the response is depicted in Fig. 2.29. Because the downstream port is shorted, the induced voltage at the upstream port will get totally reflected and the polarity reversed when it propagate to the downstream port according to Eq.(2.49).

From the illustrations shown in Fig. 2.29, the resulting voltage measured at the feedthrough is given by:

$$\begin{aligned} V_{out} &= Re\left(V_A - V_A e^{-i2\omega\ell/c}\right) \\ &= V_A[1-\cos(2\omega\ell/c)] \\ &= 2V_A \sin^2(\omega\ell/c) \end{aligned} \tag{2.50}$$

Therefore, the frequency response of a stripline BPM with one end shorted is given by the following relation:

$$S_{\perp}(f) \propto \left|\sin^2(2\pi f\ell/c)\right| \tag{2.51}$$

where ℓ= the length of electrode plate. For a given frequency f, the output signal will be the maximum if the length of the electrode is a quarter of the wavelength. By taking into account the bunch length and frequencies of certain single bunch motions, the length of electrode plate was chosen to be the quarter wavelength of the rf frequency.

To keep the distortion of the output signal to a minimum, efforts were made to use a copper taper to smooth the transition from the electrode plate to the feedthrough tip. High quality cables with low power dissipation and low frequency dispersion were used to relay the output signal to the experiment station.

C. Concepts of beam feedback

1. Definitions

1.1 Transfer function The response of a system to external excitation is characterized by the transfer function, H, which is defined as the ratio of the output relative to the input:[9]

$$H = \frac{V_{out}}{V_{in}} \tag{2.52}$$

A canonical feedback system is depicted in Fig. 2.30, where the input goes through A (denoted by its transfer function), then feeds back through B to correct the input. The transfer function A is defined as the forward transfer function, and B is the feedback transfer function. The open-loop transfer function is defined as AB,[22] and the closed-loop transfer function is defined as:[22]

$$H = \frac{V_{out}}{V_{in}} = \frac{A}{1 + AB} \tag{2.53}$$

1.2 Damper gain Consider a feedback system implemented in an accelerator for damping the coherent beam oscillation as depicted in Fig. 2.31. If one uses a macroparticle to represent a bunch and assumes that the kicker deflection is small compared with the external focusing force, then the equation describing the transverse motion of a bunch is given by the following:

$$\ddot{x}(t) + \omega_\beta^2 x(t) = G\, x(t - \tau) \tag{2.54}$$

where G is a positive quantity characterizing the response of the feedback system, and τ is the delay time from the BPM to the kicker. Note that G is a function of the frequency and the beam intensity. The right-hand side of Eq.(3.54) is the output signal of kicker which is derived from the input signal $x(t-\tau)$ measured by the BPM at a previous time $t-\tau$.

For a bunch undergoing coherent oscillation in an accelerator, one expects the motion to be in sinusoidal form: $x(t)= Ae^{-i\omega t}$. When there is coherent beam oscillation in an accelerator, it will create a perturbation to the external focusing force. When the perturbation is small, Eq.(3.54) can be approximated as:

$$\ddot{x}(t)+\omega_\beta^2 x(t)=Ge^{i\omega_\beta\tau}x(t) \tag{2.55}$$

The solution of Eq.(3.55) is given by:

$$\begin{aligned} x(t) &= Ae^{-i\omega_\beta t\sqrt{1+z}} \\ z &= \frac{-G}{\omega_\beta^2}\left[\cos(\omega_\beta\tau)+i\sin(\omega_\beta\tau)\right] \end{aligned} \tag{2.56}$$

Using the following complex expansion,[23]

$$\sqrt{a+ib}=(a^2+b^2)^{1/4}\left\{\cos[\tfrac{1}{2}\tan^{-1}(\tfrac{b}{a})]+i\sin[\tfrac{1}{2}\tan^{-1}(\tfrac{b}{a})]\right\} \tag{2.57}$$

the solution of Eq.(3.55) can be written as:

$$x(t)=Ae^{-i\omega_\beta t\cdot Re(\Lambda)}\cdot e^{\omega_\beta t\cdot Im(\Lambda)} \tag{2.58}$$

where

$$\Lambda = \left(1 - \frac{2G}{\omega_\beta^2}\cos(\omega_\beta\tau) + \frac{G^2}{\omega_\beta^4}\right)^{1/4}\left[\cos(\frac{\theta}{2}) + i\sin(\frac{\theta}{2})\right] \tag{2.59}$$

$$\begin{aligned} \theta &= \tan^{-1}\left(\frac{b}{a}\right) \\ b &= -\frac{G}{\omega_\beta^2}\sin(\omega_\beta\tau) \\ a &= 1 - \frac{G}{\omega_\beta^2}\cos(\omega_\beta\tau) \end{aligned} \tag{2.60}$$

For a given value of G, the maximum damping occurs when $\sin(\omega_\beta\tau)$ equals to one. This result imposes a constraint on the delay time τ between the BPM and the kicker with the following form:

$$\begin{aligned} &(1)\,\text{maximum damping} : \omega_\beta\tau = \frac{\pi}{2} + 2\pi n \\ &(2)\,\text{maximum antidamping} : \omega_\beta\tau = \frac{3\pi}{2} + 2\pi n \end{aligned} \tag{2.61}$$

where n is any integer. Therefore, the delay time from the BPM to the kicker has to be a quarter of the betatron oscillation period for the feedback system to achieve a maximum damping effect.

If the damping time is defined in such a way that the power of coherent oscillation is reduced by a factor of e^{-1} after one turn, Eq.(2.58) can be rewritten in the following form:

$$\begin{aligned} x(t) &= A e^{-i\omega_\beta t \cdot Re(\Lambda)} \cdot e^{2T\omega_\beta Im(\Lambda)\cdot t/(2T)} \\ &= A e^{-i\omega_\beta t \cdot Re(\Lambda)} \cdot e^{-gt/(2T)}. \end{aligned} \tag{2.62}$$

$$g = -2T\omega_\beta Im(\Lambda) \tag{2.63}$$

where T is the revolution period and g is called damper gain. The damper gain g satisfies the following relation:

$$\frac{T_d}{T} = \frac{2}{g} \tag{2.64}$$

where T_d is the e^{-1} damping time of the oscillation amplitude. From Eqs.(2.59), (2.60) and (2.63), one readily realizes that an inappropriate setting of delay time will reduce the effective damper gain. Therefore, both the delay time and the damper gain need to be carefully evaluated before the implementation of a feedback system. Figure 2.32 depicts the dependence of damper gain g on the delay time τ. If the delay time is properly set, a higher damper gain will result in a shorter damping time. Higher damper gain also places more demand on the power requirement of amplifiers in the system.

To examine the effect on the beam motion caused by the kicker only, one considers the equation of motion given in Eq.(2.54) without the focusing term given by quadrupole magnets:

$$\ddot{x}(t) = G\,x(t-\tau) \tag{2.65}$$

Suppose the deflection strength G remains approximately constant through the kicker area, the change in the slope of the particle trajectory is given by:

$$\int_0^\ell x''(s)ds = \frac{1}{c^2}\int_0^\ell G\,x(s-c\tau)ds \tag{2.66}$$

$$\Delta(x'(s)) \approx \frac{G\ell}{c^2} x(s - c\tau) \tag{2.67}$$

where c is the speed of light, and ℓ is the length of the kicker electrode. As shown in Eq.(2.67), the change in the slope of the particle trajectory after each passage is proportional to the beam displacement x(s- $c\tau$) at the location of the BPM. If the beam does not undergo coherent oscillation, the measured displacement is zero. There will be no need for damping the beam motion. But there is a pitfall for such a simple feedback system. Suppose there is coherent beam oscillation and the beam happens to have zero displacement but maximum slope in its trajectory at the location of the BPM. The feedback system will not detect the coherent beam oscillation and will not apply appropriate correction to the beam. A remedy for such situation is to install a second BPM and a second kicker at a quarter of betatron period apart from the first ones. A schematic sketch of the 2BPM-2kicker system is depicted in Fig. 2.33.

1.3 Power requirement of kicker For a given excitation mode of the beam kicker as depicted in Fig. 2.34, the input power P_k is given by:

$$P_k = \frac{V_k^2}{2Z_0} \tag{2.68}$$

where Z_0= the characteristic impedance of input transmission line, and V_k= the excitation voltage for a given mode.

From the definition of the kicker constant given by Eq.(2.38), one can rewrite the input power in terms of the angular kick received by the beam as the following:

$$P_k = \frac{(\Delta p_\perp \beta c)^2}{2Z_0 |eK_\perp|^2} \tag{2.69}$$

The angular kick per passage only presents a small perturbation to the beam motion. Therefore, one can approximate the transverse momentum change as:

$$\begin{aligned} \Delta p_\perp &= p \cdot \sin\theta \\ &= p \cdot \sin(\Delta x') \\ &\approx p \Delta x' \end{aligned} \tag{2.70}$$

where θ is the deflection angle. For relativistic beams, the input power of the kicker is given by:

$$P_k = \frac{(\Delta x' E)^2}{2Z_0 |eK_\perp|^2} \tag{2.71}$$

where E= beam energy. For a given angular kick, the larger the kicker constant is, the less the input power is required.

When one reverses the operation of a kicker, it can function as a BPM. The passage of off-centered beams will induce an output voltage, V_p, at the output port of transmission line. In this case, the frequency response of BPM to the excitation created by the beam is given by the detector sensitivity, $S_\perp(f)$. This dual functionality can be described by the following relation:[13]

$$S_\perp(f) = \frac{i\omega Z_0 K_\perp(f)}{2\beta c} \tag{2.72}$$

Equation (2.72) was derived by applying the Lorentz reciprocity theorem,[21] $\beta \approx 1$ for relativistic particles. By using Eq.(2.72), one can rewrite the expression of required kicker power as:

$$P_k = \frac{\omega^2 Z_0 (\Delta x' E)^2}{8\beta^2 c^2 e^2 |S_\perp|^2} \tag{2.73}$$

From Eq.(2.73), one finds that it takes more input power to create a given angular kick for a higher frequency mode.

2. Stability of feedback system

2.1 Nyquist stability plot The stability of a feedback system as depicted in Fig. 2.30 is determined by its open-loop transfer function. When the denominator of Eq.(2.53) approaches zero, the closed-loop transfer function goes to infinity. The feedback system is unstable when the real part of the open-loop transfer function approaches -1. The stability condition of the feedback system can be expressed in terms of Nyquist stability plot,[22] which is plotted as the imaginary part of open-loop transfer function vs. the real part. Figure 2.35 is an example of Nyquist stability plots and the corresponding plots of closed-loop transfer function for both the stable and unstable feedback systems. When the feedback system is unstable, the amplitude of output voltage will grow larger as shown in Fig. 2.35*(4)* and the phase near the resonance frequency will get distorted as shown in Fig. 2.35*(6)*.

2.2 Stability diagram Since the closed-loop transfer function is proportional to the output voltage, sometimes it is useful to examine the polar plot of the inverse of closed-loop transfer function:

$$\frac{1}{H} = \frac{1}{A} + B \tag{2.74}$$

The polar plot of the inverse of the closed-loop transfer function is called the stability diagram. The contribution of the feedback transfer function B is to displace the stability diagram away from the origin. Once the forward transfer function A, is known, one can derive the feedback transfer function B, by examining the stability diagram. Figure 2.36 is an example of the stability diagrams for both stable and unstable feedback systems.

When the stability diagram is approaching the origin of the polar plot, the inverse of the magnitude of the closed-loop transfer function is approaching zero. In other words, the output amplitude of the feedback system is approaching infinity. Thus, the feedback system goes unstable. The corresponding plots of closed-loop transfer function for Fig. 2.36 are depicted in Fig. 2.35.

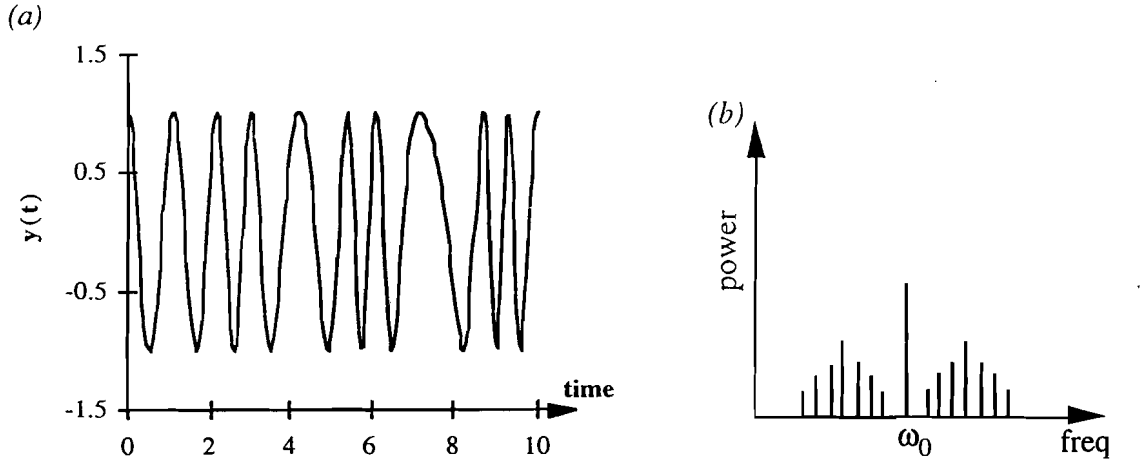

Fig. 2.1. Frequency modulation *(a)* the time domain picture *(b)* the frequency domain picture.

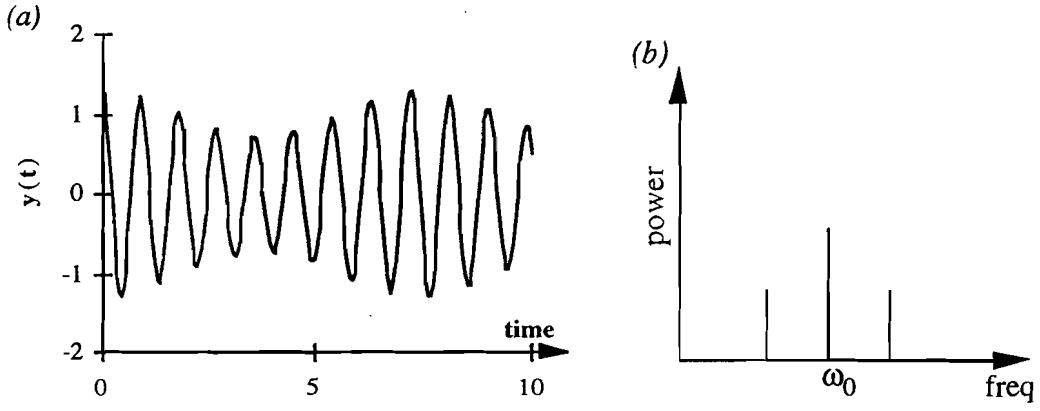

Fig. 2.2. Amplitude modulation in *(a)* the time domain picture *(b)* the frequency domain picture.

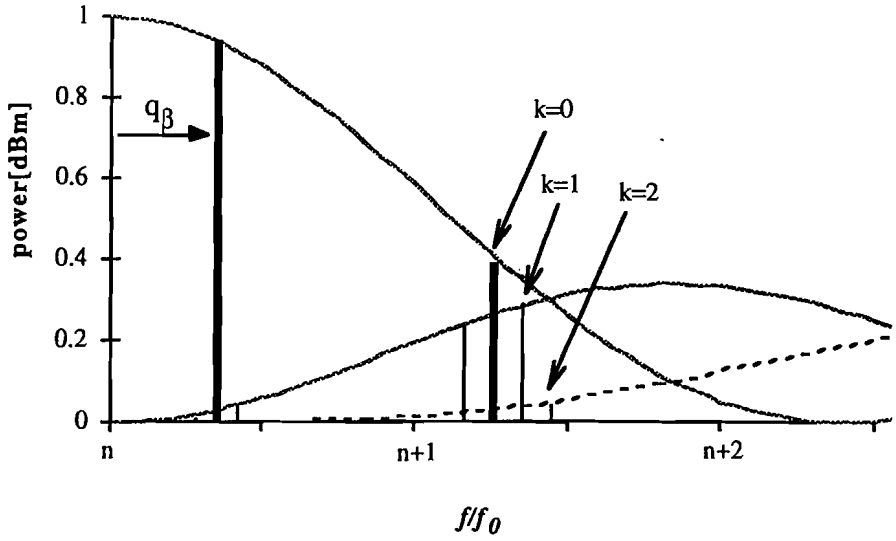

Fig. 2.3. The power spectrum of the transverse beam signal without a closed orbit error, and chromaticity= 0. The thick solid lines are the betatron sidebands. The thin solid lines nearby are the synchrotron sidebands corresponding to the betatron sideband.

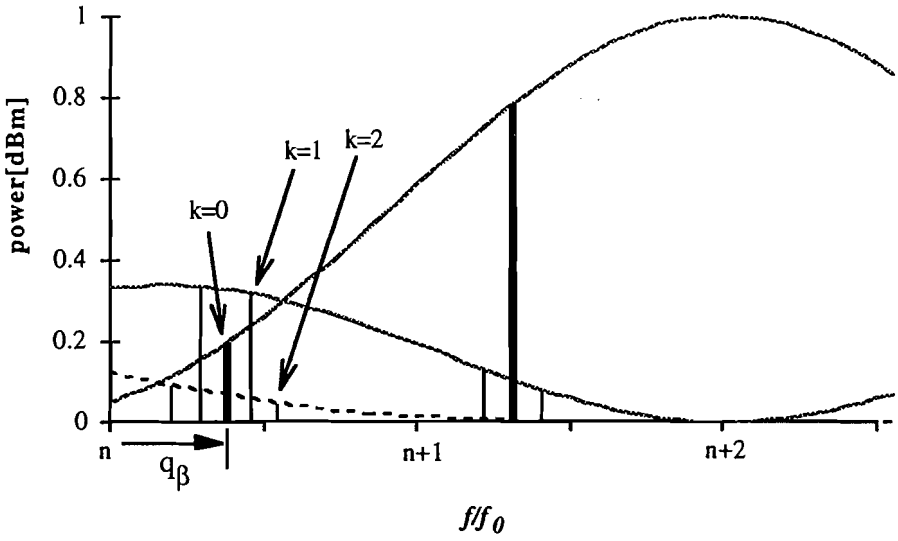

Fig. 2.4. The power spectrum of the transverse beam signal without a closed orbit error, and chromaticity≠ 0. The thick solid lines are the betatron sidebands. The thin solid lines nearby are the synchrotron sidebands corresponding to the betatron sideband.

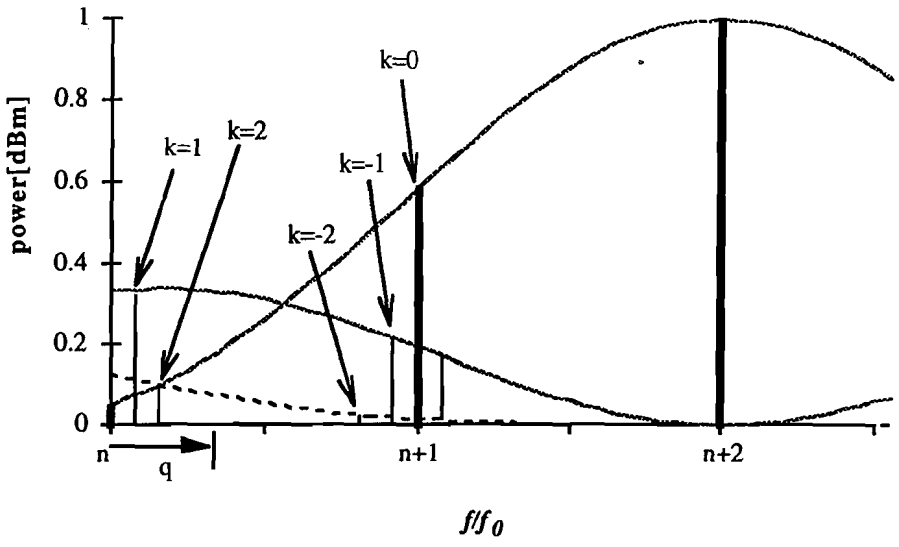

Fig. 2.5. The contribution of a closed orbit offset to the transverse beam spectrum. The thick solid lines are the results of injection offset. The thin solid lines are their corresponding synchrotron sidebands. The chromaticity is not zero in this case.

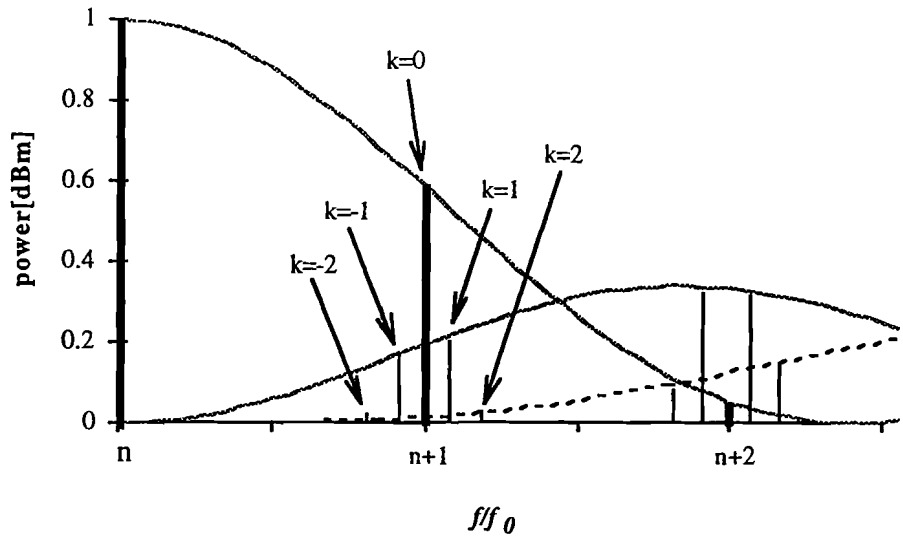

Fig. 2.6. The longitudinal beam spectrum for a single bunch. The thick solid lines are the revolution harmonic lines. The thin solid lines are their corresponding synchrotron sidebands.

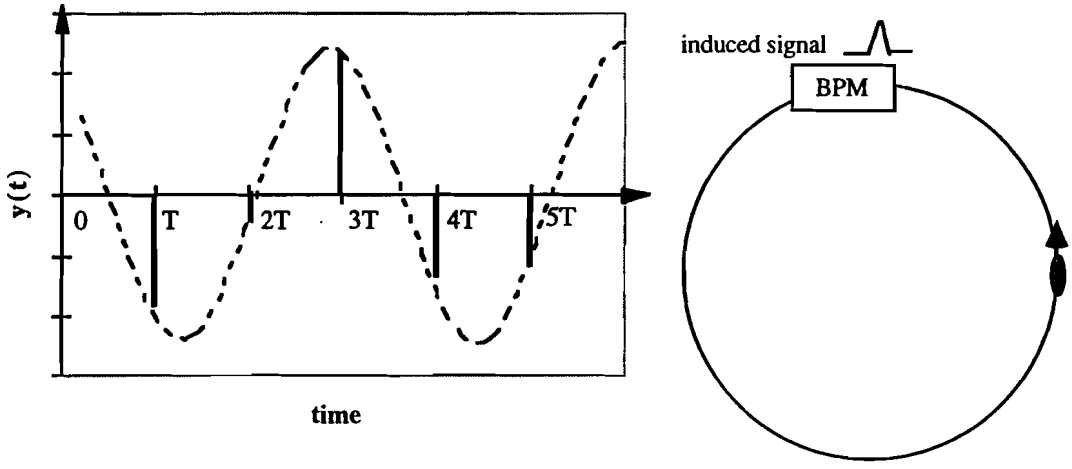

Fig. 2.7. The induced signal on the BPM by a bunch undergoing betatron oscillation in a storage ring. The left picture is a train of discrete pulses induced on the BPM, the dashed line is one interpretation of the beam motion.

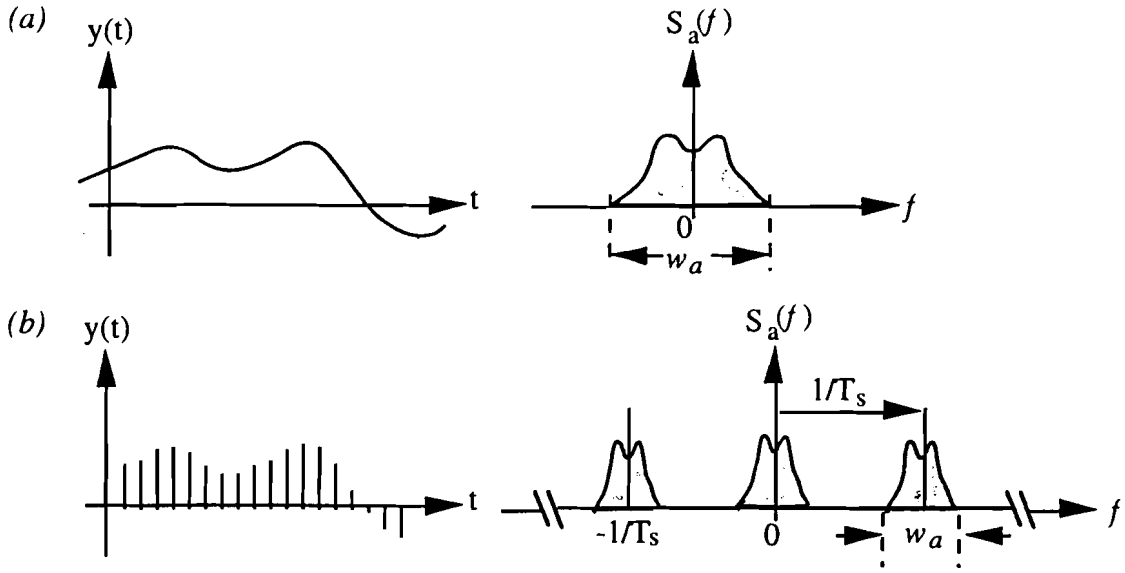

Fig. 2.8. The frequency spectrum from discrete sampling of an analog signal *(a)* the original analog signal and its frequency spectrum *(b)* the analog signal sampled by an infinite train of δ-function pulses and its corresponding spectrum.

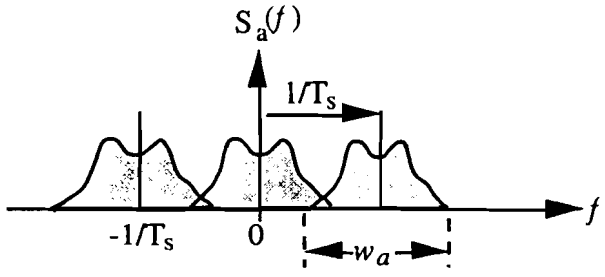

Fig. 2.9. The contamination of frequency spectrum due to undersampling.

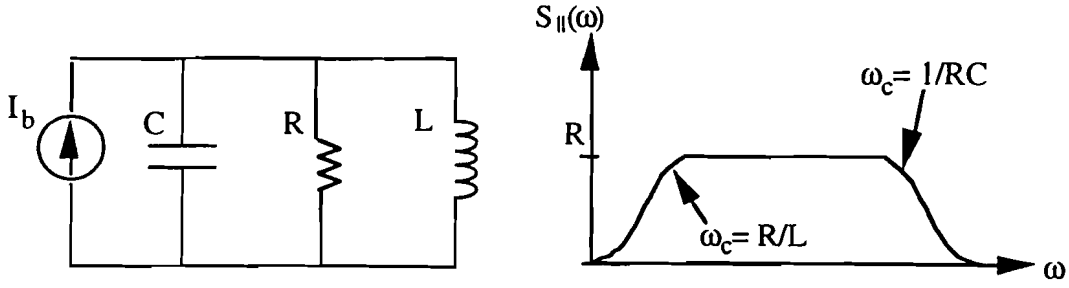

Fig. 2.14. Equivalent circuit model of the resistive wall current monitor and its frequency response.

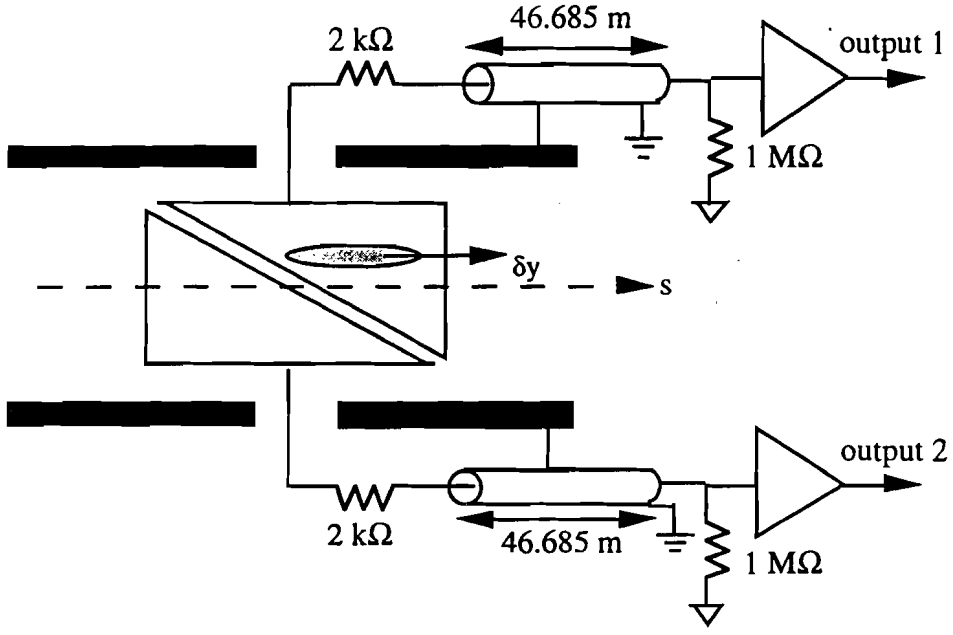

Fig. 2.15. The side view of the E49 capacitive BPM. The series resistor was connected to a 7/8 inch heliax cable. The other end of cable was connected to an operational amplifier with high input impedance.

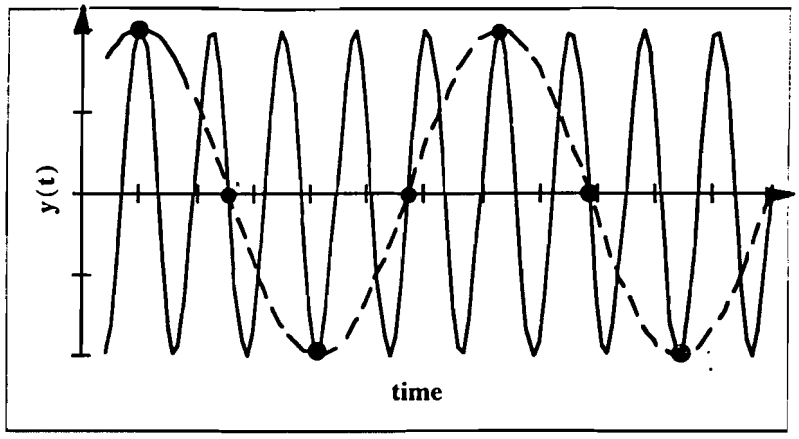

Fig. 2.10. The aliasing effect caused by undersampling a high frequency signal in the time domain. The solid line is the actual signal, and the dashed line is the aliased signal.

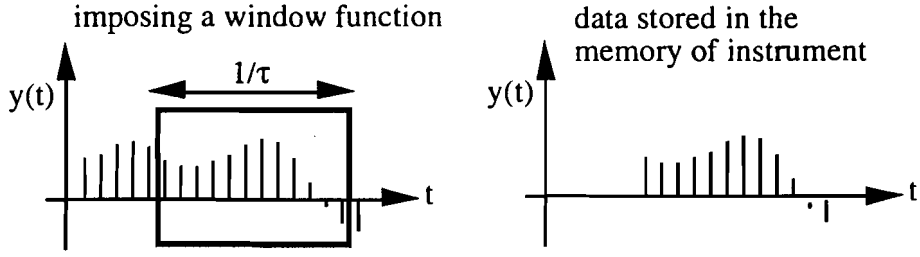

Fig. 2.11. The windowing procedure used by the measuring instrument to store sampled data points for later processing.

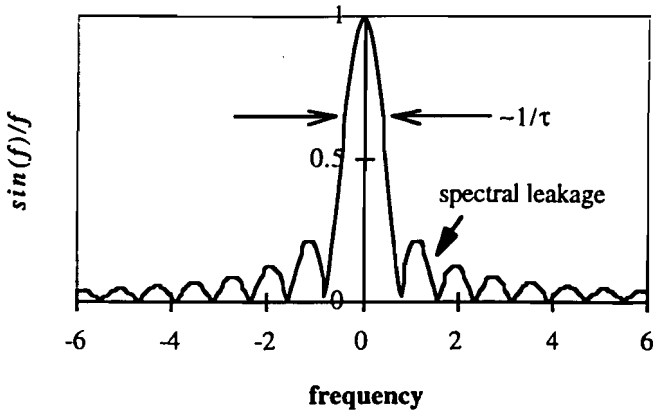

Fig. 2.12. The frequency spectrum of a rectangular window function. The ripples are caused by the truncation of the window function of finite length.

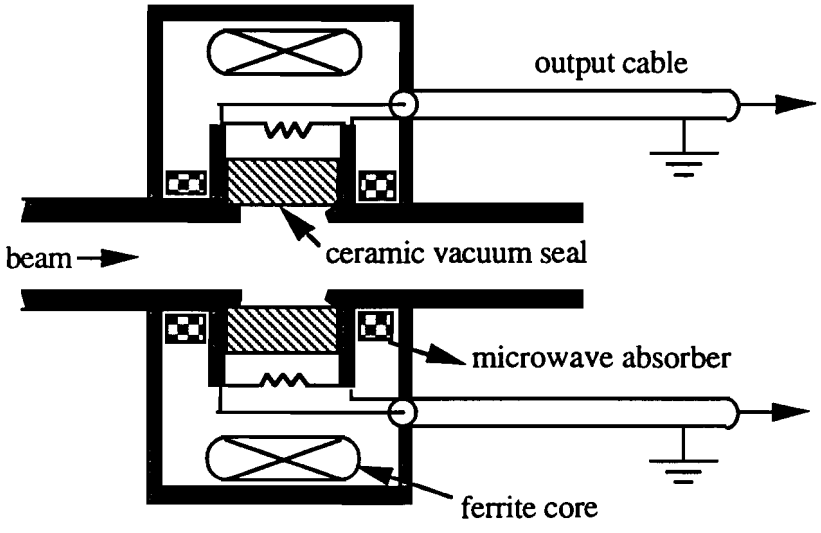

Fig. 2.13. A side view of the Main Ring resistive wall current monitor at the E48 lattice location. The detector has axial symmetry.

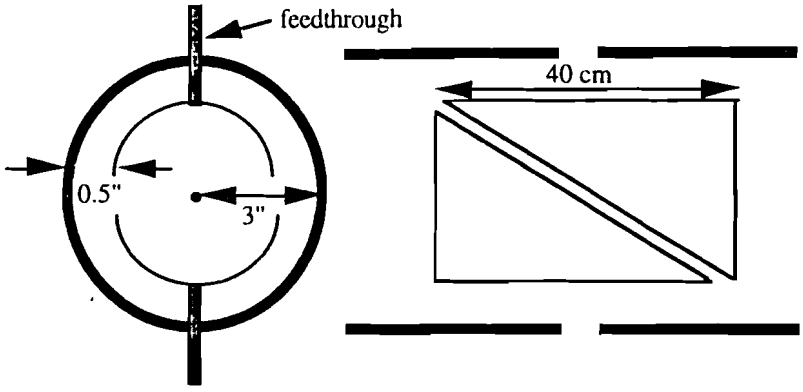

Fig. 2.16. The mechanical layout of E49 capacitive BPM. The left side is the cross sectional view and the right side is the side view.

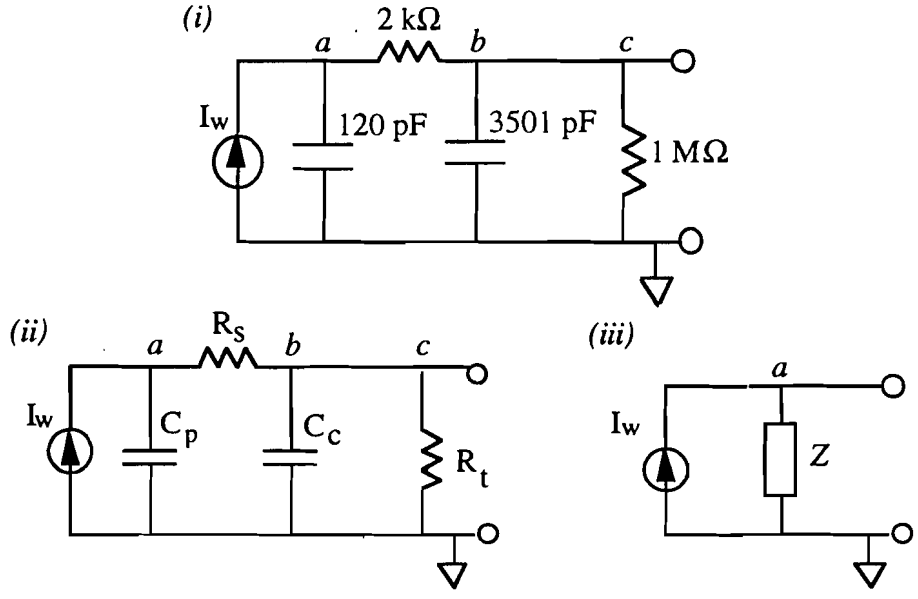

Fig. 2.17. The equivalent circuit model for each output port *(i)* the detailed circuit diagram *(ii)* and *(iii)* the simplified diagrams represented by symbols.

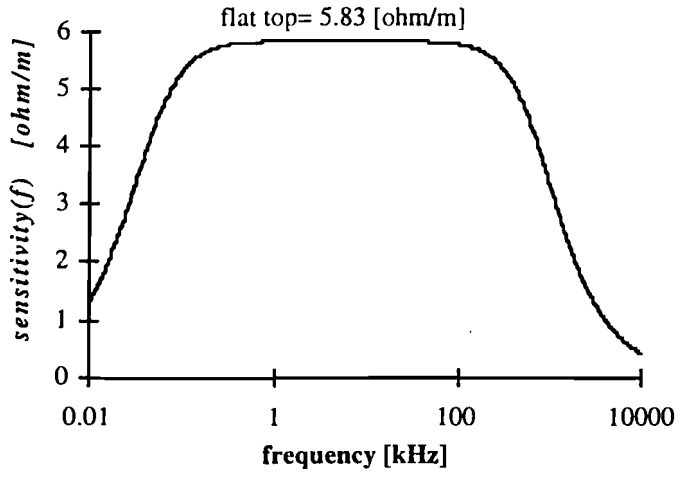

Fig. 2.18. The calculated detector sensitivity of the E49 BPM. The sensitivity is 5.83 [Ω/m] in the 3 dB bandwidth. The horizontal axis is a log scale.

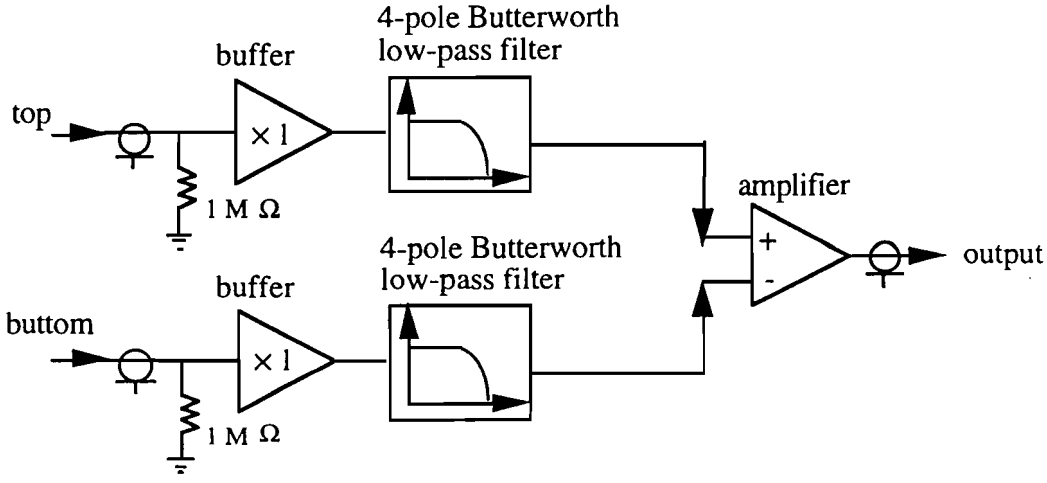

Fig. 2.19. The conceptual block diagram of receiver circuit for E49 BPM.

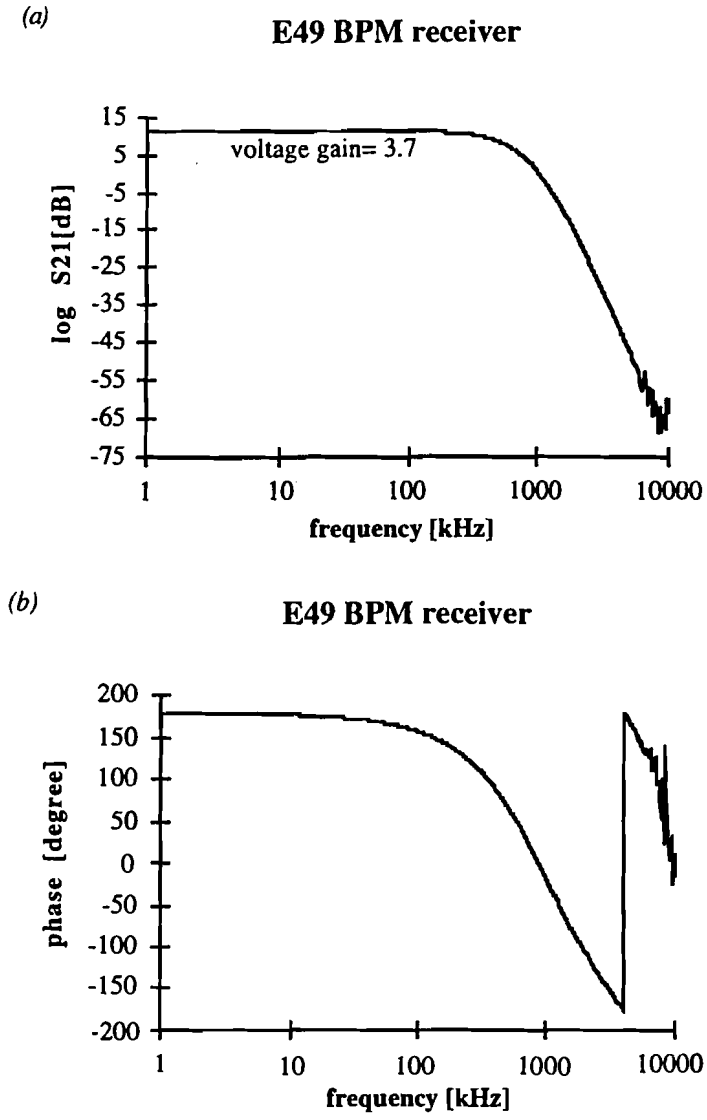

Fig. 2.20. The measured frequency response of E49 BPM receiver *(a)* the amplitude of transfer function S_{21} *(b)* the phase of transfer function S_{21}. The total voltage gain is 11 dB, the 3dB bandwidth is 460 kHz, and the horizontal axis is in log scale.

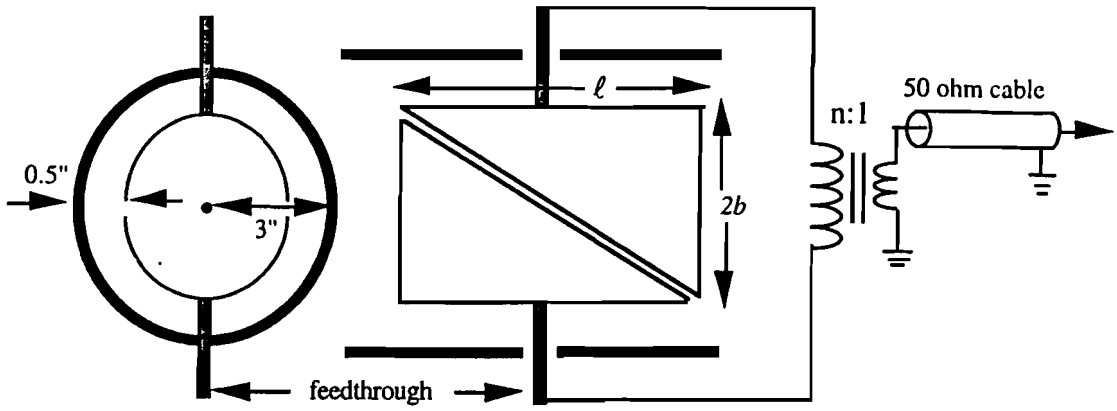

Fig. 2.21. The mechanical layout of the Main Ring Schottky detector at the A17 lattice location, b= the radius of the electrode, and ℓ= the length of the electrode.

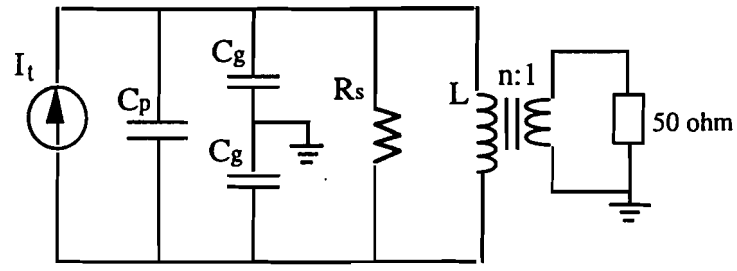

Fig. 2.22. The equivalent circuit model of the Main Ring Schottky detector, C_p= the capacitance between the two electrodes, C_g= the capacitance between the electrode and the beam pipe, R_s= the resistance of the inductor, and L= the inductance of primary inductor.

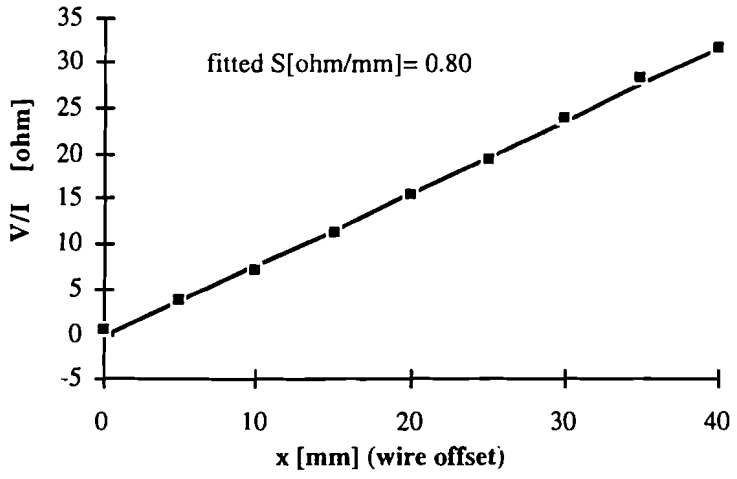

Fig. 2.23. The calibration of the Schottky detector performed by using the stretched-wire method on the bench. The solid line is the fit result.

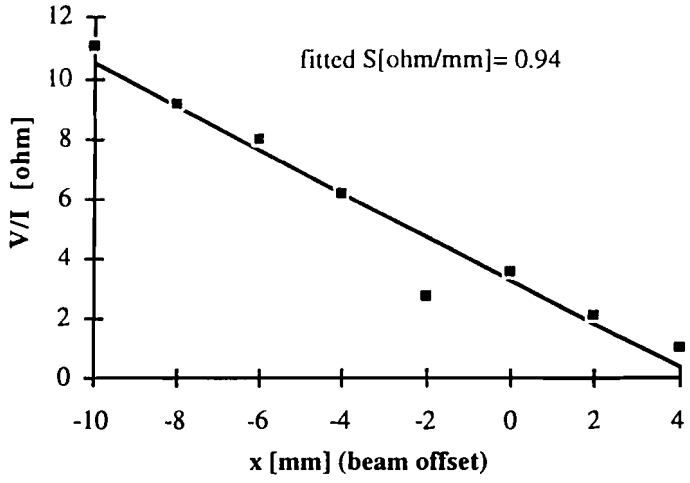

Fig. 2.24. The calibration of the Schottky detector performed by using off-centered beam. The solid line is the fit result.

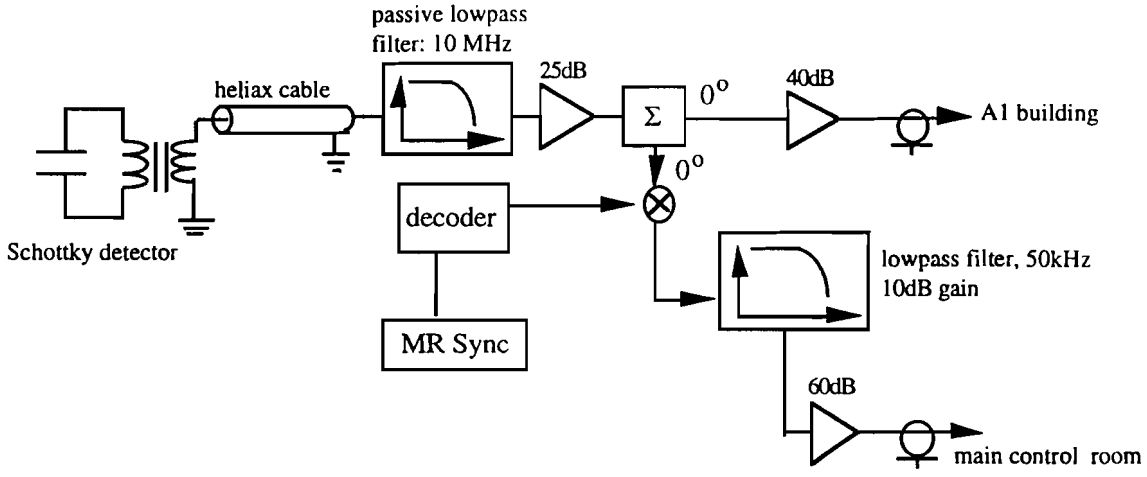

Fig. 2.25. The block diagram of signal processing scheme for the Main Ring Schottky detector.

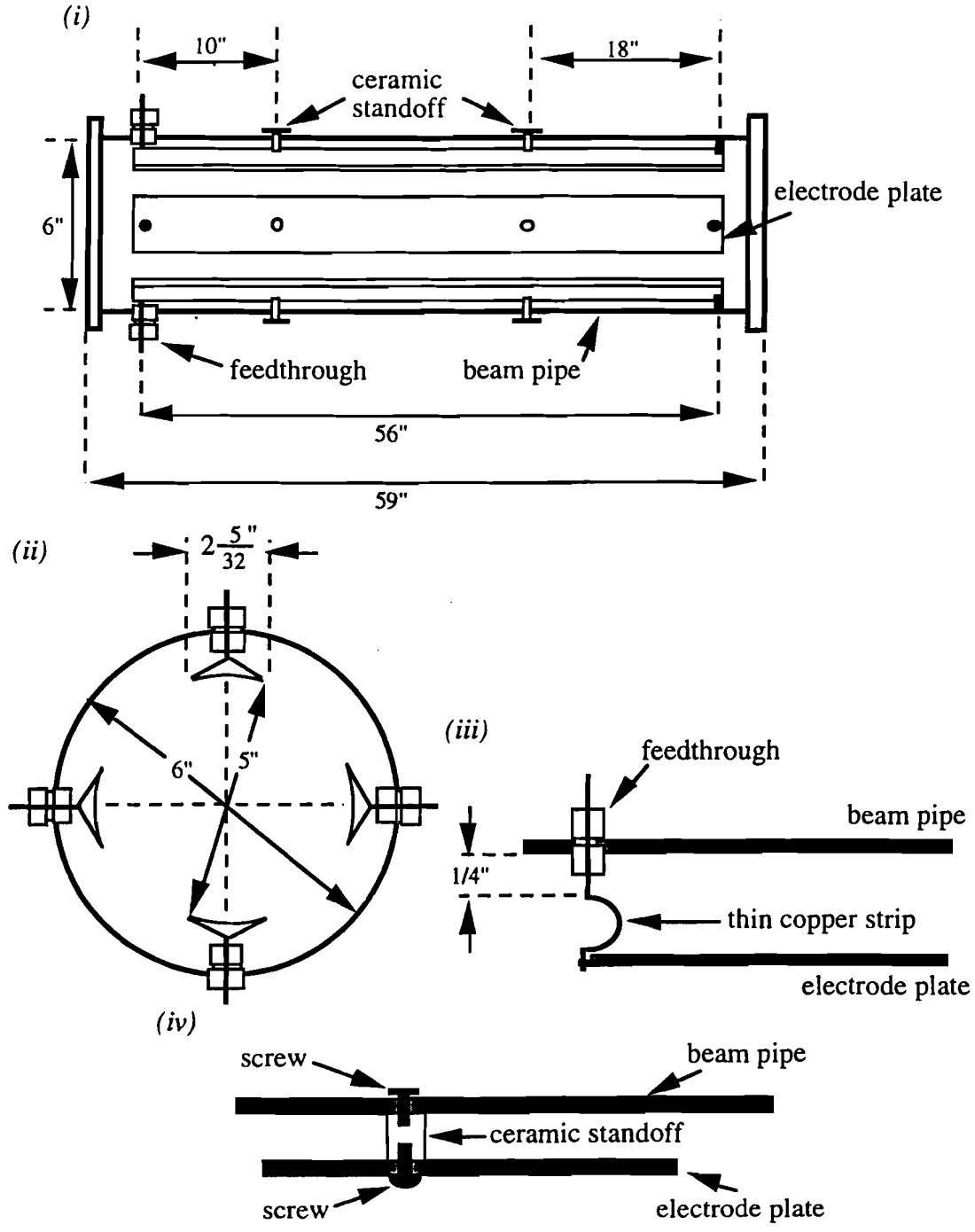

Fig. 2.26. The mechanical layout of the F14 stripline BPM *(i)* the side view of detector *(ii)* the cross-sectional view of detector looking from the feedthrough electrode *(iii)* the closeup view of electric contact between the feedthrough and the electrode plate *(iv)* the closeup view of ceramic standoff. The downstream end of electrode plates were welded to the beam pipe.

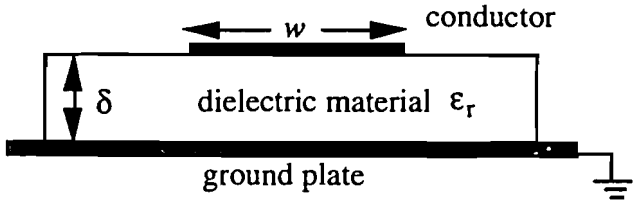

Fig. 2.27. The cross-sectional view of microstrip line. A conductor was laid on top of a uniform dielectric material with relative permittivity ε_r.

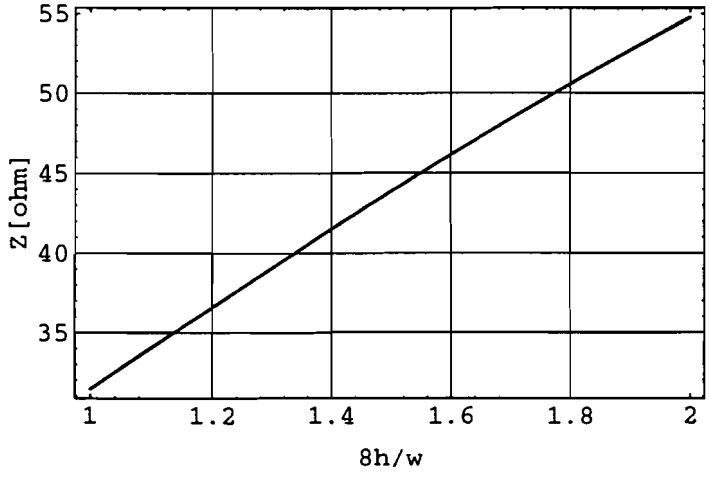

Fig. 2.28. The characteristic impedance of microstrip line as function of $8h/w$.

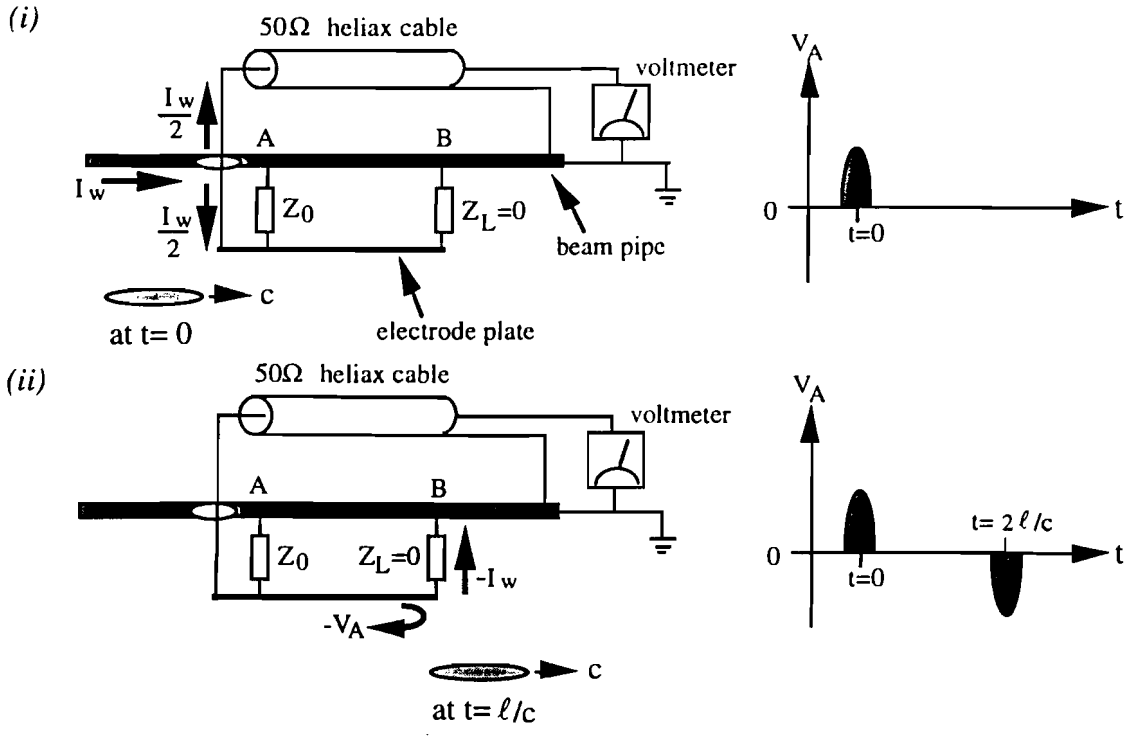

Fig. 2.29. The induced signal of the stripline BPM, the length of electrode plate is ℓ *(i)* the induced signal at the feedthrough port when t= 0 *(ii)* the induced signal at the feedthrough port when t= $2\ell/c$.

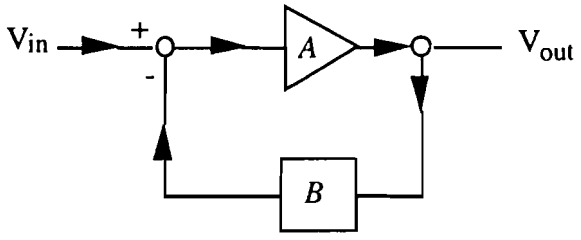

Fig. 2.30. The block diagram of a negative feedback loop.

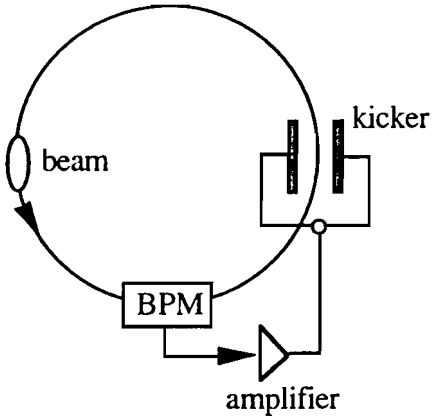

Fig. 2.31. A generic configuration of damper system.

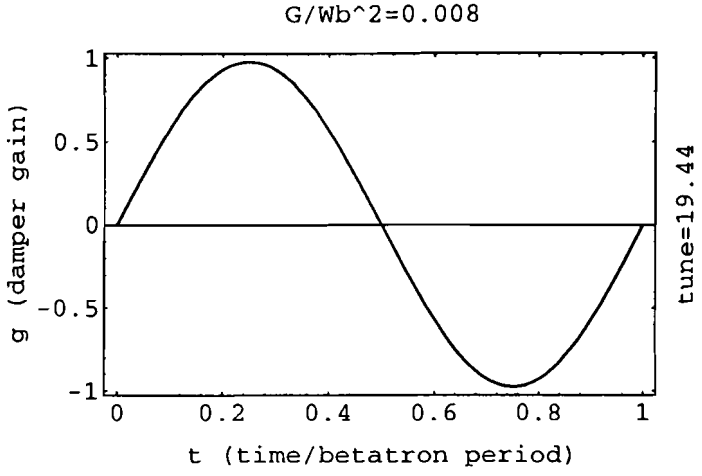

Fig. 2.32. Damper gain vs. delay time, where $G/(\omega_\beta)^2 = 0.008$. The abscissa is the delay time normalized by the period of betatron oscillation, and the ordinate is the damper gain g defined in Eq.(2.63). Positive values for damper gain mean damping effect, and negative values for damper gain mean antidamping effect.

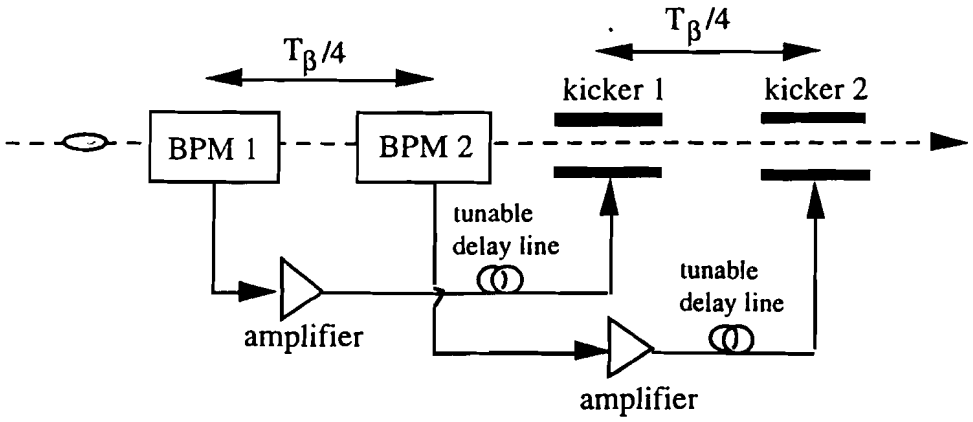

Fig. 2.33. A schematic sketch of the 2BPM-2kicker feedback system. The first BPM and the second BPM are separated by a quarter of the betatron period T_β, and the second kicker is placed a quarter of the betatron period apart from the first one.

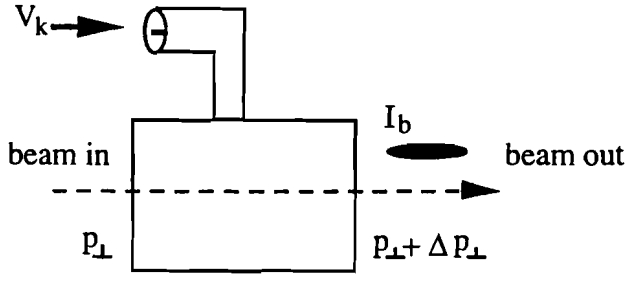

Fig. 2.34. A schematic sketch of the excitation of a kicker.

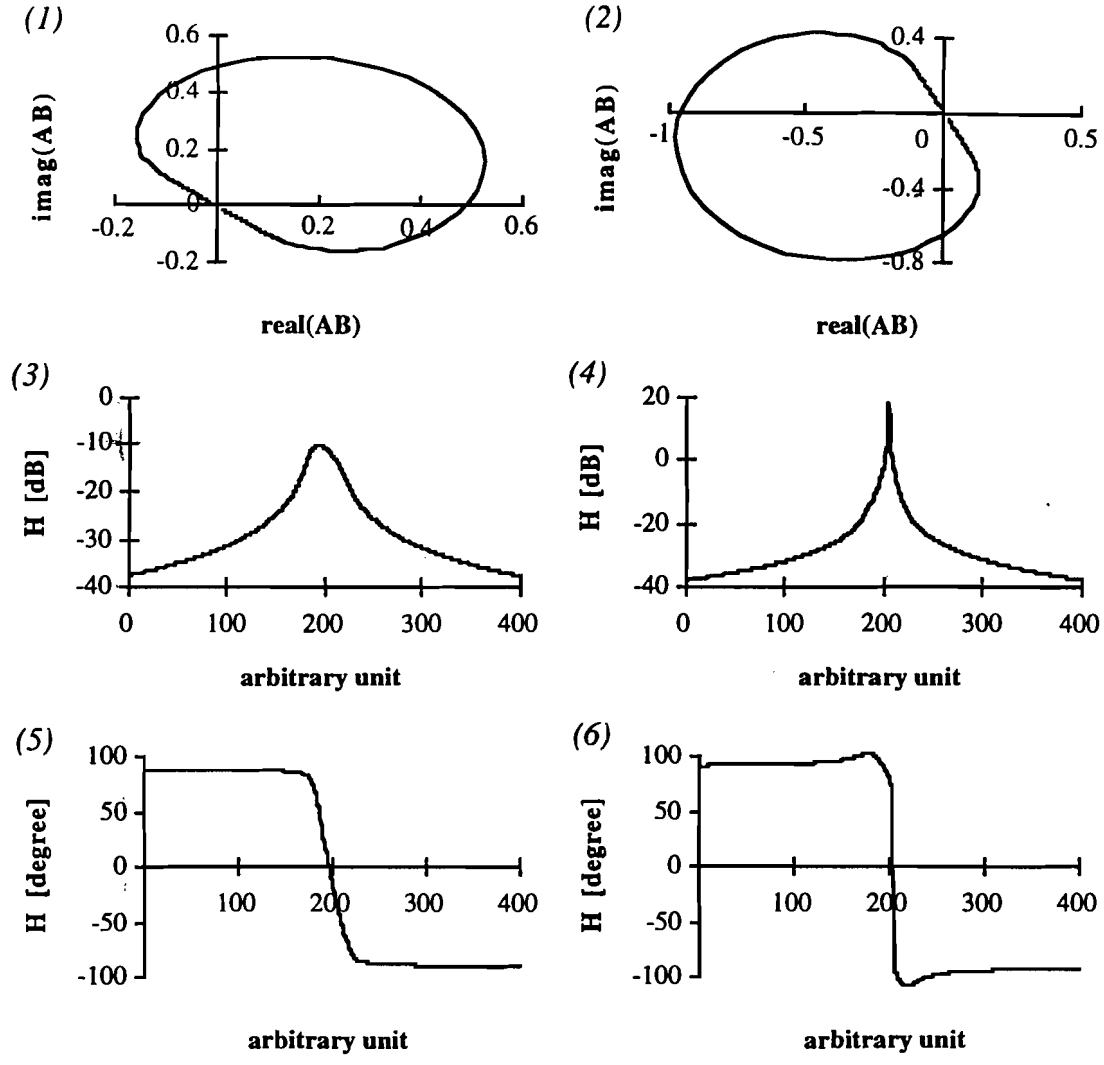

Fig. 2.35. The plots on the left side are for the stable feedback system, and those in the right side are for the unstable one *(1)* and *(2)* are the Nyquist stability plots, *(3)* and *(4)* are the magnitude of closed-loop transfer function, *(5)* and *(6)* are the phase of closed-loop transfer function.

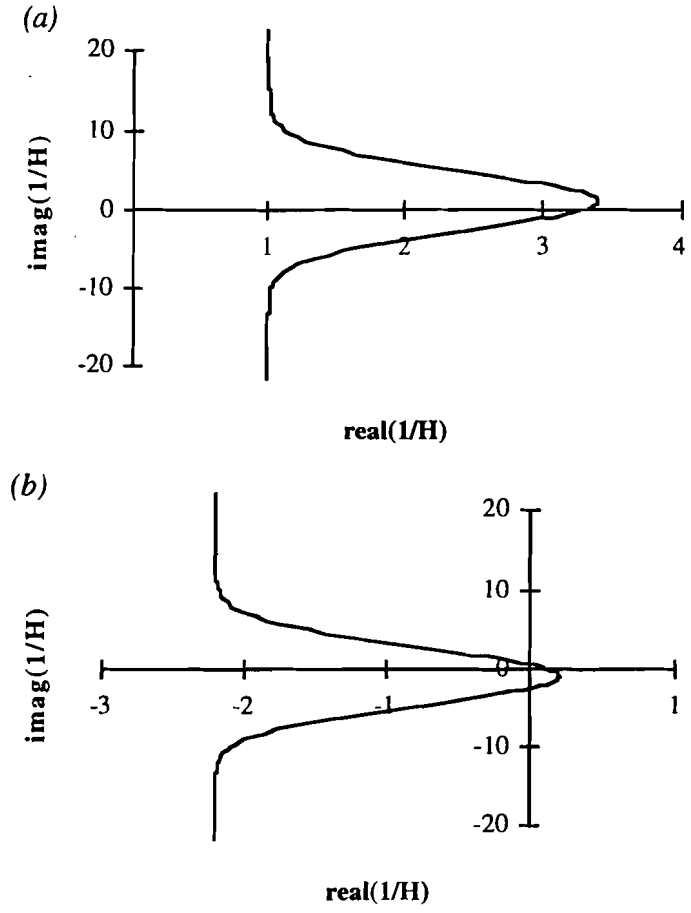

Fig. 2.36. The stability diagrams for stable and unstable feedback systems *(a)* the stable case *(b)* the unstable case.

CHAPTER 3

BASIC CONCEPTS OF TRANSVERSE COLLECTIVE EFFECTS

A. Mechanism of self-coupling

When charged particles travel together in an accelerator, each individual particle will experience an electromagnetic force caused by the interaction between the vacuum chamber and all other charged particles. The net electromagnetic force is generated by charged particles acting coherently as a whole. This electromagnetic force will affect the particle motion and thus create a self-coupling effect on charged particles. Because of the requirement of causality, each particle only sees the electromagnetic force induced by preceding particles. Hence the self-coupling electromagnetic force generated by the interaction between the vacuum chamber and charged particles is named the wake force.

The linear component of the transverse wake force only depends on the center of mass motion of particle beams. On the contrary, the nonlinear component of transverse wake force depends on the shape of particle beams. The linear wake force is the dominant effect in the transverse direction, and it presents a perturbation to the external focusing force provided by quadrupole magnets. Without proper measures being taken, the transverse wake force will cause the deterioration of beam quality or even beam loss.

1. Concepts of wake function and impedance

The kinetic energy of the protons at injection is 8 GeV for the Main Ring. The corresponding speed of protons at injection is $0.994c$, where c is the speed of light. It is a good approximation to treat protons as relativistic particles at the injection stage. For an off-centered relativistic particle traveling near the speed of light in free space, as depicted in Fig. 3.1, the radial electrical field in the comoving frame is given by:[24]

$$E_r^* = \frac{qd}{4\pi\varepsilon_0(d^2+\gamma^2\upsilon^2t^2)^{3/2}} \tag{3.1}$$

where γ= the Lorentz relativistic factor, ε_0= the dielectric constant of vacuum, q= the charge of particle, t= the time in the lab frame, υ= the velocity of particle, and d is its radial position. The electromagnetic field in the lab frame is given by the Lorentz transformation:[24]

$$\begin{aligned}\vec{E}_\perp &\approx \gamma\vec{E}_\perp^* = \frac{\gamma q\, d\hat{n}}{4\pi\varepsilon_0(d^2+\gamma^2\upsilon^2t^2)^{3/2}} \\ \vec{B}_\perp &\approx \gamma\hat{s}\times\vec{E}_\perp^*\end{aligned} \tag{3.2}$$

where $\hat{n}$ is the transverse unit vector in the lab frame.

Because of the Lorentz contraction, there is almost no longitudinal field in the lab frame; the transverse field is squeezed into a very narrow cone with the longitudinal angle roughly equal to $1/\gamma$. The pattern of field lines in the comoving frame and the lab frame is depicted in Fig. 3.2.[24] For a proton of the injection energy in the Main Ring, the field lines are squeezed into a narrow cone with a temporal width $b/c\gamma$, where b is the radius of vacuum chamber. The temporal width of field distribution is approximately equal to 10

psec at a radius of 3 cm for 8 GeV protons. Inside an accelerator, the field lines are truncated by the metallic beam pipe.

In reality the material of the beam pipe has a certain resistance. This will generate a retarded electromagnetic field behind the charged particle. But a relativistic particle will not see any electromagnetic field in front of it. Therefore, the electromagnetic field of a relativistic charged particle inside the vacuum chamber has to satisfy the requirement of causality. Because of the above characteristics, this electromagnetic field is called a wake field. A qualitative picture of wake fields is depicted in Fig. 3.3.[25] Only the case of the relativistic limit where $\gamma \rightarrow \infty$ will be considered in this text.

To study collective beam effects, one first needs to have a good knowledge of the wake fields generated by particle beams. This involves solving Maxwell's equations with a charge distribution inside the vacuum chamber. Maxwell's equations are solved by assuming that the particle beam has not been affected by the wake field. Therefore, it is not a self-consistent solution for the wake field. Then the approximate solution of the wake field is used to solve the self-consistent equation of motion for charged particles.

1.1 Definitions Suppose there are two charged particles traveling along the longitudinal direction, the leading particle *A* has charge Q and the trailing particle *B* has charge q as depicted in Fig. 3.4. When the longitudinal position of leading particle *A* coincides with some reference point in the accelerator, the time is chosen to be t= 0. Particle *A* will be used as the source to generate wake fields and particle *B* will be the witness.

Suppose particle *B* is at the location s on the longitudinal axis, it will see the wake field generated by particle A at a previous time t- (s'- s)/*c*. If one integrates the

instantaneous work done on particle B by the longitudinal wake force $F_{\|}$ of particle A, one can define the longitudinal wake function $W_{\|}$ generated by a point charge as:

$$\int_{-\infty}^{t} F_{\|}(s,t' = t - \tfrac{s'-s}{c}) \cdot c\,dt' = -qQW_{\|}(z) \tag{3.3}$$

The longitudinal effect caused by the wake force of particle A can be represented by the wake function $W_{\|}$ in the right-hand side of Eq.(3.3). The longitudinal wake function $W_{\|}$ does not depend on the charge of the source particle. It only depends on the longitudinal separation z and properties of the vacuum chamber. From the requirement of causality one can readily get $W_{\|}= 0$ for $z> 0$. The longitudinal wake function has the MKS dimension of volt per coulomb.

When the wake force is generated by a charge distribution traveling near the speed of light, the witness particle will only see the wake force generated by those charges which passed by the reference location at a previous time. This results from the requirement of causality. Hence, the energy change of witness particles caused by the wake force of a charge distribution is given by:

$$\int_{-\infty}^{t} F_{\|}(s,t' = t - \tfrac{s'-s}{c}) \cdot c\,dt' = -q\int_{t}^{\infty} I_b(s,t')W_{\|}(z) \cdot dt' \tag{3.4}$$

where I_b is the corresponding beam current of the source distribution. One can rewrite Eq.(3.4) as the following:

$$\int_{-\infty}^{t} F_{\|}(s,t')\cdot c\,dt' = -\frac{q}{c}\int_{s}^{\infty} I_b(s,t-\tfrac{s'-s}{c})\,W_{\|}(z)\cdot ds' = \frac{-q}{c}\int_{-\infty}^{0} I_b(s,t+\tfrac{z}{c})\,W_{\|}(z)\cdot dz \tag{3.5}$$

The harmonic representation of the beam current is given by the following:

$$I_b(s,t) = \tilde{I}_b\, e^{i(ks-\omega t)} \tag{3.6}$$

If one substitutes Eq.(3.6) into Eq.(3.5) and uses the requirement of causality, one will obtain the following result:

$$\frac{1}{q}\int_{-\infty}^{t} F_{\|}(s,t')\cdot c\,dt' = -I_b(s,t)\cdot\left[\int_{-\infty}^{\infty} e^{-i\omega z/c}\,W_{\|}(z)\cdot dz/c\right] \tag{3.7}$$

The left-hand side of Eq.(3.7) has the dimensionality of voltage, and the right-hand side equals to the beam current multiplied by a bracket. This readily suggests one to use the concept of impedance to represent the wakefield effect. The equivalent voltage corresponding to Eq.(3.7) is:

$$V_{\|}(s,t) = -I_b(s,t)\cdot Z_{\|}(\omega) \tag{3.8}$$

Therefore, one can define a longitudinal impedance to represent the longitudinal effect of the vacuum chamber by using Eq.(3.8). The longitudinal impedance of an accelerator is defined as:[25]

$$Z_{\parallel}(\omega) = \frac{1}{c}[\int_{-\infty}^{\infty} e^{-i\omega z/c} W_{\parallel}(z) \cdot dz] \tag{3.9}$$

The longitudinal impedance $Z_{\parallel}$ has the MKS dimension of ohms.

To describe the wakefield effect in the transverse direction, one looks at the integrated transverse kick received by the witness particle *B* due to the transverse wake force $\vec{F}_{\perp}$ generated by particle *A*. Only the linear component of the transverse wake force which depends on the transverse displacement of the source particle is considered. The transverse wake function $W_{\perp}$ for a point charge is defined as:

$$\int_{-\infty}^{t} \vec{F}_{\perp}(s, t' = t - \tfrac{s'-s}{c}) \cdot c\, dt' = -qQ\bar{r} \cdot W_{\perp}(z) \tag{3.10}$$

where $\bar{r}$ is the transverse displacement of the source particle. The transverse wake function $W_{\perp}$ does not depend on the charge nor the displacement of the source particle. It only depends on the longitudinal separation z and properties of the vacuum chamber. It has the MKS dimensions of volt per coulomb per meter.

When the source is not a single particle but a charge distribution, the integrated transverse kick received by the witness particle is given by:

$$\int_{-\infty}^{t} \vec{F}_{\perp}(s, t' = t - \tfrac{s'-s}{c}) \cdot c\, dt' = -q \int_{t}^{\infty} \langle \bar{r}(t') \rangle I_b(s, t') W_{\perp}(z) \cdot dt' \tag{3.11}$$

where $\langle \bar{r} \rangle$ is the transverse displacement of the center of mass motion of the source charge distribution. If one substitutes Eq.(3.6) into Eq.(3.11) and repeats the same calculation as in the longitudinal case, one will get the following result:

$$\frac{1}{q}\int_{-\infty}^{t}\vec{F}_{\perp}(s,t')\cdot c\,dt' = -\langle\vec{r}\rangle I_b(s,t)\left[\int_{-\infty}^{\infty}e^{-i\omega z/c}\,W_{\perp}(z)\cdot dz/c\right] \tag{3.12}$$

Similarly the left-hand side of Eq.(3.12) has the dimensionality of voltage, and the right-hand side is equal to the beam current multiplied by the transverse displacement and a bracket. The equivalent voltage corresponding to Eq.(3.12) is given by:

$$V_{\perp}(s,t) = i\langle\vec{r}\rangle I_b(s,t)\cdot Z_{\perp}(\omega) \tag{3.13}$$

where the factor i indicates the sine-like feature of transverse wake function. The transverse impedance is defined as:[25]

$$Z_{\perp}(\omega) = \frac{i}{c}\left[\int_{-\infty}^{\infty}e^{-i\omega z/c}\,W_{\perp}(z)\cdot dz\right] \tag{3.14}$$

The transverse impedance $Z_{\perp}$ has the dimensionality of ohms per meter.

1.2 General properties From the definitions of longitudinal and transverse wake functions given by Eqs.(3.3) and (3.10), one learns that the wake function is determined by the boundary condition (vacuum chamber), not by the beam properties. The impedance can be obtained by performing a Fourier transform on the wake function. In fact, the impedance is the frequency representation of self-coupling effects caused by the interaction with the vacuum chamber. The reciprocal relation between the wake function and the impedance is given by the following equations:

$$W_{\parallel}(z) = \frac{1}{2\pi}\int_{-\infty}^{\infty} e^{i\omega z/c} Z_{\parallel}(\omega)\cdot d\omega \tag{3.15}$$

$$W_{\perp}(z) = \frac{-i}{2\pi}\int_{-\infty}^{\infty} e^{i\omega z/c} Z_{\perp}(\omega)\cdot d\omega \tag{3.16}$$

Since a charged particle can only see the wake force in front of it, on the average it sees only half of the electric field it itself generates. The net energy loss associated with the longitudinal wake force seen by a charge distribution itself is:[25]

$$\Delta E = -\frac{Q^2}{2} W_{\parallel}(0) \tag{3.17}$$

where Q is the total charge of the distribution. This is a general result from the requirement of causality. It is referred to as the fundamental theorem of beam loading.[25]

If the beam pipe has axial symmetry, one will get a result which relates the longitudinal and transverse wake functions together by the following expression:

$$\nabla_{\perp}\oint F_{\parallel}\cdot ds = \frac{\partial}{\partial z}\oint \vec{F}_{\perp}\cdot ds \tag{3.18}$$

The above result means that the transverse gradient of an integrated energy loss is equal to the longitudinal gradient of an integrated transverse kick. This result is referred to as the Panofsky-Wenzel theorem.[25]

The wake functions have the following general properties:[25] *i)* the longitudinal wake function is cosine-like and the transverse wake function is sine-like, *ii)* the wake function has to satisfy the requirement of causality, *iii)* right behind the source particle

the longitudinal wake force tends to retard the witness particle and the transverse wake force tends to deflect the witness particle away from the axis, *iv)* the source particle sees exactly half of its own longitudinal wake force and none from its transverse wake. A schematic sketch of wake functions vs. the longitudinal separation z is depicted in Fig. 3.5. Because the wake function is a real quantity, one can get the following relations for the impedance from Eqs.(3.9) and (3.14):

$$\begin{aligned} Z_{\parallel}^{*}(\omega) &= Z_{\parallel}(-\omega) \\ Z_{\perp}^{*}(\omega) &= -Z_{\perp}(-\omega) \end{aligned} \tag{3.19}$$

i.e., $Re\,Z_{\parallel}$ and $Im\,Z_{\perp}$ are even functions of ω; $Re\,Z_{\perp}$ and $Im\,Z_{\parallel}$ are odd functions of ω. A schematic sketch of the above results is depicted in Fig. 3.6.

2. Impedances of various accelerator components

Various vacuum components of accelerators have different geometries than a smooth beam pipe. Accelerator impedances can be cast into three major categories: the resonator impedance, the resistive wall impedance and the inductive wall impedance.

Besides the vacuum chamber, the charge beam itself also presents an equivalent impedance caused by its own image charge flowing on the surface of beam pipe; it is referred to as the space-charge impedance.

2.1 Resonator impedance For resonator structures, the longitudinal impedance can be modeled by a lumped element electrical resonant circuit. The impedance of the parallel RCL circuit depicted in Fig. 3.7 is given by:

$$Z_{\|} = \frac{R}{1 + iQ(\frac{\omega_c}{\omega} - \frac{\omega}{\omega_c})} \tag{3.20}$$

where $Q = R\sqrt{C/L}$ is the quality factor, the shunt impedance R is in units of [Ω] and $\omega_c = 1/\sqrt{LC}$ is the angular resonant frequency.

The transverse impedance for a resonator structure can be modeled by the following expression:[25]

$$Z_{\perp} = \frac{R_t \frac{\omega_c}{\omega}}{1 + iQ(\frac{\omega_c}{\omega} - \frac{\omega}{\omega_c})} \tag{3.21}$$

where the transverse shunt impedance R_t is in units of [Ω/m], and ω_c is the angular resonant frequency. An example of transverse resonator impedance is depicted in Fig. 3.8. When the resistive power dissipation is very small for the resonator structure (Q >> 1), the corresponding wake functions can be approximated by the following equations:

$$\begin{aligned} W_{\|}(z = 0) &= \frac{\omega_c R}{2Q} \\ W_{\|}(z < 0) &= \frac{\omega_c R}{Q} e^{\alpha z/c} \cos(\bar{\omega} z/c) \end{aligned} \tag{3.22}$$

$$W_{\perp}(z < 0) = \frac{\omega_c^2 R_t}{\bar{\omega} Q} e^{\alpha z/c} \sin(\bar{\omega} z/c) \tag{3.23}$$

where $\alpha = \omega_c/2Q$ and $\bar{\omega} = \sqrt{\omega_c^2 - \alpha^2}$. An example of the transverse wake function generated by a point charge passing by a resonator structure is depicted in Fig. 3.9.

In an accelerator, the major source of transverse resonator impedance comes from the high order modes of rf cavities. In the high frequency range (around few GHz), the corrugations of the beam pipe at bellows may become an important type of resonator structure. They can contribute to resonator impedances in the high frequency range.

2.2 Resistive wall impedance Besides the cavity-like structures, the resistance of a smooth beam pipe also contributes to the accelerator impedance. Suppose the entire accelerator is only comprised by the smooth beam pipe with circular cross section of radius b. The surface current K_s on the beam pipe is given by:

$$K_s = \frac{I_b}{2\pi b} \tag{3.24}$$

The average power dissipation per unit area due to the longitudinal impedance is given by:

$$\begin{aligned} \frac{dP}{dA} &= \frac{I_b^2 Z_{\|}}{2(2\pi b)(2\pi \bar{R})} \\ &= \left(\frac{2\pi b}{2\pi \bar{R}}\right)\frac{K_s^2 Z_{\|}}{2} \end{aligned} \tag{3.25}$$

where $\bar{R}$ is the mean radius of accelerator. From the definition of surface resistance R_s,[24] one has the following relation:

$$\frac{dP}{dA} = \frac{K_s^2 R_s}{2} \tag{3.26}$$

Therefore, the longitudinal resistive wall impedance is given by:

$$Z_{\parallel} = \frac{2\pi\bar{R}}{2\pi b} R_s \tag{3.27}$$

The surface resistance R_s is in units of [Ω].

When the frequency is sufficiently below the cutoff frequency of beam pipe, $0.4c/b$ approximately[10], the formulas for calculating the surface resistance is listed for the following cases:

i) when the skin depth is smaller than the thickness of the beam pipe[24]

$$R_s = (1-i)\frac{\rho}{\delta} \tag{3.28}$$

ii) when the skin depth is comparable to the thickness of the beam pipe[26]

$$R_s = \frac{\rho}{d} \tag{3.29}$$

where ρ is the resistivity of beam pipe, d is the thickness of beam pipe and δ is the skin depth. The formula for calculating the skin depth is given by:[10]

$$\delta[\mathrm{cm}] = \frac{6.61}{\sqrt{f}}\sqrt{\frac{\rho}{\mu_r \rho_c}} \tag{3.30}$$

where $f = \omega/2\pi$ is the frequency in units of [Hz], μ_r is the relative permeability of conductor materials, $\mu_r = 1$ for copper and other nonmagnetic materials, ρ_c is the resistivity of copper at the temperature 20 °C.

The most popular materials for accelerator beam pipes are stainless steel and aluminum. Table 3.1 summarizes the properties for some conductor materials.[10] For the Main Ring beam pipe, the resistive component of the longitudinal impedance has a value of 182.6 [ohm] at the frequency of 1 MHz.

Table 3.1: Resistivity of some conductor materials measured at temperature 20 °C.

Material	Resistivity ($\times 10^{-6}$ ohm-cm)	Form
Copper	1.7241	solid
Aluminum	2.62	solid
Steel, stainless	76	solid

For a circular beam pipe, the transverse impedance can be related to the longitudinal impedance through the Panofsky-Wenzel theorem. The transverse resistive wall impedance can be derived from the longitudinal impedance as:[26]

$$Z_{\perp} = \frac{2c}{b^2}\frac{Z_{\parallel}}{\omega} \tag{3.31}$$

or in terms of the normalized longitudinal impedance as:

$$Z_{\perp} = \frac{2\overline{R}}{b^2}\frac{Z_{\parallel}}{n} \tag{3.32}$$

where $\frac{Z_{\parallel}}{n}$ is the normalized longitudinal impedance, n= ω/ω_0 and ω_0 is the angular revolution frequency. Note that the above result is only valid for circular beam pipes.

In the low frequency limit, when the skin depth is comparable to the thickness of beam pipe (thin-wall model), the transverse resistive wall impedance can be derived from Eqs.(3.27), (3.29) and (3.31):

$$Z_{\perp}[\Omega/\mathrm{m}] = \frac{c\rho\overline{R}\cdot sgn(f)}{\pi d b^3 f} \tag{3.33}$$

When the skin depth is smaller than the thickness of beam pipe (thick-wall model), the transverse resistive wall impedance can be derived from Eqs.(3.27), (3.28), (3.30), and (3.31):

$$Z_{\perp}[\Omega/\mathrm{m}] = \frac{c\rho\overline{R}\cdot[sgn(f)-i]}{6.61\pi b^3 f^{1/2}\mu_r^{1/2}}\sqrt{\frac{\rho}{\rho_c}} \tag{3.34}$$

Note that the signum function *sgn(f)* has been introduced in Eqs.(3.33) and (3.34). It results from the properties of wake functions. The real part of transverse resistive wall impedance for the Main Ring beam pipe is calculated and shown in Fig. 3.10. The material used for the beam pipe is stainless steel, and a circular cross section is assumed all around the Main Ring. The impedance is larger for the thin-wall model in the low frequency limit, where skin depth is comparable to the thickness of beam pipe.

2.3 Inductive wall impedance It is inevitable to introduce some variations in the cross section of vacuum chambers in order to accommodate some accelerator components and particle detectors. In the low frequency limit, the depth of cross sectional change is

much smaller than the wavelength of induced wake fields. Variations in the cross section of beam pipes present a source of inductive impedance in the low frequency range. For example, the transverse impedance of bellows, as depicted in Fig. 3.11, in the low frequency range is given in cgs units as:[27]

$$Z_{\perp} = -i\frac{dL}{cb^3} \tag{3.35}$$

Following from the conversion 1 Ω= 1/30c = $\frac{1}{9} \times 10^{-11}$ s/cm, Eq.(3.35) can be rewritten in the MKS units as:

$$Z_{\perp}[\Omega / \mathrm{m}] = -i\frac{30d[\mathrm{m}]L[\mathrm{m}]}{b^3[\mathrm{m}]} \tag{3.36}$$

Besides the corrugation of the beam pipe, some opening cuts on the surface of beam pipes are necessary for reasons of vacuum engineering. Circular holes and rectangular slots are common designs for the screens of vacuum pumps. In the low frequency range, they contribute to the inductive impedance only.[28] Therefore, small variations in the beam pipe geometry do not cause significant power dissipation in the low frequency range.

2.4 Space-charge impedance The image charge of a relativistic beam travels along the surface of beam pipe at the same speed. Even if the beam pipe is made of perfectly conducting material, the image charge still interacts with the particle beam through the electromagnetic field between them. This is a local effect to the particle beam. The effect of space-charge interaction in a perfectly conducting beam pipe is represented by the transverse space-charge impedance as:[26]

$$Z_{\perp} = i\frac{\bar{R}Z_0}{\beta^2\gamma^2}\left(\frac{1}{a^2} - \frac{1}{b^2}\right) \tag{3.37}$$

where a is the radius of beam, b is the radius of circular beam pipe and Z_0= 377 Ω is the impedance of free space. In contrast to the impedance of cross-sectional variations of a beam pipe in the low frequency range, the space-charge impedance is capacitive.

2.5 Broad-band impedance model In the frequency range above the cutoff of waveguide modes in the beam pipe, beam pipe corrugations could appear as resonator structures to the beam. Since their size are usually smaller than the pipe radius b, the resonant frequencies of those structures are generally well above the cutoff frequency of beam pipe. Those induced wake fields of resonator structures can propagate along the beam pipe and accumulate with each other. So one will expect the impedance to form a continuum in this frequency range.

To describe the general property of this cumulative effect due to all these resonator structures in the high frequency range, a low-Q resonant circuit model was proposed to represent this effect.[29] It is an empirical model but proved to be a good approximation.

According to the broad-band impedance model, the whole accelerator impedance can be approximated by a Q= 1 resonator impedance. From Eq.(3.32), one readily realizes that the normalized longitudinal impedance $\frac{Z_{\parallel}}{n}$ has the same property as the transverse impedance. The broad-band impedance is calculated by setting Q= 1 in Eq.(3.21) and the result is depicted in Fig. 3.12. In the low frequency limit (f << cutoff frequency) the transverse impedance is mostly inductive. This inductive impedance is contributed by the variations in the cross section of beam pipe. In order to reduce the inductive impedance in the low frequency range, one needs to make the beam pipe

surface as smooth as possible. In the high frequency limit ($f >>$ cutoff frequency) the transverse impedance is mostly capacitive.

2.6 Total accelerator impedance The broad-band impedance model needs some modification in order to account for the long-range wake force in the low frequency limit ($f <<$ cutoff frequency) and the high frequency limit ($f >>$ cutoff frequency). Some vacuum components also need to be treated separately, e.g. the rf cavity and ferrite kicker. The impedances of those components can then be added to the broad-band model.

In the frequency range close to dc ($f \leq 1$ MHz), the resistive wall impedance has significant contribution to the resistive part. For rf cavities used for particle acceleration, they contribute to the sharp resonant impedances at discrete frequencies with high quality factor.

In the frequency range below the cutoff of propagating waveguide modes in the beam pipe, some trapped modes with frequencies slightly below the cutoff frequency of beam pipe could develop in the vicinity of small beam pipe enlargements.[30] These trapped modes could survive for many revolution periods. They could contribute to the sharp resonant impedances at discrete frequencies slightly below the cutoff frequency of beam pipe. At present, there is no reported observation on the trapped modes below cutoff frequency. But the theory has been compared with numerical codes and is in good agreement.[31]

When the frequency of induced wake fields in a resonator structure is above the cutoff frequency, the wake field leaks out of the structure and propagates in the beam pipe. But trapped modes with frequency up to three times the cutoff frequency has been reported in experiments.[32] At present, the explanation of the origin of trapped modes

above cutoff has not yet been settled. A possible mechanism is that the mixture of degenerate cavity modes could generate a trapped mode.[33] The trapped modes above cutoff frequency could contribute to sharp resonant impedances with high quality factor.

Adding all those modifications to the broad-band model, one can get a qualitative description for the total accelerator impedance. A conceptual sketch is depicted in Fig. 3.13. In the low frequency range, the impedance is mostly contributed by the resistive wall which decreases rapidly as the frequency increases. In the intermediate frequency range, some narrow resonance impedances due to the high order modes of rf cavities could exist. As the frequency approaches the cutoff frequency, some trapped modes below cutoff could show up in the form of narrow resonance impedances, which are caused by small enlargements on the surface of the beam pipe. In the region beyond the cutoff frequency of beam pipe, one may still encounter some narrow resonance impedances at discrete frequencies, which are believed to be caused by the mixture of degenerate cavity modes.

B. The physics of collective beam instabilities

1. The response of a driven harmonic oscillator

1.1 The self-coupling force and impedance From the definition of transverse impedance given by Eq.(3.14), one can rewrite the transverse wake force generated by a charge distribution in Eq.(3.12) as the following:

$$\frac{1}{q}\int_{-\infty}^{t}\vec{F}_{\perp}(s,t')\cdot c\,dt' = i\langle\vec{r}\rangle I_b(s,t)Z_{\perp}(\omega) \tag{3.38}$$

where q is the charge of the witness particle. One can get the average wake force $\langle\vec{F}_{\perp}\rangle$ with the following form:

$$\begin{aligned}\left\langle\vec{F}_{\perp}(s,t)\right\rangle &= iq\langle\vec{r}\rangle I_b(s,t)\frac{Z_{\perp}(\omega)}{2\pi\bar{R}}\\ &= iq\langle d(t)\rangle\frac{Z_{\perp}(\omega)}{2\pi\bar{R}}\end{aligned} \tag{3.39}$$

where $\langle d(t)\rangle$ is the average transverse dipole current derived from Eq.(2.6), $\bar{R}$ is the mean radius of accelerator, and a single mode excitation is assumed.

A more general expression can be given by using the Fourier representation of the transverse current:

$$\langle d(s,t)\rangle = \int_{-\infty}^{\infty} e^{-i\omega t}\left\langle\tilde{d}(s,\omega)\right\rangle d\omega \tag{3.40}$$

Then the average wake force becomes:

$$\left\langle \bar{F}_{\perp}(s,t) \right\rangle = \frac{iq}{2\pi\bar{R}} \int_{-\infty}^{\infty} e^{-i\omega t} \left\langle \tilde{d}(s,\omega) \right\rangle Z_{\perp}(\omega) d\omega \tag{3.41}$$

For a witness particle undergoing synchrotron oscillations inside a beam bunch, the longitudinal coordinate of the witness particle satisfies the following relation:

$$s = \bar{R}\omega_0 \left(t - \tau(t) \right) \tag{3.42}$$

where $\tau(t)$ is the deviation of longitudinal position of the witness particle with respect to the synchronous particle in the bunch, and the time reference t= 0 is defined when the synchronous particle passes the s= 0 reference location. The synchrotron oscillation of the witness particle $\tau(t)$ is described by Eq.(2.7).

1.2 Single particle model Suppose there is only one frequency component in the induced wake force and no damping force exists in the accelerator. A single particle model can be used to study the general property of the self-coupling effect. From Eq.(3.39) the equation of motion is given by:

$$\ddot{y}(t) + \Omega^2 y(t) = \frac{iq}{\gamma m_0 2\pi\bar{R}} \tilde{I}_b Z_{\perp}(\Omega) y(t) \tag{3.43}$$

where m_0= rest mass of witness particle, and γ= Lorentz relativistic factor.

The solution can be written in the harmonic representation: $y(t) = \tilde{y} e^{-i\Omega_c t}$. Substituting the harmonic representation into Eq.(3.43), one can get the solution for the equation of motion, which is given by the following relationships:

$$y(t) = \tilde{y}\, e^{-Re(Z_{eff})t}\, e^{-i\Omega_c t} \tag{3.44}$$

$$Z_{eff} = \frac{q\tilde{I}_b Z_\perp(\Omega)}{2\Omega_c \gamma m_0 2\pi\bar{R}} \tag{3.45}$$

$$\Omega_c \approx \left[\Omega^2 + Im\left(\frac{q\tilde{I}_b Z_\perp(\Omega)}{2\Omega\gamma m_0 2\pi\bar{R}}\right)\right]^{1/2} \tag{3.46}$$

From the above results, one finds that the growth rate of oscillation is given by the real part of the product of the beam power spectrum and the impedance. The coherent frequency shift is given by the imaginary part of the product of the beam power spectrum and the impedance. In reality the wake force has rich frequency content, the product of the power spectrum and the impedance is replaced by the convolution product of the beam power spectrum and the impedance.

The stability criteria can be derived from results in Eqs.(3.45) and (3.46) given a simplified model. When the real part of the convolution product of the beam power spectrum and the impedance is negative, the motion is unstable. When the real part of the convolution product is positive, the motion is stable. From Eq.(3.46) one finds that the coherent frequency will be shifted downward (smaller than the unperturbed frequency), if the imaginary part of the convolution product is negative, i.e. the resulting reactance is inductive. If the resulting reactance is capacitive, i.e. the imaginary part of the convolution product is positive, the coherent frequency will be shifted upward (larger than the unperturbed frequency). The same conclusions for the stability criteria can be derived from a more rigorous treatment by using the Vlasov equation.

2. Single bunch instability

2.1 Basic concepts When a harmonic oscillator is driven by an external force, a resonance occurs when the driven frequency is equal to the natural frequency of oscillator. The drive force and the displacement of the oscillator are 90° out of phase on resonance. Each constituent particle of a proton bunch can be represented by a harmonic oscillator. When the wake force is 90° out of phase with the transverse displacement of the particle, the particle motion will be driven on resonance and the motion becomes unbounded.

When the coherent beam instability occurs, each constituent particle in a beam bunch conspires together to oscillate in a coherent way. This particle coherence also gives rise to some harmonic structures in the particle distribution in transverse phase space. A single bunch instability will give rise to some standing wave patterns in the observed beam signal. When the particle coherence exists, every particle has the same betatron amplitude for a given synchrotron amplitude. The signal from all particles on the same trajectory will add up coherently.

For simplicity, one first considers an uniform bunch which has a constant betatron amplitude for all synchrotron amplitudes. When all particles have the same initial betatron phases around the trajectory in the longitudinal phase space, they will be deflected by the wake force in the same direction and result in a rigid bunch displacement. This is the case for the m= 0 mode head-tail oscillation.

The m= 0 mode has nonzero center of mass motion and the frequency of bunch oscillation equals to the betatron frequency f_β. An overlay plot for five consecutive turns of the observed bunch motion is depicted in Fig.3.14 for the m= 0 mode head-tail oscillation of an uniform bunch with zero chromaticity.

When the betatron phase of each particle along the synchrotron amplitude is arranged in such a way that the head and the tail of the bunch are 180° out of phase, then the head of the bunch will be deflected by the wake force in the opposite direction as the tail of the bunch. This kind of structure for particle distribution gives rise to the m= 1 mode head-tail oscillation. An overlay plot for five consecutive turns is depicted in Fig. 3.15 for the m= 1 mode head-tail oscillation of an uniform bunch with zero chromaticity. There is a node in the middle of beam signal. This is the characteristics of the m= 1 mode head-tail motion. There is no center of mass motion for the m= 1 mode head-tail motion.

The time evolution of the betatron phase of four equally spaced particles along a given synchrotron amplitude is depicted in Fig. 3.16 for the m= 1 mode head-tail oscillation of an uniform bunch. In Fig. 3.16 when t= 0, particle *A* and *C* correspond to the head and the tail of the bunch respectively, and particle *B* and *D* correspond to the center of the bunch. During one cycle of synchrotron oscillation, each particles gradually trades its place with others. After one complete synchrotron period T_s, all particles resume to their original positions at t= 0. The projection of transverse displacement along the longitudinal axis for the m= 1 mode head-tail oscillation is depicted in Fig. 3.17.

For the m= 1 mode head-tail oscillation as depicted in Figs. 3.16 and 3.17, the bunch has made one complete betatron oscillation after one synchrotron oscillation period, which is one more cycle than it would in the absence of synchrotron motion . Hence the frequency of the m= 1 mode head-tail oscillation is $f_\beta + f_s$. In general, the coherent signal of mode m head-tail motion oscillates at $f_\beta \pm m f_s$[34] where m is an integer, and the signal has m nodes along the temporal profile of the beam signal. The corresponding frequency spectrum for mode m head-tail oscillation has a maximum near $\omega_m = \pi(m+1)/\tau_L$ for $m \neq 0$,[34] where $\omega_m = 2\pi f_m$, and τ_L= full bunch length in time units.

When the chromaticity is not zero, the instantaneous betatron phase is given by Eq.(2.7). The phase difference between the head and the tail is given by $\omega_\xi \tau_L + (\psi_2 - \psi_1)$, where τ_L= the full bunch length, and ψ_1, ψ_2= the initial betatron phase of the head and the tail respectively. Because of the addition of chromatic phase shift $\omega_\xi \tau_L$ to the tail of the bunch, the signal of head-tail oscillation will have different appearance. Using a bunch length of 5 nsec and the chromatic frequency given in Table 1.4, the overlay plots for the m= 0 and the m= 1 mode head-tail oscillation are depicted in Figs. 3.18 and 3.19.

When the chromaticity is large, the m= 1 mode head-tail oscillation begins to develop non-negligible center of mass motion which can be detected by a transverse feedback system. For the m= 0 mode, the motion gets distorted and no longer results in a rigid bunch displacement. The bunch begins to develop some wiggling motion due to the chromatic phase shift. As it has been discussed in Chap.2, the transverse beam spectrum of all modes will be shifted by the chromatic frequency f_ξ. Various modes of head-tail motion derived from a more realistic particle distribution are depicted in Fig. 3.20.[35] The line charge density is assumed to be $\sqrt{(\tau_L)^2 - s^2}$, where τ_L= the full bunch length in time units, and s= the longitudinal coordinate in time units. This model of particle distribution is called a water-bag bunch.

2.2 Sacherer's perturbation formalism A rigorous and unified treatment of the bunched beam instability is provided by the theoretical framework devised by Frank Sacherer[35] at CERN. Since a beam bunch usually contains more than 1×10^{10} charged particles, the best approach to study their dynamics in a macroscopic scale is statistical mechanics and electrodynamics. Because the radiation damping effect is negligible for proton beams at 8 GeV, Louville's theorem still holds for the phase space of particle motion. The particle population density in phase space is described by a 6-dimensional

distribution function which is a statistical average of the microscopic distribution of particles. From Louville's theorem, the distribution function $\lambda(\bar{x},\bar{\upsilon},t)$ has to satisfy the equation of continuity with the following form:[35]

$$\partial_t \lambda(\bar{x},\bar{\upsilon},t)+\bar{\upsilon}\cdot\nabla_{\bar{x}}\lambda(\bar{x},\bar{\upsilon},t)+\frac{e}{\gamma m_0}(\bar{E}+\bar{\upsilon}\times\bar{B})\cdot\nabla_{\bar{\upsilon}}\lambda(\bar{x},\bar{\upsilon},t)=0 \qquad (3.47)$$

where e is the charge of a single particle, m_0 is the rest mass of a single particle, $\bar{x}$ is a 3-dimensional displacement vector, and $\bar{\upsilon}$ is the time derivative of the displacement vector. Equation (3.47) is called Vlasov equation or collisionless Boltzmann equation. Because the fluctuations due to particle discreteness have been averaged out in the Vlasov equation, the Lorentz force used in the Vlasov equation is the ensemble average force. For the stored beams in an accelerator, the force term in the Vlasov equation is given by the wake force.

To correlate the macroscopic observables with the distribution function in phase space, the measured transverse signal in a position monitor is given by integrating the single particle signal over the distribution function:

$$\langle d(t)\rangle = P\int d(t)\lambda(A_\beta,\tau_a,\phi_0,\psi_0,t)A_\beta\tau_a dA_\beta d\tau_a d\phi_0 d\psi_0 \qquad (3.48)$$

where d(t) is the transverse signal induced by a single particle, $\lambda(A_\beta, \tau_a, \phi_0, \psi_0, t)$ is the normalized distribution function, A_β= the betatron amplitude, τ_a= the synchrotron amplitude, ϕ_0= the initial synchrotron phase, ψ_0= the initial betatron, and P= the total number of particles. Only one transverse dimension is considered for the purpose of illustration. For the single bunch case, the transverse signal induced by a single particle

is given by Eq.(2.6). If the distribution function is known, the macroscopic observables can be calculated from Eq.(3.48).

When the beam is unperturbed, the distribution function is stationary and it only depends on the betatron amplitude and the synchrotron amplitude in the equilibrium state. For a stationary distribution function $\lambda_0(A_\beta, \tau_a)$, the transverse signal measured by a BPM is zero:

$$\begin{aligned} \langle d(t) \rangle &= P\int d(t)\lambda_0(A_\beta,\tau_a)\,A_\beta\tau_a dA_\beta d\tau_a d\phi_0 d\psi_0 \\ &= 0 \end{aligned} \tag{3.49}$$

When the beam is perturbed and the induced wake force is small compared to the external focusing force, the particle orbit is still periodic in phase space. Thus the perturbed distribution function can be expressed by the following form:

$$\lambda(A_\beta,\tau_a,\phi_0,\psi_0,t) = \lambda_0(A_\beta,\tau_a) + \Delta\lambda(A_\beta,\tau_a,\phi_0,\psi_0,t) \tag{3.50}$$

$$\Delta\lambda(A_\beta,\tau_a,\phi_0,\psi_0,t) = \sum_{m=-\infty}^{\infty} h_m(A_\beta,\tau_a)e^{i(m\phi_0+\psi_0)}e^{-i\Omega t} \tag{3.51}$$

where $\Delta\lambda(A_\beta, \tau_a, \phi_0, \psi_0, t)$ is the perturbation added to the stationary distribution function. The transverse signal due to the coherent beam motion is given by the integral of single particle signal over the perturbation of distribution function:

$$\langle d(t) \rangle = P\int d(t)\Delta\lambda(A_\beta,\tau_a,\phi_0,\psi_0,t)\,A_\beta\tau_a dA_\beta d\tau_a d\phi_0 d\psi_0 \tag{3.52}$$

Substituting Eq.(3.50) into the Vlasov equation in Eq.(3.47) and keeping the first order terms of the perturbation only, the linearized Vlasov equation is given by the following:

$$\frac{\partial}{\partial t}\Delta\lambda(A_\beta,\tau_a,\phi_0,\psi_0,t)+\dot{\tau}_a\frac{\partial}{\partial t}\lambda_0(A_\beta,\tau_a)+\dot{A}_\beta\frac{\partial}{\partial A_\beta}\lambda_0(A_\beta,\tau_a)=0 \qquad (3.53)$$

The time derivative of the betatron amplitude is given by the transverse equation of motion:

$$A_\beta=\sqrt{x(t)^2+\dot{x}(t)^2/\dot{\psi}_\beta(t)^2} \qquad (3.54)$$

$$\begin{aligned}\dot{A}_\beta &= \dot{x}(t)\frac{\partial A_\beta}{\partial x(t)}+\ddot{x}(t)\frac{\partial A_\beta}{\partial \dot{x}(t)}\\ &\approx -\frac{\sin\psi_\beta(t)}{\omega_\beta}\frac{e}{\gamma m_0}(\vec{E}+\dot{\vec{x}}\times\vec{B})\end{aligned} \qquad (3.55)$$

where $x(t)$ and $\psi_\beta(t)$ are defined in Eqs.(2.6) and (2.7), and ω_β is defined in Eq.(1.45).

When there is no coherent beam motion in the longitudinal direction, the synchrotron amplitude remains constant. Using the results in Eqs.(3.53) and (3.55), the linearized Vlasov equation becomes:

$$\begin{aligned}&-i\Omega\cdot\Delta\lambda(A_\beta,\tau_a,\phi_0,\psi_0,t)\\ &=\frac{e}{\gamma m_0\omega_\beta}\cdot\frac{e^{i\psi_\beta(t)}-e^{-i\psi_\beta(t)}}{2i}\left(\vec{E}+\dot{\vec{x}}\times\vec{B}\right)\frac{\partial}{\partial A_\beta}\lambda_0(A_\beta,\tau_a)\end{aligned} \qquad (3.56)$$

In principle, the perturbation of the distribution function can excite different modes of azimuthal structure in phase space as indicated in Eq.(3.51). Each mode of excitation

will induce its corresponding wake force which in turn will affect the time evolution of other excitation modes and itself. As long as the wake force is a small perturbation compared with the external focusing force, the coupling between different excitation modes can be neglected. Then, it is a good approximation to treat each excitation mode as an eigenmode. Using those assumptions and the linear transverse wake force in Eq.(3.41), the linearized Vlasov equation is further reduced to the following form for a single mode excitation:[36]

$$-i\Omega h_m(A_\beta,\tau_a) = \frac{e^2 P}{4\gamma m_0 Q_x \bar{R}} \sum_{n=-\infty}^{\infty} i^m \sigma_m(n) Z_\perp\big((n+Q_x)\omega_0\big) \times J_m\Big((n+Q_x)\omega_0\tau_a - \omega_\xi\tau_a\Big)\cdot\frac{\partial}{\partial A_\beta}\lambda_0(A_\beta,\tau_a) \tag{3.57}$$

where Q_x is the betatron tune, J_m is the Bessel function of the m-th order, and $\sigma_m(n)$ is given by the following:

$$\sigma_m(n) = i^{-m}\int_0^\infty h_m(A_\beta,\tau_a) J_m\Big((n+Q_x)\omega_0\tau_a - \omega_\xi\tau_a\Big) A_\beta^2\tau_a \, dA_\beta d\tau_a \tag{3.58}$$

Various techniques have been devised to solve the integral equation given in Eq.(3.57).[36]

The solution for the complex frequency shift Ω for the m-th mode head-tail motion has some general characteristics of the following form:[26]

$$\Omega = AI_b \frac{-i\sum_{n=-\infty}^{\infty} Z_\perp((n+Q_x)\omega_0+k\omega_s+\Omega)\left|\sigma_m\Big((n+Q_x)\omega_0\tau_L-\omega_\xi\tau_L\Big)\right|^2}{\sum_{n=-\infty}^{\infty}\left|\sigma_m\Big((n+Q_x)\omega_0\tau_L-\omega_\xi\tau_L\Big)\right|^2} \tag{3.59}$$

where $\sigma_m(n)$ is the spectral amplitude of the transverse beam spectrum for the m-th synchrotron sideband at the frequency $(n+Q_x)\omega_0 - \omega_\xi$, A is a constant depending on the accelerator design, I_b is the beam current of a beam bunch, and τ_L is the full bunch length in time units. A summation over the harmonic alias is involved in Eq.(3.59). The square of the spectral amplitude gives the power spectrum of the beam. The numerator of Eq.(3.59) means the convolution of the power spectrum and the accelerator impedance. This is similar to the expression for power dissipation in a resistor, I^2Z, where I is the current and Z is the resistance. For the single bunch instability, the coherent frequency is given by:

$$f_c = (n + Q_x) f_0 + m f_s + \Omega \tag{3.60}$$

where n is any integer. In the observed transverse beam spectrum, there will be prominent spectral lines at frequencies given in Eq.(3.60).

Equation (3.59) can be rewritten as a formal expression:

$$\Omega = -iAI_b \sum_{n=-\infty}^{\infty} F_m\left(\chi(n) - \omega_\xi \tau_L\right) Z_\perp\left((n + Q_x)\omega_0 + m\omega_s + \Omega\right) \tag{3.61}$$

and

$$F_m(\chi(n)) = \frac{|\sigma_m(\chi(n))|^2}{\sum_{n=-\infty}^{\infty} |\sigma_m(\chi(n))|^2} \; ; \; \chi(n) = (n + Q_x)\omega_0 \tau_L \tag{3.62}$$

where $\chi(n)$ is in units of [radian]. The expression $F_m(\chi)$ is called bunch form factor of the m-th mode. The bunch form factor is an even function in the frequency domain. As

shown in Eq.(3.61), the bunch form factor $F_m(\chi)$ is being shifted along the abscissa by $\omega_\xi \tau_L$ due to nonzero chromaticity. This is the same property as the transverse beam spectrum discussed in Chap. 2.

Some general conclusions can be drawn from Eqs.(3.61) and (3.62). The real part of Eq.(3.61) gives the coherent frequency shift, i.e. the imaginary part of the convolution product of the power spectrum and the impedance gives the coherent frequency shift. The imaginary part of Eq.(3.61) gives the amplitude growth rate, i.e. the real part of the convolution of the power spectrum and the impedance gives the growth rate of the instability. Those conclusions are the same as the results derived from a single particle model discussed in Sec. B.1.2. The stability criteria can be summarized in a graphical format as depicted in Fig. 3.21.[34]

When the chromatic frequency shift is positive, the form factor $F_m(\chi)$ is being shifted towards the positive frequency direction as depicted in Fig. 3.21*(ii)*. The convolution for the m= 0 mode is positive, which results in a damping effect for the m= 0 mode head-tail motion. But the convolution for some higher order modes could become negative, which will result in an antidamping effect and lead to high order mode head-tail instability.

On the contrary, when the chromatic frequency shift is negative, the form factor is shifted towards the negative frequency direction as depicted in Fig. 3.21*(i)*. The convolution for the m= 0 mode is negative, which results in an antidamping effect and leads to the m= 0 mode head-tail instability. But the convolution for some higher order modes could become positive, which will result in a damping effect for higher order mode head-tail motion.

3. Coupled bunch instability

3.1 Continuous beam instability[34] Suppose there is a continuous beam in a circular accelerator. A perturbation is applied to the beam such that each given slice of beam at the azimuthal location θ is being displaced transversely by $x(0, \theta)$. The transverse perturbation can be decomposed into a Fourier series which is comprised by many oscillation patterns:

$$x(0,\theta) = \sum_{n=-\infty}^{\infty} \hat{x} e^{in\theta} \tag{3.63}$$

where θ is the azimuthal coordinate along the accelerator circumference. The time evolution of each oscillation pattern is described by:

$$x(t,\theta) = x_n e^{-i[(n+Q_\beta)\omega_0 t - n\theta]} \tag{3.64}$$

A snapshot of the coherent beam oscillation for a given pattern is depicted in Fig. 3.22 as an example.

Because an impedance source will sample the beam signal continuously, there will be no aliased spectral lines in the frequency domain. Therefore, the convolution of the power spectrum and the impedance has a nonzero solution only at the frequency $(n+Q_\beta)\omega_0$. There is no summation over the aliased spectral lines for the continuous beam case. For beam instability to occur, the frequency $(n+Q_\beta)\omega_0$ must fall in the negative frequency domain, where the resistive impedance is negative. For an oscillation pattern of harmonic number n which satisfies $n+Q_\beta < 0$, the beam motion is unstable. If the coherent beam oscillation is observed at a fixed location, the beam signal observed by a

BPM is given by $x(t, \theta_0)= x_n \exp[-i(n+Q_\beta)\omega_0 t+in\theta_0]$ which has the same frequency of the signal observed by the impedance in the frequency domain.

3.2 Bunch train with cyclic symmetry Suppose there are M equally spaced, equal intensity bunches in a circular accelerator undergoing coupled bunch oscillation. A BPM at a fixed location samples the oscillation pattern of the bunch train at every discrete time interval T/M, where T is the revolution period of the accelerator. The oscillating bunch train will induce a series of discrete pulses similar to the picture depicted in Fig. 2.7. The information about the coupled bunch oscillation is encoded in the oscillatory waveform of the induced pulse train. Instead of a BPM, an impedance source at the same location will sample the beam signal at every discrete time interval T/M. According to the discussions about the spectrum aliasing in Sec. A.2, Chap.2, the impedance will observe the beam spectrum not only at the fundamental frequency f_N of the bunch train oscillation, but also at all alias frequencies $f_N + kf_B$, where f_B is the bunching frequency M/T and k is any integer. If M equals to the rf harmonic number, then the bunching frequency equals to the rf frequency. Therefore, the convolution product of the power spectrum and the impedance needs to be summed over all alias frequencies at every frequency interval of f_B. For M coupled oscillators, there are M different modes of oscillation pattern. The bunch train oscillation also has M different modes for a total of M bunches in an accelerator.

The growth rate of a coupled bunch instability has the same form as the single bunch case given in Eq.(3.61), except the magnitude is M times larger and the convolution product is summed at every M-th harmonics of revolution frequency instead of every revolution harmonics. An explicit expression of the growth rate for a given coupled bunch mode is given by the following:[26]

$$\Omega = -iMAI_b \sum_{n=-\infty}^{\infty} F_m\left(\chi(Mn+\mu) - \omega_\xi \tau_L\right) Z_\perp\left((Mn+\mu+Q_x)\omega_0 + m\omega_s + \Omega\right) \quad (3.65)$$

and

$$\begin{aligned} &\chi(Mn+\mu) = (Mn+\mu+Q_x)\omega_0\tau_L \\ &\mu = 0, 1, 2, \ldots, M-1 \end{aligned} \quad (3.66)$$

where μ is the coupled bunch mode number. The coherent frequency of the coupled bunch instability is given by:

$$f_c = (Mn+\mu+Q_x)f_0 + mf_s + \Omega \quad (3.67)$$

where n is any integer. In the observed transverse beam spectrum, there will be prominent spectral lines at frequencies given in Eq.(3.67) for a given coupled bunch mode. In contrast to the single bunch instability, the spectral lines only show up at every M-th harmonics of the revolution frequency instead of every revolution harmonics. For a given coupled bunch mode μ, if one rotates by an azimuthal angle of $2\pi\mu/M$, one will still observe the same oscillation pattern in the snapshot. The coupled bunch coherence introduces a coherent phase shift between the adjacent bunches. The transverse motion of adjacent bunches only differs by a phase factor $\exp[-i2\pi\mu/M]$ for a given mode number μ. There is cyclic symmetry in the coupled bunch oscillation of equally spaced, equal intensity bunches. Because of the cyclic symmetry, the signals induced by each bunch add up coherently at frequencies given in Eq.(3.67), and cancel out completely at other frequencies.

The coupled bunch oscillation can be thought of as the extreme case of the continuous beam oscillation, if one just stretches the bunch length to the limit of continuous beam. The main difference is at the alias frequencies due to the discrete nature of the bunched beam. The cross-coupling among bunches is provided by a long range wake force which decays slowly compared with the spacing between adjacent bunches. Because of the coherent phase shift between adjacent bunches and the slow decay of the wake force, it becomes possible to have the necessary 90° phase difference between the wake force and the bunch displacement for a driven resonance.[34] When the wake force decays in much less than the bunch spacing interval, it will only affect the single bunch motion. Then there will be no coupled bunch coherence in the bunch train.

4. Landau damping

Because synchrotron radiation damping is negligible for proton beams at 8 GeV, each proton bunch can be represented by a collection of lossless identical oscillators. When an external driving force is applied to an ensemble of identical oscillators with a spread in their natural oscillation frequencies, the damping of center of mass motion may occur if the oscillators are coupled and the excitation frequency overlaps with the frequency spread of oscillators.

Figure 3.23 qualitatively depicts a particle distribution $\rho(\omega)$ as a function of the betatron frequency ω for a proton bunch. When the coherent frequency of the wake force ω_c falls in the betatron frequency spread, those particles whose natural frequencies are close to the coherent frequency ω_c will be driven near the resonance.

In the linear approximation, the amplitude of near-resonance particles grow as a linear function of time, and the number of near-resonance particles decreases as a linear function of time.[34] Therefore, the ensemble average of betatron amplitude does not grow,

even though there is steady energy absorption by those near-resonance particles. Because the increase of energy is proportional to the square of time for near-resonance particles, the net increase of energy for all near-resonance particles is proportional to time. As long as those near-resonance particles can absorb energy faster than the wake force can provide, the coherent beam motion is damped. This stabilizing mechanism is called Landau damping.[37]

There is another mechanism which can also damp the center of mass motion called decoherence (also called filamentation or phase-mixing). Although decoherence can damp the center of mass motion, it is a totally different physical mechanism from Landau damping. When there is frequency spread among an ensemble of oscillators caused by the amplitude dependence, the particle distribution in phase space will smear out as the time evolves. Although the particle energy remains constant, the ensemble average of particle displacement decreases as the time evolves. The following example illustrates the damping effect due to the decoherence. Suppose the amplitude dependence of frequency is given by the following relation:

$$f(\mathrm{A}) = f_0(1 - \alpha \mathrm{A}^2) \tag{3.68}$$

where A is the oscillation amplitude, α is the decoherence coefficient, and f_0 is the natural frequency of linear oscillation. If one assumes f_0 to be unity, the displacement of each particle is described by:

$$\mathrm{x(n)} = \mathrm{A}\cos\left(2\pi \mathrm{n}(1 - \alpha \mathrm{A}^2)\right) + \mathrm{x(0)} \tag{3.69}$$

where x(0) is the initial position, and n is the number of turns. For a collection of 342 particles randomly populated in a sector area in the phase space, the time evolution of particle distribution in the phase space is depicted in Fig. 3.24, and the ensemble average of particle displacement is depicted in Fig. 3.25.

As depicted in Fig. 3.25, the particle oscillation is damped from a macroscopic point of view. The decoherence damping is due to the phase slip between particles. The dependence of frequency on the oscillation amplitude is a nonlinear effect. For bunched beams, the amplitude dependence is mainly caused by the octupole magnetic fields due to the imperfection of the magnetic fields in magnets.[34]

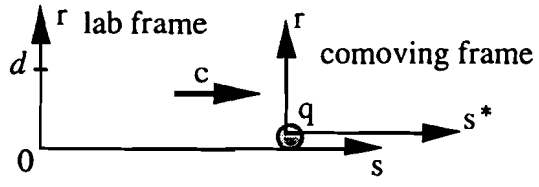

Fig. 3.1. The coordinate systems for a charged particle travels with the speed of light in the free space.

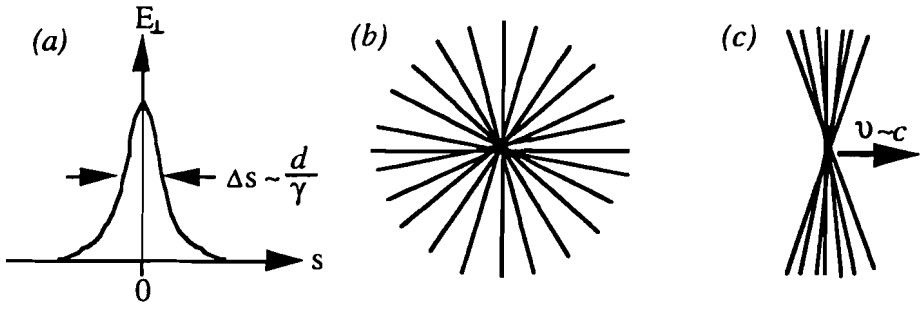

Fig. 3.2. The spatial snapshot of electrical field for a moving charged particle in the vacuum *(a)* the transverse electrical field of a relativistic particle observed in the lab frame *(b)* the field lines in the comoving frame *(c)* the field lines in the lab frame.

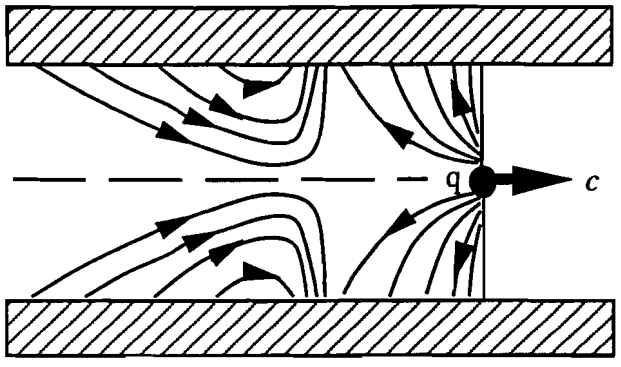

Fig. 3.3. The electrical field lines generated by a relativistic charged particle inside a resistive beam pipe.

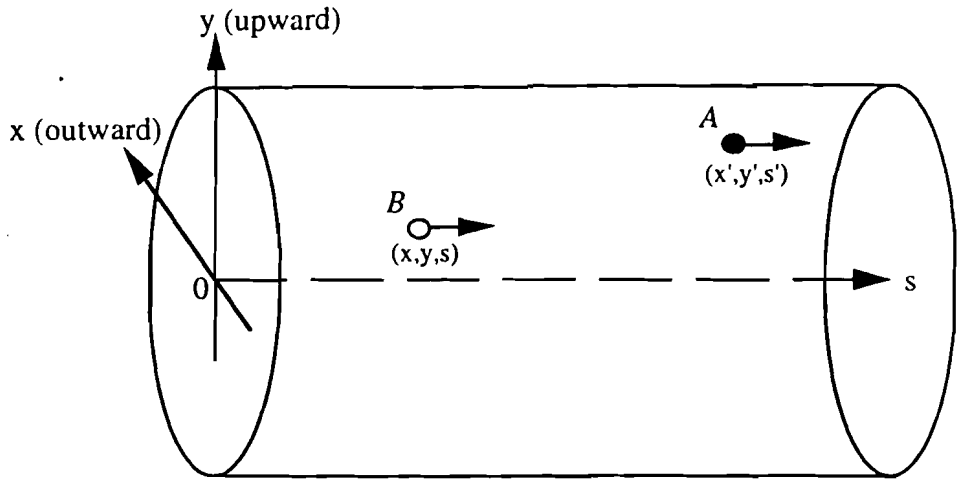

Fig. 3.4. Two charged particles travel along the longitudinal direction in the beam pipe. The longitudinal separation between them is defined as $z = s - s'$.

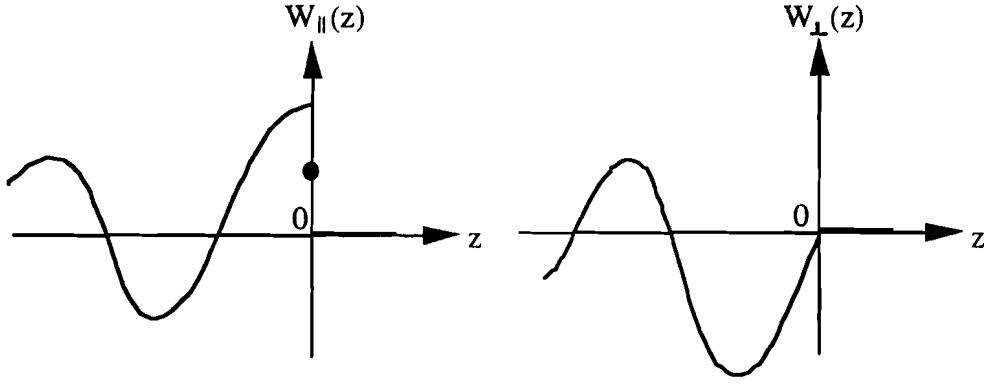

Fig. 3.5. Schematic sketches of the longitudinal and transverse wake functions. Both wake functions vanish for $z > 0$ as a result of causality. The longitudinal wake seen by the charge itself is half of $W_{\parallel}$ at $z = 0$ as indicated by the solid dot, according to the fundamental theorem of beam loading.

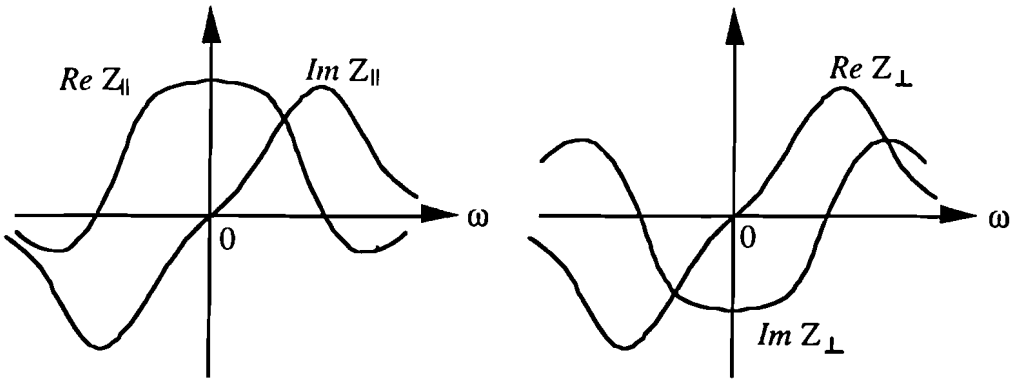

Fig. 3.6. Qualitative illustrations for the longitudinal and transverse impedance in the frequency domain.

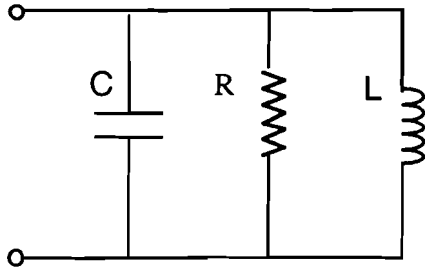

Fig. 3.7. The resonant circuit model is used to represent the longitudinal impedance of resonator structures.

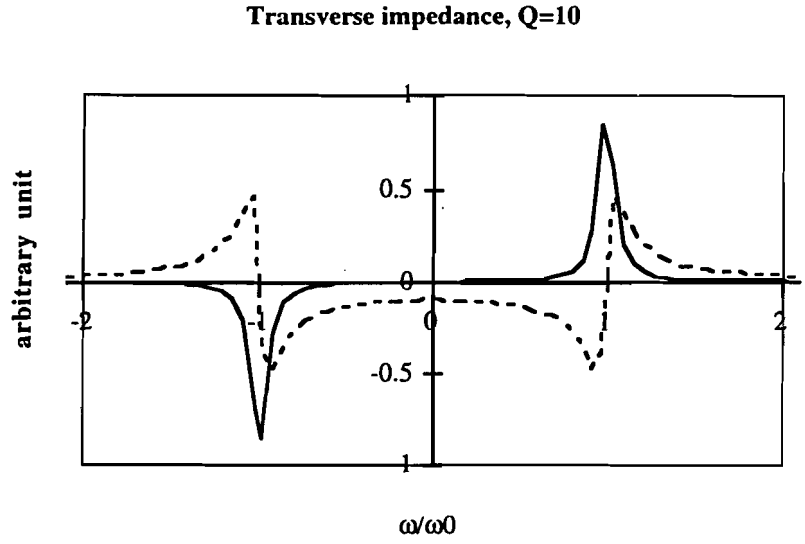

Fig. 3.8. The transverse resonator impedance vs. frequency. The solid line is the real part, and the dashed line is the imaginary part of impedance.

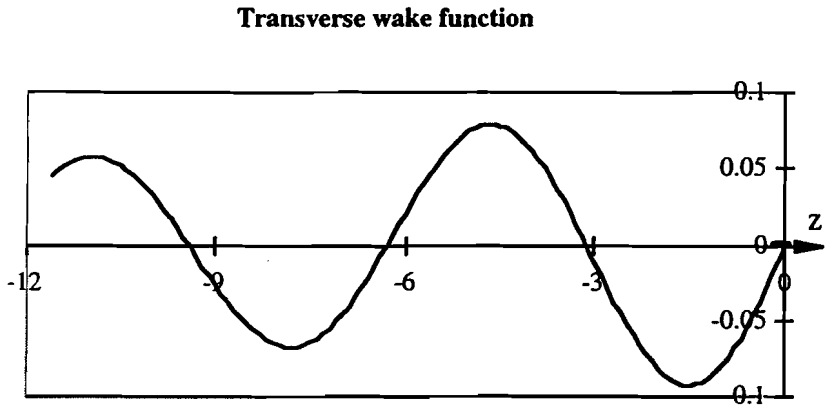

Fig. 3.9. The transverse wake function generated by a point charge passing by a resonator structure.

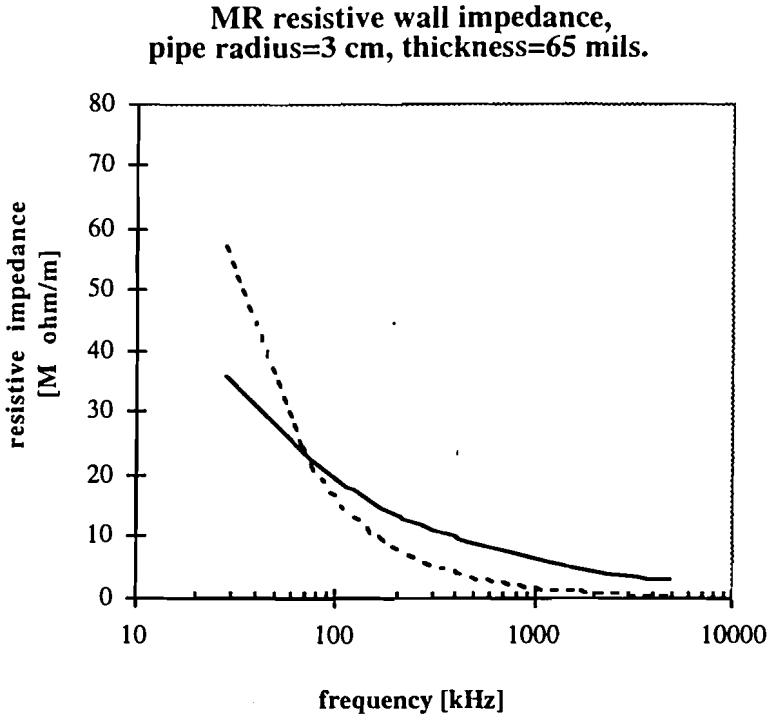

Fig. 3.10. Calculated resistive wall impedance for the Main Ring beam pipe. The solid line is the result of thick-wall model, and the dashed line is the result of thin-wall model.

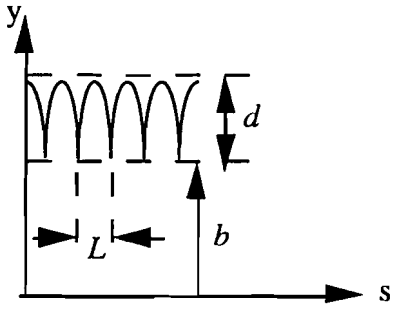

Fig. 3.11. Schematic layout of the bellows.

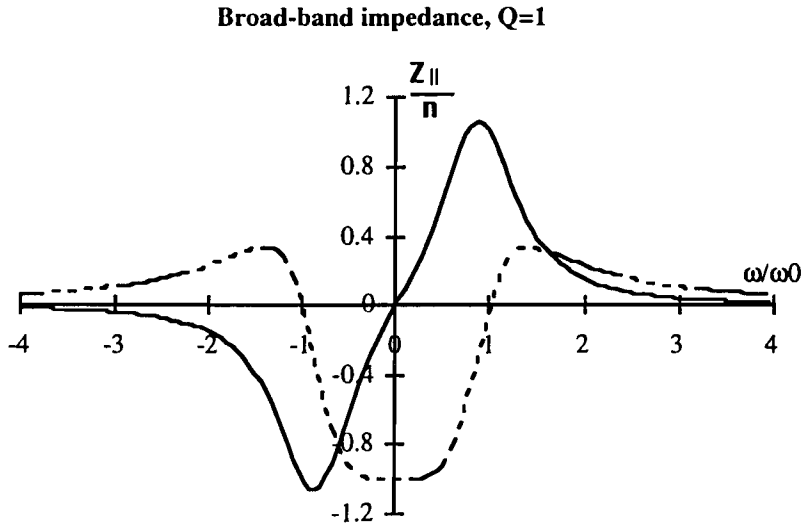

Fig. 3.12. The frequency response of the broad-band impedance model. The frequency is normalized by the cutoff frequency of the beam pipe. The solid line represents the real part of the impedance, and the dashed line represents the imaginary part.

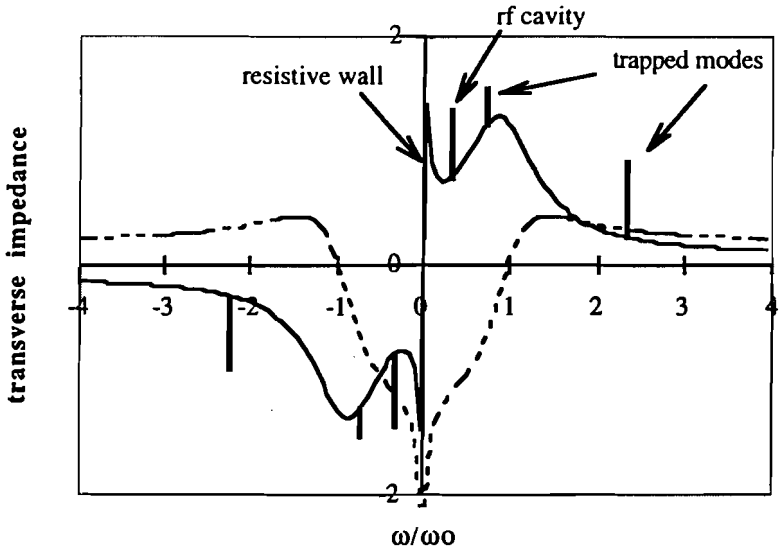

Fig. 3.13. A conceptual illustration of total accelerator impedance in the frequency domain. The solid line represents the resistive impedance and the dashed line represents the reactive impedance. The frequency is normalized by the cutoff frequency of beam pipe.

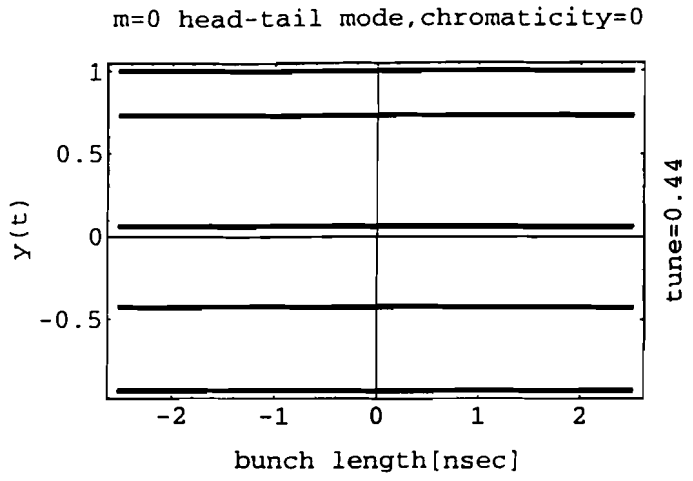

Fig. 3.14. An overlay plot of the m= 0 mode head-tail oscillation for five consecutive turns. An uniform bunch is assumed for chromaticity= 0.

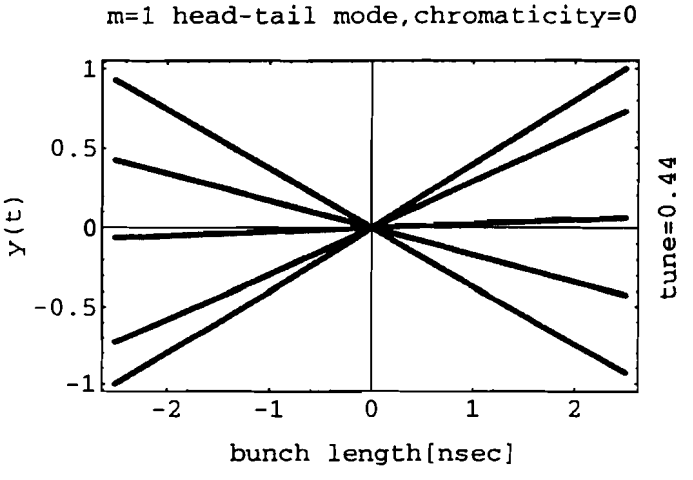

Fig. 3.15. An overlay plot of the m= 1 mode head-tail oscillation for five consecutive turns. An uniform bunch is assumed for chromaticity= 0.

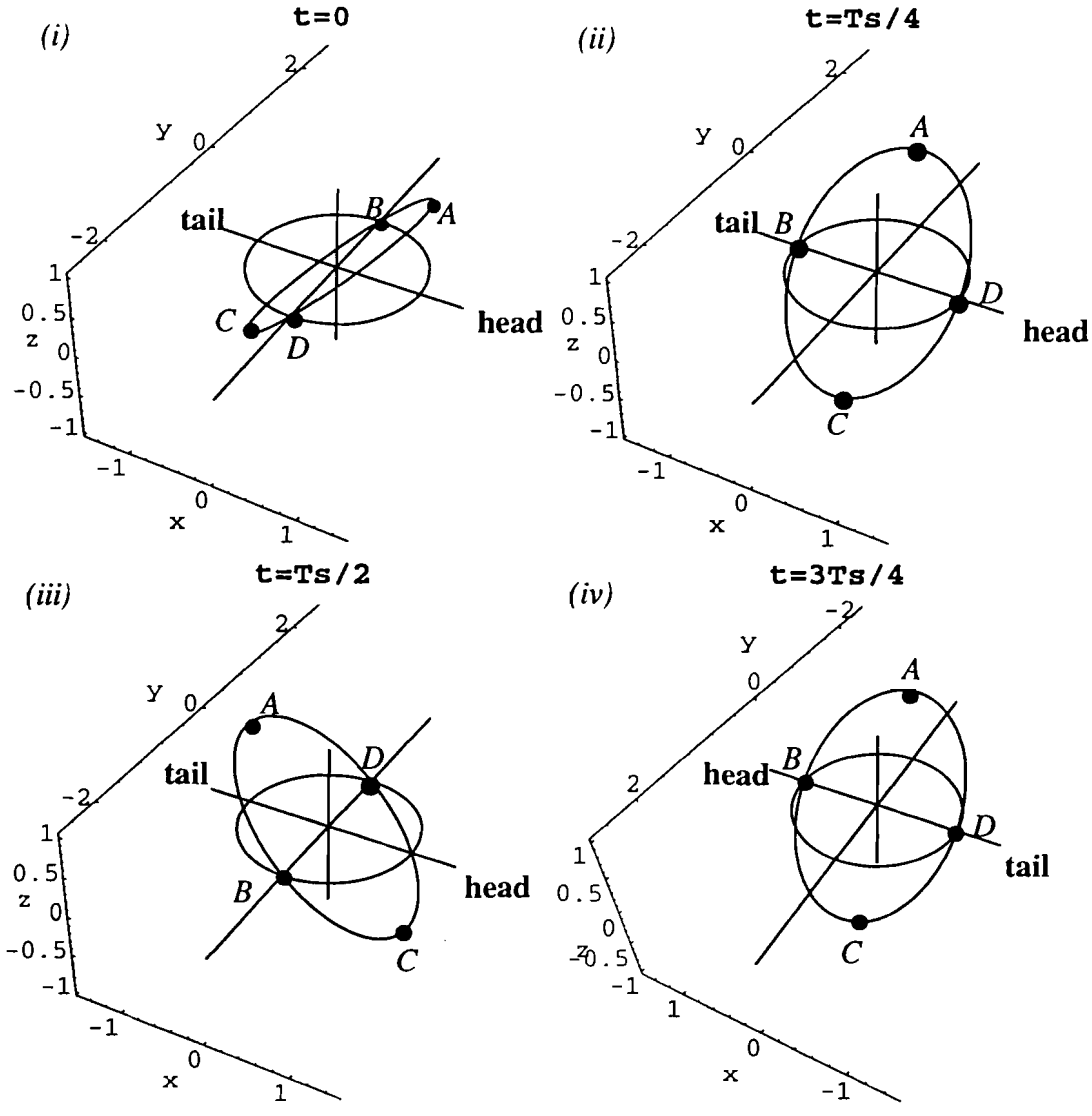

Fig. 3.16. The time evolution of betatron phase along a given synchrotron amplitude for the m= 1 mode head-tail motion. The x-y plane represents the longitudinal phase space, where x and y axes denote the bunch length $\tau(t)$ and the energy deviation $\dot{\tau}(t)/\omega_s$ respectively, and the z axis denotes the betatron phase in units of π. The time interval between adjacent pictures is a quarter of the synchrotron oscillation period. Note that picture *(iv)* is viewed from the opposite direction of y axis.

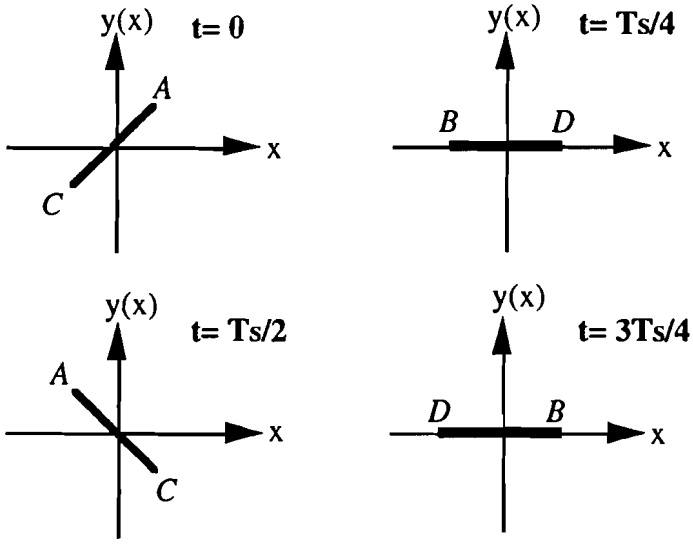

Fig. 3.17. The time evolution of transverse displacement projected on the longitudinal axis for the m= 1 head-tail oscillation, where x denotes the longitudinal coordinate and y(x) denotes transverse displacement. The time interval between adjacent pictures is a quarter of the synchrotron oscillation period. An uniform bunch is assumed, and the chromaticity is zero.

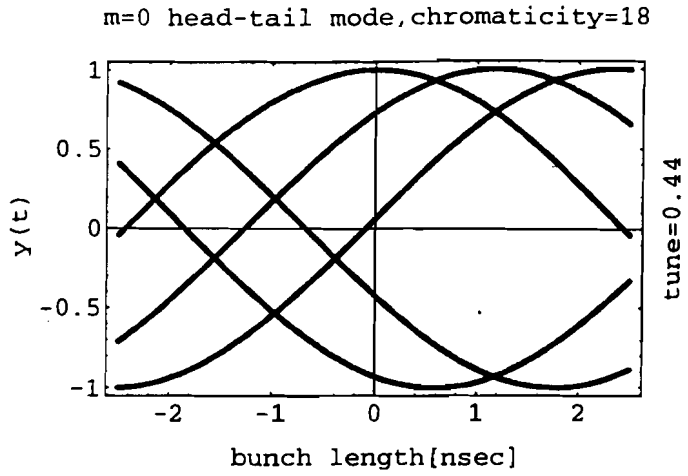

Fig. 3.18. An overlay plot of the m= 0 mode head-tail oscillation for five consecutive turns. An uniform bunch is assumed. The chromatic phase shift between the head and the tail is π.

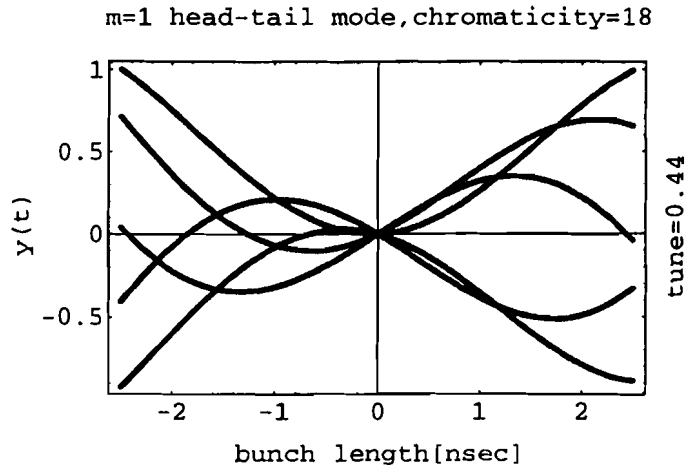

Fig. 3.19. An overlay plot of the m= 1 mode head-tail oscillation for five consecutive turns. An uniform bunch is assumed. The chromatic phase shift between the head and the tail is π.

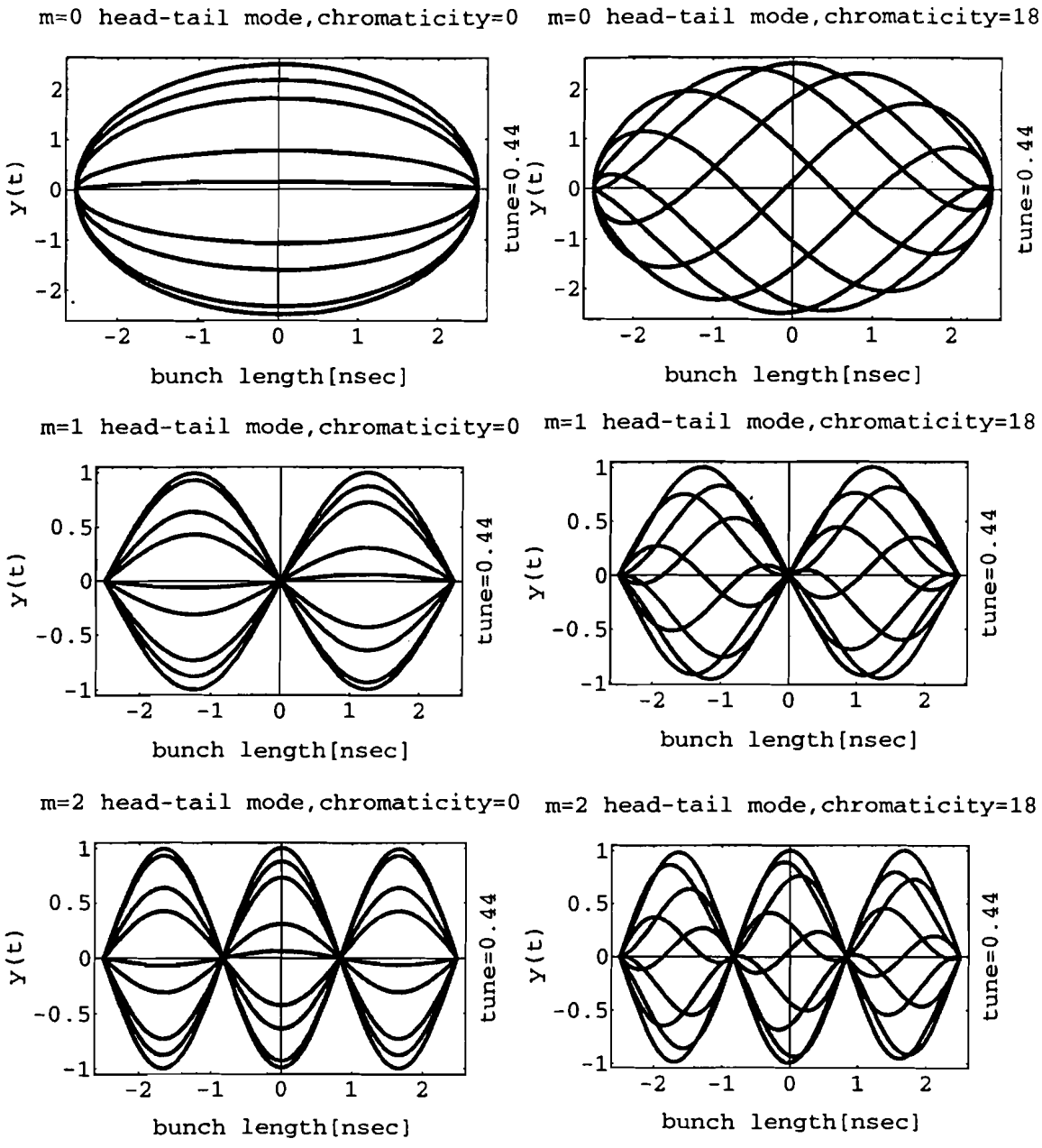

Fig. 3.20. Overlay plots of transverse head-tail motion for nine consecutive turns. A water-bag bunch is assumed. The left column depicts the head-tail motion of zero chromaticity for a bunch length of 5 nsec. The right column depicts the head-tail motion for a chromatic phase shift of π between the head and the tail of a beam bunch.

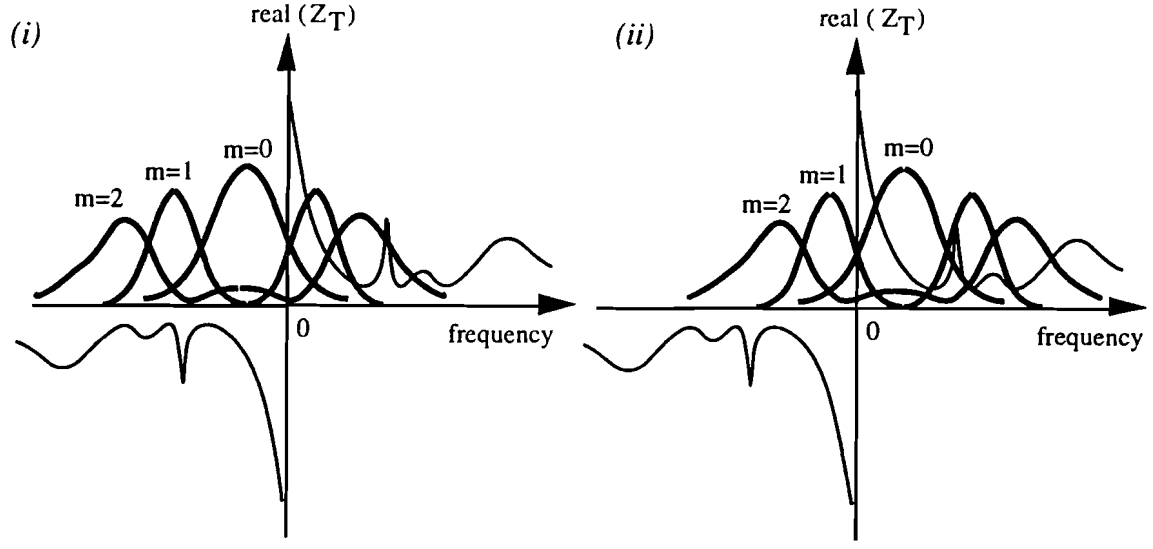

Fig. 3.21. The convolution of the power spectrum and the accelerator impedance in the frequency domain *(i)* the bunch form factor $F_m(\chi)$ is shifted towards the negative frequency direction when the chromatic frequency $f\xi$ is negative *(ii)* the bunch form factor $F_m(\chi)$ is shifted towards the positive frequency direction when the chromatic frequency $f\xi$ is positive.

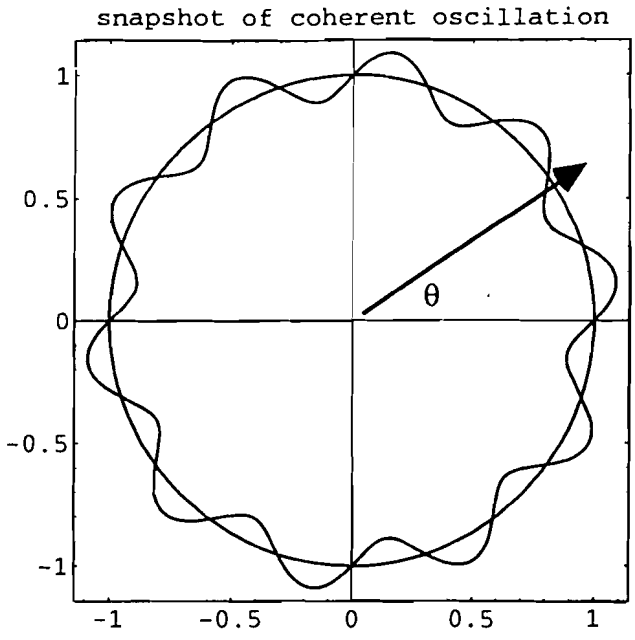

Fig. 3.22. A snapshot of a coherent beam oscillation for a continuous beam.

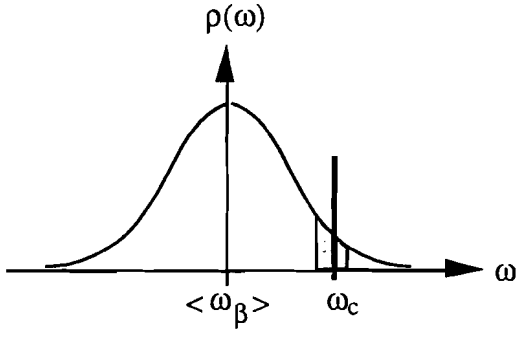

Fig. 3.23. The betatron frequency spread for a proton bunch, where $<\omega_\beta>$ is the mean betatron frequency and ω_c is the frequency of external driving force. The shaded area represents the near-resonance particles.

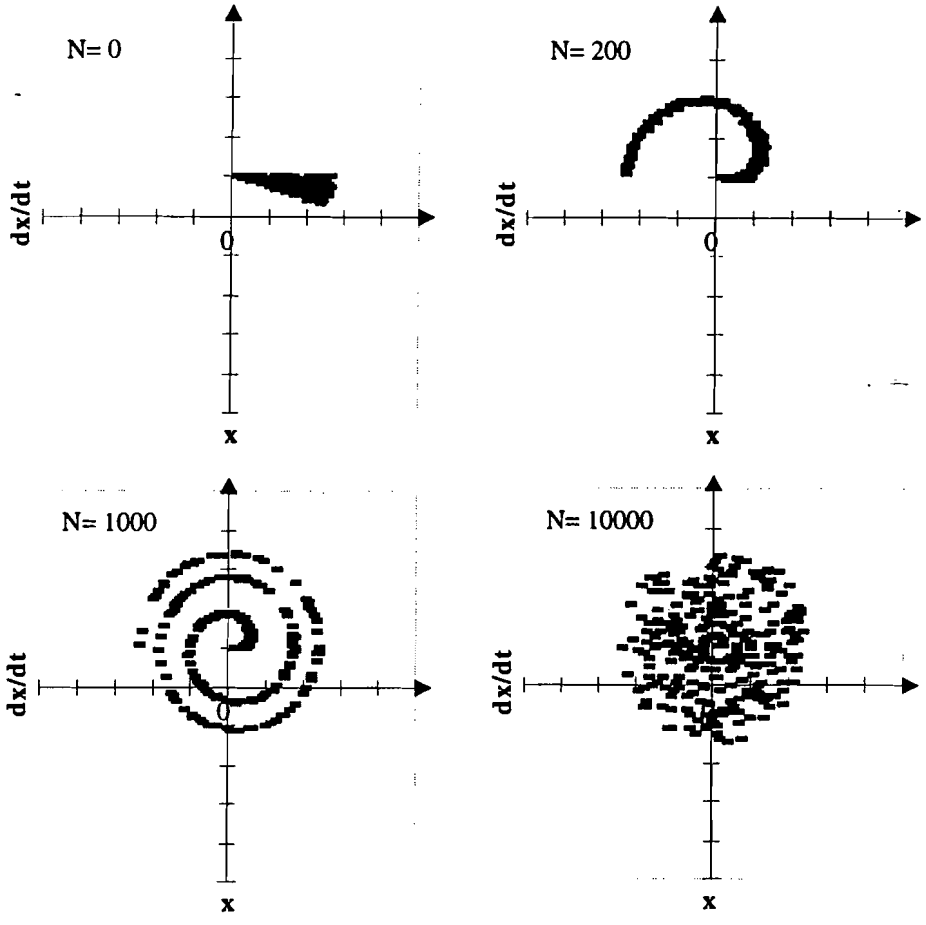

Fig. 3.24. The time evolution of particle distribution in the phase space where the oscillation frequency is dependent on the amplitude. The decoherence coefficient α is set to 0.01.

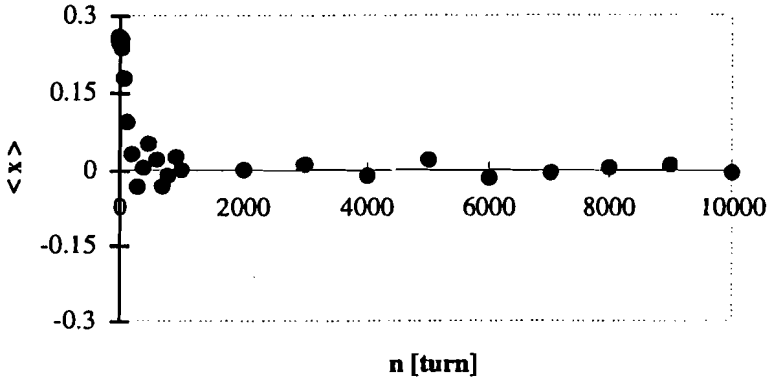

Fig. 3.25. The time evolution of the ensemble average of particle displacements.

CHAPTER 4

RESULTS AND ANALYSIS OF BEAM MEASUREMENTS

A. Operation of Main Ring during Run Ib

One first needs to know some jargon used in the operation of the Main Ring. The harmonic number of the Main Ring is 1113, as listed in Table 1.4. This means that there are 1113 rf buckets equally spaced along the circumference of the Main Ring. The complete injection of the Main Ring is achieved by 13 consecutive deliveries of proton beam from the Booster synchrotron. Each delivery from the Booster synchrotron is called one booster batch. Each booster batch can contain up to 84 bunches. Because the repetition rate of the Linac is 15 Hz, the Booster synchrotron can only send out one batch of proton beams every 67 msec. For antiproton production during the collider run, only one booster batch of 84 proton bunches is injected into the Main Ring. The protons are then accelerated to 120 GeV and directed to the target area. This is called the antiproton stacking cycle. In the fixed target run, 12 consecutive booster batches are injected into the Main Ring instead of 13. The empty gap is reserved for the risetime of the radiation safety abort kicker.

Figure 4.1 depicts a typical setting of chromaticity values at different beam energies during the pbar stacking cycle. From the viewpoint of collective beam instability, this should not be a favorite choice. According to the present theory, a positive chromaticity

will make beam unstable at energies below transition, but stable at energies above transition. In Fig. 4.1 the vertical chromaticity is certainly set with the wrong sign at beam energies below transition. Nevertheless, this is the optimum setting found by operators in the main control room.

To make sure the chromaticity values actually carry the sign as depicted in Fig. 4.1, a careful calibration was performed at the injection kinetic energy of 8 GeV (momentum= 8.889 GeV/c). A small change of beam momentum is made by tuning a parameter of the rf system (M3ROF) which changes the rf frequency, then the betatron tune is measured by using the Main Ring Schottky detector discussed in Chap. 2. Knowing the fractional change of beam momentum, the actual machine chromaticity can be derived by using Eq.(1.42) and the following relations:

$$\begin{aligned} df_{rf} &= h \cdot df_0 \\ \frac{df_0}{f_0} &= -\eta \frac{dp}{p} \\ df_{rf} &= -h\eta f_0 \frac{dp}{p} \end{aligned} \tag{4.1}$$

The calibration result of fractional change in beam momentum vs. rf parameter M3ROF is depicted in Fig. 4.2. The proportionality constant is derived by performing a linear fit to the measured data.

The results of actual chromaticity vs. the nominal value are depicted in Figs. 4.3 and 4.4 for the vertical and horizontal planes respectively. The measured vertical chromaticity does not show as good linearity as the horizontal. In order to get an estimate on the real zero of vertical chromaticity, data points corresponding to the nominal chromaticity of 2 and 5 are discarded. Then a linear fit is applied to the rest of data points. The fit results are summarized below:

(i) vertical chromaticity— *actual value= nominal value - 3.6* $\pm$ 0.5

(ii) horizontal chromaticity— *actual value= nominal value* + *2.7* $\pm$ 0.2

Similar measurements at different beam energies are repeated without error estimates. The results show that all settings in the chromaticity table as depicted in Fig. 4.1 carry the correct sign.

Figure 4.5 depicts a fast time plot of Main Ring parameters at the injection stage in a typical pbar stacking cycle. In Fig. 4.5, the parameter m:ibeamm represents the total number of protons, m:blmon represents the full bunch length (95 % of temporal profile) in units of [nsec], and m:ering represents the total energy of beam in units of [GeV]. As shown in Fig. 4.5, there is about 5 % beam loss at the injection energy. All dampers are turned on, and all parameters are optimized for the best beam lifetime and maximum stored beam intensity.

A plot of beam intensity vs. time at the injection energy is depicted in Fig. 4.6, where all transverse dampers are turned off and the horizontal chromaticity is set to -25. According to the present theory of bunched beam instability, a negative vertical chromaticity will stabilize the beam and a positive one will destabilize it. When all the transverse dampers are turned off, the beam does behave as the present theory has predicted.

When all the transverse dampers are turned back on and other parameters all keep the same, the beam lifetime is better for the case where the vertical chromaticity is set to a positive value given by the chromaticity table in Fig. 4.1. Figure 4.7 depicts the corresponding time plot of beam intensity. When all the dampers are turned on, a vertical

chromaticity value of 10 gives a better beam lifetime below transition, which seems to contradict to the presented theory of bunched beam instability.

B. Observation of transverse instabilities

1. Performance of existing transverse dampers

1.1 Time domain measurements The performance of transverse dampers presently installed in the Main Ring is evaluated by examining the turn-by-turn transverse beam position signals. Technical documents of transverse dampers are scarcely available.[38, 39] There is one bunch-by-bunch feedback system (super damper) and one narrow band feedback system (slow damper) presently installed in the vertical plane. The horizontal plane has only one slow damper system installed.

The Main Ring turn-by-turn beam position display system only gives the average of beam positions from seven consecutive bunches.[40] It is not a single-bunch, turn-by-turn beam position display system. To remove the effect of head-tail damping, the chromaticity is set close to the real zero value according to the calibration, which is -2.7 for the horizontal plane and 3.6 for the vertical plane. The beam energy is set to 8 GeV, the injection energy of the Main Ring. The trigger time is set right after the injection of beams. One booster batch of 84 beam bunches is used for the measurements. The settings of betatron tune in a typical pbar stacking cycle are used.

Figure 4.8 depicts the results where the vertical super damper is on and both slow dampers are off. The envelopes of horizontal and vertical oscillations are 90 degrees out of phase as depicted in Fig. 4.8, which is the signature of a coupled oscillation. This clearly shows the existence of linear coupling between the horizontal and vertical planes. The total beam intensity used for the measurement is 7×10^{11} protons. The e^{-1} damping time is about 200 turns. The revolution period at 8 Gev (injection energy) is 21 μsec according to Table 1.4. Note that there is only one super damper system installed in the Main Ring. Figure 4.8 shows that the super damper alone is able to suppress the coherent

beam oscillation in the vertical plane at this beam intensity. The damping of horizontal beam oscillation is caused by the vertical super damper through the linear coupling. The same accelerator parameters are used for the case where both slow dampers are on and the vertical super damper is off. The results are depicted in Fig. 4.9.

Once the vertical super damper is off, both planes begin to show amplitude growth in the transverse motion, even though both slow dampers are on. Since the intensity threshold of horizontal instability is about five times higher than the vertical one,[4] the amplitude growth of the horizontal motion shown in Fig. 4.9 should come from the leakage of vertical amplitude growth through the linear coupling between both planes.

When the vertical slow damper is left alone to handle the coherent beam oscillation, Fig. 4.9 clearly shows the inadequacy of vertical slow damper. Apparently there is some coherent modes which are beyond the frequency bandwidth of the slow damper system. The total beam intensity of a typical pbar stacking cycle in the collider run is about five times larger than the one used for measurements in Figs. 4.8 and 4.9.

When both slow dampers and the super damper are off, beam loss occurs. An example of this case is depicted in Fig. 4.10. When there is no damper system used in the Main Ring, both the horizontal and the vertical planes show the unstable beam oscillation. The beam loss is depicted in the time plot of total beam intensity in Fig. 4.10*(c)*.

1.2 Frequency domain measurements Since the vertical collective instability has an intensity threshold around 1×10^{12} protons,[4] most attention is paid studying the vertical damper systems in the frequency domain. The experimental setup is depicted in Fig. 4.11. The low frequency capacitive beam position monitor (BPM) discussed in Sec. B.2.1 of Chap. 2 is used to measure the induced signal from vertical beam motion in the

low frequency range. A swept type spectrum analyzer is used to measure the power spectrum of this signal. The data acquisition process is controlled by a control system console through the GPIB interface of the spectrum analyzer. The accelerator parameters used in the measurements are listed in Table 4.1.

When both vertical dampers are on and the chromaticity is set close to zero in the horizontal and the vertical plane respectively, the threshold intensity of vertical beam instability is found to be around 6×10^{12} protons. The corresponding fast time plot of Main Ring parameters is depicted in Fig. 4.12, and the vertical beam spectrum is depicted in Fig. 4.13. There are 8 empty rf buckets between adjacent batches for the beam used in Figs. 4.12 and 4.13. The choice of 8 empty rf buckets is to arrange 12 booster batches in such a way that the spacing between adjacent batches is approximately equal.

Table 4.1. Parameters used for the vertical damper evaluation.

parameter	value
beam energy (GeV)	8
number of booster batch	12
number of bunch per batch	84
beam intensity per bunch (1×10^9 protons)	8

In Fig. 4.13, there are many revolution harmonic lines with significant signal level. The revolution frequency of the Main Ring is 47.4 kHz at 8 GeV. Those revolution

harmonic lines indicate a substantial contribution of closed orbit offset to the measured vertical beam signal. The low-end betatron sidebands are quite pronounced in Fig. 4.13, which means a large amplitude in the vertical betatron oscillation. The spectral amplitude of 1- q_β and 2- q_β betatron sidebands is about the same as the adjacent revolution harmonic lines, where q_β represents the fractional betatron tune. This phenomenon suggests the existence of resistive wall instability, which is detrimental only in the low frequency range.

A zoom-in picture of the vertical beam spectrum is depicted in Fig. 4.14. Both vertical dampers are on, vertical chromaticity$\approx$ 0, and there are 8 empty rf buckets between adjacent batches. The spectrum analyzer is triggered at the injection of the 11th batch. The amplitude of betatron sidebands is comparable to the adjacent revolution harmonic lines as depicted in Fig. 4.14.

For any spectral line existing within the bandwidth of a feedback system, the feedback system will try to damp it indiscriminately. When the feedback system tries to damp the revolution harmonic lines, it actually tries to correct the closed orbit offset. When the Main Ring is suffering from severe vertical instabilities, the diversion of system power to the correction of closed orbit offset is unwanted. The closed orbit offset ought to be corrected by using the correction dipole magnets which are built specifically for this purpose. From Figs. 4.12 to 4.14, one readily concludes that both vertical dampers are inadequate to suppress the coherent beam oscillation without invoking the head-tail damping by tuning the chromaticity value.

To evaluate the performance of individual dampers, the power of a single betatron sideband as a function of time is measured by setting the frequency span of the spectrum analyzer to zero. Only a single damper is turned on at a time. Figure 4.15 depicts the

results when only the vertical super damper is turned on after the injection of the fourth batch .

Figure 4.15 is equivalent to the plot of betatron oscillation amplitude vs. time for a given frequency component. Each peak in Fig. 4.15 corresponds to the injection of one booster batch. An injection offset is created deliberately in order to induce the coherent betatron oscillation. The betatron oscillation amplitude is large at the beginning of every injection, then it is gradually damped out by the super damper. The effect of the super damper is clearly shown in Fig. 4.15*(a)* after it is turned on at 0.35 second. When the total beam intensity increases as the subsequent injections occur, the betatron amplitude begin to grow. After the injection of batch 9, the betatron amplitude grows to such an extent that it eventually hits the aperture limit of the vacuum chamber and beam loss occurs. The super damper is able to hold the beam until the injection of batch 9, which corresponds to a total beam intensity of 4.5×10^{12} protons. From Fig. 4.15*(b)*, the growth of betatron amplitude is clearly shown after the injection of batch 9 and then it drops away when the beam loss occurs.

Repeating the measurement with the same parameters used in Fig. 4.15, Fig. 4.16 depicts the result when only the vertical slow damper is turned on after the injection of the fourth batch . The beam becomes unstable after the injection of batch 7, which corresponds to a total beam intensity of 3.8×10^{12} protons. When both vertical dampers are turned off, the result of the measurement is depicted in Fig. 4.17.

From Figs. 4.11 to 4.17, the conclusion is that neither the super damper nor the slow damper is effective enough to suppress the collective beam instabilities at large beam intensity. It is also found that the slow damper is less effective compared with the super damper.

2. Dependence on beam intensity

Since the growth rate of collective instability is proportional to the beam intensity, measurements of growth rate vs. beam intensity can provide a direct proof whether the observed betatron amplitude growth is caused by the collective instability or not. The accelerator parameters used for the measurements are listed in Table 4.2. The experimental setup of measurements is depicted in Fig. 4.11.

Table 4.2. Parameters used for the measurements of growth rate vs. beam intensity.

parameter	value
beam energy (GeV)	8
number of booster batch	12
number of bunch per batch	84
batch gap (rf bucket)	8
horizontal chromaticity	-12
vertical chromaticity	0

From the definition of the unit [dBm][41] and the expression of amplitude growth $y(t)= Ae^{\alpha t}$, where A is the oscillation amplitude and α is the growth rate in units of [sec^{-1}], the growth rate can be derived from the measured power spectrum of vertical beam signal by the following:

$$\alpha = \frac{P_1 - P_2}{20 log_{10} e(t_1 - t_2)} = \frac{P_1 - P_2}{20(0.43429)(t_1 - t_2)} \tag{4.2}$$

where P_1 and P_2 are the measured power levels in units of [dBm] at two different time instants, t_1 and t_2 are their corresponding time indexes in units of [sec].

The oscillation amplitude of the 1- q_β betatron sideband vs. time for a beam intensity of 4×10^9 protons per bunch is depicted in Fig. 4.18. Both vertical dampers are turned on from the start until just before the injection of batch 6. In Fig. 4.18, the betatron amplitude begins to grow after the injection of batch 6 until it hits the aperture limit of vacuum chamber. The same measurement is repeated but the beam intensity per bunch is doubled, i.e. 8×10^9 protons per bunch. The result is depicted in Fig. 4.19. All the settings of spectrum analyzer are kept the same for both Figs. 4.18 and 4.19.

Comparing Fig. 4.19 with Fig. 4.18, the growth of betatron amplitude clearly increased significantly after the beam intensity is doubled. This gives an indisputable proof that the amplitude growth is indeed caused by collective beam instabilities.

To demonstrate the dependence of growth rate on the total beam intensity, measurements are repeated with the same conditions as used in Fig. 4.18 except the number of bunches per batch. The number of bunches per batch is varied accordingly for each measurement of growth rate. The measured results as depicted in Fig. 4.20 show the dependence of growth rate on the total beam intensity. This indicates the existence of coupled bunch instability in the Main Ring.

3. Dependence on bunch length

The dependence of growth rate on the bunch length is investigated by varying the rf voltage, which in turn will change the bunch length accordingly. The higher the rf voltage, the shorter the bunch length. The accelerator parameters used for the measurements are listed in Table 4.2. The beam intensity per bunch used in the measurements is 4.6×10^9 protons. Figures 4.21 and 4.22 depict the effect on the stored total beam intensity for different bunch length respectively. As shown in Figs. 4.21 and 4.22, the beam loss is more severe when the bunch length is shorter. The bunch length is recorded by using the real-time bunch length monitor in the Main Ring.

As depicted in Fig. 4.21, the beam loss occurs after both vertical dampers are turned off right before the injection of batch 6. Since the threshold intensity is around 1×10^{12} protons, the subsequent injections are not able to survive without substantial beam loss. The final stored beam intensity is below 1×10^{12} protons. In contrast to the results in Fig. 4.21, the bunch length used in Fig. 4.22 is increased by about 50 % and the results show a better survival of the total beam intensity, almost a factor of 2 increase.

A quantitative result can be derived from measurements of growth rate for the 1- q_β betatron sideband. The experimental setup is depicted in Fig. 4. 11. Both vertical dampers are turned on from the start until the injection of batch 10. The growth rate is calculated by measuring the oscillation amplitude of 1- q_β betatron sideband during the injection of batch 10. The spectrum analyzer is set to the following state: resolution and video bandwidth= 3 kHz respectively, center frequency= 25.5 kHz, frequency span= 0 Hz. The result of growth rate vs. rf voltage with error estimate is depicted in Fig. 4.23, and the result of growth rate vs. bunch length is depicted in Fig. 4.24. Note that Figs. 4.23 and 4.24 use the same set of data.

Results from Figs. 4.21 to 4.24 exhibit a strong dependence of the growth rate on the bunch length. This indicates the existence of vertical head-tail instability, which is sensitive to the change of bunch length.

4. Dependence on chromaticity

The dependence of growth rate on the chromaticity is also investigated by measuring the oscillation amplitude of 1- q_β betatron sideband vs. time. The accelerator parameters used in the measurements are listed in Table 4.2. The beam intensity per bunch is 4.5×10^9 protons. The bunch length is about 4 [nsec].

The growth rate of the betatron oscillation amplitude is measured during the injection of the 11th batch. Both vertical dampers are turned on from the start until just before the injection of the 11th batch. The measured growth rate is depicted in Fig. 4.25. Each data point in Figs. 4.25 is the average result of four repetitive measurements.

From the theory of bunched beam instability, the dependence of growth rate on the chromaticity indicates the existence of head-tail instability. Knowing that a capacitive beam position monitor can only detect the center of mass motion, the growth of betatron amplitude for negative chromaticity can only be attributed to the coupled bunch instability. From discussions in Sec. B.2 of Chap. 3, a negative chromaticity at the energy below transition will results in a damping effect for the rigid bunch displacement (m= 0 mode head-tail damping). Therefore, the change of the chromaticity value will affect the measured growth rate, and it can be used to help tune the accelerator.

5. Dependence on injection sequence

The strength of coupled bunch instability replies on the coherent coupling between the bunches. If the coherent coupling between bunches is disrupted, the strength of the

coupled bunch instability will be reduced. Different injection sequences of booster batches into the Main Ring could provide a possible mechanism to help suppress the coupled bunch instability.

Two different injection schemes are studies by using the accelerator parameters listed in Table 4.2. The beam intensity per bunch is 8.4×10^9 protons. Two injection schemes used for the measurements are depicted in Fig. 4.26 schematically. Each booster batch is separated by 8 empty rf buckets except the first and the last batch. There are 17 empty rf buckets between the first batch and the last batch.

The oscillation amplitude of the 1- q_β betatron sideband vs. time is measured. The results are depicted in Fig. 4.27. The alternate injection sequence as depicted in Fig. 4.26*(b)* is able to deter the onset of beam instability and raises the threshold intensity by about 10 %. A random sequence for the injection of booster batches is expected to raise the threshold intensity of beam instability higher than the alternate sequence. But it is expected only to provide some marginal improvement. This method is not sufficient enough to support the ambitious goals for the coming fixed target run in 1996.

6. Dependence on betatron tune

The dependence of growth rate on the betatron tune is investigated by using the same accelerator parameters listed in Table 4.2. The growth of betatron amplitude is measured for the 1- q_β betatron sideband during the injection of the 10th batch. Both vertical dampers are turned on from the start until the injection of batch 10. The initial value of betatron tune is 19.48 for the horizontal plane, and 19.49 for the vertical plane according to the readings of Main Ring control system. The result is depicted in Fig. 4.28.

C. Coupled bunch instability

The conventional theory of coupled bunched instability only provides results for the case where the accelerator is filled with a complete bunch train with equally spaced, equal intensity bunches along the circumference. A quantitative extension of the conventional theory[26] is made in order to cover situations where the accelerator is filled with an incomplete bunch train or multiple bunch trains with gaps distributed around the circumference.

1. One short bunch train

1.1 Calculation of single batch form factor During the pbar stacking cycle only one booster batch is injected into the Main Ring, which takes up one thirteenth of the circumference. The bunch configuration of the pbar stacking cycle in the Main Ring is depicted in Fig. 4.29.

When both vertical dampers are turned off, the beam suffers from vertical instability unless the vertical chromaticity is set to a large negative value ($\approx$ -30). The observed beam instability depicts characteristics similar to the phenomenon of beam breakup[25] observed in a linac. In other words, there seems to be an open-loop coupled bunch instability during the pbar stacking cycle where the first bunch is not affected by the wake force. The time evolution of vertical beam oscillation is recorded by a fast digitizer. The experimental setup is depicted in Fig. 4.30.

The vertical chromaticity is set around -14 and the horizontal chromaticity is around -12. With those settings, the m=0 mode head-tail instability will not occur. The intensity per bunch is 1.5×10^{10} protons, and the bunch length is 5 [nsec]. Both vertical dampers

are turned off during the measurement. The measured bunch oscillation triggered at different time instants are depicted in Fig. 4.31. The beam energy is set to 8 Gev.

Note that the induced signal on a stripline BPM has a doublet structure.[42] Figure 4.31 depicts the vertical beam position of the first 42 bunches in the bunch train. In Fig. 4.31, the envelope of bunch train appears to be modulating smoothly. The betatron amplitude of the first bunch does not seem to change noticeably, yet the amplitude of following bunches increased gradually. The results depicted in Fig. 4.31 suggest a coupled bunch motion driven by a wake force of intermediate range which is not able to cause cumulative effects on the first bunch. Hence, it is called open-loop coupled bunch instability. This is similar to the beam breakup instability observed in a linac.

In order to interpret the observed vertical beam spectrum, an empirical theory is devised. Based on the observed phenomena, assumptions listed in Table 4.3 are used in the calculation of the transverse beam spectrum for a short bunch train. The nomenclature of bunch index for a short bunch train is depicted in Fig. 4.32. In order to make the analytical calculation possible, the betatron amplitude is assumed to be the same for all bunches which is not the case in reality.

Table 4.3: Assumptions used for calculating the transverse beam spectrum of an incomplete bunch train.

Assumptions
1. each bunch is represented by a macroparticle
2. considering the steady state only, no transient response
3. coupled bunch coherence is established
4. single mode excitation
5. assuming the same betatron amplitude, the same closed orbit offset, and the same charge for every bunch

The first bunch is denoted by the index number 0, and the last one is denoted by L-1 for a bunch train of L bunches. For a bunch with index p, its induced transverse signal $d_p(t)$ on a BPM is given by Eq.(2.5) as:

$$d_p(t) = e \sum_{n=-\infty}^{\infty} \left[x_c + A_\beta e^{-i(q_\beta \omega_0 t + \psi_p)} \right] \delta(t - nT - p\frac{T}{h}) \qquad (4.3)$$

where q_β= the fractional betatron tune, x_c= the closed orbit offset, A_β= the betatron amplitude, h= the harmonic number of the Main Ring, and ψ_p= the initial betatron phase. The resulting signal is the sum of all signals induced by each bunch:

$$D(t) = \sum_{p=0}^{L-1} d_p(t) \qquad (4.4)$$

The Fourier transform of the resulting signal is given by the following equations:

$$\tilde{D}(\omega) = \sum_{p=0}^{L-1} \frac{1}{2\pi} \int_{-\infty}^{\infty} d_p(t) e^{i\omega t} dt \tag{4.5}$$

$$\tilde{D}(\omega) = \frac{e}{2\pi} \sum_{n=-\infty}^{\infty} \sum_{p=0}^{L-1} \left[x_c e^{i\omega(nT+pT/h)} + A_\beta e^{-i\psi_p} e^{i(\omega - q_\beta \omega_0)(nT+pT/h)} \right] \tag{4.6}$$

Substituting the Poisson's sum rule given in Eq.(2.13) into Eq.(4.6), the transverse beam spectrum becomes:

$$\begin{aligned} \tilde{D}(\omega) = \frac{e}{T} \sum_{n=-\infty}^{\infty} \sum_{p=0}^{L-1} \Big[& x_c e^{i2\pi np/h} \delta(\omega - n\omega_0) + \\ & A_\beta e^{-i\psi_p} e^{i2\pi np/h} \delta(\omega - n\omega_0 - q_\beta \omega_0) \Big] \end{aligned} \tag{4.7}$$

Because of the coupled bunch coherence, the displacement of each bunch differs from its neighboring bunch only by a phase factor. The betatron phase for the bunch with index p can be derived from the following expression:

$$\begin{aligned} \psi_p &= \theta + \psi_{p-1} \\ &= 2\theta + \psi_{p-2} \\ &\cdots\cdots \\ &= p\theta + \psi_0 \end{aligned} \tag{4.8}$$

where θ= the coherent phase of coupled bunch motion, and ψ_0= the initial phase of the first bunch. The coherent phase θ is still given by the same expression used for the coupled bunch mode with cyclic symmetry[25] (an accelerator filled with equally spaced, equal bunches):

$$\theta = \frac{2\pi\mu}{h} ; \mu \in \{0,1,2,\cdots,h-1\} \tag{4.9}$$

where μ is the coupled bunch mode number in the range shown above. Substituting the expression of coherent phase into Eq.(4.7), the transverse beam spectrum becomes:

$$\tilde{D}(\omega) = \frac{e}{T} \sum_{n=-\infty}^{\infty} \sum_{p=0}^{L-1} \Big[x_c e^{i2\pi np/h} \delta(\omega - n\omega_0) + A_\beta e^{-i\psi_0} e^{i\frac{2\pi}{h}(n-\mu)p} \delta(\omega - n\omega_0 - q_\beta \omega_0) \Big] \tag{4.10}$$

From the formula of geometric progression:

$$\sum_{k=0}^{N-1} as^k = \frac{a(s^N - 1)}{s-1}, \text{when } s \neq 1$$
$$\text{or} \tag{4.11}$$
$$= Na, \text{when } s = 1$$

Eq.(4.10) becomes as:

$$\tilde{D}(\omega) = \frac{e}{T} \sum_{n=-\infty}^{\infty} \Big[F(n,L) x_c \delta(\omega - n\omega_0) + F(n-\mu, L) A_\beta e^{-i\psi_0} \delta(\omega - n\omega_0 - q_\beta \omega_0) \Big] \tag{4.12}$$

where F(n, L) is the envelope of spectral amplitude for the revolution harmonic lines, and F(n-μ, L) is the envelope of spectral amplitude for the betatron sidebands. Since F(n, L) results from the bunch configuration of a single bunch train, it is named single batch form factor. Its explicit expression is given by the following:

$$F(n,L) = \left| \frac{e^{i2\pi nL/h} - 1}{e^{i2\pi n/h} - 1} \right| ; \text{for } n \neq h\ell \tag{4.13}$$

or,

$$F(n,L) = L \ ; \text{for } n = h\ell \tag{4.14}$$

where ℓ is any integer. For the envelope of betatron sidebands, one simply replaces the variable n in Eqs.(4.13) and (4.14) by n- μ. The coherent frequency of coupled bunch oscillation is given by the following expression:

$$f = (h\ell + \mu) f_0 + q_\beta f_0 \tag{4.15}$$

where ℓ= any integer, μ= an integer in the range from 0 to h-1, and μ is the mode number of coupled bunch motion.

The transverse beam spectrum has maximum response at frequencies given by Eq.(4.15). The induced signals from all bunches interact coherently for signal components corresponding to frequencies given in Eq.(4.15); the signals are all in phase and they all add up. For those signal components not corresponding to the coherent frequency and its alias frequencies, they cancel with each other. Because of the missing bunches, the cyclic symmetry is broken and the cancellation is incomplete. In contrast to the case of cyclic symmetry, those spectral lines not corresponding to frequencies given in Eq.(4.15) could still have nonzero amplitude. For the case of cyclic symmetry, only those spectral lines corresponding to the coherent frequency and its alias frequencies will

show up, and others all have zero amplitude due to the complete cancellation of induced signals.

From Eq.(4.12), one readily realizes that the form factor is the same for revolution harmonic lines and betatron sidebands, except that the form factor of betatron sidebands is shifted by the coupled bunch mode number μ.

1.2 Interpretation of single batch form factor To illuminate the meaning of single batch form factor given in Eqs.(4.12) and (4.13), an accelerator with four equally spaced, equal bunches is assumed. Suppose there is transverse coupled bunch oscillation in the accelerator, then the transverse beam spectrum measured by a BPM is given by the following result:

$$\tilde{D}(\omega) = \frac{e}{T} \sum_{n=-\infty}^{\infty} \sum_{p=0}^{3} \Big[x_c \, e^{i2\pi np/4} \, \delta(\omega - n\omega_0) + A_\beta \, e^{-i\psi_0} \, e^{i\frac{2\pi}{4}(n-\mu)p} \, \delta(\omega - n\omega_0 - q_\beta \omega_0) \Big] \tag{4.16}$$

For any given betatron sideband, its amplitude is determined by the sum of four complex phase vectors, whose expression is given by $\exp[i2\pi(n-\mu)p/4]$. For those spectral lines not corresponding to the coherent mode number μ and its alias ($\mu + 4\ell$, ℓ= integer), the exponent of phase vector is not zero. The sum of four phase vectors can be performed graphically on a unit circle as depicted in Fig. 4.33.

As one will expect from the conventional theory of bunch beam instability, the amplitude of spectral lines at frequencies given in Eq.(4.15) is four times the signal of a single bunch case. The amplitude of the spectral lines at frequencies other than those given in Eq.(4.15) is zero, because of the complete cancellation between signals induced

by each bunch. Those results are caused by the coupled bunch coherence and the cyclic symmetry.

Now suppose the last bunch is missing, whose bunch index is 3. The transverse beam spectrum measured by a BPM will become:

$$\tilde{D}(\omega) = \frac{e}{T} \sum_{n=-\infty}^{\infty} \sum_{p=0}^{2} \left[x_c \, e^{i2\pi np/4} \, \delta(\omega - n\omega_0) + A_\beta \, e^{-i\psi_0} \, e^{i\frac{2\pi}{4}(n-\mu)p} \, \delta(\omega - n\omega_0 - q_\beta \omega_0) \right] \tag{4.17}$$

, notice that the upper limit of sum over bunch index p is 2 instead of 3 in Eq.(4.17). The sum of three complex phase vectors is depicted in Fig. 4.34.

In contrast to the conclusion for the case where the accelerator is filled with equally spaced, equal intensity bunches, the amplitude of the spectral lines at frequencies which are not given in Eq.(4.15), could be nonzero due to the incomplete cancellation of signals induced by each bunch. This is the meaning behind the mathematical expression in Eq.(4.13).

The single batch form factor can also be understood from the perspective of discrete signal processing. Suppose the accelerator is filled with four equally spaced, equal bunches as the previous example, the signal of transverse coupled bunch oscillation observed by a BPM is depicted in Fig. 4.35.

Now suppose that the last bunch (index= 3) is missing, and the coupled bunch coherence still exists. The observed transverse signal for a short bunch train is depicted in Fig. 4.36*(a)*. Figure 4.36*(b)* depicts the periodic window function which gives the resulting bunch configuration for the case where the last bunch (index= 3) is missing. The observed signal from the transverse coupled bunch oscillation of a short bunch train

is equal to the convolution of the beam signal for the symmetric case depicted in Fig. 4.35*(a)* and the periodic window function *w(t)* depicted in Fig. 4.36*(b)*. This is equivalent to the windowing process used in discrete signal processing by any realistic measuring instrument (see Sec. A.2 of Chap. 2). The effect caused by the periodic window function *w(t)* on the observed beam spectrum is the same as in the signal processing, it introduces the spectral leakage (see Sec. A.2 of Chap. 2) into the observed beam spectrum of bunch trains with gaps. This is the reason why those spectral lines not corresponding to the coherent frequency and its alias as given in Eq.(4.15) could have nonzero amplitude.

1.3 Analysis of observed beam spectrum Using the experimental setup depicted in Fig. 4.11, the vertical beam signal is measured with the following accelerator parameters: one booster batch of 84 beam bunches, both vertical dampers are off, the chromaticity is set to zero for the horizontal and vertical planes according to the calibrated values, and the beam intensity is 1.2×10^{10} protons per bunch. The fit of the calculated spectral envelope to the measured vertical beam spectrum is depicted in Fig. 4.37.

The fit of calculated spectral envelope to the measured vertical beam spectrum shows good agreement qualitatively. The location of valley in the measured spectral envelope of revolution harmonic lines is well predicted by the calculation, which is around the n= 13 harmonic line. The minor discrepancy between the measured spectral amplitude and the calculated value could be caused by the unequal population of particles in each bunch. There is about 50 % beam loss being observed during the measurement. Since the trailing bunches tend to develop amplitude growth earlier than those bunches moving in the front, the particle loss will occur to those trailing bunches first. This will result in the violation of one of the assumptions listed in Table 4.3. Since the growth

time of vertical instability is about 50 [msec] for the beam intensity used in Fig. 4.37, a spectrum analyzer with a shorter data acquisition time should further reduce the discrepancy between the calculated result and the measured data. Note that the frequency response of the receiver has been taken into account in the data fit.

When the total number of bunches is reduced from 84 to 11 and the beam intensity per bunch is doubled, there is only about 10 % beam loss being observed during the measurement. The fit of measured vertical beam spectrum to the calculated spectral envelope is depicted in Fig. 4.38. No prominent betatron sidebands are observed for a bunch train of 11 beam bunches. Figure 4.38 shows good agreement between the measured data and the calculation. This implies that there is coupled bunch coherence developed among bunches. Each bunch in the bunch train does not move independently.

2. Multiple bunch trains

2.1 Calculation of multibatch form factor During the fixed target experiments, 12 batches of proton beam are injected into the Main Ring. An illustration of the multibatch configuration is given in Fig. 4.26. All the gaps between each batch account for 9.4 % of the circumference. An analytical tool is required for a proper interpretation of the measured vertical beam spectrum. The calculation of single batch form factor needs to be extended to the multibatch operation mode. The same assumptions listed in Table 4.3 are used. The nomenclature of bunch index for the multibatch configuration is depicted in Fig. 4.39. The gap between adjacent bunch trains is represented by g rf buckets, and there are L bunches per batch. The first bunch of the first batch is denoted by the index number 0. The index number of subsequent bunches is assigned in an ascending order.

A new variable m is introduced to represent the order of batches. The first batch is denoted by the index number 0. Suppose there are $\hat{m}$ batches in a circular accelerator,

each separated by a gap of g rf buckets. The transverse signal induced by a bunch with bunch index p is given by Eq.(4.3). With careful bookkeeping, the resulting signal induced by $\hat{m}$ batches with L bunches per batch is given by the following:

$$\begin{aligned} D(t) &= \sum_{p=0}^{L-1} d_p(t) + \sum_{p=L+g}^{(L+g)+L-1} d_p(t) + \sum_{p=2(L+g)}^{2(L+g)+L-1} d_p(t) + \ldots + \sum_{p=m(L+g)}^{m(L+g)+L-1} d_p(t) + \ldots \\ &= \sum_{m=0}^{\hat{m}-1} \sum_{p=m(L+g)}^{m(L+g)+L-1} d_p(t) \end{aligned} \tag{4.18}$$

The measured transverse beam spectrum is given by using Eq.(4.7):

$$\begin{aligned} \tilde{D}(\omega) = \frac{e}{T} \sum_{n=-\infty}^{\infty} \sum_{m=0}^{\hat{m}-1} \sum_{p=m(L+g)}^{m(L+g)+L-1} \Big[& x_c\, e^{i2\pi np/h}\, \delta(\omega - n\omega_0) + \\ & A_\beta\, e^{-i\psi_p}\, e^{i2\pi np/h}\, \delta(\omega - n\omega_0 - q_\beta \omega_0) \Big] \end{aligned} \tag{4.19}$$

Substituting the expression of the coherent phase of coupled bunch motion in Eq.(4.9) into Eq.(4.19), the transverse beam spectrum becomes:

$$\begin{aligned} \tilde{D}(\omega) = \frac{e}{T} \sum_{n=-\infty}^{\infty} \sum_{m=0}^{\hat{m}-1} \sum_{p=m(L+g)}^{m(L+g)+L-1} \Big[& x_c\, e^{i2\pi np/h}\, \delta(\omega - n\omega_0) + \\ & A_\beta\, e^{-i\psi_0}\, e^{i\frac{2\pi}{h}(n-\mu)p}\, \delta(\omega - n\omega_0 - q_\beta \omega_0) \Big] \end{aligned} \tag{4.20}$$

Carrying out the sum over the phase vectors by using Eq.(4.11), the measured transverse beam spectrum can be written as:

$$\tilde{D}(\omega) = \frac{e}{T}\sum_{n=-\infty}^{\infty}\Big[F(n,L)B(n,L,g,\hat{m})x_c\,\delta(\omega - n\omega_0) + F(n-\mu,L)\,B(n-\mu,L,g,\hat{m})A_\beta\, e^{-i\psi_0}\,\delta(\omega - n\omega_0 - q_\beta\omega_0)\Big] \tag{4.21}$$

where $B(n,L,g,\hat{m})$ is a form factor containing information about the configuration of bunch trains. $B(n,L,g,\hat{m})$ is named the multibatch form factor. The explicit expression of the multibatch form factor $B(n,L,g,\hat{m})$ is given by the following results:

$$B(n,L,g,\hat{m}) = \left|\frac{\exp[i2\pi n(L+g)\hat{m}/h]-1}{\exp[i2\pi n(L+g)/h]-1}\right|;\text{for } n \neq h\ell \tag{4.22}$$

or,

$$B(n,L,g,\hat{m}) = \hat{m}L;\text{for } n = h\ell \tag{4.23}$$

where ℓ is any integer. The envelope of revolution harmonic lines is given by the product of the single batch form factor and the multibatch form factor, i.e. $F(n, L)B(n, L, g, \hat{m})$. The envelope of betatron sidebands is given by $F(n-\mu, L)B(n-\mu, L, g, \hat{m})$, where μ is the coupled bunch mode number ranging from 0 to h-1. The spectral envelope is the same for the revolution harmonic lines and the betatron sidebands, except that the spectral envelope of betatron sidebands is shifted by the coupled bunch mode number μ. The coherent frequency of the coupled bunch oscillation is still given in Eq.(4.15). Equation (4.23) is a quantitative extension of the conventional theory[25] of bunched beam instability.

2.2 Analysis of observed beam spectrum Multibatch injection is used to test the theoretical results given in Eqs.(4.22) and (4.23). Twelve batches of proton beams are

injected into the Main Ring. The experimental setup is depicted in Fig. 4.11. Figure 4.40 depicts the measured vertical beam spectrum for the following accelerator parameters: horizontal chromaticity≈ 0, vertical chromaticity≈ -14, 84 beam bunches per batch, batch spacing= 8 empty rf buckets, both vertical dampers are on, intensity= 8.8×10^9 protons per bunch, and the bunch configuration is depicted in Fig. 4.26*(a)*.

The agreement between the calculated spectral envelope and the data is better for the first three betatron sidebands. Since there is beam loss during the injection of 12 booster batches, this could provide an explanation for the discrepancy between the calculation and the measured data. The long data acquisition time is also part of the reason for the discrepancy. The spectral envelope calculated by using Eq.(4.22) does predict the pattern of measured envelope pretty well in Fig. 4.40. Because of the inadequacy of damper systems, the beam still suffers from the coupled bunch instability even for vertical chromaticity≈ -14 and both vertical dampers are on. The mode number is fitted to be $\mu = 1$, and the coherent phase is fitted to be $2\pi/1113$. This means that the frequency of unstable mode corresponds to the $1\text{-}q_\beta$ betatron sideband, which is around 26.5 kHz. A different perspective seen from the time domain is depicted in Fig. 4.41, which is recorded by a digital oscilloscope for five consecutive turns.

Figure 4.41*(b)* depicts the vertical coupled bunch oscillation in the time domain. The envelope of the bunch oscillation has a periodicity about 20 μs. The batch spacing is about 160 nsec, which makes it difficult to be resolved with the time scale used in Fig. 4.41*(b)*. Knowing that the induced signal on a stripline BPM has a doublet structure in the time domain, the actual period of coupled bunch oscillation in Fig. 4.41*(b)* is around 40 μs instead of 20 μs. This corresponds to an oscillation frequency around 25 kHz, which agree with the conclusion deduced from the measured beam spectrum in Fig. 4.40. Therefore, the observed coupled bunch oscillation is caused by the μ=1 mode.

The electrical response of a stripline BPM to a train of bunches in the time domain is depicted in Fig. 4.42. The signal induced by a train of bunches on the electrode of a stripline BPM is depicted in Fig. 4.42*(a)*. Each beam bunch induces a voltage pulse on the electrode. The induced pulse travels along the electrode plate with the beam and then gets reflected back at the downstream end. Because the downstream end is shorted, the reflected voltage pulse reverses its polarity. On an oscilloscope, one will see the reflected pulse being delayed by an interval of $2\ell/c$, where ℓ is the length of electrode. Because of the reflected pulse, it gives one an illusion that the period of coupled bunch oscillation is 20 μs in Fig. 4.41*(b)*. Actually it should be twice the observed period.

When the number of bunches per booster batch is reduced by half, the growth rate of the instability is reduced, as is the beam loss. The calculated spectral envelope of the betatron sidebands fits the measured data better in this case than in Fig. 4.40. Figure 4.43 depicts the measured vertical beam spectrum for the case where 12 booster batches are used, and each batch contains 40 bunches. The coupled bunch mode is fitted to be $\mu=1$, and the coherent phase is fitted to be $2\pi/1113$. The coherent frequency corresponds to the $1-q_\beta$ betatron sideband. The vertical bunch oscillation recorded by a digital oscilloscope in the time domain for five consecutive turns are depicted in Fig. 4.44.

When the number of bunches per booster batch is reduced to 13, the total beam intensity is slightly below 1×10^{12} protons (the threshold intensity). The beam does not become unstable, but the coupled bunch coherence is well developed. The calculated spectral envelope of the revolution harmonic lines fits quite well to the measured beam spectrum. The vertical bunch oscillation in the time domain is recorded by a digital oscilloscope for five consecutive turns, both results are depicted in Fig. 4.45. Since the beam does not become unstable, the vertical beam spectrum does not show any prominent betatron sidebands.

From results depicted in Figs. 4.40– 4.45, the unstable coupled bunch mode is found to be dominated by the $\mu = 1$ mode which corresponds to the 1- q_β betatron sideband. The coupled bunch instability can still occur when both vertical dampers are turned on. The bunch length used in those measurements is about 6 nsec. One could use a longer bunch length and constantly tune the accelerator chromaticity to increase the threshold intensity, but this approach will not be sufficient to achieve the goals of next fixed target run. The head-tail damping mechanism could be invoked to alleviate the situation by setting the vertical chromaticity to a large negative value, but this will also reduce the dynamic aperture of the Main Ring. The empirical theory of multibatch form factor proves to be a useful tool for identifying the unstable mode of the coupled bunch instability.

D. Single bunch instability

1. Observation of head-tail motion

The experimental setup for measuring the single bunch head-tail motion is depicted in Fig. 4.30. Since the bunch length is on the order of 5 nsec, a high quality cable is required for this measurement. The Tektronix transient digitizer RTD720 is set to a sampling rate of 2 GSample/sec. The finest time resolution of the recorded trace is 0.5 [nsec] per step. One booster batch of 84 proton bunches is used in the measurements. The beam energy is set to 8 GeV, the injection energy. The horizontal chromaticity is set close to -12. The vertical chromaticity is varied in order to induce different modes of head-tail motion. The m= 0 mode (rigid bunch mode) and m= 1 mode head-tail motion are found in the Main Ring. Figures 4.46 and 4.47 depict the m= 0 mode head-tail oscillation for vertical chromaticity≈ 0 with different bunch lengths. Fig. 4.48 depicts the m= 0 mode head-tail oscillation for vertical chromaticity≈ 16.

To investigate the effect of slow damper on the single bunch instability, measurements are performed by turning on the slow damper only. Results show that the slow damper has no effect on the single bunch head-tail instability. Figure 4.49 depicts the result for vertical chromaticity≈ 6 and slow damper on.

As depicted in Fig. 3.19, the m= 1 mode head-tail motion can result in a non-negligible center of mass motion when the chromaticity is large. Thus, the m= 1 mode head-tail motion can be induced by setting the vertical chromaticity to a large negative value and perturbing the beam with a kicker. Because the m= 0 mode head-tail motion is stable for a negative chromaticity below transition but the m= 1 mode is not, the m= 1 mode head-tail motion will grow and can be detected later on. The measurement is triggered 5 [msec] after the excitation. Figures 4.50 and 4.51 depict the m= 1 mode head-

tail oscillation observed in the Main Ring. The characteristics of m= 1 mode head-tail oscillation is a node in the middle of induced signal.

Because of the limitation on the time resolution set by the maximum sampling rate of the digitizer, attempts were unsuccessful to observe the head-tail motion higher than the m=1 mode. Besides the limitation of instrumentation, it is also harder to excite the higher order mode of head-tail motion. Larger beam intensity and precise tuning of chromaticity are required. From the measured results shown in Figs. 4.46– 4.51 and the failed attempts to excite higher order modes, it is concluded that the m= 0 mode (rigid bunch mode) is the most detrimental single bunch instability in the Main Ring. Fortunately, the m= 0 mode results in a nonzero center of mass motion which can be detected and corrected by a fast feedback system working on a bunch-by-bunch time base.

2. Measurements of bunch form factor

To understand the single bunch instability, one needs to have a good knowledge of the bunch form factor $F_m(\chi)$ and the accelerator impedance, where $\chi = 2\pi f \tau_L$, τ_L= full bunch length [sec], and f= frequency [Hz]. From discussions found in Ref. 34 and Ref. 36, the bunch form factor is the same for both the longitudinal case and the transverse case. The difference only occurs when the chromaticity is not zero. In such cases, the transverse bunch form factor is simply shifted by the chromatic frequency, $F_m(\chi - 2\pi f_\xi \tau_L)$, as depicted in Eqs.(3.61). Therefore, the transverse bunch form factor $F_m(\chi)$ can be determined by measuring the longitudinal bunch form factor. The experimental setup for the measurement of longitudinal bunch form factor is depicted in Fig. 4.52. In order to map out the bunch form factor, one needs to collect data points in a wide

frequency range. Therefore, a high quality cable with low power dissipation and low frequency dispersion is required for this measurement.

Because of the bunch configuration of a booster batch and the existence of the coupled bunch coherence, the longitudinal beam spectrum will be complicated by the single batch form factor given in Eq.(4.13). As the result shown in Eq.(4.13), when the frequency is a multiple of the rf frequency, the spectral amplitude is simply L times the amplitude of the single bunch case, assuming there are L bunches in one bunch train. To simplify the data analysis, the spectral amplitude at multiple harmonics of the rf frequency is measured.

To map out the bunch form factor $F_0(\chi)$ for the m= 0 mode, the spectral amplitude of revolution harmonic lines at frequencies equal to multiples of the rf frequency are measured. To map out the bunch form factor $F_1(\chi)$ for the m= 1 mode, the injection phase of the rf system is deliberately mismatched so that the longitudinal dipole mode is induced. The amplitudes of the m= 1 synchrotron sidebands around the revolution harmonic lines of multiple rf frequencies are measured. To map out the bunch form factor $F_2(\chi)$ for the m= 2 mode, the rf voltage is deliberately mismatched so that the longitudinal quadrupole mode is induced. Then the amplitudes of the m= 2 synchrotron sidebands around the revolution harmonic lines of multiple rf frequencies are measured. When the rf voltage is mismatched, it is also possible that other higher order modes could be induced. The amplitudes of the m= 3 synchrotron sidebands around the revolution harmonic lines of multiple rf frequencies are also measured. The form factor can be derived from the power spectrum of the beam by the following expression (see Eqs.(3.62) and (3.65)):

$$F_m(p) = \frac{\left|\sigma_m(\chi(\mu + ph))\right|^2}{\sum_{p=-\infty}^{\infty}\left|\sigma_m(\chi(\mu + ph))\right|^2} \tag{4.24}$$

where σ_m is the spectral amplitude of the longitudinal beam spectrum for the m-th synchrotron sideband, μ is the coupled bunch mode number, p is an integer, and h is the rf harmonic number. The measured power level of each spectral line needs to be normalized by the sum of power level over all alias frequencies. The measured bunch form factor $F_m(\chi)$ is depicted in Fig. 4.53.

Assuming a water-bag model for the particle distribution in the longitudinal phase space, the power level of the m-th synchrotron sideband can be approximated by the following expression:[43]

$$\left|\sigma_m(\chi)\right|^2 = \frac{(m+1)^2\left[1 + (-1)^m \cos\chi\right]}{\left[(\chi/\pi)^2 - (m+1)^2\right]^2} \tag{4.25}$$

where $\chi = 2\pi f \tau_L$. The calculated bunch form factor is depicted in Fig. 4.54. The measured peak location of each form factor is very close to the results predicted by the theoretical approximation.

3. *Answers to the puzzle raised by Main Ring operations*

Since the existence of the vertical head-tail instability has been confirmed from results shown in previous sections, the puzzling setting of chromaticity value for the Main Ring as depicted in Fig. 4.1 can be answered. From discussions presented in Chap. 3, the transverse head-tail instability will occur if the convolution of the resistive

impedance and the transverse bunch form factor $F_m(\chi - 2\pi f_\xi \tau_L)$ is negative for a given mode number m and the chromaticity. The typical accelerator parameters used at the injection stage of the pbar stacking cycle are: bunch length≈ 10 nsec, vertical chromaticity≈ 8. Using the typical value of bunch length, the abscissa of measured bunch form factor can be converted into the units of [MHz], the result is depicted in Fig. 4.55. At injection, the convolution of the accelerator impedance and the vertical bunch form factor is depicted in Fig. 4.56 qualitatively. The vertical bunch form factor is shifted by -46 MHz, according to the value of chromatic frequency given in Table 1.4 for one unit of chromaticity

As depicted in Fig. 4.56, the convolution is negative for the m= 0 head-tail mode. Therefore, there will be the m= 0 mode head-tail instability at injection for an off-centered beam. Because the m= 0 mode head-tail instability results in a nonzero center of mass motion, a bunch-by-bunch feedback system with enough voltage gain can cure this single bunch instability. This explains why the vertical super damper is so crucial in the Main Ring operation. On the contrary, the convolution is positive for the m= 1 head-tail mode. Hence, there will not be any m= 1 mode head-tail instability, which can not be cured by a resistive feedback system. As long as the super damper has enough voltage gain to suppress the m= 0 mode head-tail instability, the typical setting of chromaticity value as depicted in Fig. 4.1 remains as a favorite choice for the Main Ring operation.

One may ask why not choose a small negative value for the vertical chromaticity to avoid the m= 0 mode head-tail instability? Since the injection energy is below transition, a negative chromaticity will shift the transverse bunch form factor toward the positive direction of frequency axis as depicted in Fig. 4.57.

Although this setting does result in a damping effect for the m= 0 mode head-tail motion, it also sets the m= 1 mode head-tail motion unstable. Since a conventional

feedback system requires a nonzero center of mass motion as the input, it is ineffective in suppressing the m= 1 mode head-tail instability. One could, however, use a much larger negative value for the vertical chromaticity so that both the vertical bunch form factors of the m= 0 mode and m= 1 mode overlap with the impedance in the positive region of frequency axis. But this will make the m= 2 mode head-tail motion unstable.

There are other issues one needs to be concerned about. Suppose both the vertical bunch form factor of the m= 0 mode and m= 1 mode are being shifted to the positive region of frequency axis. This will require the vertical chromaticity to be set at -16 or a larger negative value. Knowing that each proton is also undergoing synchrotron oscillation, this results in a modulation of betatron tune with an amplitude given by $\xi(dp/p)$. For a typical value of fractional energy deviation in the Main Ring, 0.3 %, the amplitude of tune modulation is about 0.05. The synchrotron tune is about 0.011 at 8 Gev, i.e. the synchrotron period is about 90 turns. This means that the betatron tune of a single proton is sweeping across the transverse tune plane depicted in Fig. 1.9 within a range of tune value 0.1 in every 90 turns. From the transverse tune plane depicted in Fig. 1.9, it is readily realized that several unstable high order resonance lines have been crossed. This will result in a deterioration of beam lifetime. Also, when a large chromaticity value is used, the stable area in the transverse phase space will be reduced due to the increasing contribution of nonlinearity. This is the reason why the setting shown in Fig. 4.1 is the optimum value found by operators in the main control room.

M3.07 ADJUST file 13 FASTER PBOLA - 800 GEV/SEC**2
*file dir *ch-rf *ch-plot *ch-const *ch-ramp *CH-CHROM *c
RESET(29) *calc *delete *insert *tune
*send chrom curve *original *compare

SEQ	P(GeV/c)	Horz	Vert	SEQ	P(GeV/c)	Horz	Vert
1	8.889	-10	10				
2	10.91	-25	15				
3	12.91	-25	25				
4	14.91	-35	25				
5	16.91	-35	20				
6	17.3	-35	20				
7	18.75	-25	35				
8	20.92	10	10				
9	25.92	10	10				
10	50.93	10	13				
11	75.93	14	15				
12	120	14	15				
13	150	0	0				

(injection energy)

(transition energy)

Fig. 4.1. A typical setting of chromaticity values at different beam energies during the pbar stacking cycle. From the right: the first column is the vertical chromaticity, the second one is the horizontal chromaticity, and the third one is the kinetic momentum of beam.

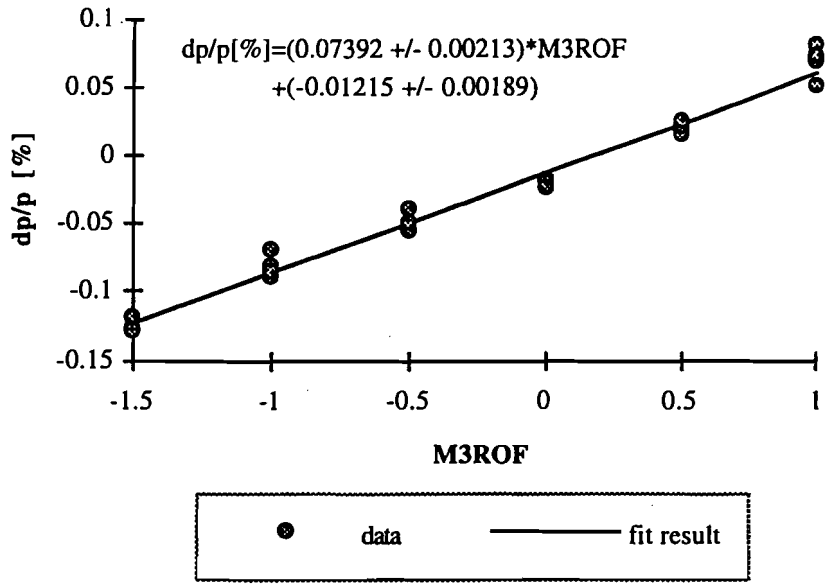

Fig. 4.2. The calibration result of fractional change in beam momentum vs. rf parameter M3ROF.

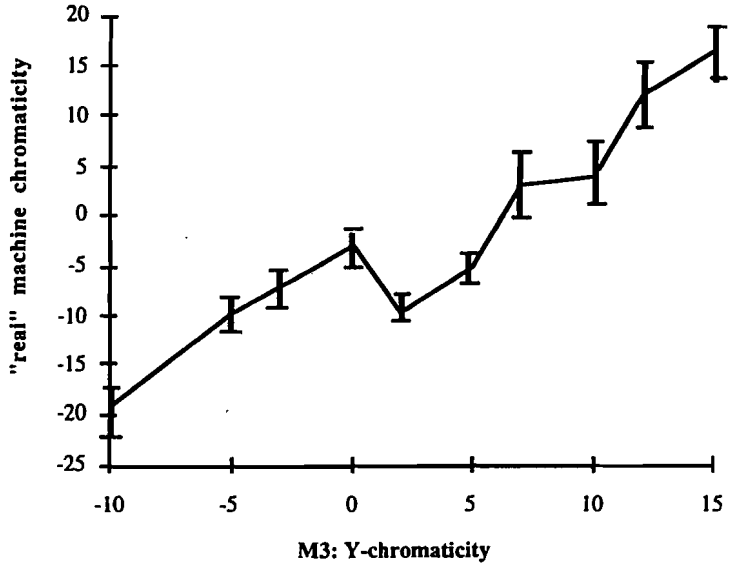

Fig. 4.3. The actual vertical chromaticity vs. the nominal value listed in the control page.

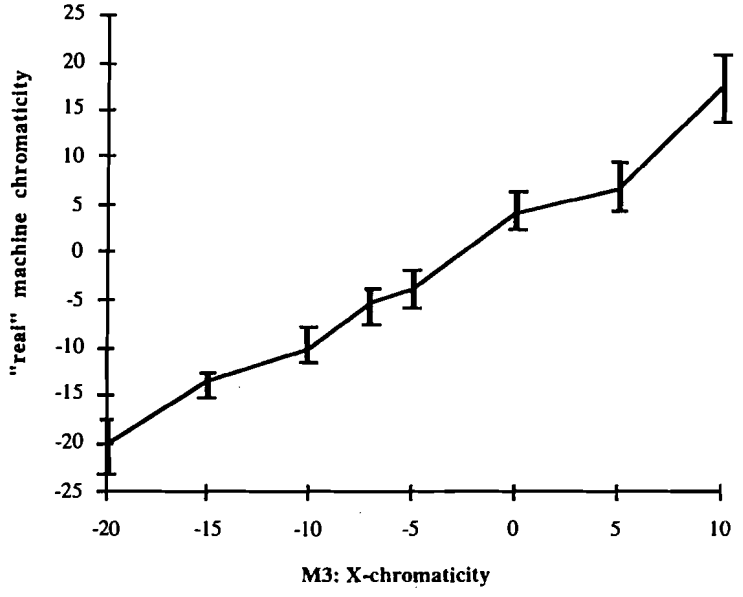

Fig. 4.4. The actual horizontal chromaticity vs. the nominal value listed in the control page.

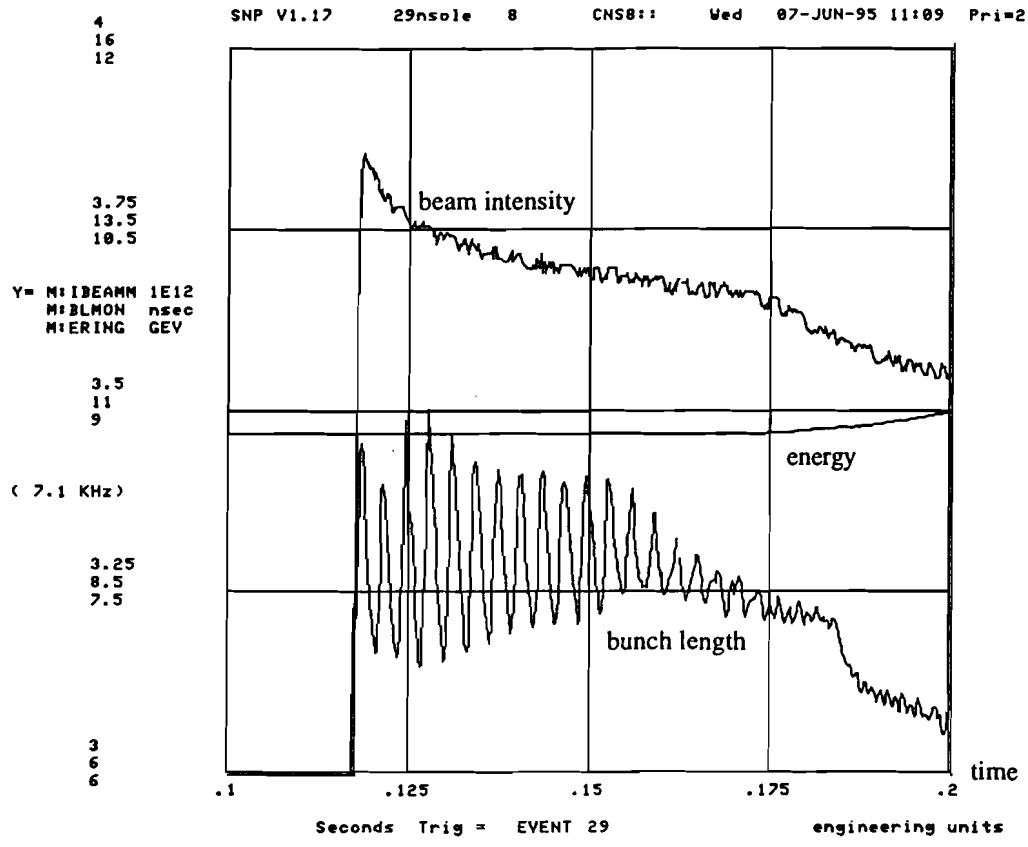

Fig. 4.5. The fast time plot of Main Ring parameters at the injection stage in a typical pbar stacking cycle.

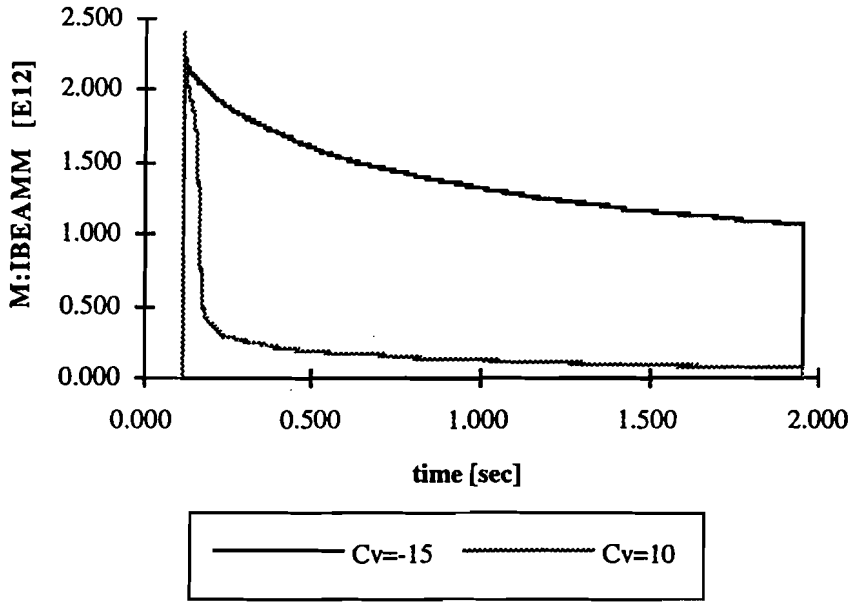

Fig. 4.6. A plot of beam intensity vs. time at the injection energy. All the transverse dampers are turned off. The solid line corresponds to the negative vertical chromaticity, and the dashed line corresponds to the positive vertical chromaticity.

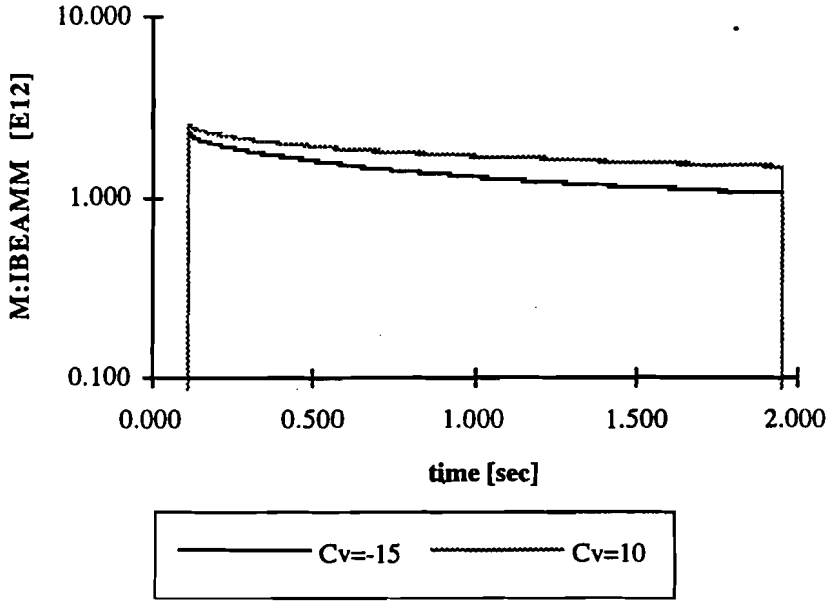

Fig. 4.7. A time plot of beam intensity at the injection energy, plotted in semi-log scale. All the transverse dampers are on. The solid line corresponds to the negative vertical chromaticity, and the dashed line corresponds to the positive vertical chromaticity.

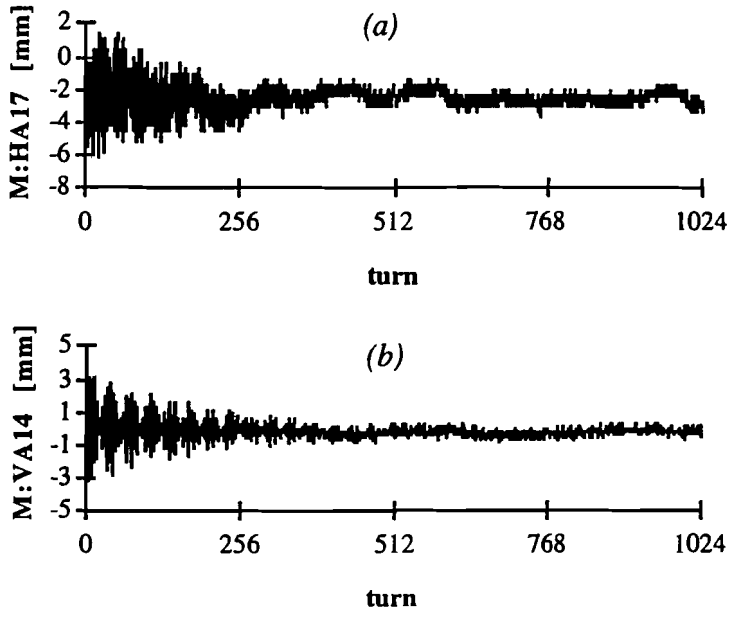

Fig. 4.8. The turn-by-turn display of transverse beam position triggered right after the injection of beams into the Main Ring *(a)* the horizontal plane *(b)* the vertical plane. The vertical super damper is on and both slow dampers are off. The total beam intensity is 7 $\times 10^{11}$ protons.

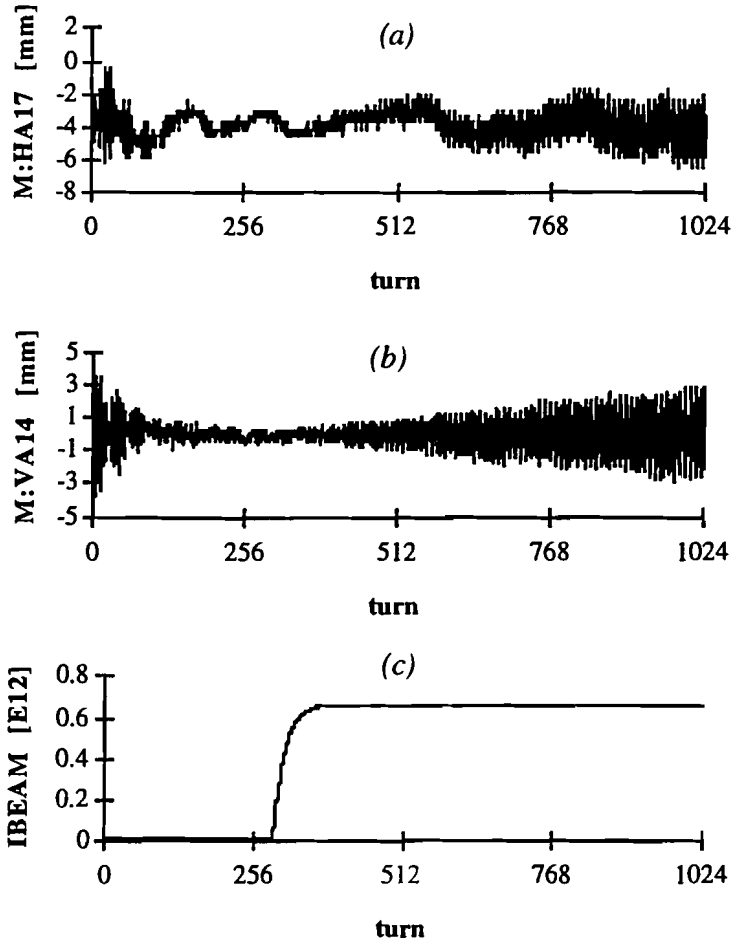

Fig. 4.9. The turn-by-turn display of transverse beam position triggered right after the injection of beams into the Main Ring *(a)* the horizontal plane *(b)* the vertical plane *(c)* the plot of total beam intensity, where the time delay is caused by the risetime of low-pass filters and the delay in the readout system of DC current transformer. The vertical super damper is off and both slow dampers are on. The total beam intensity is 7×10^{11} protons.

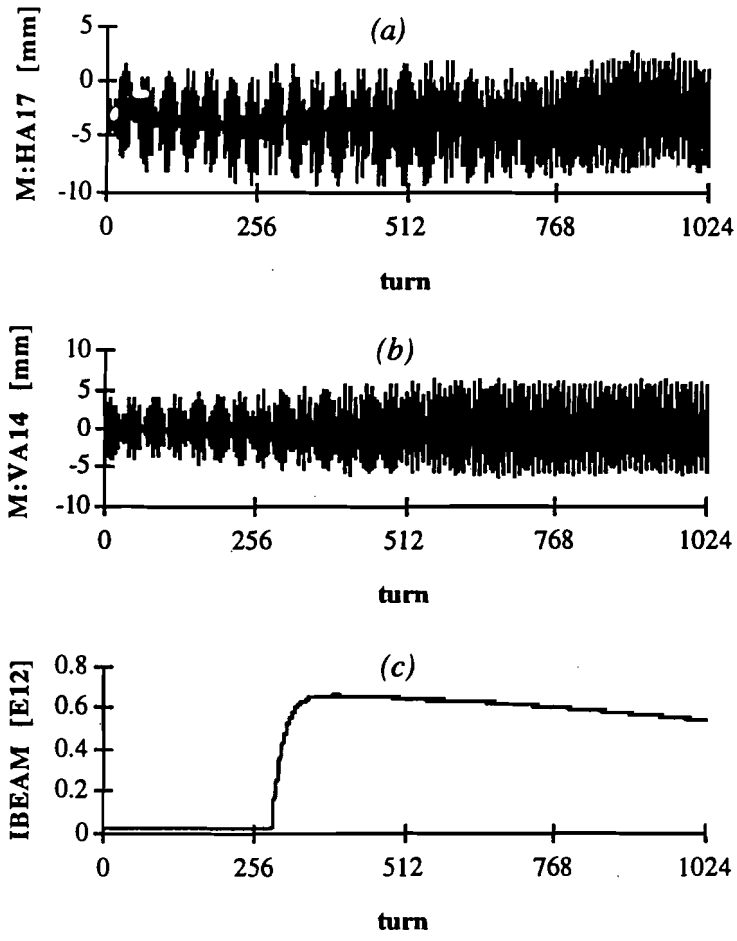

Fig. 4.10. The turn-by-turn display of transverse beam position triggered right after the injection of beams into the Main Ring *(a)* the horizontal plane *(b)* the vertical plane *(c)* the plot of total beam intensity. All transverse dampers are off. The total beam intensity is 7×10^{11} protons at injection, then gradually drops due to beam loss.

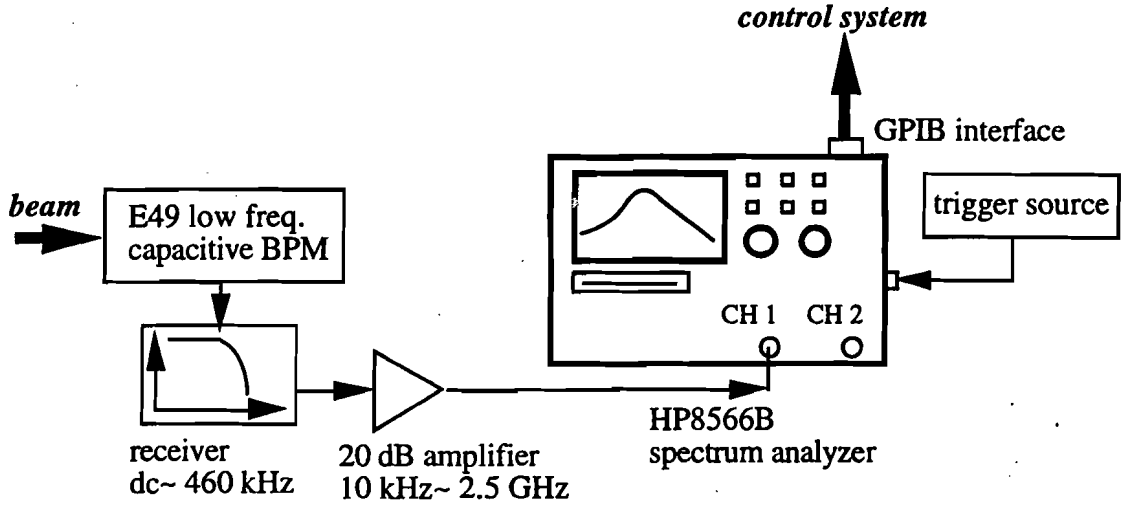

Fig. 4.11. The experimental setup for the measurements of vertical beam oscillation in the low frequency range.

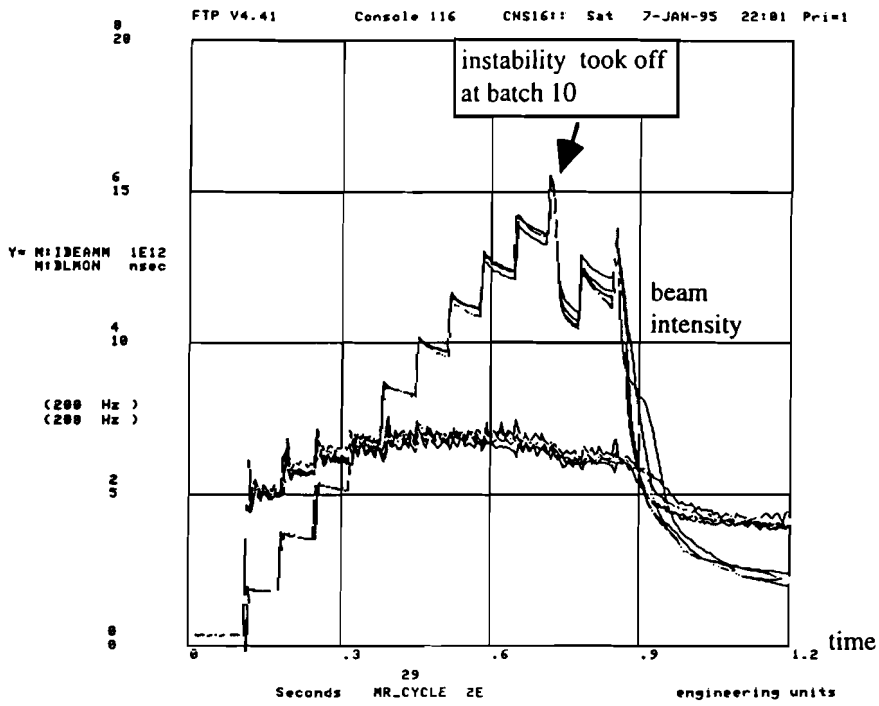

Fig. 4.12. The fast time plot of 12 batches injected into the Main Ring with both vertical dampers on. The upper trace is the total beam intensity (m:ibeamm), and the lower trace is the bunch length (m:blmon). The chromaticity is set close to zero in both the horizontal and vertical planes.

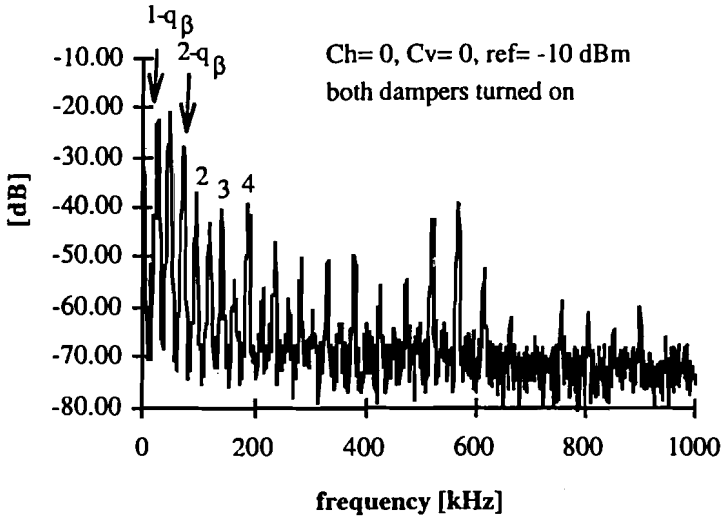

Fig. 4.13. The vertical beam spectrum of 12 batches in the Main Ring, both the vertical dampers are on and chromaticity≈ 0. The spectrum analyzer is set to: resolution and video bandwidth= 3 and 10 kHz respectively, sweep time= 0.3 sec, triggered after the injection of batch 12.

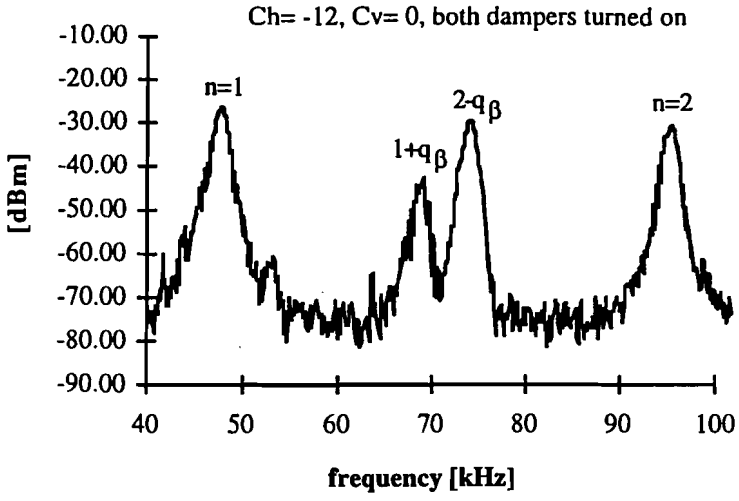

Fig. 4.14. A zoom-in picture of the vertical beam spectrum, both vertical dampers are on, vertical chromaticity≈ 0, and horizontal chromaticity≈ -12. The spectrum analyzer is set to: resolution and video bandwidth= 1 kHz respectively, sweep time= 0.3 sec, triggered at the injection of the 11th batch.

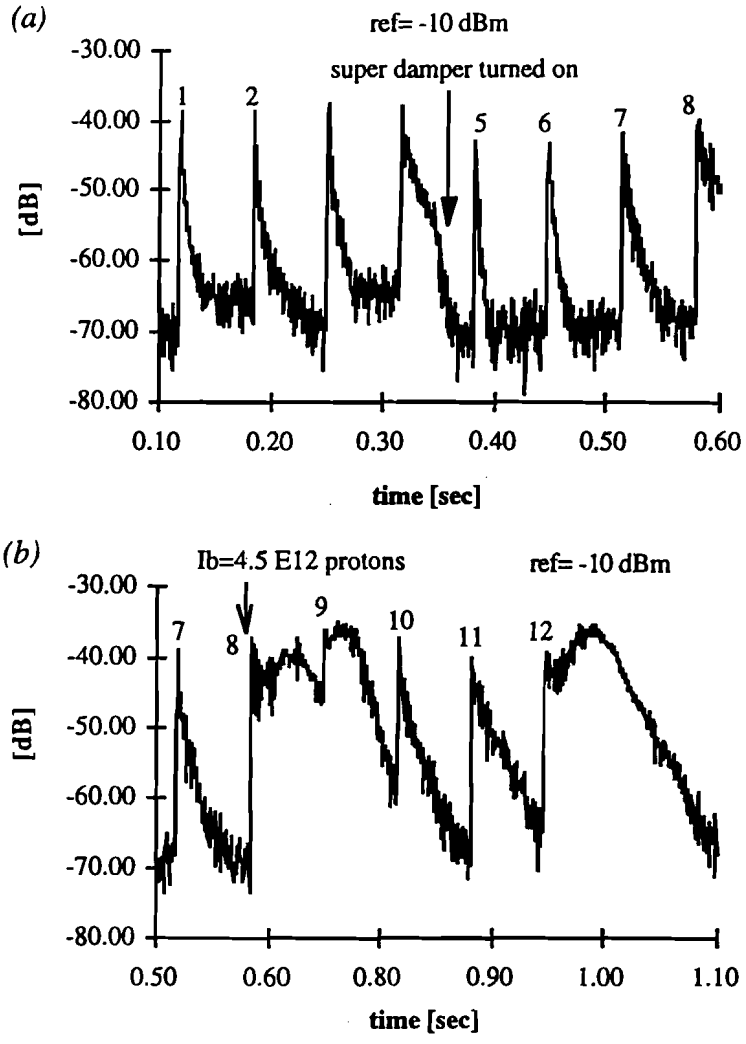

Fig. 4.15. The oscillation amplitude of the 1- q_β betatron sideband vs. time, the slow damper is off and the super damper is on after the injection of the fourth batch *(a)* the injection from batch 1 to batch 7 *(b)* the injection from batch 7 to batch 12. The spectrum analyzer is set to: resolution and video bandwidth= 3 kHz respectively, frequency span= 0 Hz, center frequency= 25.5 kHz.

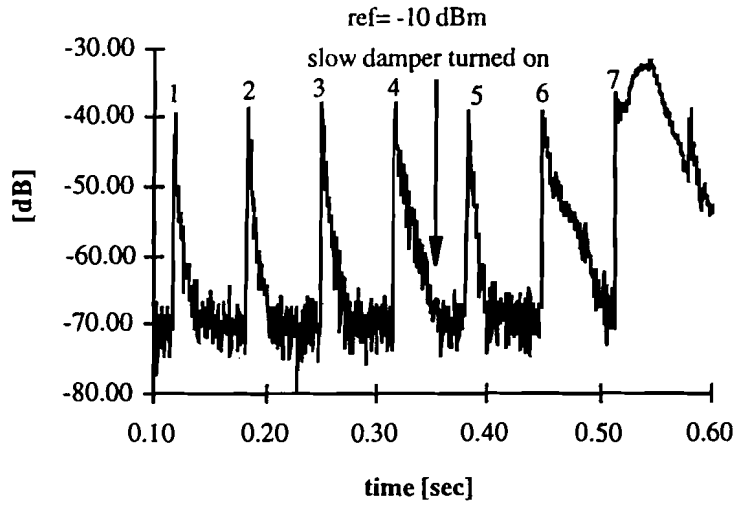

Fig. 4.16. The oscillation amplitude of the 1- q_β betatron sideband vs. time, the super damper is off and the slow damper is on after the injection of the fourth batch. The spectrum analyzer is set to: resolution and video bandwidth= 3 kHz respectively, frequency span= 0 Hz, center frequency= 25.5 kHz.

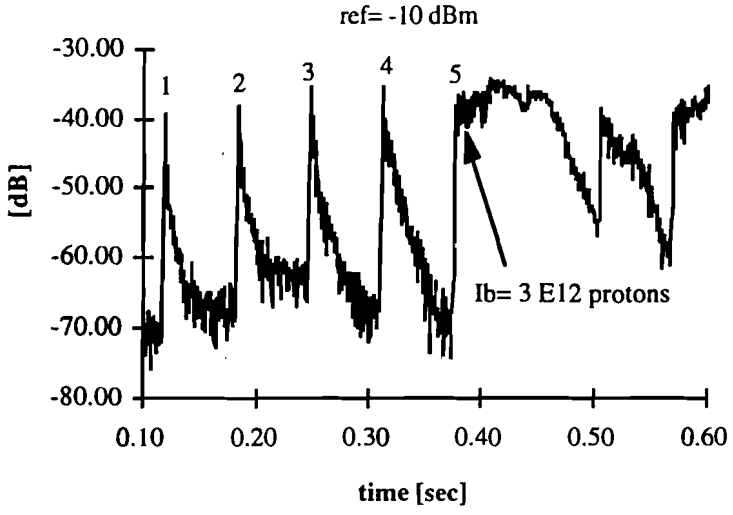

Fig. 4.17. The oscillation amplitude of the 1- q_β betatron sideband, both vertical dampers are off, and vertical chromaticity≈ 0. The spectrum analyzer is set to: resolution bandwidth and video bandwidth= 3 kHz respectively, frequency span= 0 Hz, center frequency= 25.5 kHz.

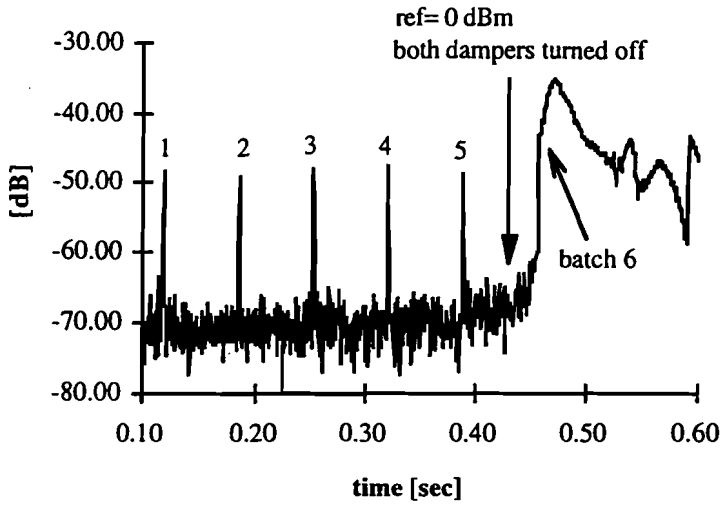

Fig. 4.18. The oscillation amplitude of the 1- q_β betatron sideband vs. time for a beam intensity of 4×10^9 protons per bunch. The spectrum analyzer is set to: resolution and video bandwidth= 3 kHz respectively, frequency span= 0 Hz, center frequency= 25.5 kHz.

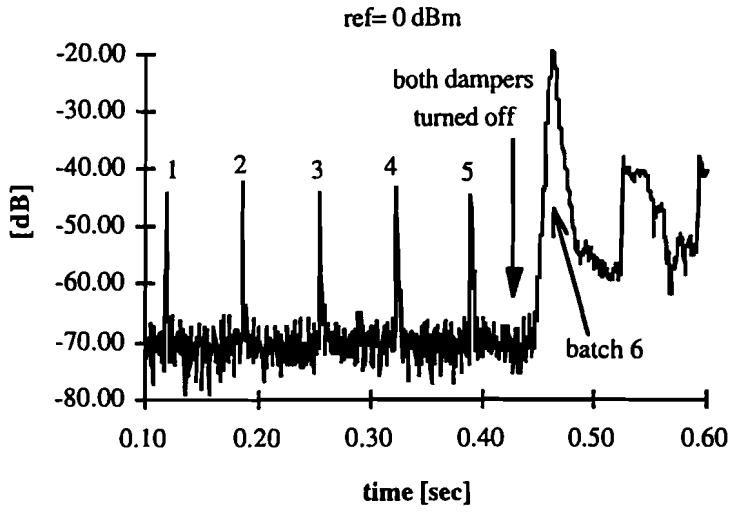

Fig. 4.19. The oscillation amplitude of the 1- q_β betatron sideband vs. time for a beam intensity of 8×10^9 protons per bunch.

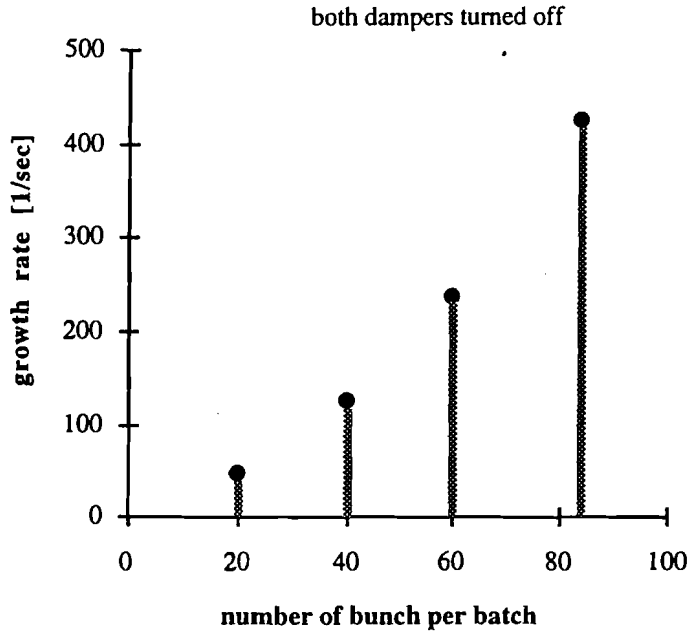

Fig. 4.20. The dependence of growth rate on the total number of beam bunch. Each data point is the averaged result of four repetitive measurements. The averaging process is performed internally by the spectrum analyzer, no error bar is available.

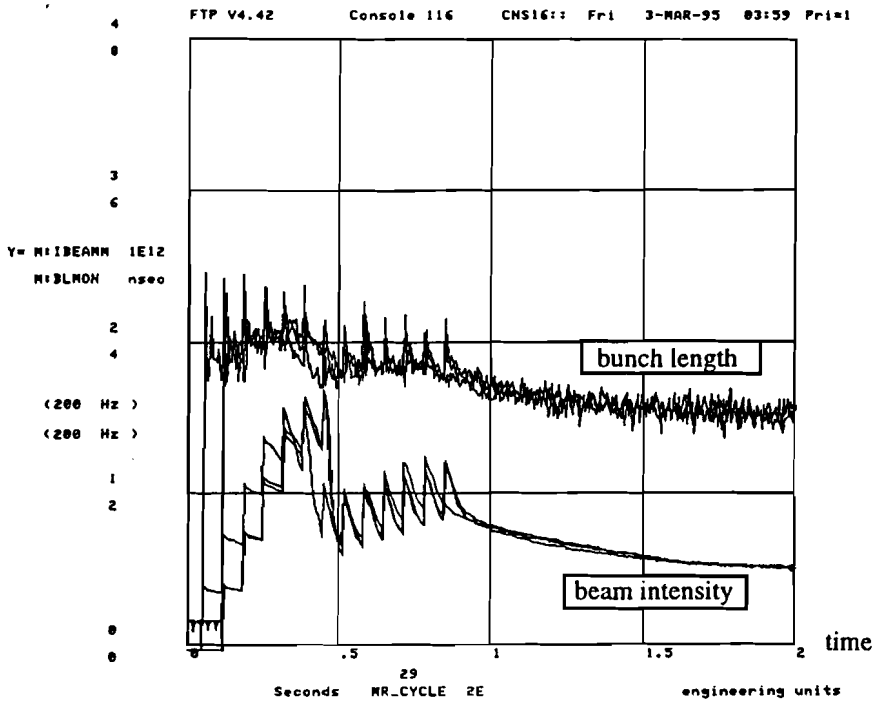

Fig. 4.21. The fast time plot of Main Ring parameters for rf voltage= 1.5 MV, both vertical dampers are turned on from the start until the injection of batch 6. The parameter m:ibeamm denotes the total beam intensity in units of 1×10^{12} protons, and m:blmon denotes the bunch length in units of [nsec].

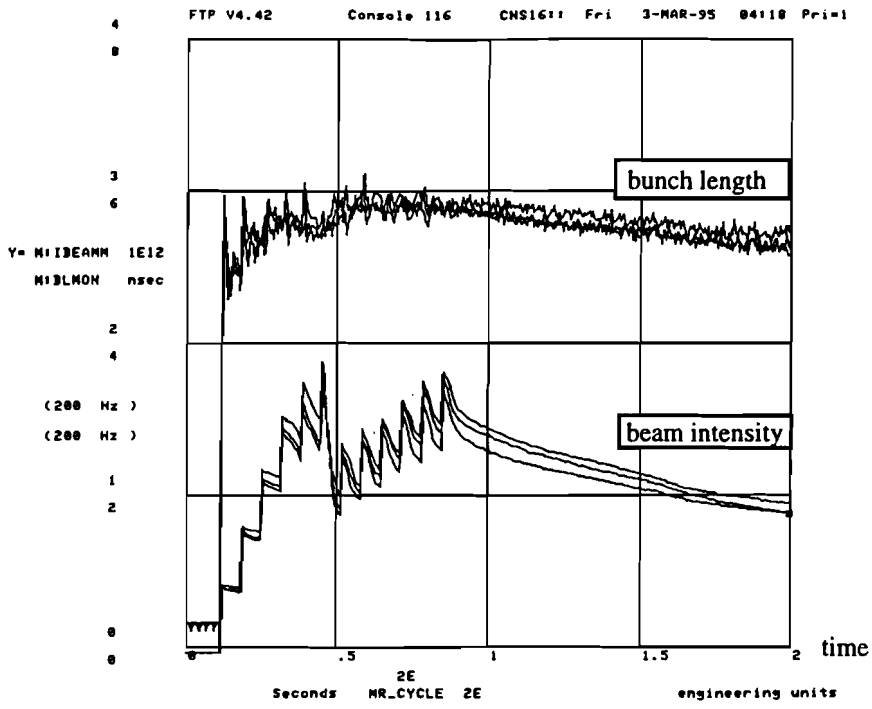

Fig. 4.22. The fast time plot of Main Ring parameters for rf voltage= 0.5 MV, both vertical dampers are turned on from the start until the injection of batch 6.

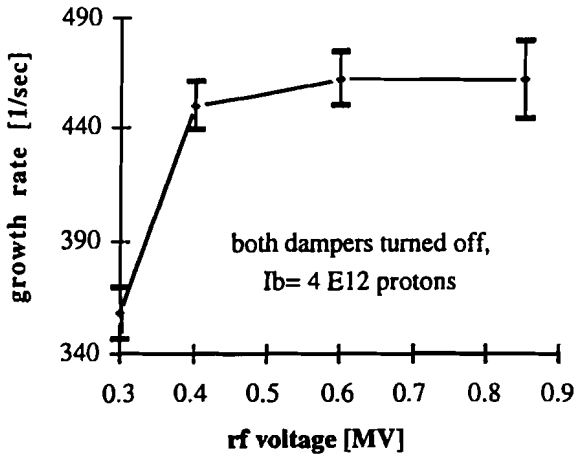

Fig. 4.23. The growth rate of vertical betatron oscillation vs. rf voltage of the Main Ring.

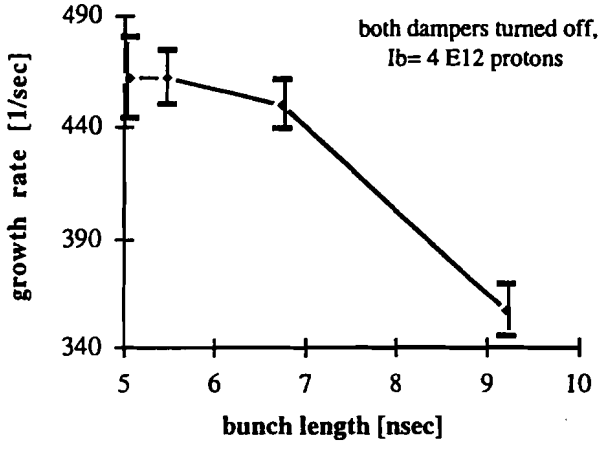

Fig. 4.24. The growth rate of vertical betatron oscillation vs. bunch length.

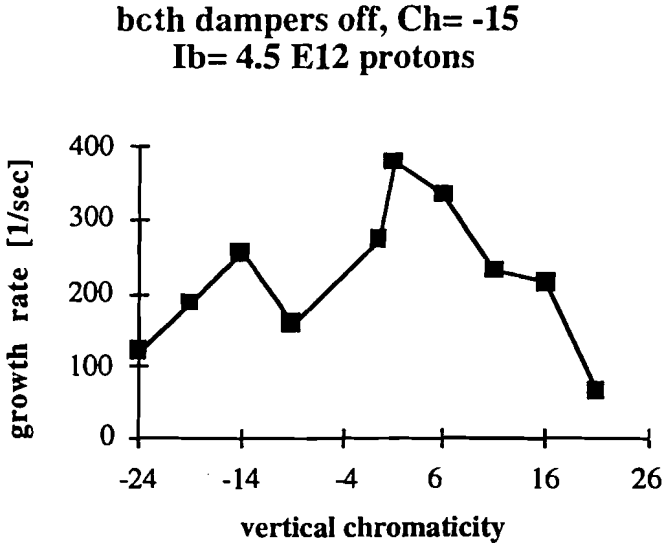

Fig. 4.25. The growth rate of vertical instability measured at different chromaticity values. Each data point is the averaged result of four repetitive measurements. The averaging process is performed by the spectrum analyzer internally, no error bar is available.

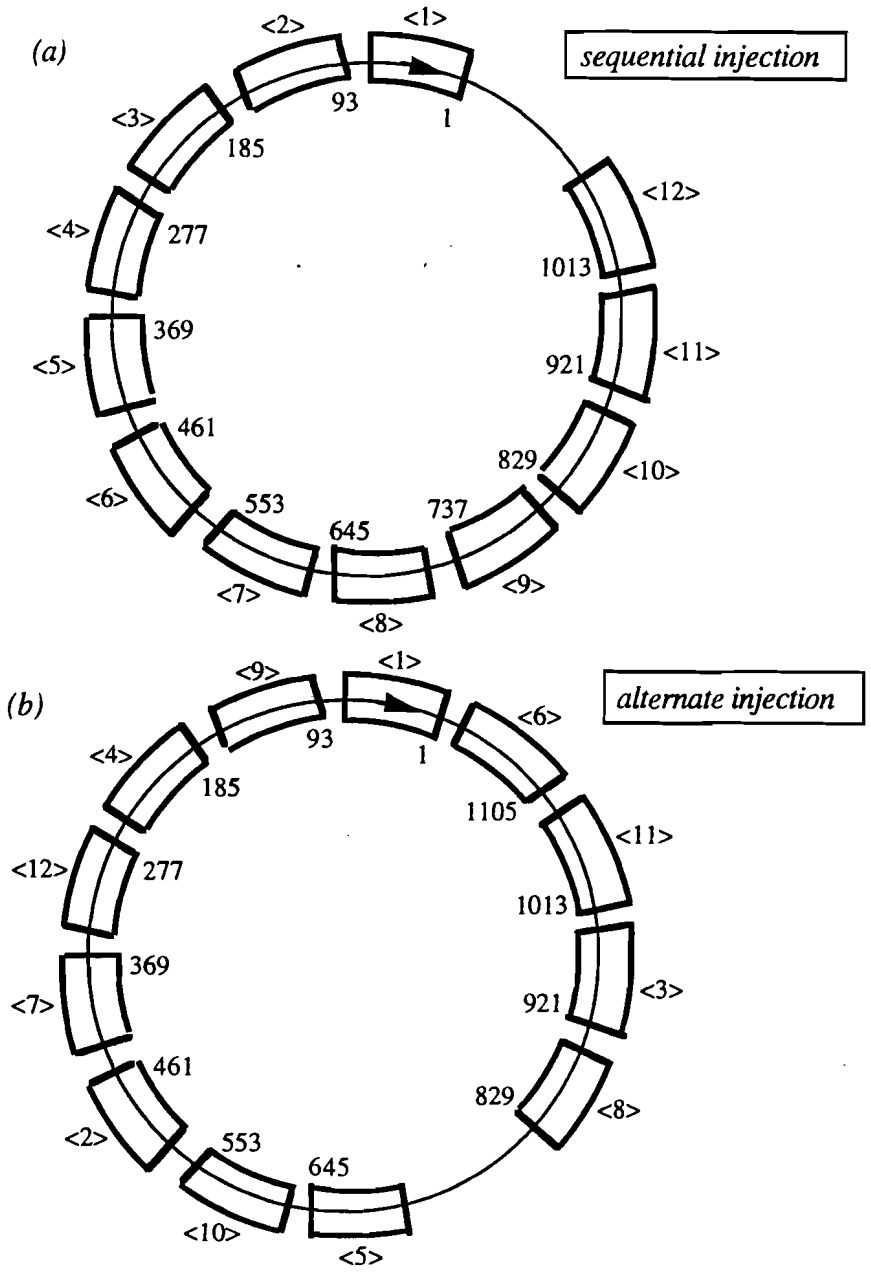

Fig. 4.26. An exaggerated sketch of the batch configuration in the Main Ring for two different injection schemes. Each segment represents one booster batch of 84 beam bunches. The label of the first bunch in every batch is shown by the numbers inside the circle, and the label of each booster batch corresponding to their injection sequence is denoted by the number inside the bracket.

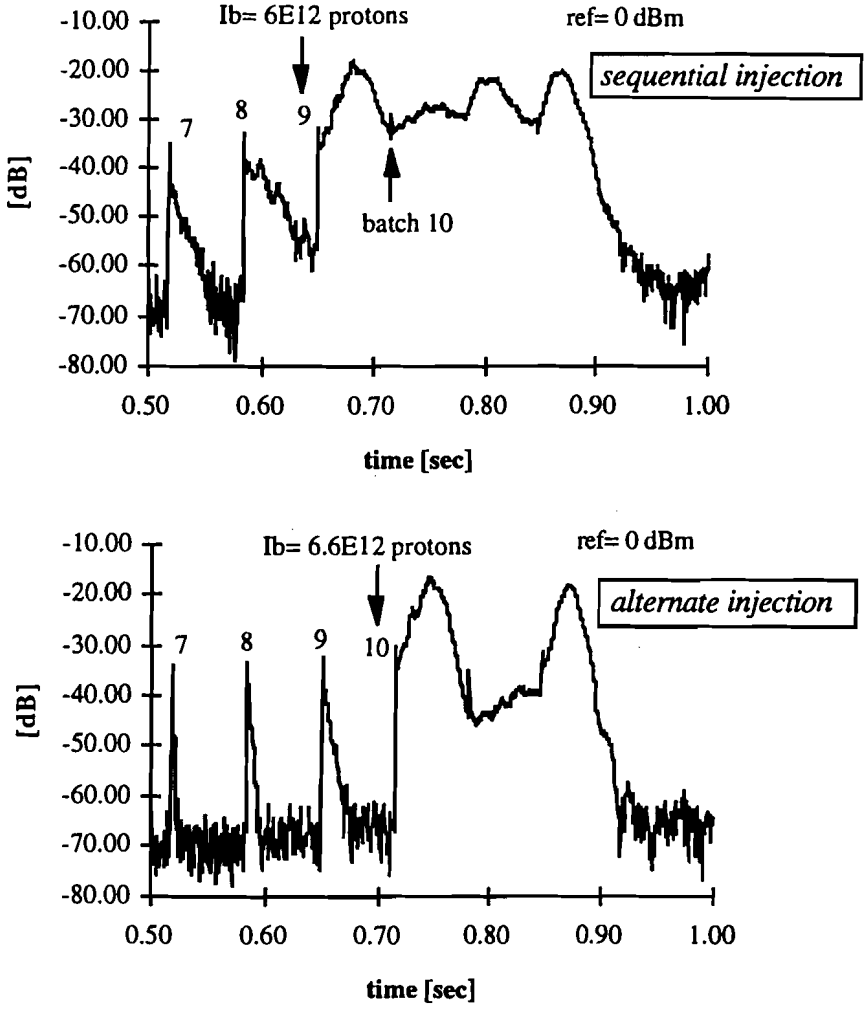

Fig. 4.27. The growth of betatron amplitude vs. time for different injection schemes. The spectrum analyzer is set to: center frequency= 25.5 kHz, resolution and video bandwidth= 3 kHz respectively, and frequency span= 0 Hz. Both vertical dampers are turned on during the measurements.

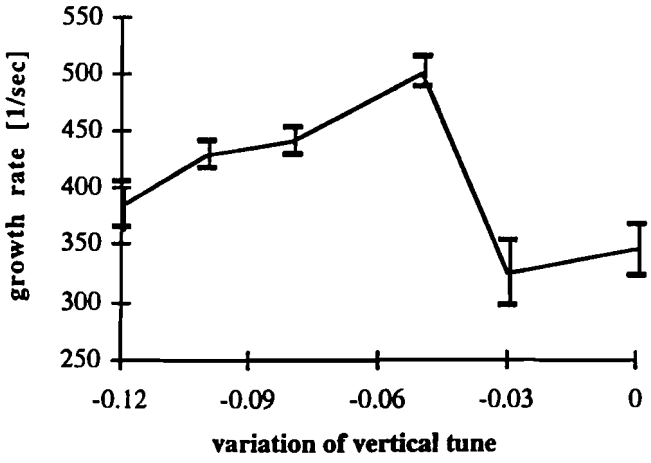

Fig. 4.28. The growth rate vs. the change of vertical betatron tune.

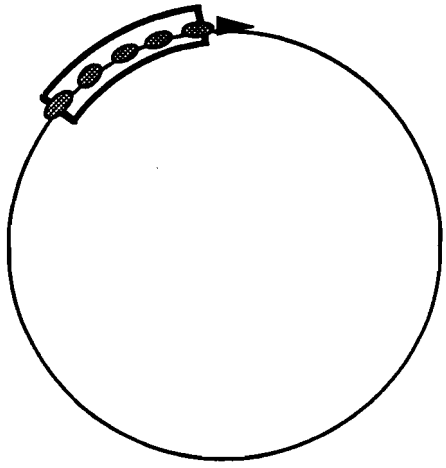

Fig. 4.29. A schematic sketch for the bunch configuration of the pbar stacking cycle during the Collider Run I from 1992 to 1995. Only one booster batch of 84 proton bunches is injected into the Main Ring.

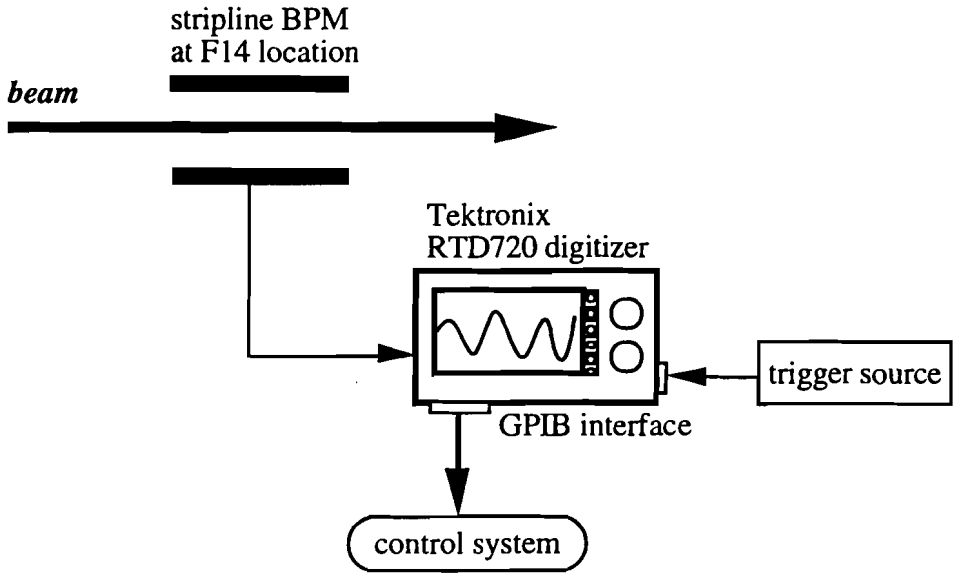

Fig. 4.30. The experimental setup for recording the time evolution of vertical oscillation of one short bunch train in the Main Ring.

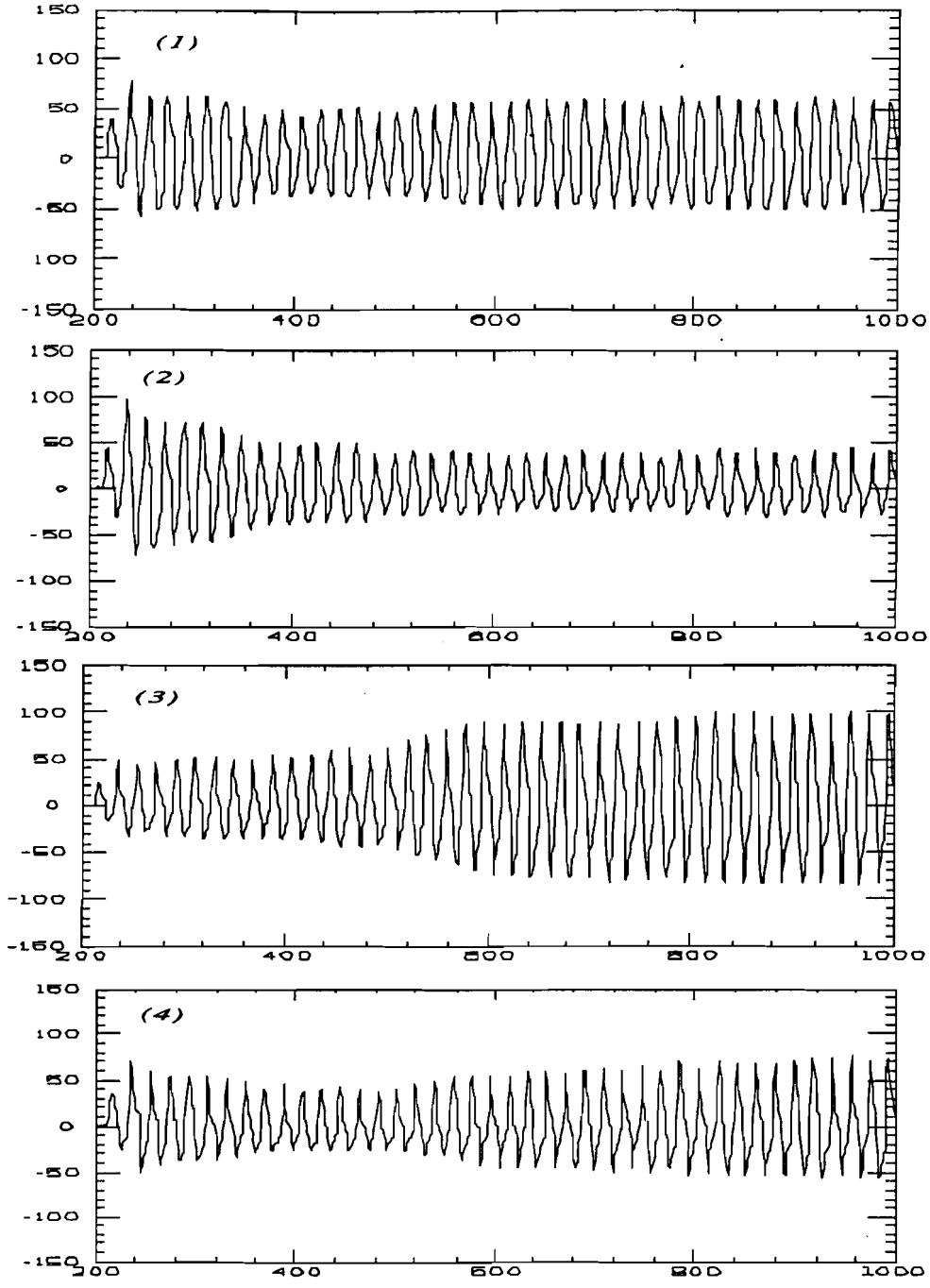

Fig. 4.31. The time plots of vertical bunch oscillation for one short bunch train in the Main Ring during the pbar stacking cycle, horizontal unit= 1nsec, triggered at *(1)* the first turn after the injection into the Main Ring *(2)* the 12th turn *(3)* the 18th turn *(4)* the 69th turn.

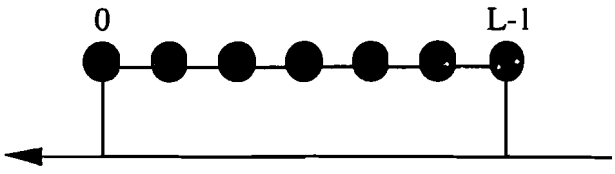

Fig. 4.32. The nomenclature of bunch index for a short bunch train of L bunches.

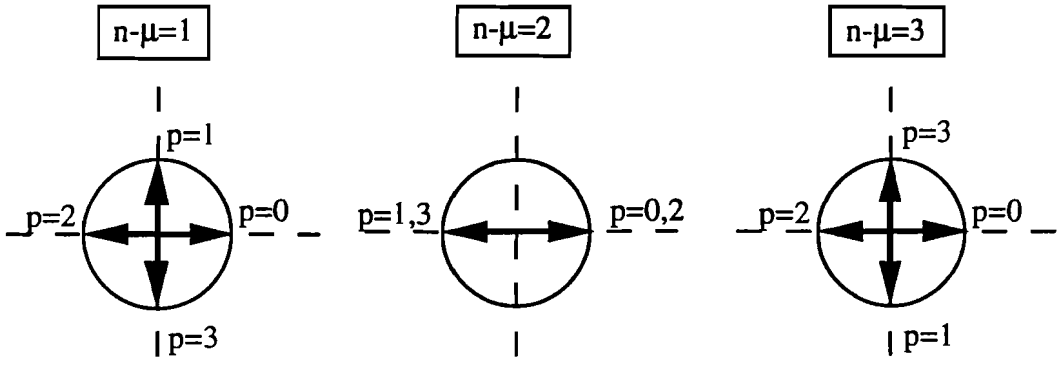

Fig. 4.33. The vector sum of induced signals from four equal bunches undergoing coupled bunch oscillation. This depicts the resulting signal for those spectral lines not corresponding to the coherent frequency and its alias. A complete cancellation of induced signals is demonstrated for the case of equally spaced, equal bunches.

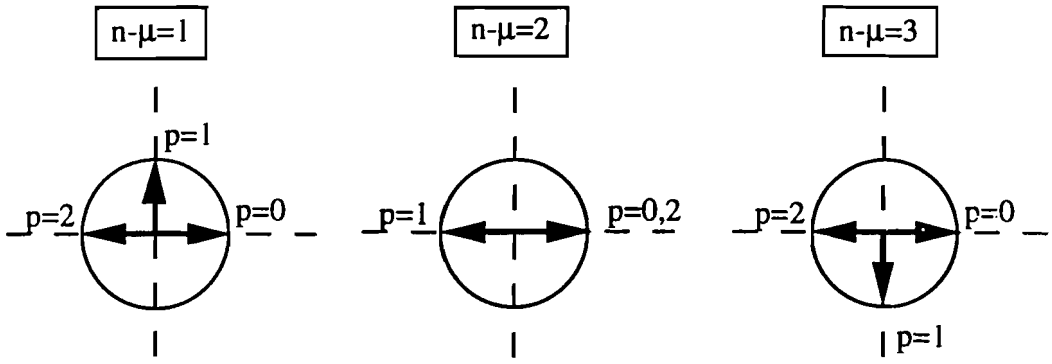

Fig. 4.34. The vector sum of induced signals from a bunch train of three equal bunches undergoing coupled bunch oscillation. This depicts the resulting signal for those spectral lines not corresponding to the coherent frequency and its alias. An incomplete cancellation of induced signals is demonstrated for the case of one short bunch train.

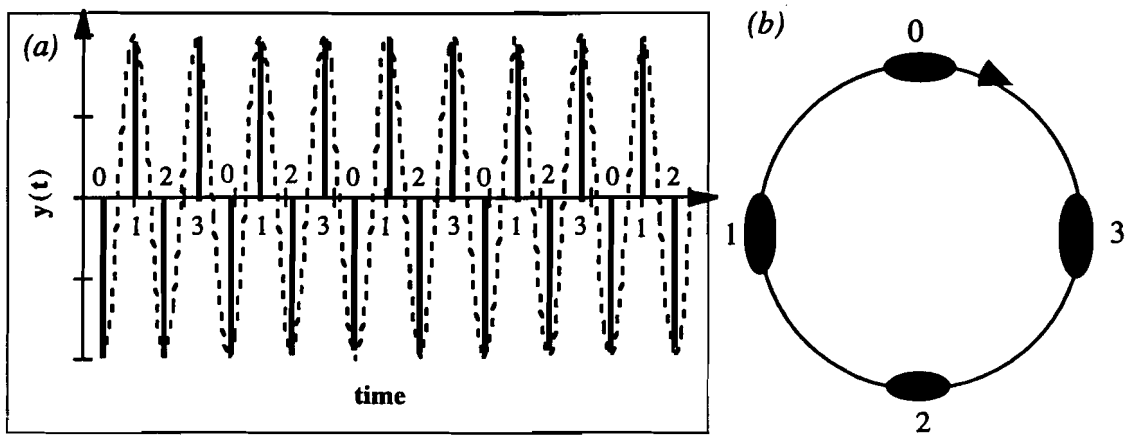

Fig. 4.35. The transverse coupled bunch oscillation observed by a BPM *(a)* the signal induced by a train of four equally spaced, equal intensity bunches in a circular accelerator *(b)* the configuration of the bunch train. The first bunch is labeled by index 0, and the last bunch is labeled by index 3. Each bunch induces a delta-function like pulse on the transverse BPM. The dashed line depicts the envelope of bunch oscillation.

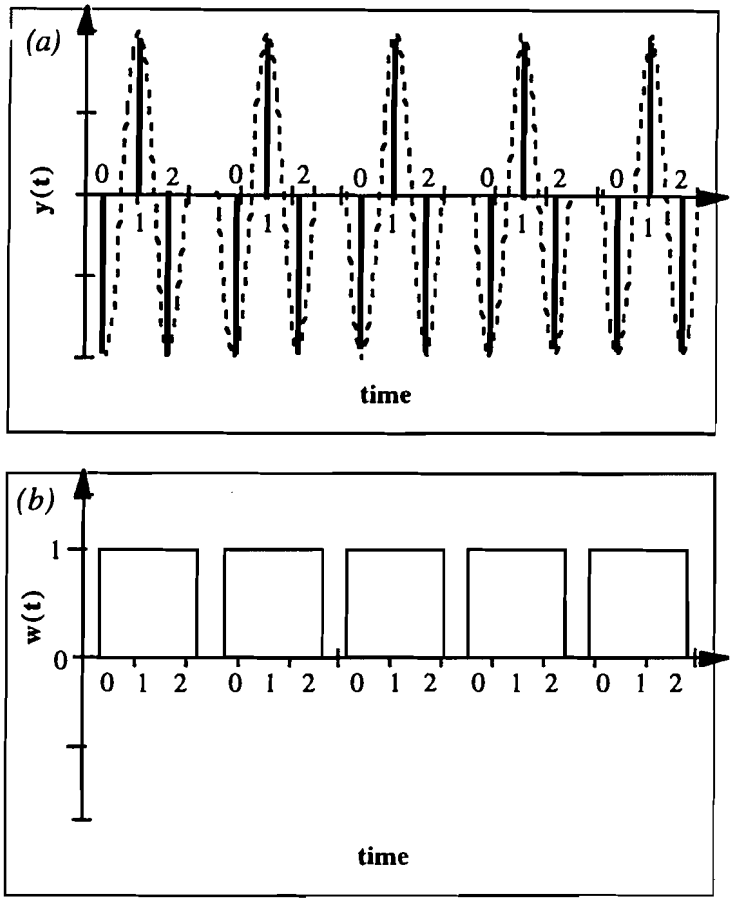

Fig. 4.36. The transverse coupled bunch oscillation of a short bunch train observed by a BPM *(a)* the signal induced by a bunch train which is comprised by three equal bunches in a circular accelerator *(b)* the periodic window function which causes the resulting signal as depicted in *(a)*. The bunch index is labeled beneath the horizontal axis.

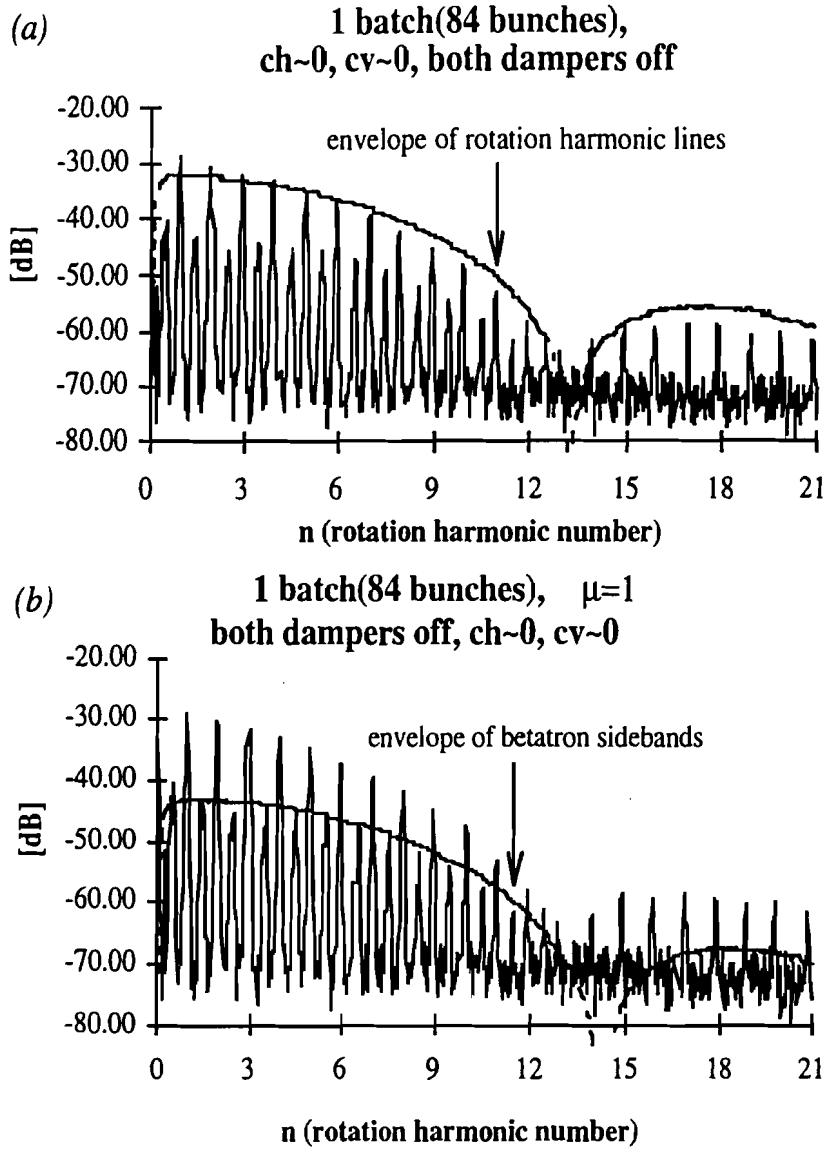

Fig. 4.37. The fit of calculated spectral envelope to the measured vertical beam spectrum of a short bunch train comprised of 84 beam bunches *(a)* the calculated spectral envelope of revolution harmonic lines caused by closed orbit offset *(b)* the calculated spectral envelope of betatron sidebands caused by coupled bunch oscillation. The coherent phase of coupled bunch motion is fitted to be $2\pi/1113$. The spectrum analyzer is set to: resolution and video bandwidth= 3 and 10 kHz respectively, sweep time= 0.3 [sec], average= 5.

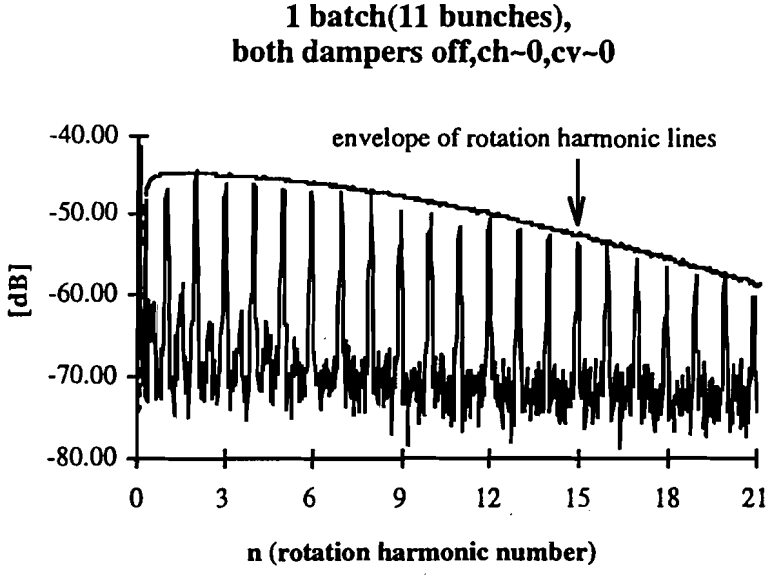

Fig. 4.38. The fit of calculated spectral envelope to the measured vertical beam spectrum for a short bunch train comprised of 11 beam bunches. The spectrum analyzer is set to: resolution and video bandwidth= 3 and 10 kHz respectively, sweep time= 0.3 [sec], average= 6.

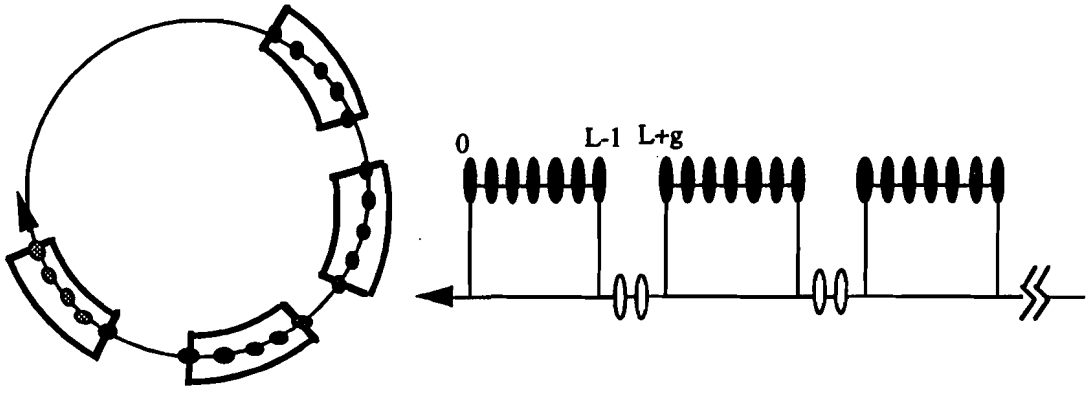

Fig. 4.39. The nomenclature of bunch index for the multibatch operation in the Main Ring. The open circles represent the empty rf buckets between adjacent bunch trains, and the dark circles represent the proton bunches in each batch.

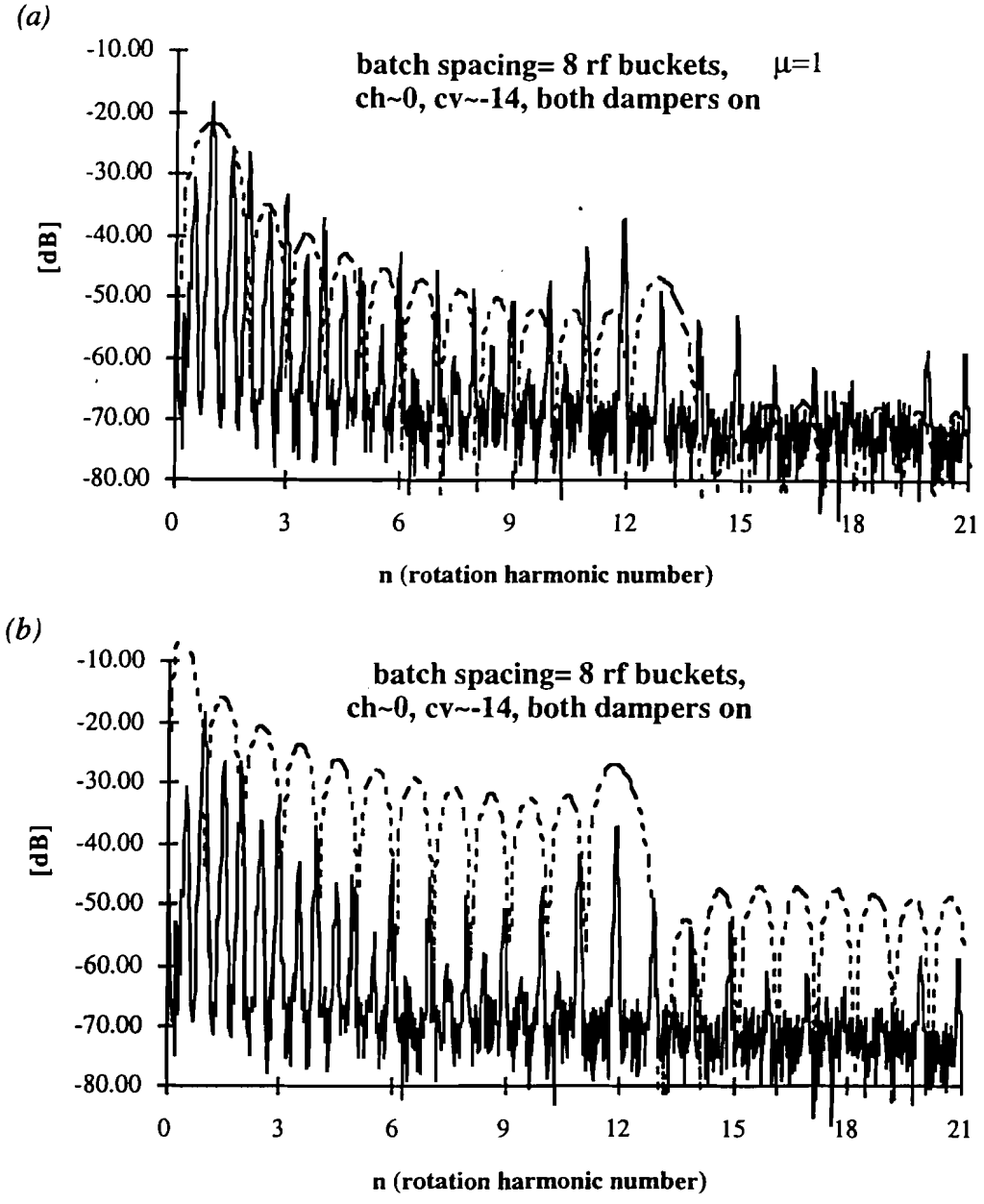

Fig. 4.40. The fit of calculated spectral envelope to the measured beam spectrum, the dashed line is the calculated spectral envelope *(a)* the spectral envelope of betatron sidebands *(b)* the spectral envelope of revolution harmonic lines. The spectrum analyzer is set to: resolution and video bandwidth= 3 and 10 kHz respectively, sweep time= 0.3 [sec], triggered after the injection of batch 12. There are 12 batches, each containing 84 bunches. The vertical chromaticity is around -14, and both vertical dampers are on.

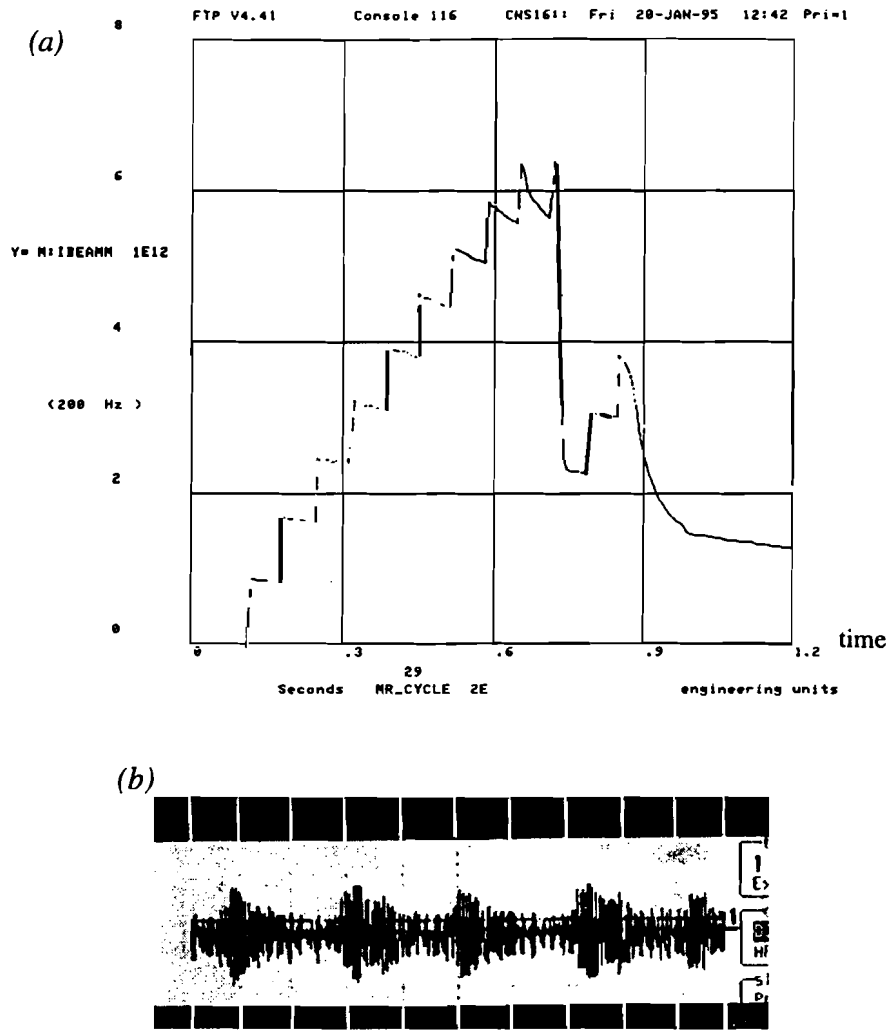

Fig. 4.41. The signal of vertical coupled bunch instability in the time domain (a) the total beam intensity vs. time (b) the vertical difference signal observed by a stripline BPM with a digital oscilloscope (LeCroy 9354L) of 500 MHz bandwidth and 8 MB memory, horizontal division= 10 μs, triggered at 0.86 sec. Both vertical dampers are on, vertical chromaticity≈ -14, and horizontal chromaticity≈ 0.

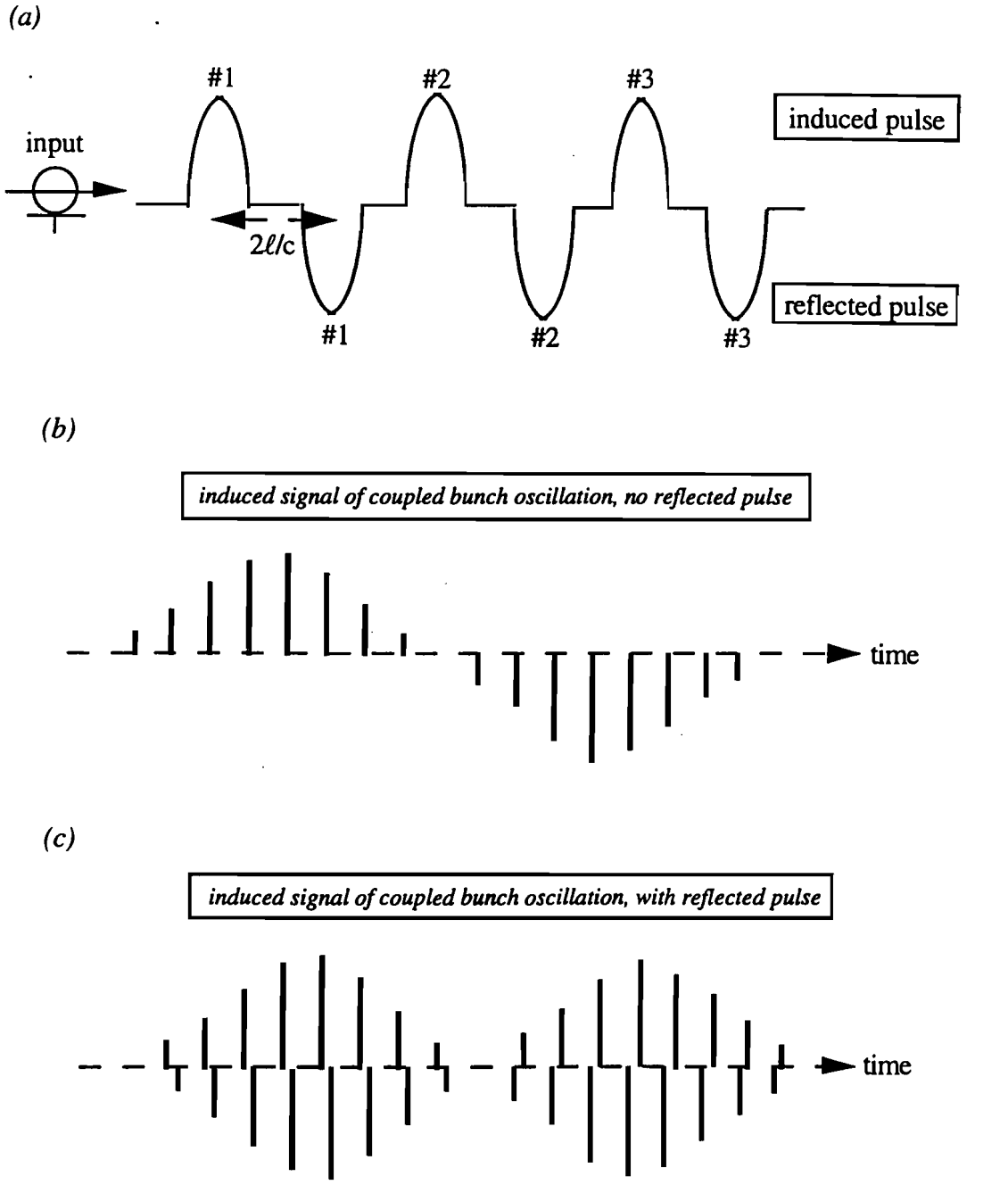

Fig. 4.42. The electrical response of a stripline BPM to a train of bunches *(a)* the induced voltage pulses on the electrode *(b)* the theoretical response of a stripline BPM to a train of bunches undergoing coupled bunch oscillation *(c)* the actual response of a stripline BPM to a train of bunches undergoing coupled bunch oscillation.

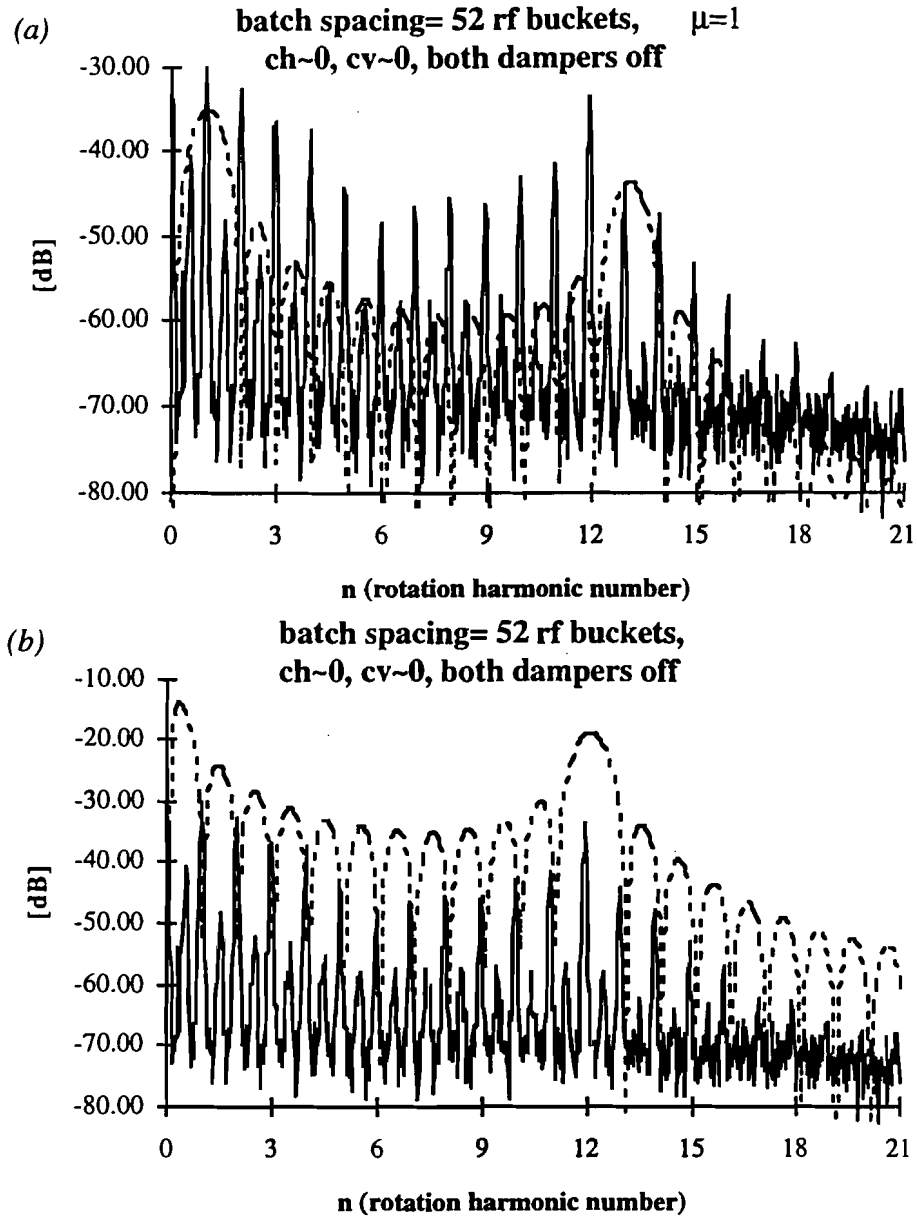

Fig. 4.43. The fit of calculated spectral envelope to the measured beam spectrum, the dashed line is the calculated spectral envelope *(a)* the spectral envelope of betatron sidebands *(b)* the spectral envelope of revolution harmonic lines. The spectrum analyzer is set to: resolution and video bandwidth= 3 and 10 kHz respectively, sweep time= 0.3 [sec], triggered after the injection of batch 12. There are 12 batches of beam, each containing 40 bunches. The vertical chromaticity is around 0, and both vertical dampers are off.

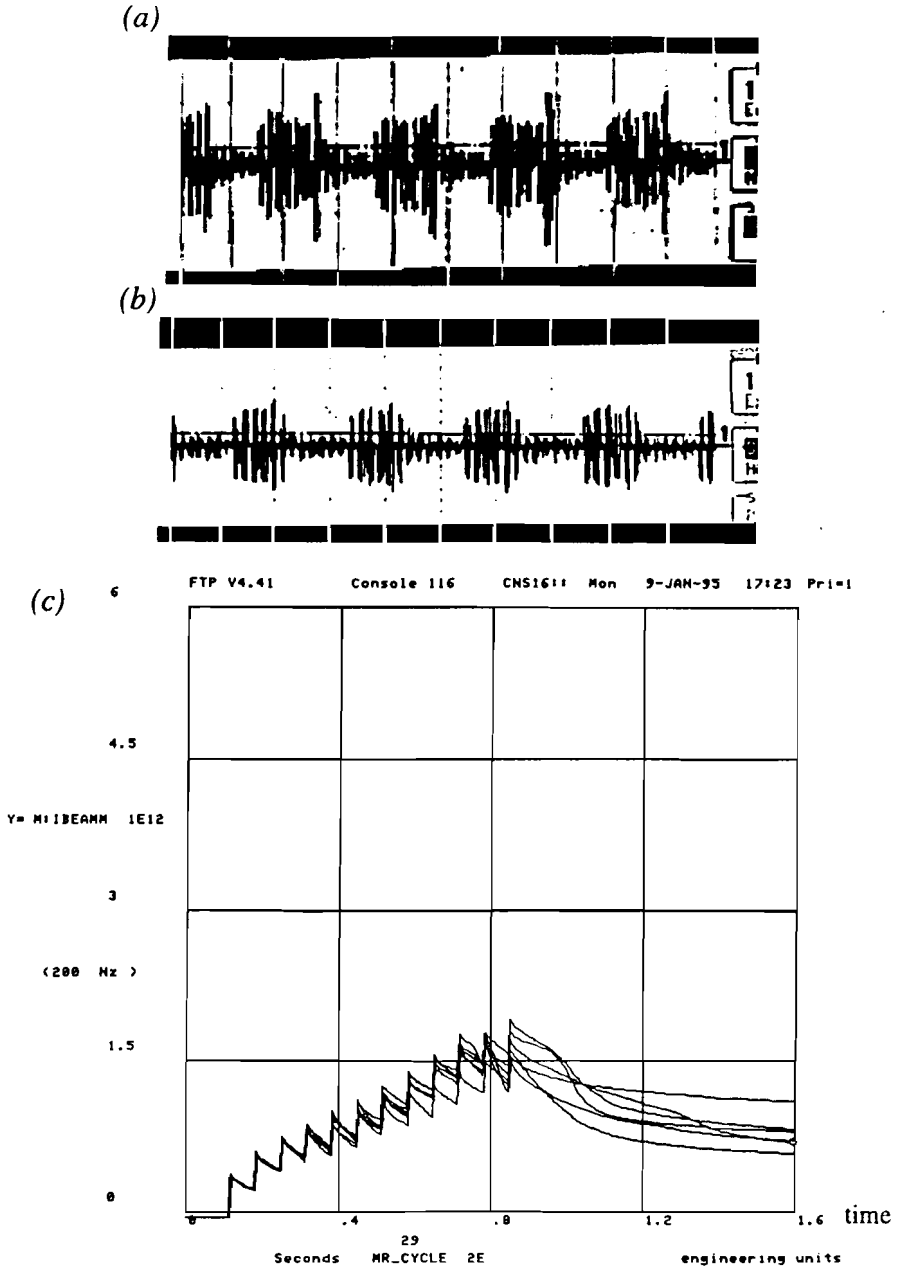

Fig. 4.44. The vertical coupled bunch oscillation in the time domain for five consecutive turns *(a)* both vertical dampers are off, horizontal division= 10 μs, vertical division= 50 mV, triggered at 0.86 sec *(b)* both vertical dampers are on, horizontal division= 10 μs, vertical division= 0.1 V, triggered at 0.86 sec *(c)* the total beam intensity vs. time. There are 12 booster batches of beams, each batch containing 40 proton bunches, both the vertical and the horizontal chromaticity are set close to zero.

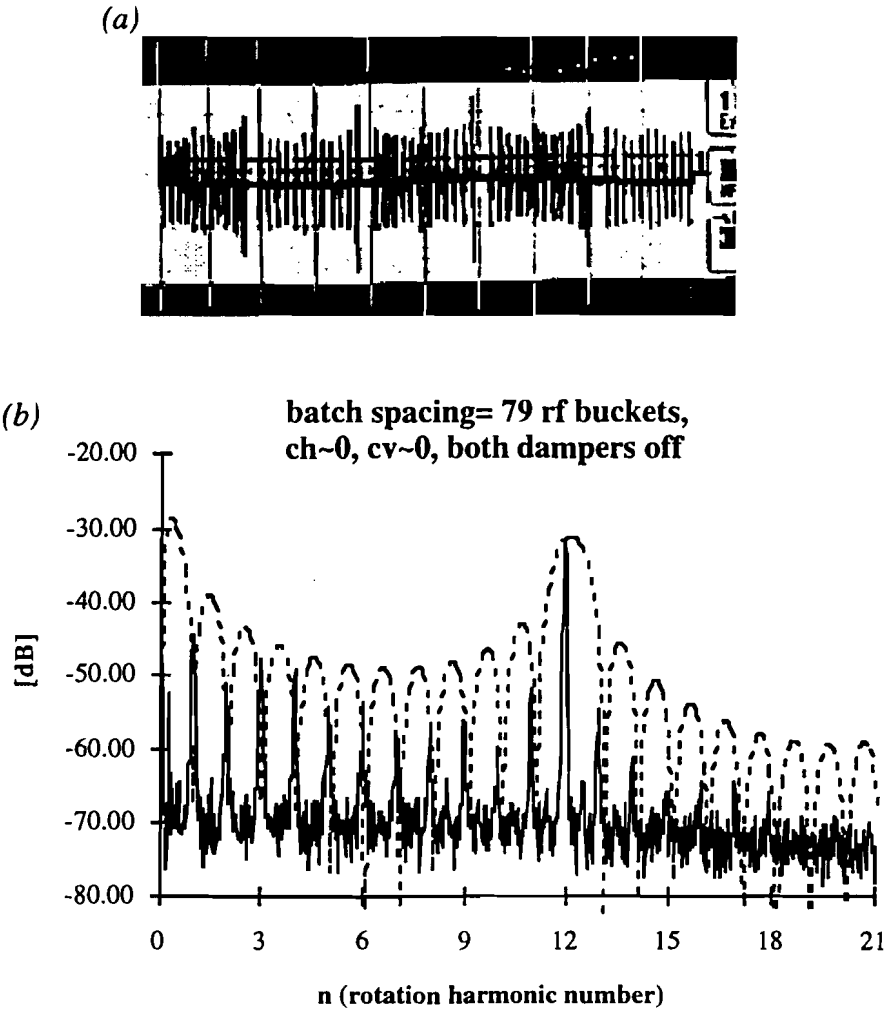

Fig. 4.45. The vertical coupled bunch oscillation observed in both the frequency domain and the time domain *(a)* the vertical coupled bunch oscillation in the time domain, horizontal division= 10 μs *(b)* the measured vertical beam spectrum, the dashed line is the calculated spectral envelope of revolution harmonic lines.

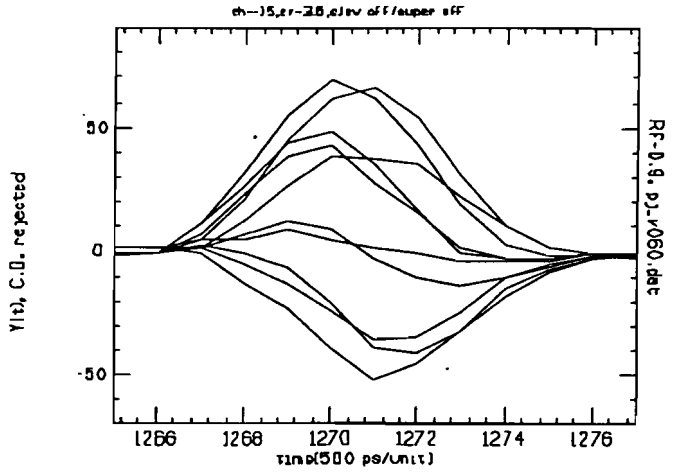

Fig. 4.46. The overlay plot of the m= 0 mode vertical head-tail oscillation for ten consecutive turns, horizontal unit= 0.5 nsec. Both vertical dampers are off, vertical chromaticity≈ 0, bunch length≈ 5 nsec, and beam intensity= 1×10^{10} protons per bunch.

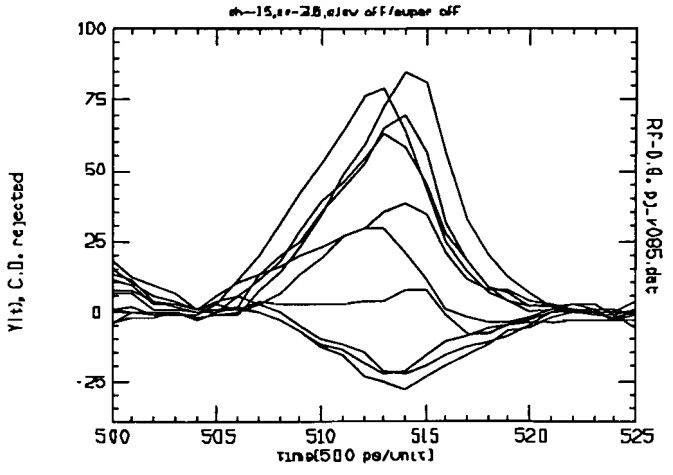

Fig. 4.47. The overlay plot of the m= 0 mode vertical head-tail oscillation for ten consecutive turns, horizontal unit= 0.5 nsec. Both vertical dampers are off, vertical chromaticity≈ 0, bunch length≈ 7 nsec, and beam intensity= 1×10^{10} protons per bunch.

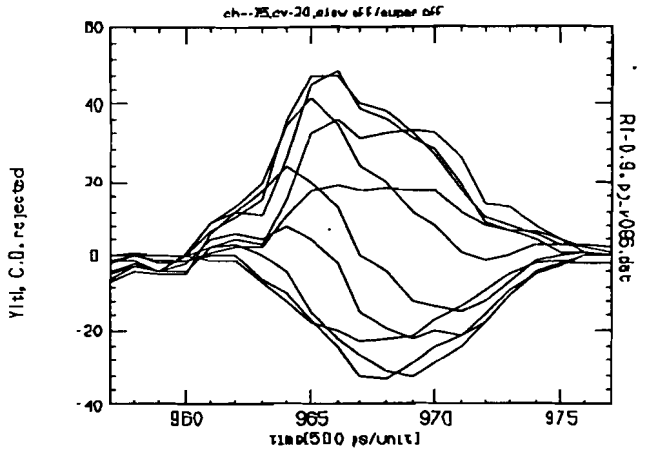

Fig. 4.48. The overlay plot of the m= 0 mode vertical head-tail oscillation for ten consecutive turns, horizontal unit= 0.5 nsec. Both vertical dampers are off, vertical chromaticity≈ 16, bunch length≈ 7 nsec, and beam intensity= 1×10^{10} protons per bunch.

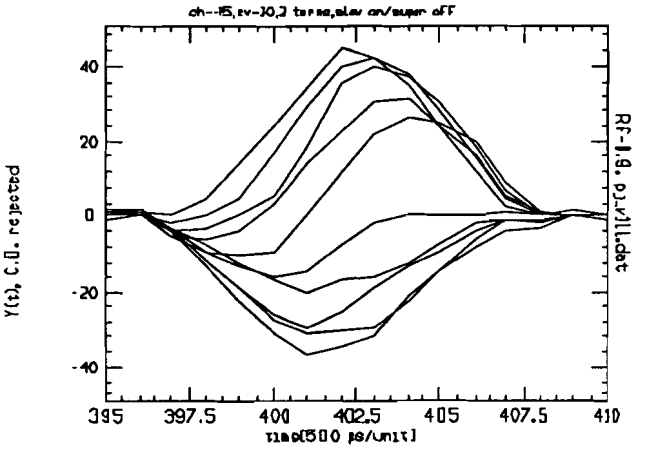

Fig. 4.49. The overlay plot of the m= 0 mode vertical head-tail oscillation for ten consecutive turns, horizontal unit= 0.5 nsec. The vertical dampers is off, slow damper is on, vertical chromaticity≈ 6, bunch length≈ 5 nsec, and beam intensity= 1×10^{10} protons per bunch. Beam loss still occurs during the measurement.

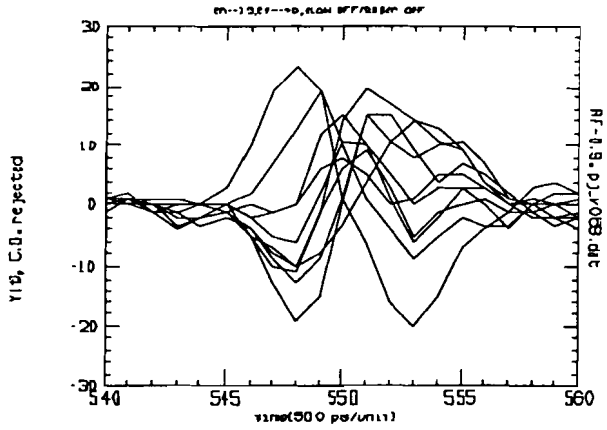

Fig. 4.50. The overlay plot of the m= 1 mode vertical head-tail oscillation for ten consecutive turns, horizontal unit= 0.5 nsec. Both vertical dampers are off, vertical chromaticity≈ -43, bunch length≈ 5 nsec, and beam intensity= 1.6×10^{10} protons per bunch.

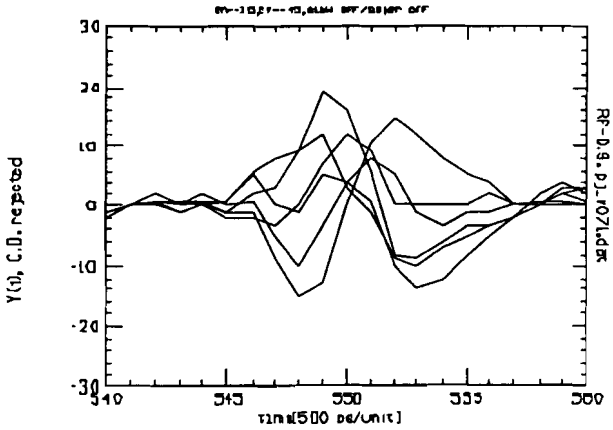

Fig. 4.51. The overlay plot of the m= 1 mode vertical head-tail oscillation for six consecutive turns, horizontal unit= 0.5 nsec. Both vertical dampers are off, vertical chromaticity≈ -48, bunch length≈ 5 nsec, and beam intensity= 1.6×10^{10} protons per bunch.

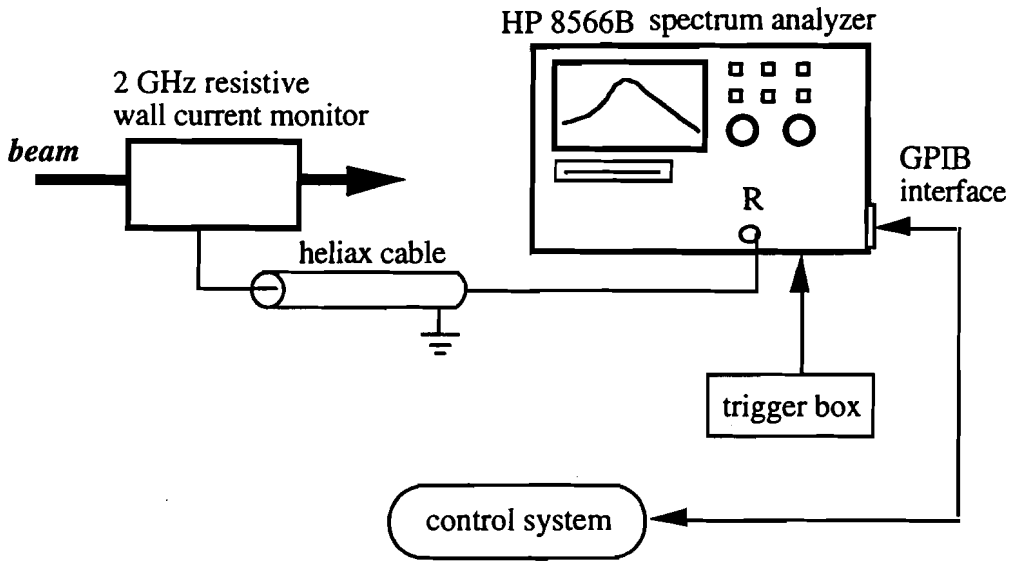

Fig. 4.52. The experimental setup for the measurement of longitudinal bunch form factor.

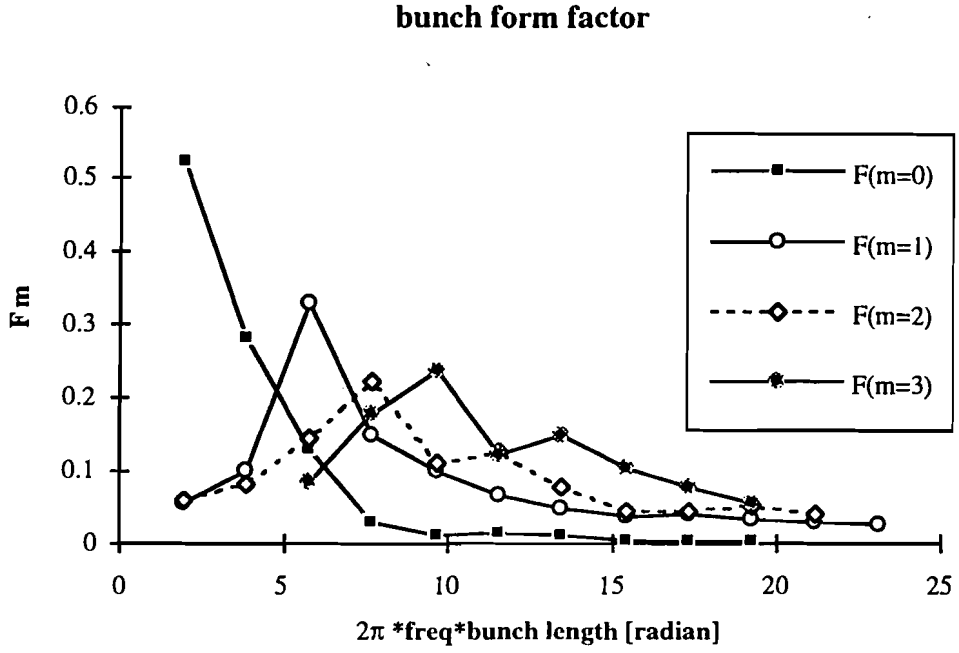

Fig. 4.53: The measured bunch form factor $F_m(\chi)$ at the injection energy of the Main Ring. The bunch form factor is symmetric with respect to the ordinate.

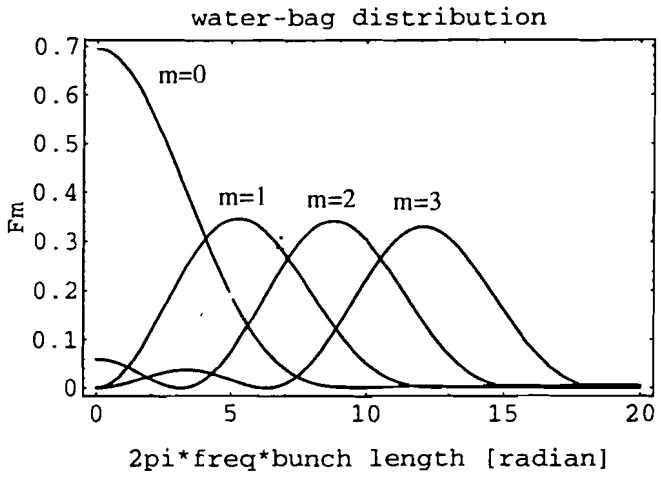

Fig. 4.54: The calculated bunch form factor for a water-bag bunch.

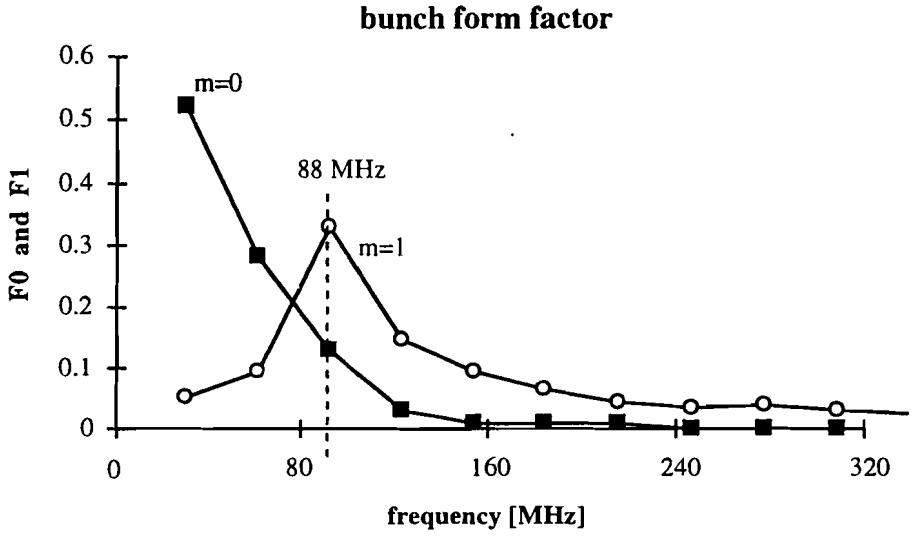

Fig. 4.55: The measured bunch form factor of the m=0 and m=1 modes for a bunch length of 10 [nsec].

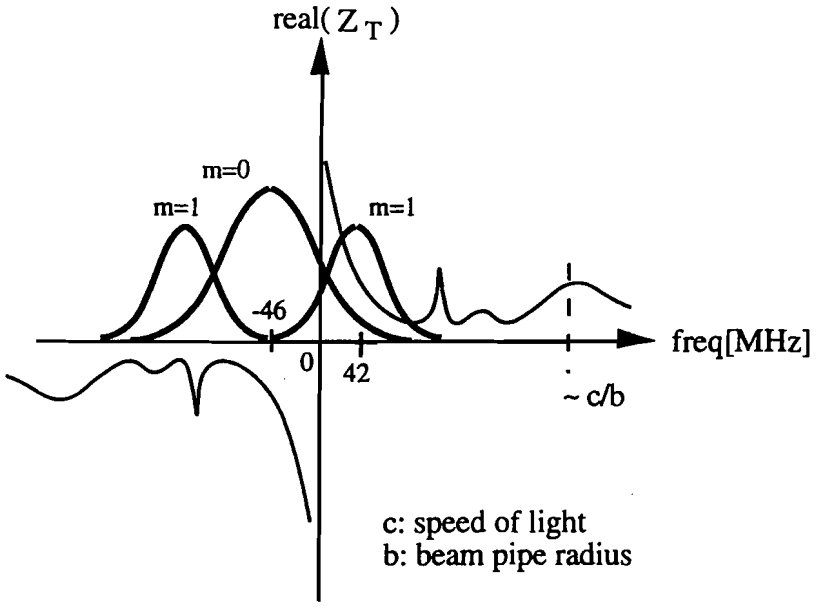

Fig. 4.56: The convolution of the resistive impedance and the vertical bunch form factor at the injection stage of the Main Ring in a typical pbar stacking cycle (with a positive vertical chromaticity). The m= 0 head-tail mode is unstable, but the m= 1 head-tail mode is stable.

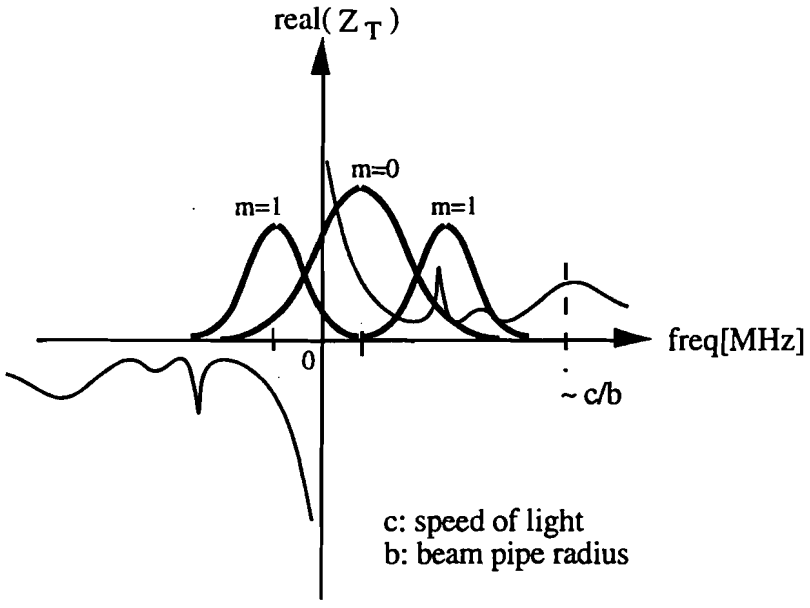

Fig. 4.57: The convolution of the resistive impedance and the vertical bunch form factor at the injection stage of the Main Ring, the vertical chromaticity is set to a small negative value. The m= 0 head-tail mode is stable, but the m= 1 head-tail mode is unstable.

CHAPTER 5

MEASUREMENT OF WAKE FIELDS IN THE MAIN RING

Because the knowledge of wake fields is essential to the understanding of observed beam instabilities both quantitatively and qualitatively, beam measurements are performed to determine the vertical wake fields in the Main Ring. Basic principles of measurement techniques as well as hardware setups are described. Measurement techniques in both the time domain and the frequency domain are explored, and the results are depicted.

A. Impedance measurement— frequency domain

The knowledge on the accelerator impedance is essential to the analysis of beam instability in the frequency domain. The impedance of individual accelerator components can be obtained by performing bench measurements[44] before installation. For the overall impedance in an accelerator, beam measurements still stand as the most conclusive approach. The overall impedance is determined from the measured beam transfer function (BTF). Continuous beam is required for the BTF measurement.

1. Basic principles of beam transfer function measurement

The theory of continuous beam transfer function measurements was first published by D. Möhl and A.M. Sessler,[45] and the first experimental results were obtained at CERN.[46] The experimental setup for Main Ring BTF measurements in the vertical

direction is depicted in Fig. 5.1. As depicted in Fig. 5.1, an rf excitation is imposed on the beam by using the kicker of the existing slow damper system in the Main Ring. The frequency range of rf excitation only covers one betatron sideband. The feedback loop is disrupted so that an open-loop transfer function is measured. The response of the beam to the rf excitation is measured by a downstream beam position monitor (BPM). Since results shown in Chap. 4 clearly pointed to the resistive wall impedance, attention was focused on measurements in the low frequency range. The capacitive BPM at E49 location discussed in Sec. B.2.1 of Chap.2 was used for the BTF measurements.

The equation of motion for a single particle at the location of kicker is given by:

$$\frac{d^2y}{dt^2} + \omega_\beta^2 y(t) = Ge^{-i\Omega t} + i\frac{eI_b}{\gamma m_0}\frac{Z_\perp(\Omega)}{2\pi\bar{R}}\langle y\rangle \tag{5.1}$$

where e= the charge of a proton, I_b= the beam current, m_0= the rest mass of a proton, $\bar{R}$= the mean radius of accelerator, <y>= the averaged beam displacement, Ω= the angular frequency of external rf excitation, ω_β= the angular betatron frequency, and $Z_\perp$ is the vertical impedance.

Assuming a wave solution $y(t)= y_0\exp[i(n\theta - \Omega t)]$ and using the time derivative $d/dt= \partial/\partial t + \omega_0\partial/\partial\theta$, where ω_0 is the angular revolution frequency. The transverse displacement of a single particle seen by the downstream BPM is:

$$y_0 = \frac{-\left(e^{-in\theta}G + i\frac{eI_b}{\gamma m_0}\frac{Z_\perp}{2\pi\bar{R}}\langle y_0\rangle\right)}{\left[\Omega - \omega_0(n+Q_\beta)\right]\left[\Omega - \omega_0(n-Q_\beta)\right]} \tag{5.2}$$

where θ is the azimuthal angle between the kicker and the BPM, and n is the revolution harmonic number. If the frequency range of rf excitation only covers one betatron sideband, Eq.(5.2) can be approximated as the following:

$$y_0 \approx (-/+)\frac{\left(e^{-in\theta}G + i\frac{eI_b}{\gamma m_0}\frac{Z_\perp}{2\pi R}\langle y_0\rangle\right)}{2\langle\omega_\beta\rangle(\Omega-\omega)} \tag{5.3}$$

where ω is the angular frequency of either the n+ Q_β betatron sideband (fast wave) or the n- Q_β betatron sideband (slow wave), and $<\omega_\beta>$ is the mean angular betatron frequency. The sign (-/+) corresponds to the (fast wave/ slow wave) betatron sideband. If $\rho(\omega)$ is the normalized betatron frequency distribution of the particle beam, the averaged displacement of the particle beam seen by the BPM is given by the following:

$$\langle y_0\rangle \approx \left(e^{-in\theta}G + i\frac{eI_b}{\gamma m_0}\frac{Z_\perp}{2\pi R}\langle y_0\rangle\right)\left(\frac{(-/+)}{2\langle\omega_\beta\rangle}\int\frac{\rho(\omega)d\omega}{\Omega-\omega}\right) \tag{5.4}$$

A beam transfer function (BTF) is defined as the measured frequency response of the beam normalized by the frequency content of the rf excitation. The measured frequency response by the BPM is given by $<y_0>e^{in\theta}$. Therefore, the explicit expression for the BTF is given by the following form:[47]

$$B(\Omega) \equiv -i\langle\omega_\beta\rangle\frac{\langle y_0\rangle e^{in\theta}}{G} \tag{5.5}$$

Because the more relevant quantity is $\dot{y}(t)$ and the absorbed power is proportional to $G\dot{y}(t)$, the factor $-i$ is included in the definition of BTF. Using the definition for the BTF in Eq.(5.5), Eq.(5.4) can be reduced to:

$$B(\Omega) = \left(1 - \frac{eI_b Z_\perp}{\gamma m_0 2\pi\bar{R}} B(\Omega)\right)\left(\frac{-i(-/+)}{2}\int \frac{\rho(\omega)d\omega}{\Omega-\omega}\right) \tag{5.6}$$

When there is no self-coupling force caused by the impedance, the BTF is given by:

$$B_0(\Omega) = \frac{-i(-/+)}{2}\int \frac{\rho(\omega)d\omega}{\Omega-\omega} \tag{5.7}$$

Suppose ω_1 and ω_2 are the lower and upper limits of betatron frequency distribution respectively, the dispersion integral in Eq.(5.7) is given by the followings:

$$\begin{aligned}\int_{\omega_1}^{\omega_2} \frac{\rho(\omega)d\omega}{\Omega-\omega} &= \int_{\omega_1}^{\Omega-\varepsilon} \frac{\rho(\omega)d\omega}{\Omega-\omega} + \int_{\Omega+\varepsilon}^{\omega_2} \frac{\rho(\omega)d\omega}{\Omega-\omega} + \int_C \frac{\rho(\omega)d\omega}{\Omega-\omega} \\ &= P\int_{\omega_1}^{\omega_2} \frac{\rho(\omega)d\omega}{\Omega-\omega} + \int_C \frac{\rho(\omega)d\omega}{\Omega-\omega}\end{aligned} \tag{5.8}$$

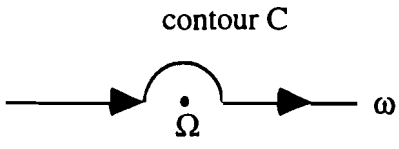

$$\begin{aligned}\int_C \frac{\rho(\omega)d\omega}{\Omega-\omega} &= -\lim_{\varepsilon\to 0}\int_\pi^0 \frac{\rho(\Omega+\varepsilon e^{i\theta})}{\varepsilon e^{i\theta}} i\varepsilon e^{i\theta} d\theta \\ &= i\pi\rho(\Omega)\end{aligned} \tag{5.9}$$

therefore,

$$B_0(\Omega) = \frac{(-/+)}{2}\left(\pi\rho(\Omega) + iP\int_{\omega_1}^{\omega_2}\frac{\rho(\omega)d\omega}{\omega-\Omega}\right) \tag{5.10}$$

where $P\int$ means the principle value integral. The contour C is chosen in such a way that the beam will become unstable if it is driven at the n- Q_β betatron sideband (slow wave) by the rf excitation (see Sec. B.3.1, Chap. 3). The real part of the absorbed power is positive when the rf excitation is driving the beam at the frequency of ω_0(n- Q_β), which means the amplitude of the transverse displacement is growing.

If one combines Eqs.(5.6) and (5.7) together, one will arrive at the following relation, which has a similar appearance to Eq.(2.74):

$$\frac{1}{B(\Omega)} = \frac{1}{B_0(\Omega)} + \frac{eI_b Z_\perp(\Omega)}{\gamma m_0 2\pi\bar{R}\langle\omega_\beta\rangle} \tag{5.11}$$

If one plots the imaginary part of $[B(\Omega)]^{-1}$ vs. the real part in a complex plane, one will get a contour called the stability diagram (see Sec. C.2.2, Chap. 2). The inverse of the BTF for an ideal accelerator without impedance, $[B_0(\Omega)]^{-1}$, will be displaced by a complex vector (impedance) in the complex plane, and the resulting contour in that complex plane represents the inverse of the BTF for a realistic accelerator, $[B(\Omega)]^{-1}$. In engineering language, the accelerator impedance is the feedback transfer function of a closed feedback loop. The beam induced signal is fed back to affect its own motion through the accelerator impedance which serves as a self-coupling mechanism. The feedback loop corresponding to Eq.(5.11) is depicted in Fig. 5.2. From the expression of the closed-loop transfer function given in Eq.(2.53), one readily realizes that an impedance of negative value (the n- Q_β betatron sideband) will result in an unstable solution.

If one has the knowledge of the betatron frequency distribution $\rho(\omega)$, one can calculate the BTF without impedance, $B_0(\Omega)$. Then a BTF measurement can be performed in a real accelerator which contains various impedance sources. With careful calibration, one can determine the overall accelerator impedance in the frequency range of the rf excitation directly from the stability diagram. The betatron frequency distribution can be measured from the transverse Schottky signal of a continuous beam (see Sec. A.1.1, Chap. 2). This is the motivation for the construction of Main Ring Schottky detector (see Sec. B.2.2, Chap.2). The BTF without impedance, $B_0(\Omega)$, is calculated for a Gaussian distribution for both the slow wave and fast wave betatron sidebands, and the results are depicted in Fig. 5.3.

2. Calibration and noise reduction of BTF measurements

2.1 Time gating technique Since the attention is focused on the low frequency range from dc to 1 MHz, and the power level of beam signal is small in the low frequency range (see Eq.(2.45)), some efforts are required to enhance the signal-to-noise ratio. Besides the averaging of repetitive measurements, a time gating technique[48] devised at CERN is adopted for the BTF measurement in the Main Ring.

If one performs an inverse Fast Fourier Transform (FFT) on the measured BTF, one will get the response of the beam to the rf excitation in the time domain. The driven response will last for a certain time interval. After the time interval of beam response, the rest of the signal is mostly comprised by the noise from the outside environment. Since one is only interested in the physical content of beam signal but not in the rf noise from the outside world, one will get a better signal-to-noise ratio simply by applying a time gate to the measured signal in order to exclude the contribution of rf noise.

A brief summary of the time gating technique is given by the following procedures: *1)* one imposes a time gate on the signal in the time domain during the time interval of interest and excludes the rest of the signal which is believed to be rf noise only *2)* then one performs a FFT on the gated time-domain signal back to the frequency domain.

The time gate is achieved by weighting the time-domain signal with a properly chosen window function which does not distort the signal in the time interval of interest but greatly reduce the contribution of rf noise to the signal outside the width of the time gate. Recall those discussions given in Sec. A.2 of Chap. 2, the window function will introduce some unphysical response in the frequency domain called spectral leakage. Therefore, the window function must be chosen in a such a way that it keeps most of the physical signal unchanged and only introduces the spectral leakage to the least as possible. A test of the time gating technique is performed on a BTF which is measured for the betatron sideband around the rf frequency of the Main Ring (52.8 MHz). The stripline BPM of the vertical super damper is used for this test measurement. Because the frequency is much higher than 1 MHz, the signal level is higher than those measurements performed in the low frequency range from dc to 1 MHz. Figure 5.4 depicts the measured raw data of BTF before applying the time gating process.

In the subject of signal processing, the two most widely used window functions are the square window and the Hanning window. The mathematical expression of each window function is given by the followings:[41]

i) square window:

$$w(n) = 1, \text{ when } 0 \leq n \leq N \tag{5.12}$$

ii) Hanning window:

$$w(n) = \frac{1}{2}\{1 - \cos[2\pi n/(N-1)]\}, \text{ when } 0 \le n \le N \qquad (5.13)$$

where N is the width of the window function, and w(n)= 0 outside the range $0 \le n \le N$. Compared with other commonly used window functions, the Hanning window provides a better frequency resolution at the expense of less accuracy of the spectral amplitude. The window function for the BTF measurement is chosen to be a mixture of the square window and the Hanning window as described in the following form:

$$w(n) = 1, \text{ when } 1 \le n \le N_c \qquad (5.14)$$

and,

$$w(n) = \frac{1}{2}\left\{1 + \cos\left(\frac{2\pi(n-N_c)}{N}\right)\right\} \qquad (5.14)$$

where n is the bin number of data points, N_c is the time interval of interest, and N is the width of the time gate. Outside the width of the time gate, the window function equals to zero. The window function used for the BTF measurement is depicted in Fig. 5.5. The total number of data points for each record is 401, and the width of the time gate is chosen to be 300. Figure 5.6 depicts the measured BTF in Fig. 5.4 after the time gating process.

2.2 Conversion of physical quantities Because the beam transfer function (BTF) is measured by means of various diagnostic hardware, the actual frequency response of each hardware element must be included in the calibration of the measured data. In reality, what one actually measured is the S_{21} parameter given by a network analyzer in Fig. 5.1. The S_{21} parameter is defined as:[21, 41]

$$S_{21}(\Omega) = \frac{V_B(\Omega)}{V_R(\Omega)} \tag{5.15}$$

where V_B is the frequency (spectrum) content of the measured voltage at the input port B of the network analyzer, and V_R is the frequency content of the rf driving voltage at the output port R of the network analyzer.

Following the signal path depicted in Fig. 5.1, one will find the voltage across the kicker electrodes as:

$$V_k(\Omega) = D(\Omega)V_R(\Omega) \tag{5.16}$$

where D is the voltage amplification factor of the amplifier in the feedback system. If the rise time of the kicker voltage is very short compared with the time of measurement, one can get an approximate expression for the deflecting force exerting on the beam as the following:

$$\begin{aligned} F_\perp &= \frac{\Delta p_\perp}{\Delta t} \\ &\approx \frac{eK_\perp V_k}{\ell} \end{aligned} \tag{5.17}$$

where e is the charge of a proton, $K_\perp$ is the transverse kicker constant given in Eq.(2.38), and ℓ is the length of the kicker electrode. Therefore, the deflection strength G in Eq.(5.1) is given by the following form:

$$\begin{aligned} G &= \frac{eK_\perp V_k}{\gamma m_0 \ell} \\ &= \frac{eK_\perp D V_R}{\gamma m_0 \ell} \end{aligned} \tag{5.18}$$

The measured voltage V_B at the input port of the network analyzer is given by:

$$\begin{aligned} V_B(\Omega) &= T(\Omega)V_p(\Omega) \\ &= T I_b S_\perp \langle y_0 \rangle e^{in\theta} \end{aligned} \tag{5.19}$$

where T is the voltage amplification factor of the receiver, and $S_\perp$ is the transverse detector sensitivity given in Eq.(2.37). Substituting the definition of BTF given in Eq.(5.5) into Eq.(5.19), the measured voltage becomes:

$$V_B = i\frac{T I_b S_\perp BG}{\langle \omega_\beta \rangle} \tag{5.20}$$

Using the relation given in Eq.(5.18), one can relate the measured voltage V_B to the driving voltage V_R with the following form:

$$V_B = i\frac{eI_b D(\Omega)T(\Omega)S_\perp(\Omega)K_\perp(\Omega)B(\Omega)}{\gamma m_0 \ell \langle \omega_\beta \rangle} V_R \tag{5.21}$$

Therefore, the measured S_{21} parameter is given by the following result:

$$S_{21} = i\frac{eI_b D(\Omega)T(\Omega)S_\perp(\Omega)K_\perp(\Omega)B(\Omega)}{\gamma m_0 \ell \langle \omega_\beta \rangle} \tag{5.22}$$

If the cable delay between the network analyzer and the kicker or BPM is not negligible, there will be an additional phase factor $\exp(-i\Omega\tau)$ in the right-hand side of Eq.(5.21), where τ is the propagation time of electrical signal along the whole cable connection. The delay time τ will cause the phase of S_{21} to be tilted as depicted in Fig. 5.6*(3)*. Since one can simply compensate the effect by introducing a phase factor during

the data processing, the cable delay will not play any role in the physical conclusions of BTF measurements.

By using Eq.(5.22), the equation of the stability diagram can also be rewritten in terms of S_{21} with the following form:

$$\frac{i}{S'_{21}} = \frac{i}{S_{21}} + \frac{\ell Z_{\perp}}{2\pi \bar{R} D T S_{\perp} K_{\perp}} \tag{5.23}$$

where S'_{21} is the response measured in a real accelerator with the impedance source, and S_{21} is the response in an ideal accelerator without any impedance source. The ideal S_{21} parameter can be calculated from Eq.(5.10), if the Schottky spectrum $\rho(\omega)$ can be measured in the Main Ring. Note that D, T, and $K_{\perp}$ are scalar functions of frequency which carry no physical units. But $S_{\perp}$ and $Z_{\perp}$ have the MKS dimension of [Ω/ m] respectively.

From Eq.(5.23) one readily realizes that once the frequency response of each hardware component is known, the transverse impedance can be derived from the measured S_{21} parameter directly. Unfortunately, technical documents of either the slow damper or super damper system are scarcely available. The knowledge on the kicker constant is not available for the Main Ring. But since the frequency span used in the BTF measurements is only 10 kHz, one can assume the proportionality parameter in Eq.(5.23) to be constant as long as the measurement is performed within the 3 dB bandwidth of each device. Therefore, the calibration process simply involves a data fit of the calculated stability diagram to the measured one by using linear regression.

3. Results of measured vertical impedance

Because the sensitivity of the Main Ring Schottky detector was compromised to accommodate the large frequency drift during the acceleration process, the Main Ring Schottky detector is not sensitive enough to detect the transverse Schottky signal. A Gaussian function is assumed for the betatron frequency distribution in order to forego the data calibration. The BTF measurements were performed by using the capacitive BPM at the E49 location in the Main Ring tunnel (see Sec. B.2.1, Chap. 2). Because the low signal level, each record is averaged over 16 repetitive measurements for a usable signal-to-noise ratio. A thin-wall model of resistive wall impedance is used to model the displacement of the stability diagram caused by the accelerator impedance. The impedance model used in the data calibration is given with the follow form:

$$Z_{\perp}(f) = \frac{a_1}{f} + i a_2 f \tag{5.24}$$

where a_1 and a_2 are constants to be determined, and f is the frequency.

An example of the measured S_{21} parameter is depicted in Fig. 5.7 for the $1+ q_\beta$ betatron sideband, where q_β is the fractional betatron tune. Notice that the stability diagram depicted in Fig. 5.7*(3)* has been shifted across the vertical axis which implies a large resistive impedance inside the frequency range of measurement.

Because the low signal-to-noise ratio, only data points around the resonance frequency are used to determine the accelerator impedance. Some fit results of measured stability diagrams are depicted in Fig. 5.8. The fitted value of vertical impedance in the Main Ring is depicted in Figs. 5.9 and 5.10 for the resistance and the reactance respectively. The skin depth calculated from Eq.(3.30) for a circular beam pipe made with stainless steel is depicted in Fig. 5.11.

As depicted in Fig. 5.11, the thick-wall impedance model is not applicable for the Main Ring in the frequency range below 100 kHz. Therefore, one expects to get the frequency dependence of vertical impedance with the following form (see Sec. A.2.2, Chap. 3):

$$\begin{cases} Z_{\perp} \propto \frac{1}{f} \text{ ; when } f \leq 100\,\text{kHz} \\ Z_{\perp} \propto \frac{1}{\sqrt{f}} \text{ ; when } f \geq 100\,\text{kHz} \end{cases} \tag{5.25}$$

If one approximates the geometry of the vacuum chamber in the Main Ring as a circular beam pipe around the entire circumference, then the calculated resistance of the Main Ring impedance is depicted in Fig. 3.10. The measured results depicted in Fig. 5.9 do not show the kind of frequency dependence one would expect from the theory of a circular beam pipe. Besides the results of measured resistance, the measured reactance does not show the frequency dependence given by the theory of a circular beam pipe which predicts the same dependence on the frequency as given in Eq.(5.25). According to the theoretical results, one should expect the reactance to be purely inductive and have the same magnitude as the resistance. Instead of large inductive reactance, the measured reactance depicted in Fig. 5.10 clearly indicates a significant contribution from an impedance source which is purely capacitive.

One possible source of capacitive impedance is the space-charge impedance (see Sec. A.2.4, Chap. 3). Because of the poor signal-to-noise ratio in the measured response from the E49 BPM in the low frequency range, a large beam intensity is used for the BTF measurements, around 1×10^{12} protons. The beam size used in the BTF measurements is estimated by performing a profile scan with the flying wire system.[49] The parameters used to estimate the space-charge impedance is depicted in Table 5.1. The formula given in

Eq.(3.37) is used for the calculation. The estimated capacitive impedance due to the space-charge effect is about i(231 MΩ/ m) which is sufficient to explain the results depicted in Fig. 5.10.

Table 5.1. The parameters used for the estimation of space-charge impedance.

parameter	value
mean radius of the Main Ring [km]	1
radius of proton beams [mm]	4
relativistic factor γ (8 GeV)	10
radius of beam pipe [cm]	3

Combining all the above results, the vertical impedance in the Main Ring can be attributed to the resistive wall impedance. But the frequency dependence does not show good agreement with the result predicted by the theory of a circular beam pipe. Besides the discrepancy in the frequency dependence, the measured resistance is about three times larger than the calculated value for a circular beam pipe. Even at frequencies above 300 kHz the measured resistance still shows significant magnitude. If one uses this trend to project the resistive impedance, one will expect the resistive impedance still to be significant in the MHz range. It is possible that there may be other impedance sources besides the resistive wall in the vertical plane of the Main Ring. One possible suspect is the Main Ring kicker magnets. Another are the Lambertson magnets, which present bare steel laminations to the beam image current. Bench measurements have been performed to determine the

longitudinal impedance of kicker magnets and the results are alarming.[50] The measured longitudinal impedance of Main Ring kicker magnets shows several low Q resonance impedances in the MHz range. Measurements of transverse impedance for kicker magnets have been performed at CERN and KEK, and the results are attributed to the horizontal instabilities observed in the CERN PS Booster and KEK Booster respectively.[51, 52]

The measured vertical impedance, as depicted in Fig. 5.9, leads to a puzzling finding. Since the frequency dependence of the measured resistance is relatively flat, one will expect to see coupled bunch modes at frequencies other than $(1\text{-}q_\beta)f_0$. But the low frequency mode corresponding to $1\text{-}q_\beta$ betatron sideband is the only mode observed so far (see Figs. 4.41, 4.44 and 4.45). This strange phenomenon is not understood at present.

B. Wake function measurement— time domain

1. Basic principles of wake function measurement

If one uses a macroparticle to represent a bunch, the effect on the beam motion caused by the transverse wake force is a change in the slope of the macroparticle transverse trajectory. If one only considers the effect caused by the transverse wake force induced by a preceding particle, the change in the slope of particle trajectory can be given by Eq.(3.10):

$$\begin{aligned} &\int_{s_i}^{s_f} y''(s)\,ds = \frac{1}{E}\int_{s_i}^{s_f} F_\perp\big(t' = (s+z)/c\big)ds \\ &\Delta y'(s) = \frac{-1}{E} qQy(t')W_\perp(z) \end{aligned} \tag{5.26}$$

where E and q are the relativistic energy and the charge of the witness particle respectively, Q is the charge of the source particle, and z is the relative position of the witness particle with respective to the source particle as defined in Fig. 3.4. Therefore, the change in the slope of particle trajectory over the distance of interest (s_i–> s_f) is proportional to the transverse wake function $W_\perp$. If one can vary the distance between the source and the witness particles at will, then one will be able to probe the transverse wake function in the time domain. This is the basic principle of a wake function measurement. The first measurement of this kind was performed at Argonne National Laboratory[53] and later at ASSET in the SLC.[54]

For a circular accelerator, the minimum bunch spacing is dictated by the frequency of the rf system used for particle acceleration. The transverse wake function can be probed by using a long bunch train with a closed orbit offset intentionally created at injection. If one has the information on all the lattice functions in a transfer matrix given in Eq.(1.38), then the generic configuration of the experimental setup is depicted in Fig. 5.12.

If one labels a bunch train of N beam bunches in the following way:

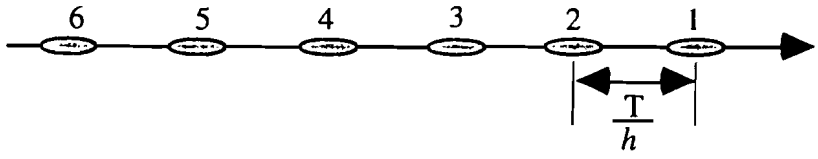

where T is the revolution period, and h is the harmonic number of accelerator. The first bunch is labeled as one, and the last bunch is labeled as N. The slope change of the transverse trajectory for a beam bunch of index p in the first turn after the injection is given by the following expression:

$$\Delta y'_p = \frac{-Q^2}{E}\sum_{j=1}^{p} W_\perp\left((j-p)T_{rf}\right) y_j\left(t-(p-j)T_{rf}\right) \tag{5.27}$$

where T_{rf}= T/ h, Q is the charge of each bunch, E is the relativistic energy of each bunch, and a bunch train of N identical beam bunches is assumed. Note that the transverse wake function equals to zero if j- p≥ 0.

If three beam position monitors (BPM) in Fig. 5.12 are placed at locations where the beta function $\beta_y(s)$ is either at its minimum or maximum, then the slope of particle trajectory at locations A and B due to the transverse focusing can be related together by the following expression (see Eq.(1.38)):

$$y'_p(B) = -(\beta_A\beta_B)^{-1/2}\sin\phi\cdot y_p(A) + \left(\frac{\beta_A}{\beta_B}\right)^{1/2}\cos\phi\cdot y'_p(A) \tag{5.28}$$

where ϕ is the betatron phase advance from A to B. If one includes the change of slope caused by the transverse wake fields, then the complete expression is given by the following form:

$$y'_p(B) = -(\beta_A\beta_B)^{-1/2}\sin\phi\cdot y_p(A) + \left(\frac{\beta_A}{\beta_B}\right)^{1/2}\cos\phi\cdot y'_p(A) - \frac{Q^2}{E}\sum_{j=1}^{p} W_\perp((j-p)T_{rf})\,y_j(A;t-(p-j)T_{rf}) \tag{5.29}$$

From Eq.(1.38) one also has the following relation:

$$y_p(B) = \left(\frac{\beta_B}{\beta_A}\right)^{1/2}\cos\phi\cdot y_p(A) + (\beta_A\beta_B)^{1/2}\sin\phi\cdot y'_p(A) \tag{5.30}$$

Since the transient waveform digitizer is capable of recording the transverse position of each bunch in the bunch train, the transverse positions of bunch p at locations A and B can be measured in the same turn. Thus one can deduce the slope $y'_p(A)$ at location A for the bunch p from Eq.(5.30) with the measured positions at locations A and B. Then one substitutes the result of $y'_p(A)$ into Eq.(5.29). Up to now, there is still one piece of information missing in Eq.(5.29), i.e. $y'_p(B)$. By repeating the same procedures, one can use the measured positions at locations B and C to deduce $y'_p(B)$. Once all the information is available, one can determine the change of slope caused by the transverse wake fields only. If one uses the notation $\Delta y'(B \mid A)$ to denote the change of slope from location A to B caused by the transverse wake fields, one can tabulate the result for each bunch in the bunch train as the followings:

$$
\begin{aligned}
&\Delta y_1'(B \mid A) = 0 \\
&\Delta y_2'(B \mid A) = -\frac{Q^2}{E} W_\perp(-T_{rf})\, y_1(A) \\
&\Delta y_3'(B \mid A) = -\frac{Q^2}{E} W_\perp(-T_{rf})\, y_2(A) - \frac{Q^2}{E} W_\perp(-2T_{rf})\, y_1(A) \\
&\cdots\cdots\cdots\cdots \\
&\Delta y_N'(B \mid A) = -\frac{Q^2}{E} W_\perp(-T_{rf})\, y_{N-1}(A) - \frac{Q^2}{E} W_\perp(-2T_{rf})\, y_{N-2}(A) \cdots\cdots \\
&\qquad\qquad -\frac{Q^2}{E} W_\perp(-(N-1)T_{rf})\, y_1(A)
\end{aligned}
\tag{5.31}
$$

There are N unknowns in a set of N algebraic equations given in Eq.(5.31). The unknown variables are listed in the following set:

$$
\left\{ W_\perp(-T_{rf}), W_\perp(-2T_{rf}), W_\perp(-3T_{rf}) \cdots, W_\perp(-(N-1)T_{rf}) \right\} \tag{5.32}
$$

Therefore, the transverse wake function is sampled at a time interval of T_{rf}. The Fourier Transform of the transverse wake function gives the impedance of the accelerator. According to the Nyquist theorem,[10] the maximum frequency bandwidth without spectral aliasing is from dc to $0.5 f_{rf}$, where f_{rf} is the rf frequency of accelerator. The frequency resolution of the accelerator impedance derived from the measured wake function is f_{rf} / (N-1).[41] The discretely sampled values of the transverse wake function given in Eq.(5.32) can be solved by applying Cramer's rule[10] in linear algebra to Eq.(5.31). To get a fine frequency resolution for the impedance from the FFT of the measured wake function, one should use a long bunch train for the measurement.

If the reliable values of lattice functions in the transfer matrix are not available, one needs to measure the actual values of lattice functions first. Reports on the lattice measurement techniques[55, 56] can be found in literature. To get good accuracy for the measurement of lattice functions, the beam intensity used in the measurement should be

small enough that the wakefield effect can be ignored but big enough that a reasonable signal level can be obtained.

2. *Observed phenomena*

Because of the lack of enough measuring instruments, quantitative results of vertical wake function in the Main Ring can not be obtained. Only qualitative measurements are performed at the injection energy of the Main Ring. The experimental setup is similar to the one depicted in Fig. 5.12 except that only one BPM and one waveform digitizer are used in the measurement. The experimental setup for the qualitative measurement of vertical wake fields is depicted in Fig. 5.13. The quarter wavelength stripline BPM at the F14 location (see Sec. B.2.3, Chap. 2) is used to measure the vertical displacement of the bunches.

Two booster batches of proton beams are injected into the Main Ring. Both the vertical super damper and the slow damper are turned on from the start until the injection of the second batch. The purpose is to eliminate any possible wakefield effects induced by the first batch. Then the second booster batch is injected with intentionally created closed orbit offset. The off-centered second batch is used to induce the vertical wake fields. The first batch serves as the witness of the vertical wake fields induced by the off-centered second batch. Each booster batch contains 84 proton bunches, and the spacing between each batch is 8 rf buckets.

Figure 5.14 depicts the time series of the vertical bunch oscillation at an interval of every 160 turns (~ 3.4 msec) with the following parameters: horizontal chromaticity≈ -12, vertical chromaticity≈ 0, bunch length= 6 [nsec], and beam intensity= 3.3×10^{10} protons per bunch. The corresponding plot of the total beam intensity for Fig. 5.14 is depicted in Fig. 5.15, and the corresponding plot of the bunch length for Fig. 5.14 is depicted in Fig. 5.16.

As depicted in Fig. 5.14, the injection of the off-centered second batch induces the vertical wake fields which last long enough to perturb the bunch motion in the first batch. The results suggest a long range wake field which can last over 19 [μsec] in the Main Ring. According to the envelope of bunch oscillation depicted in Fig. 5.14, this long range wake field is attributed to an impedance below the MHz range. Note that the beam motion depicted in Fig. 5.14 is a mixed result of the coupled bunch motion and the m= 0 mode head-tail motion.

Figure 5.17 depicts the time series of the vertical bunch oscillation at an interval of every 160 turns (~ 3.4 msec) with the following parameters: horizontal chromaticity≈ -12, vertical chromaticity≈ -13, bunch length= 6 [nsec], and beam intensity= 2.7×10^{10} protons per bunch. The corresponding plot of the total beam intensity vs. time is depicted in Fig. 5.18.

As depicted in Fig. 5.18, the m= 0 mode head-tail damping helps to slow down the beam loss in comparison with the result depicted in Fig. 5.15 where the vertical chromaticity is set close to zero. The strength of vertical head-tail damping is not strong enough to counteract the amplitude growth due to the coupled bunch instability with the vertical chromaticity≈ -13.

When the vertical chromaticity is set around -23, the m= 0 mode head-tail damping is strong enough to counteract the amplitude growth due to the coupled bunch instability. The total beam intensity as depicted in Fig. 5.19 no longer shows appreciable loss in comparison with results depicted in Figs. 5.18 and 5.15. The time series plot of the vertical bunch oscillation is depicted in Fig. 5.20. Because a large negative value is used for the vertical chromaticity, the coupled bunch oscillation is being suppressed by the m= 0 mode head-tail damping. As depicted in Fig. 5.20, the perturbance on the first batch due to the injection of the off-centered second batch is gradually damped out by the m= 0 head-tail

damping. The slow beam loss depicted in Fig. 5.19 is mainly caused by the single particle effect. Because of the large value of chromaticity, the dynamic aperture becomes smaller due to the increasing contribution from the nonlinearity of magnetic fields. Also, the amplitude of betatron tune modulation due to the synchrotron motion is about 0.07 which is large enough to cross several high order resonance lines in the transverse tune plane. Those single particle effects contribute together to cause the deterioration of beam lifetime. Therefore, a large negative value of chromaticity will not be a desirable solution.

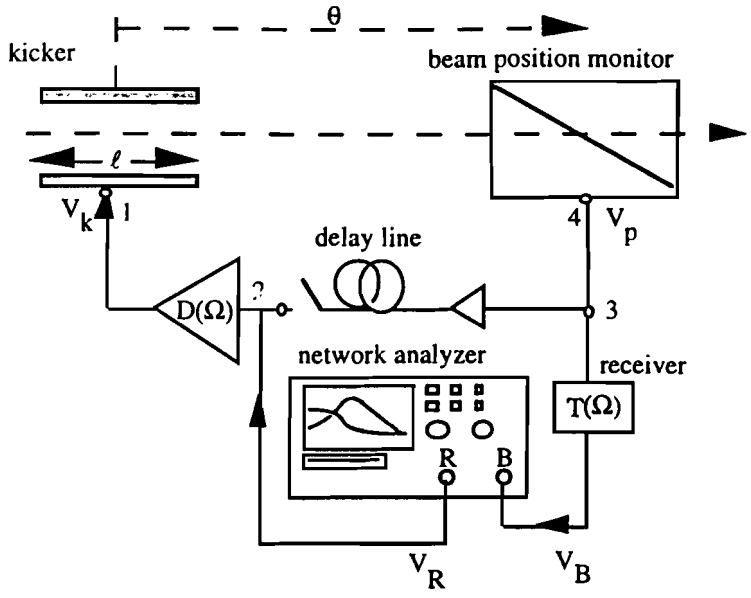

Fig. 5.1. The experimental setup for beam transfer function measurements with continuous beam in the Main Ring.

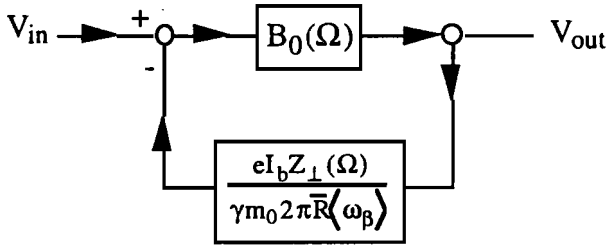

Fig. 5.2. The feedback loop corresponds to the self-coupling mechanism of particle beams in an accelerator.

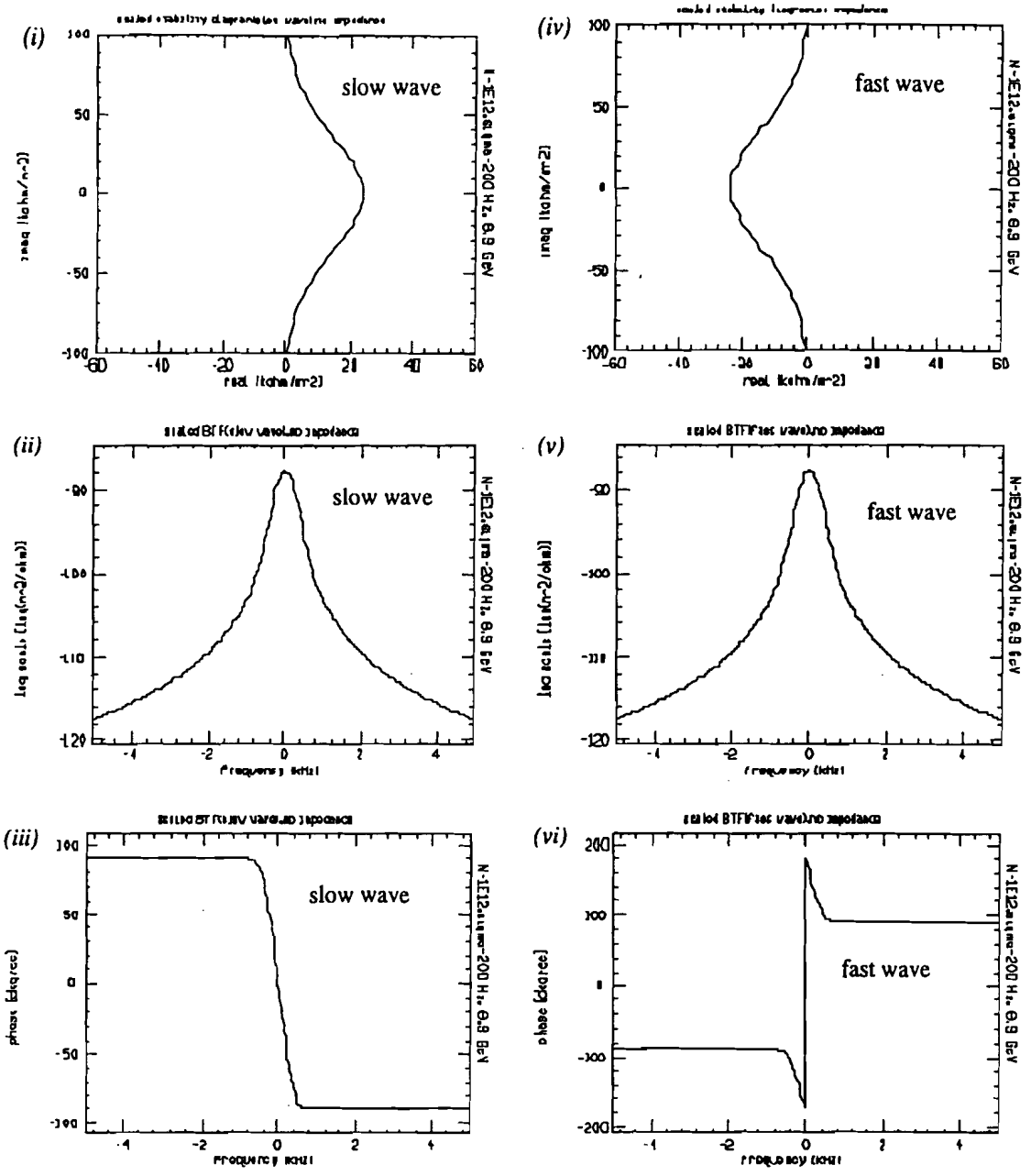

Fig. 5.3. The calculated BTF without impedance, pictures on the left side are the stability diagram, the amplitude response of the BTF is in units of [dB], and the phase response of the BTF is in units of [degree] for the slow wave betatron sideband (n- Q_β) in the order *(i)*, *(ii)*, and *(iii)* respectively. Pictures on the right side are calculated results for the fast wave betatron sideband (n+ Q_β).

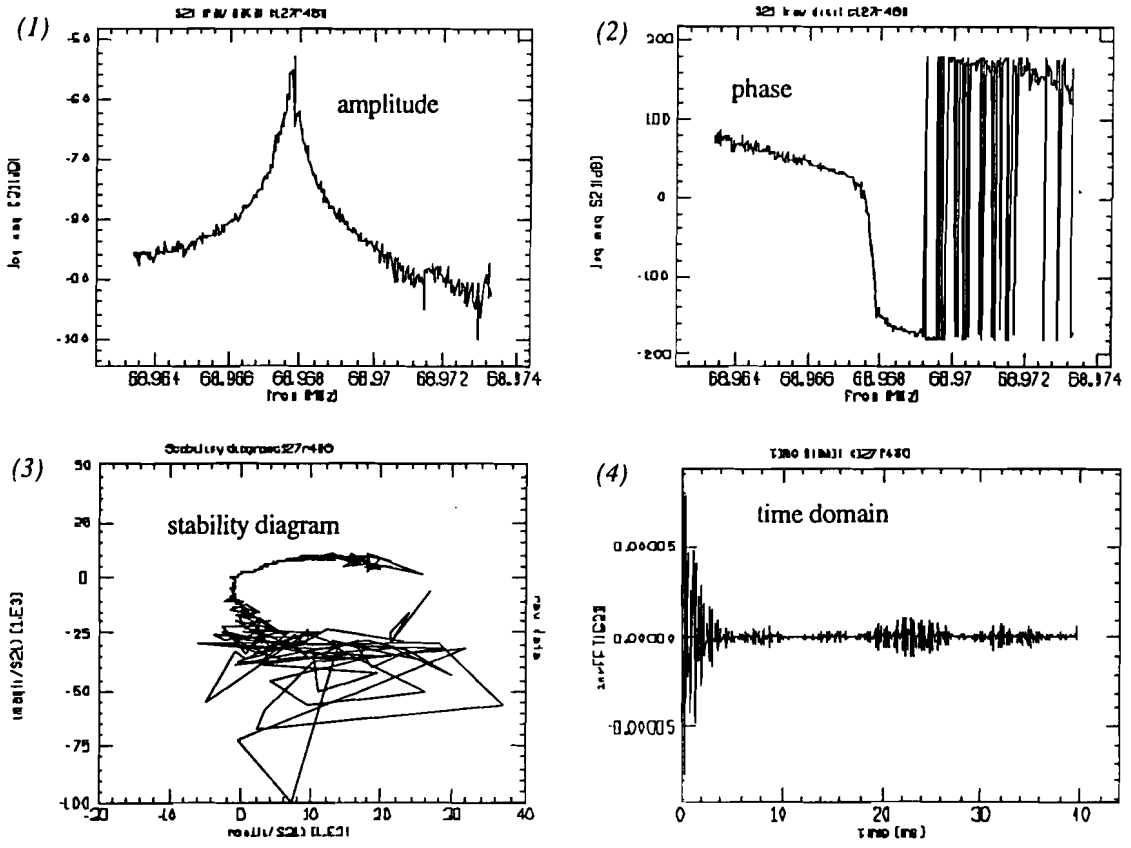

Fig. 5.4. The measured raw data of BTF before applying the time gating technique and the compensation of cable delay *(1)* the amplitude of the BTF in units of [dB] vs. frequency *(2)* the phase of the BTF in units of [degree] vs. frequency *(3)* the stability diagram *(4)* the measured BTF transformed into the time domain.

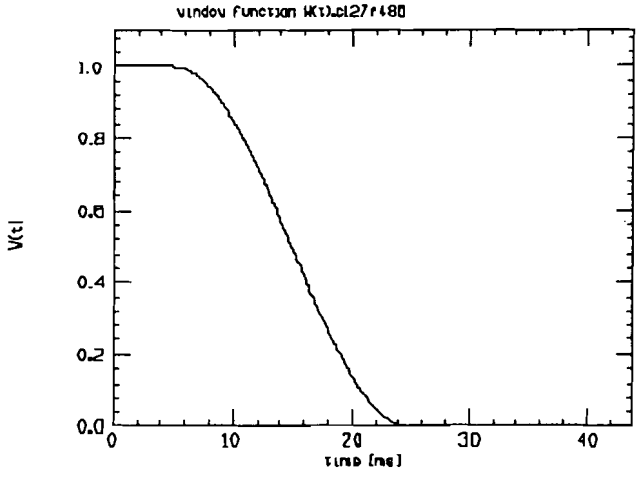

Fig. 5.5. The window function used in the time gating process for rendering data points of BTF measurements in the Main Ring.

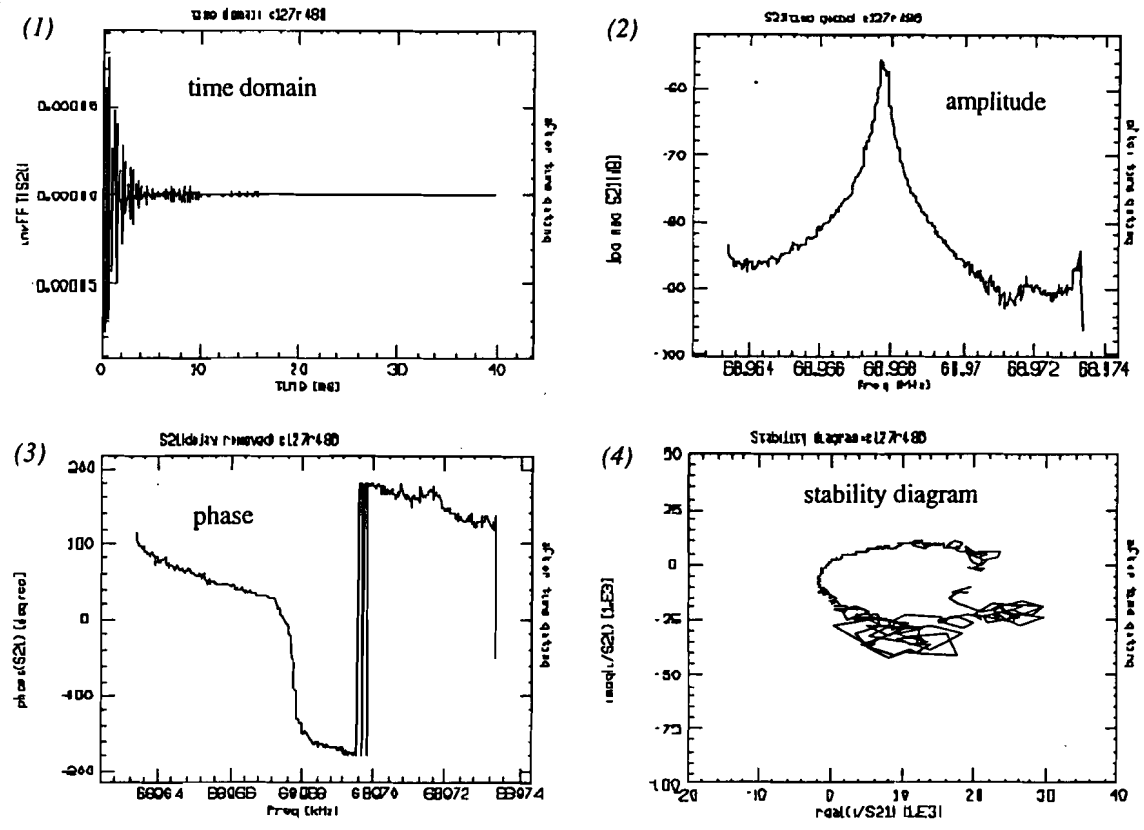

Fig. 5.6. The measured BTF after applying the time gating technique to the raw data. The signal-to-noise ratio is enhanced significantly compared with results depicted in Fig. 5.4.

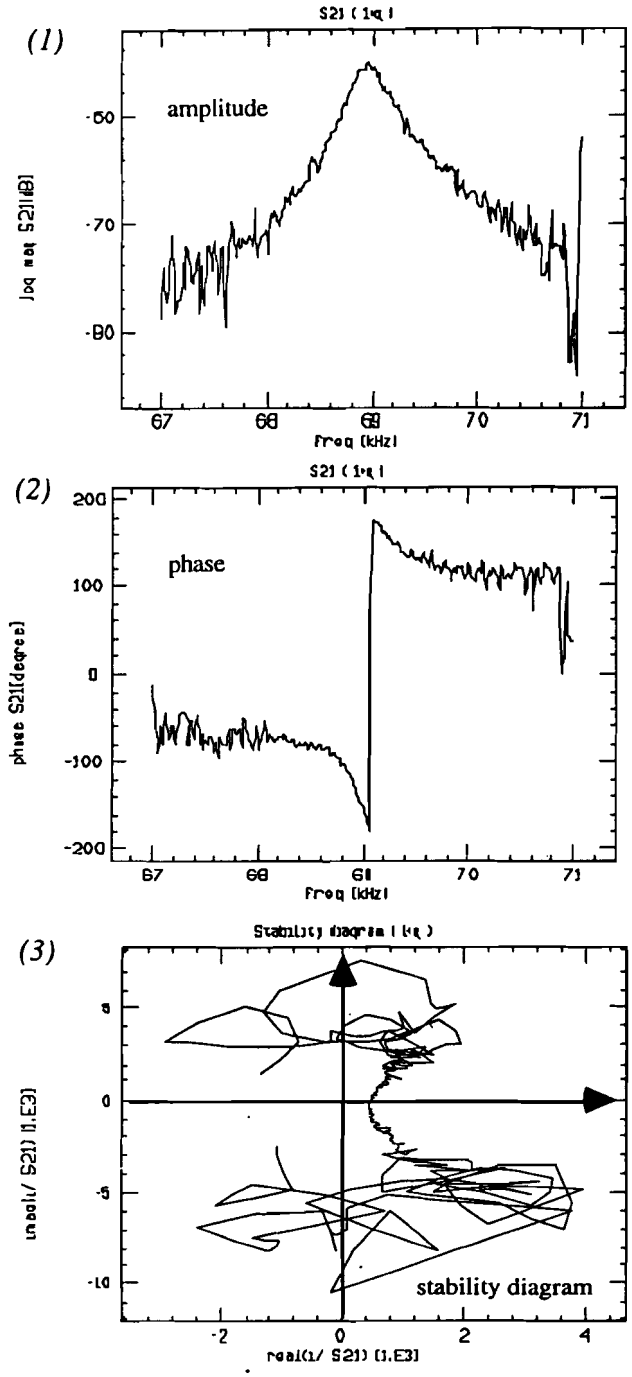

Fig. 5.7. The measured S_{21} parameter for the 1+ q_β betatron sideband *(1)* the amplitude in units of [dB] vs. frequency *(2)* the phase in units of [degree] vs. frequency *(3)* the stability diagram.

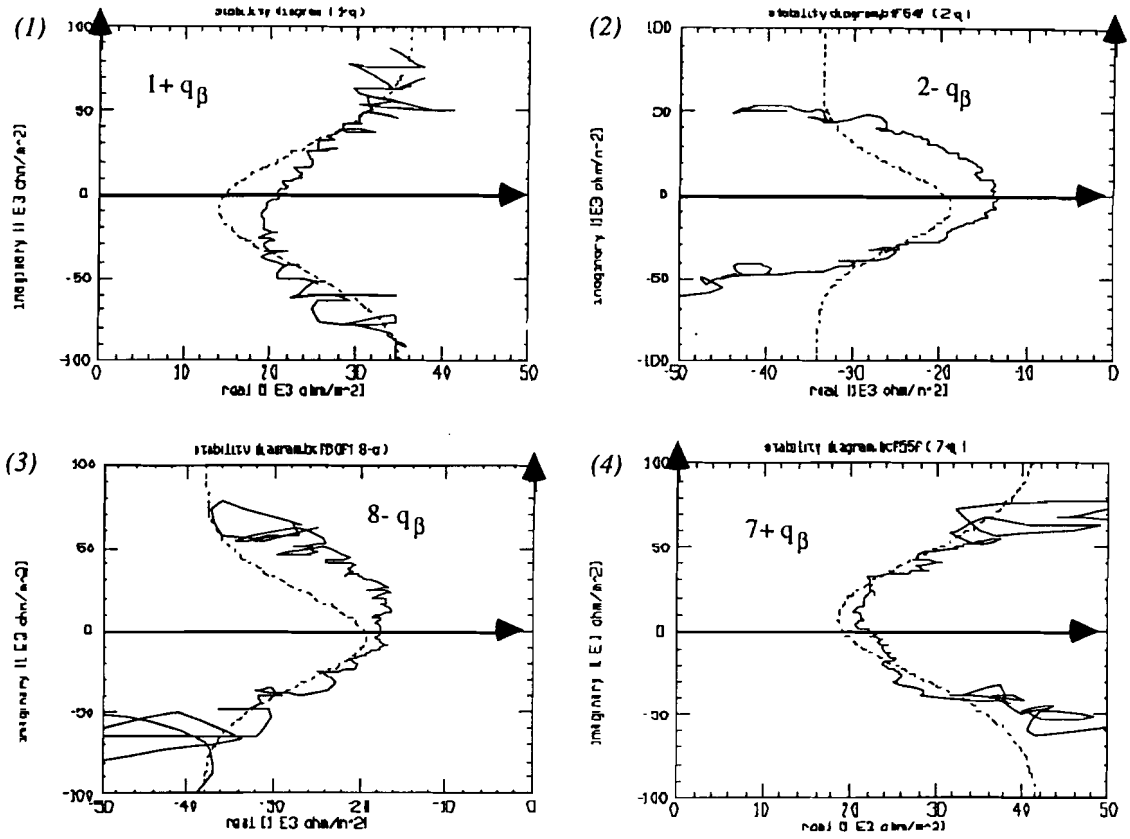

Fig. 5.8. Some fit results of measured stability diagrams to the calculated ones. *(1)* and *(4)* are stability diagrams for the fast wave component. *(2)* and *(3)* are stability diagrams for the slow wave component.

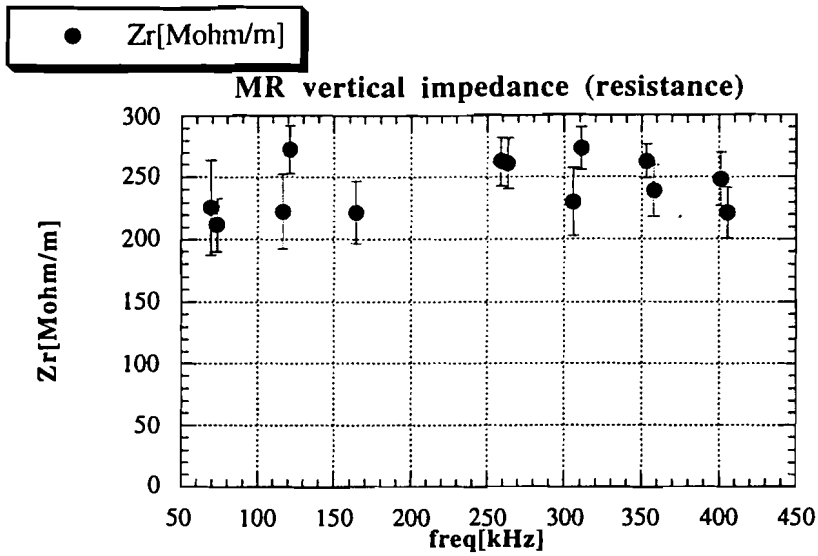

Fig. 5.9. The measured resistance of the Main Ring impedance in the vertical plane.

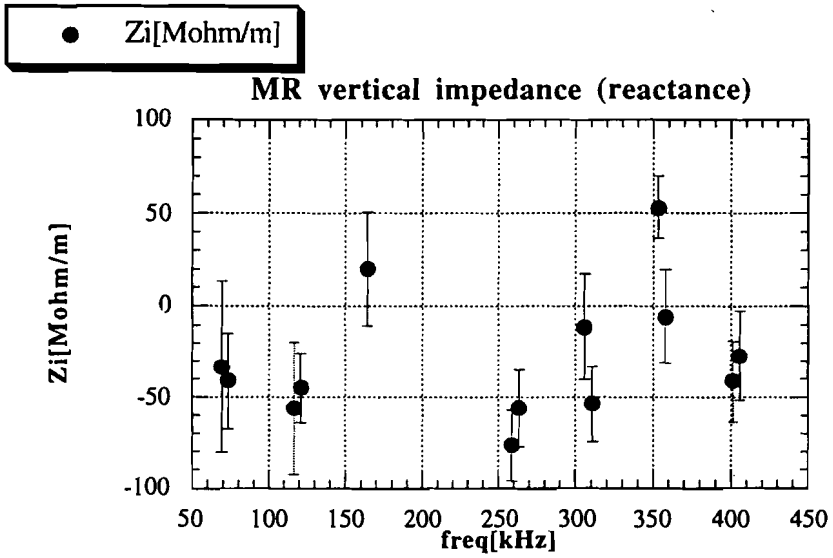

Fig. 5.10. The measured reactance of the Main Ring impedance in the vertical plane.

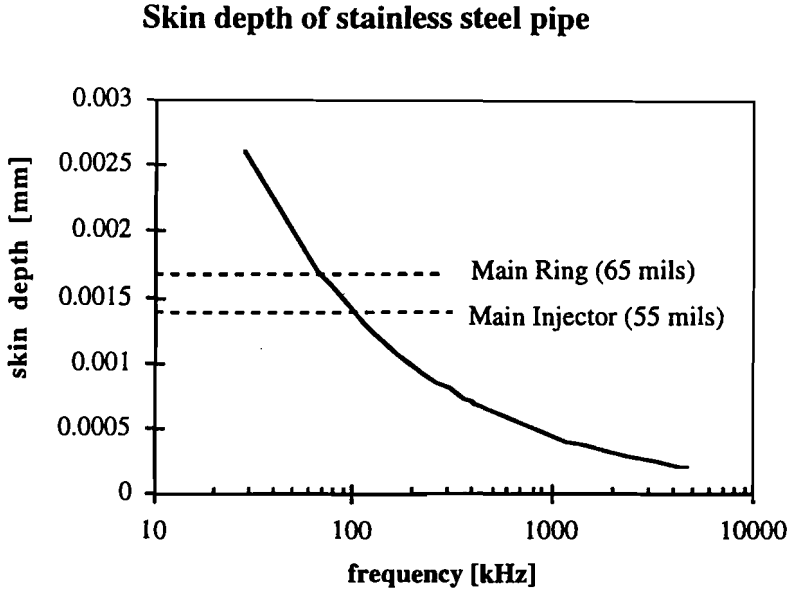

Fig. 5.11. The calculated skin depth for a circular beam pipe made with stainless steel.

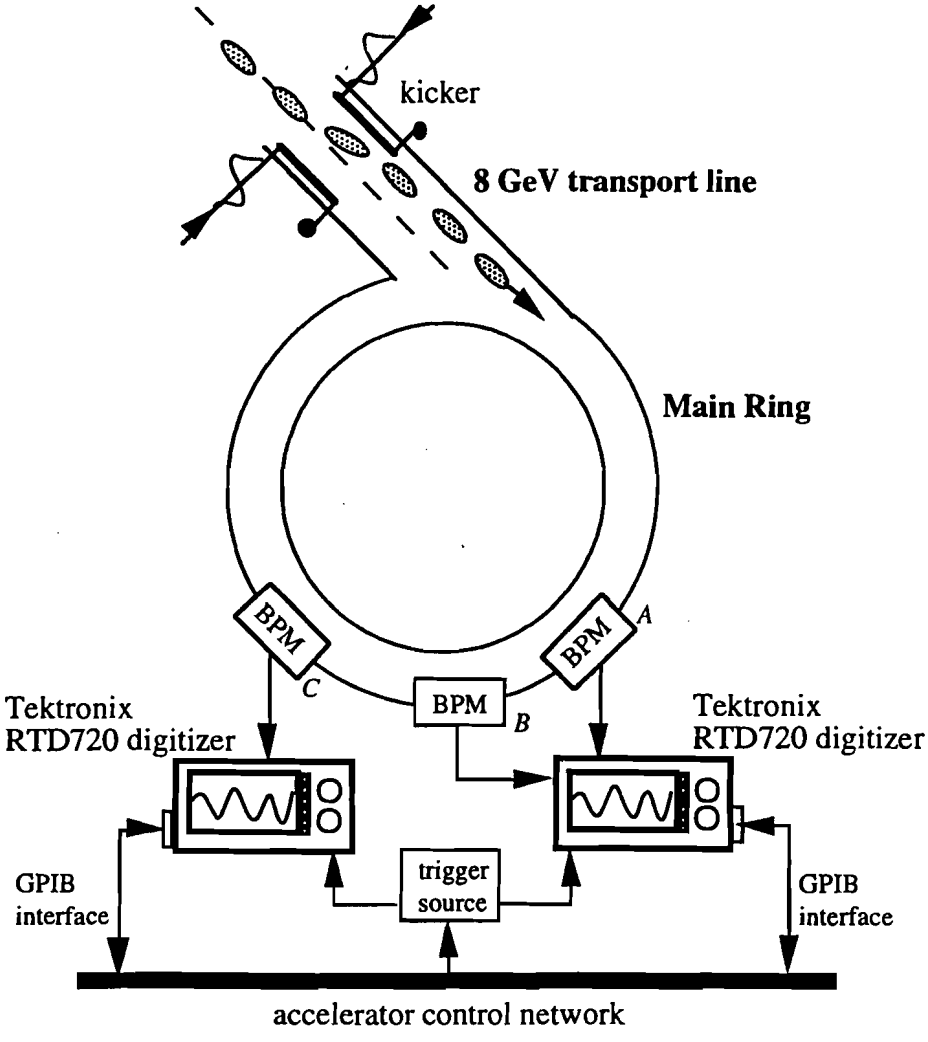

Fig. 5.12. The generic configuration of the experimental setup for the measurement of transverse wake function. All the lattice functions are assumed to be known already.

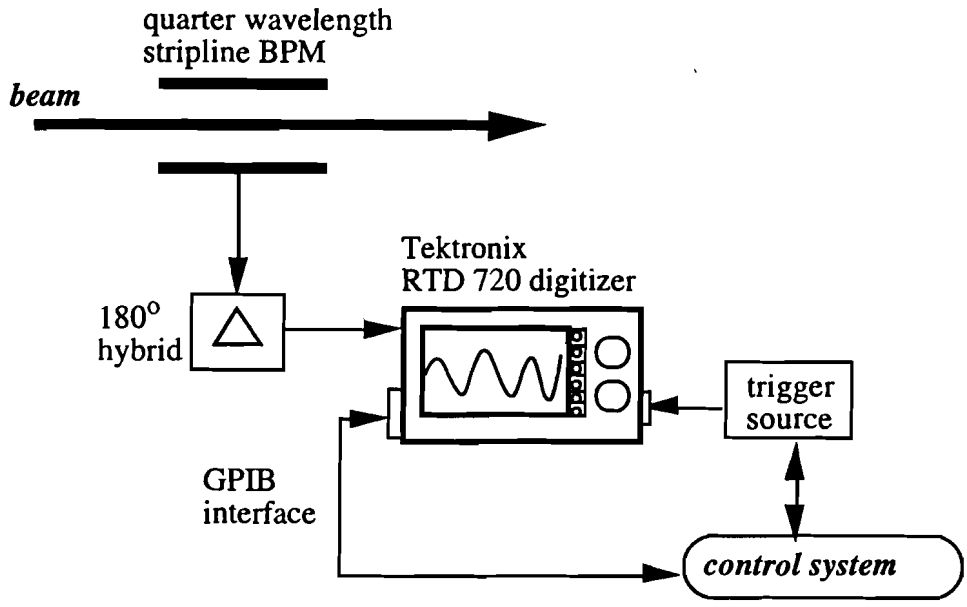

Fig. 5.13. The experimental setup for the qualitative measurement of vertical wake fields in the Main Ring.

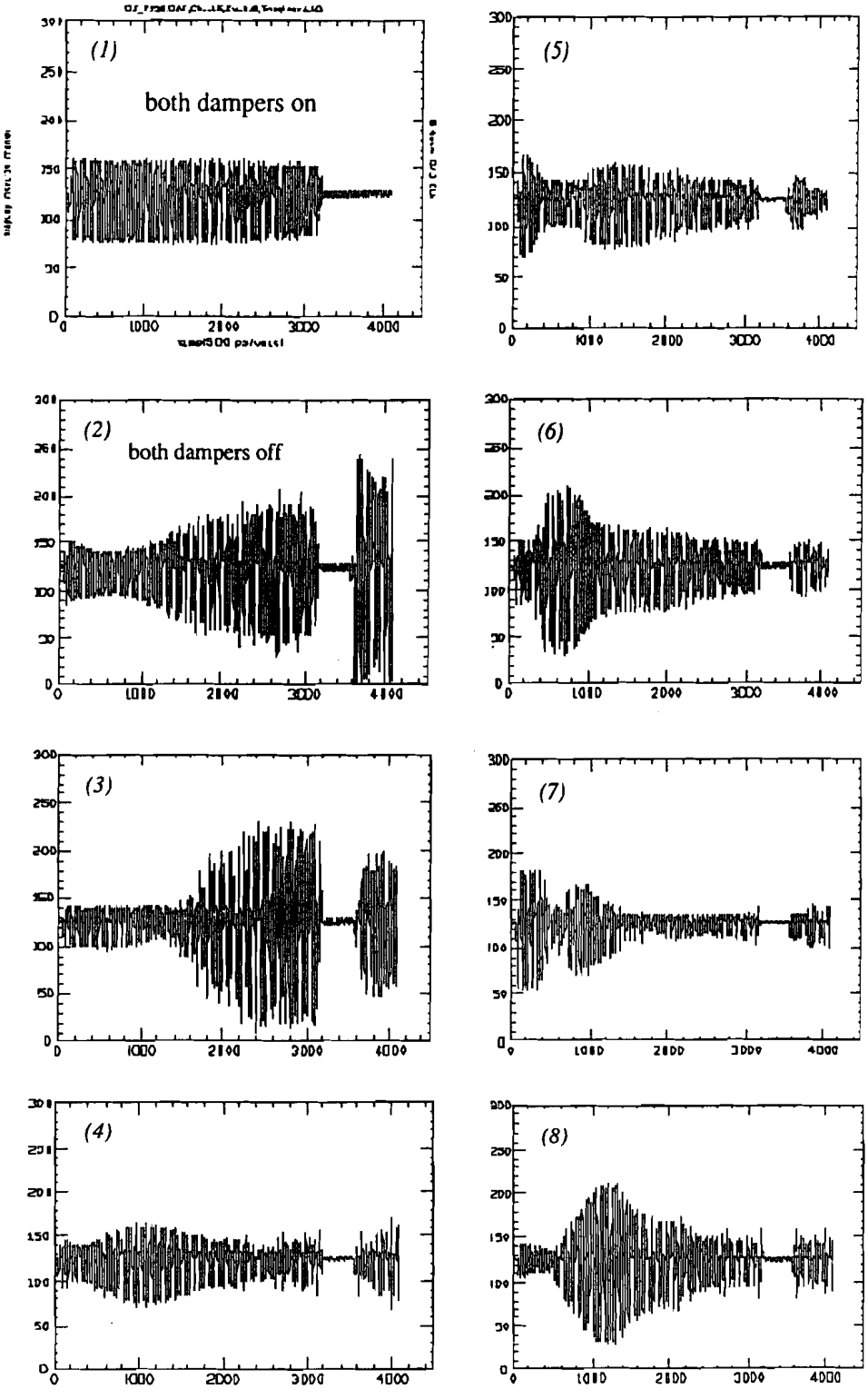
(1)
both dampers on
(2)
both dampers off
(3)
(4)
(5)
(6)
(7)
(8)

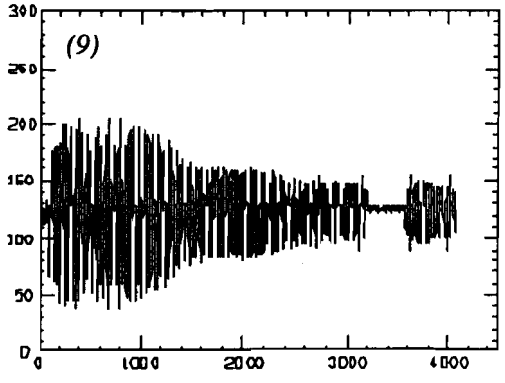

Fig. 5.14. The time series plot of the vertical bunch oscillation displayed at a time interval of every 160 turns (~ 3.4 msec). Both vertical dampers are turned on from the start until just before the injection of the second batch. The accelerator parameters used for the measurement are: horizontal chromaticity≈ -12, vertical chromaticity≈ 0, bunch length= 6 [nsec], and beam intensity= 3.3×10^{10} protons per bunch. One horizontal unit= 0.5 [nsec].

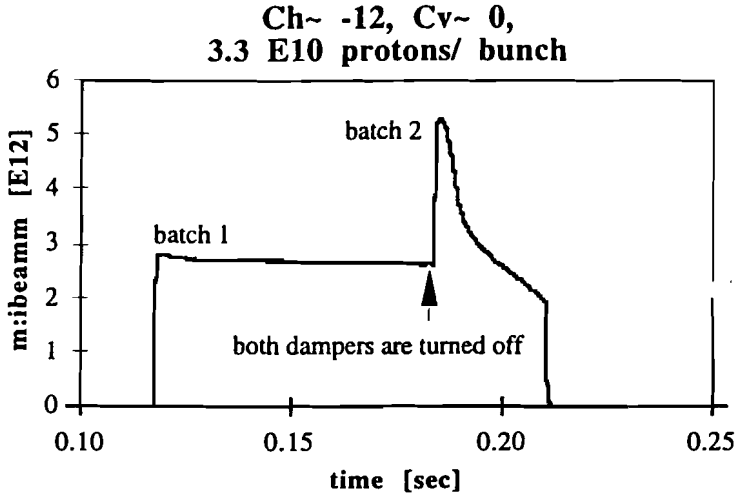

Fig. 5.15. A plot of the total beam intensity vs time in the Main Ring at 8 GeV. Both vertical dampers are turned on from the start until the injection of the second batch.

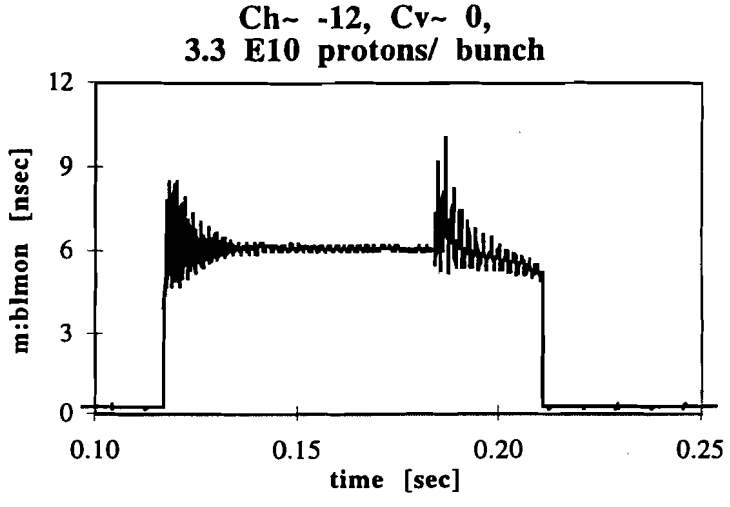

Fig. 5.16. A plot of the bunch length vs time in the Main Ring at 8 GeV. Both vertical dampers are turned on from the start until the injection of the second batch.

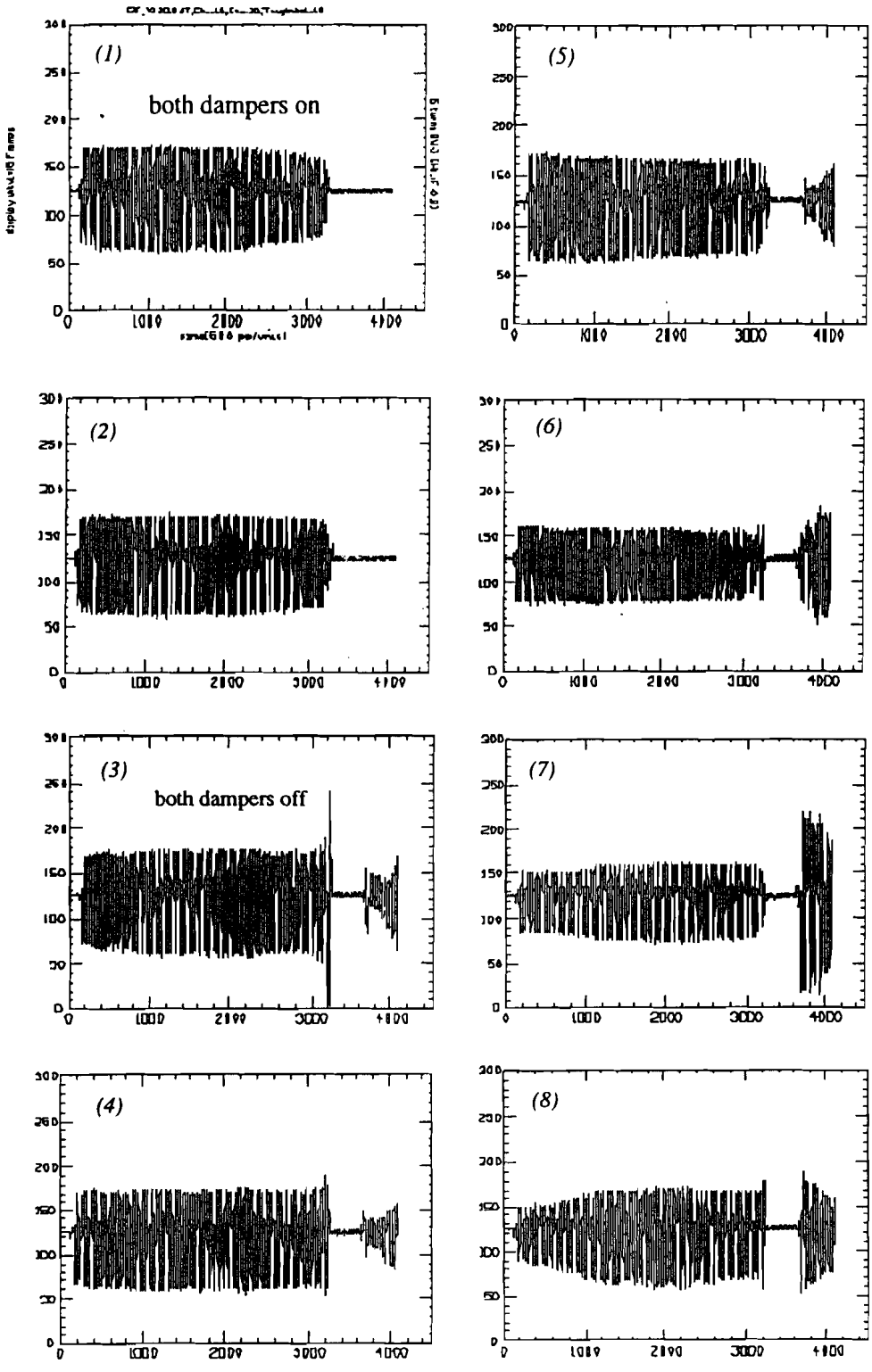
(1)
both dampers on
(2)
(3)
both dampers off
(4)
(5)
(6)
(7)
(8)

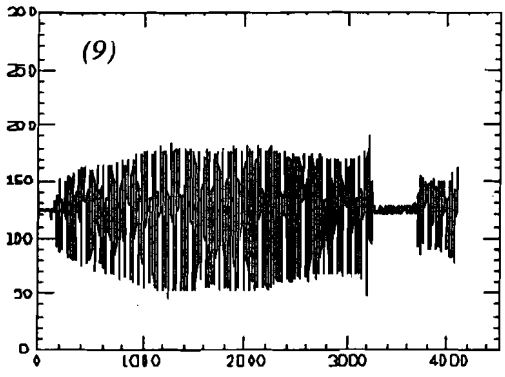

Fig. 5.17. The time series plot of the vertical bunch oscillation displayed at a time interval of every 160 turns (~ 3.4 msec). Both vertical dampers are turned on from the start until just before the injection of the second batch. The accelerator parameters used for the measurement are: horizontal chromaticity≈ -12, vertical chromaticity≈ -13, bunch length= 6 [nsec], and beam intensity= 2.7×10^{10} protons per bunch. One horizontal unit= 0.5 [nsec].

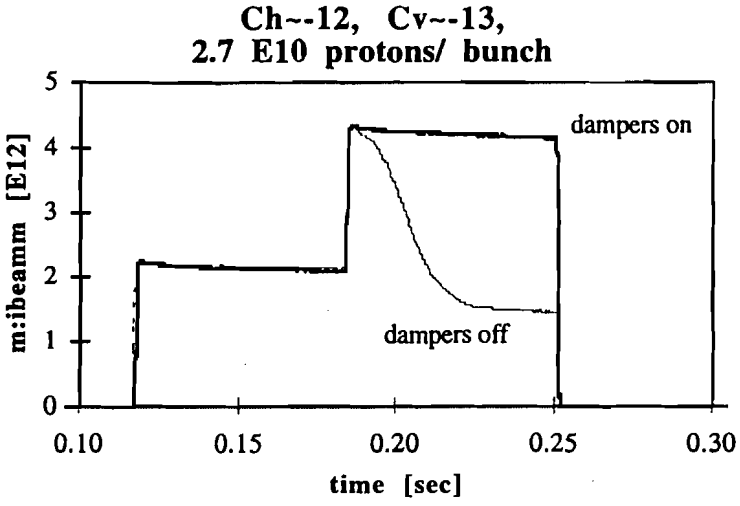

Fig. 5.18. A plot of the total beam intensity vs time in the Main Ring at 8 GeV. The thick line is the result when both vertical dampers are on all the time, and the thin line is the result when both vertical dampers are turned off right before the injection of the second batch.

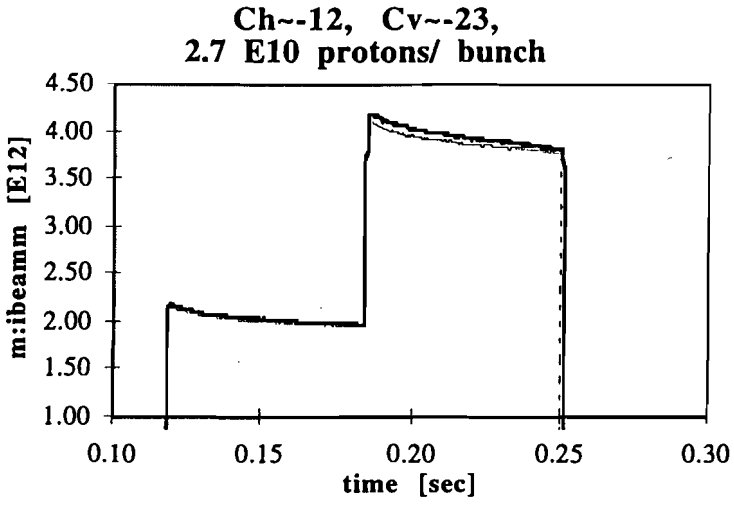

Fig. 5.19. A plot of the total beam intensity vs time in the Main Ring at 8 GeV. The thick line is the result when both vertical dampers are on all the time, and the thin line is the result when both vertical dampers are turned off right before the injection of the second batch. The m= 0 mode head-tail damping is able to counteract the coupled bunch instability with the vertical chromaticity≈ -23.

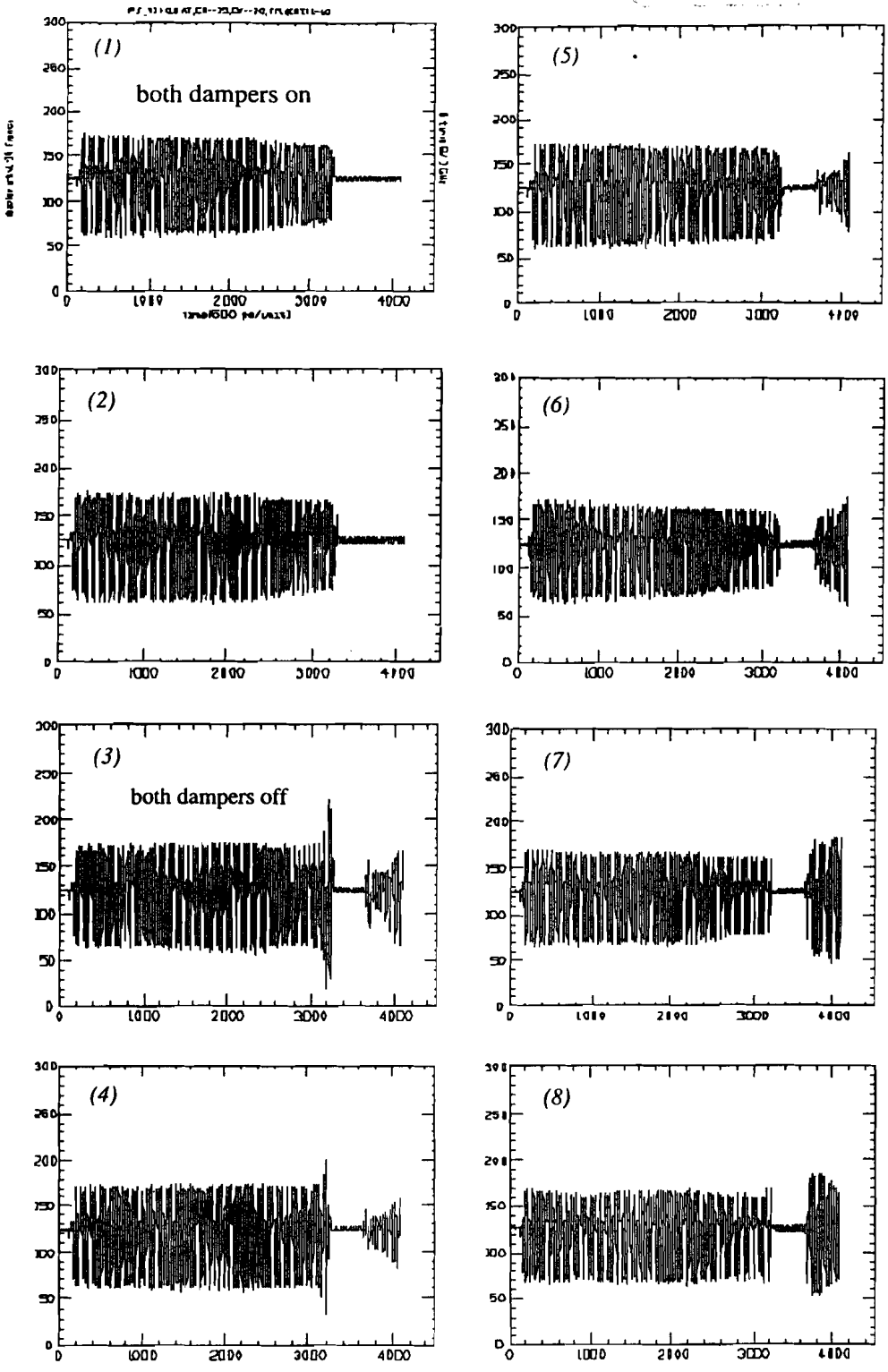

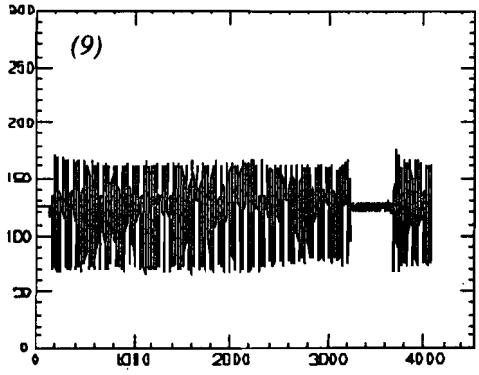

Fig. 5.20. The time series plot of the vertical bunch oscillation displayed at a time interval of every 160 turns (~ 3.4 msec). Both vertical dampers are turned on from the start until the injection of the second batch. The accelerator parameters used for the measurement are: horizontal chromaticity≈ -12, vertical chromaticity≈ -23, bunch length= 6 [nsec], and beam intensity= 2.7×10^{10} protons per bunch. One horizontal unit= 0.5 [nsec].

CHAPTER 6

DISCUSSIONS AND SUGGESTIONS

Results of beam studies reported in Chapter 4 and Chapter 5 are analyzed and satisfactory explanations are found. Once one understands the physics behind the observed beam instabilities at injection in the Main Ring, some ideas for improvement are readily realized. It is the ultimate goal of this thesis work to apply those findings to the Main Ring for even better performance, and perhaps a better design for the upcoming Main Injector.

A. Accelerator Tuning

Since the vertical head-tail instability at injection has been confirmed and observed (see Sec. D, Chap. 4), one can use a longer bunch length for the antiproton production cycle in the Main Ring. Because the growth rate of the single bunch head-tail instability decreases as the bunch length increases, a longer bunch length will help to raise the maximum beam intensity per bunch. But one must also keep in mind other issues involved in the Main Ring. Issues like the user's requirement, bunch coalescing, and the longitudinal beam instability need to be taken into account. A compromise solution is expected on the choice of maximum bunch length used in the Main Ring.

Although a negative value of chromaticity will provide the head-tail damping effect and help counteract the amplitude growth due to the coupled bunch instability, the value

required for an effective suppression of the amplitude growth is too large (see Figs 5.18 and 5.19). From the viewpoint of long-term beam lifetime, one should not use a large negative chromaticity for the operation of the Main Ring.

An ideal solution is to have a small positive value of chromaticity (below transition) for a stable m= 1 mode but unstable m= 0 mode head-tail motion. The unstable m= 0 mode head-tail motion can be cured by an active feedback system, provided the damper gain of the feedback system is large enough. This is the lesson learned from the explanation of the mysterious setting of chromaticity values found by operators in the main control room. In this way, one can get the amplitude damping for both the m= 0 and m= 1 head-tail motion which are the dominated single bunch effects observed in the Main Ring.

For the fixed target experiments, multiple booster batches are used in the Main Ring. It is recommended that Main Ring accelerator physicists adopt an alternate injection sequence for the multibatch operation, e.g. the pattern depicted in Fig. 4.26. Studies show that a 10 % increase in the total stored beam intensity can be obtained approximately.

It is also recommended that Main Ring accelerator physicists perform a measurement on the bunch form factor $F_m(\chi)$ at the beginning of accelerator turn-on after each major shutdown. Knowing the bunch form factor will help to find the appropriate values for both the horizontal and vertical chromaticity in a shorter time. A shorter time needed for commissioning the accelerator will translate into a higher efficiency of operation.

B. Hardware upgrade

Since the results of studies show the indispensable role of active feedback system as a cure of the vertical beam instabilities in the Main Ring, an upgrade of the present damper systems is necessary.

From results shown in Sec. B.1.2 of Chap. 4, the common mode rejection ratio (CMRR) of the receiver in the feedback system needs to be improved. If the power level of revolution harmonic lines due to the closed orbit offset can be significantly reduced, the feedback system will be able to work on the suppression of coherent beam motion more efficiently. The use of the notch filter or adaptive bias electronics can help to improve the CMRR.

The maximum damper gain g (see Eq.(2.64)) of the vertical super damper is found to be around 0.019 from beam studies with multiple booster batches. The vertical slow damper is not very effective, and its maximum damper gain is found to be around 0.0016. Since the growth rate of beam instability is proportional to the beam intensity, one can use the linear extrapolation to estimate the required damper gain for achieving the goal of next fixed target run and the Main Injector design. It is estimated that the damper gain of present feedback system needs to be increased by a factor of 10, i.e. the required damper gain $g \geq 0.19$.

The results of impedance measurements in the low frequency range suggest other impedance sources besides the resistive wall. It is recommended that bench measurements of the transverse impedance for major accelerator components such as rf cavities, kicker magnets, bellows and flanges be performed. Since there are alarming results obtained for the longitudinal impedance of kicker magnets,[50] it is important to perform bench measurements of the transverse impedance for the kicker magnets. To ensure the same problem will not appear in the future Main Injector, a better design to reduce the impedance of the kicker magnets should be pursued. A smooth change in the cross-sectional profile of vacuum chamber should be used for the Main Injector design. The design of beam diagnostic instrumentation should also adopt the same guide line as mentioned for the vacuum chamber.

REFERENCES

[1]A.V. Tollestrup, Fermilab Report No. Fermilab-Conf-94/378-E, 1994 (unpublished).

[2]V. Weisskopf, The Joy of Insight: Passions of a Physicist (Basic Books, New York, 1991).

[3]D.A. Edwards and M.J. Syphers, An Introduction to the Physics of High Energy Accelerators (Wiley, New York, 1993).

[4]R. Stiening and E.J.N. Wilson, Nucl. Instrum. Methods **121**, 283 (1974).

[5]G.Jackson, in Proc. IEEE Part. Accel. Conf., San Francisco (1991), p. 1755.

[6]S.D. Holmes, R.E. Gerig and D.E. Johnson, Fermilab Report No. Fermilab-Conf-89/183, 1989 (unpublished).

[7]G. Jackson, ed. "Recycler Ring Conceptual Design Study", Fermilab Report No. Fermilab-TM-1936, 1995 (unpublished).

[8]H. Wiedemann, Particle Accelerator Physics, Vol.I (Springer-Verlag, New York, 1993).

[9]P. Horowitz and W. Hill, The Art of Electronics, 2nd ed. (Cambridge, New York, 1989).

[10]E.C. Jordan (ed.), Reference Data for Engineers:Radio, Electronics, Computer, and Communications, 7th ed. (Howard W. Sams, Indiana, 1989).

[11]P.M. Morse and H. Feshbach, Methods of Theoretical Physics (McGraw-Hill, New York, 1953).

[12]R. Siemann, "Bunched Beam Diagnosis", in AIP Conf. Proc. No. 184, edited by M. Month (AIP, New York, 1989), pp. 430- 471.

[13]D.A. Goldberg and G.R. Lambertson, "Dynamic Devices: A Primer on Pickups and Kickers", in AIP Conf. Proc. No. 249, edited by M. Month (AIP, New York, 1992), pp. 537- 600.

[14]R.C. Webber, Fermilab Report No. Fermilab-Conf-94/333, 1994 (unpublished).

[15]T.Ieiri and G. Jackson, Fermilab Report No. Fermilab-TM-1600, 1989 (unpublished).

[16]R.C. Webber, Fermilab Report No. Fermilab-TM-1655, 1990 (unpublished).

[17]R.C. Webber, Fermilab Report No. Fermilab-TM-1577, 1989 (unpublished).

[18]R.H. Siemann, Fermilab Report No. Fermilab-EXP-155, 1987 (unpublished).

[19]P.J. Chou, B. Fellenz and G. Jackson, Fermilab Report No. Fermilab-TM-1941, 1995 (unpublished).

[20]B.C. Wadell, Transmission Line Design Handbook (Artech House, Norwood, MA, 1991), p. 93.

[21]R.E. Collin, Foundations for Microwave Engineering (McGraw-Hill, New York, 1966).

[22]J.J. DiStefano et al., Schaum's Outline of Theory and Problems of Feedback and Control Systems, 2nd ed. (McGraw-Hill, New York, 1990).

[23]S. Wolfram, computer program Mathematica, version 2.2 (Wolfram Research, Champaign, IL, 1993).

[24]J.D. Jackson, Classical Electrodynamics, 2nd ed. (Wiley, New York, 1975).

[25]A.W. Chao, Physics of Collective Beam Instabilities in High Energy Accelerators (Wiley, New York, 1993), Chap. 2.

[26]F.J. Sacherer, Proceedings of the 9th International Conference on High Energy Accelerators (1974), p. 347.

[27]S. Kheifets and B. Zotter, Nucl. Instrum. Methods **A243**, 13 (1986).

[28]S.S. Kurennoy, Part. Accel. **39**, 1 (1992).

[29]A. Hofmann, in Proceedings of the 11th International Conference on High Energy Accelerators, CERN (1980), edited by W.S. Newman (Birkhäuser Verlag, 1980), p.540.

[30]G.V. Stupakov and S.S. Kurennoy, Phys. Rev. E **49**, 794 (1994).

[31]S. Heifets and G. Stupakov, SLAC Report No. SLAC/AP-98, 1995 (unpublished).

[32]S. Fornaca et al., in Proc. IEEE Part. Accel. Conf., Washington (1987), p. 1818.

[33]S.A. Heifets and S.A. Kheifets, Rev. Mod. Phys. **63**, 631 (1991).

[34]J. Gareyte, "Observation and Correction of Instabilities in Circular Accelerators", in Frontiers of Particle Beams: Intensity Limitations, edited by M. Dienes et al., (Springer-Verlag, Berlin, 1992), pp. 134- 167.

[35]F. Sacherer, CERN Report No. CERN/ SI- BR/ 72-5, 1972 (unpublished).

[36]J.L. Laclare, "Bunched Beam Coherent Instabilities", in Proc. of CERN Advanced Accelerator School, Oxford (1985), edited by S. Turner, Report No. CERN 87-03 (unpublished).

[37]L. Landau, J. Phys. (U.S.S.R.) **10**, 25 (1946).

[38]M. Cornacchia et al., internal report of Fermilab accelerator division, EXP- 56, 1974 (unpublished).

[39]J. Crisp, "Modification to the Main Ring Slow Damper System" (private notes).

[40]J. Crisp and G. Jackson (private communication).

[41]Robert A. Witte, Spectrum and Network Measurements (Prentice Hall, Englewood Cliffs, NJ, 1993).

[42]Glen R. Lambertson, "Electromagnetic Detectors", in Frontiers of Particle Beams; Observation, Diagnosis and Correction, edited by M. Month and S. Turner (Springer-Verlag, New York, 1989), pp.380- 402.

[43]J.L. Laclare, in Proceedings of the 11th International Conference on High Energy Accelerators, CERN (1980), edited by W.S. Newman (Birkhäuser Verlag, 1980), p.526.

[44]F. Caspers, "Bench Methods for Beam-Coupling Impedance Measurement", in Frontiers of Particle Beams: Intensity Limitations, edited by M. Dienes et al., (Springer-Verlag, Berlin, 1992), pp. 80- 109.

[45]D. Möhl and A.M. Sessler, in Proceedings of the 8th International Conference on High Energy Accelerator, CERN (1971), edited by M. Hildred Blewett (CERN, Geneva, 1971), p. 334; also in Lawrence Berkeley National Laboratory Report No. LRL- 42 (unpublished).

[46]A. Hofmann and B. Zotter, IEEE Trans. Nucl. Sci., **NS-24**, No. 3, 1487 (1977).

[47]D. Boussard, CERN Report No. CERN/PS 93- 44 (AR), 1993 (unpublished).

[48]U. Oeftiger and F. Caspers, CERN Report No. CERN/ PS/ AR/ Note 92-19, 1992 (unpublished).

[49]A. Hahn (private communication).

[50]P.L. Colestock et al., in Proc. IEEE Part. Accel. Conf., San Francisco (1991), p. 1740.

[51]G. Nassibian and F. Sacherer, Nucl. Instrum. Methods **159**, 21 (1986).

[52]Y. Miyahara and K. Takata, Part. Accel. **10**, 125 (1980).

[53]H. Figueroa et al., Phys. Rev. Lett. **60**, 2144 (1988).

[54]C. Adolphsen et al., Phys. Rev. Lett. 74, 2475 (1995).

[55]T. Barklow et al., "Review of Lattice Measurement Techniques at the SLC", in AIP Conf. Proc. No. 255, edited by A. W. Chao, (AIP, New York, 1992), pp.347- 354.

[56]M.J. Yang, Fermilab Report No. Fermilab-TM-1922, 1995 (unpublished).